Loughborough University

This item was submitted to Loughborough's Research Repository by the author.
Items in Figshare are protected by copyright, with all rights reserved, unless otherwise indicated.

An investigation of gas void fraction and transition conditions for two-phase flow in an annular gap bubble column

PLEASE CITE THE PUBLISHED VERSION

PUBLISHER

Loughborough University

LICENCE

CC BY-NC-ND 4.0

REPOSITORY RECORD

Al-Oufi, Fahd M.. 2011. “An Investigation of Gas Void Fraction and Transition Conditions for Two-phase Flow in an Annular Gap Bubble Column”. figshare. https://hdl.handle.net/2134/8499.

Loughborough University

This item was submitted to Loughborough's Institutional Repository (https://dspace.lboro.ac.uk/) by the author and is made available under the following Creative Commons Licence conditions.

creative commons

COMMONS DEED

Attribution-NonCommercial-NoDerivs 2.5

You are free:

- to copy, distribute, display, and perform the work

Under the following conditions:



Attribution. You must attribute the work in the manner specified by the author or licensor.



Noncommercial. You may not use this work for commercial purposes.



No Derivative Works. You may not alter, transform, or build upon this work.

- For any reuse or distribution, you must make clear to others the license terms of this work.
- Any of these conditions can be waived if you get permission from the copyright holder.

Your fair use and other rights are in no way affected by the above.

This is a human-readable summary of the Legal Code (the full license).

Disclaimer

For the full text of this licence, please go to:
http://creativecommons.org/licenses/by-nc-nd/2.5/



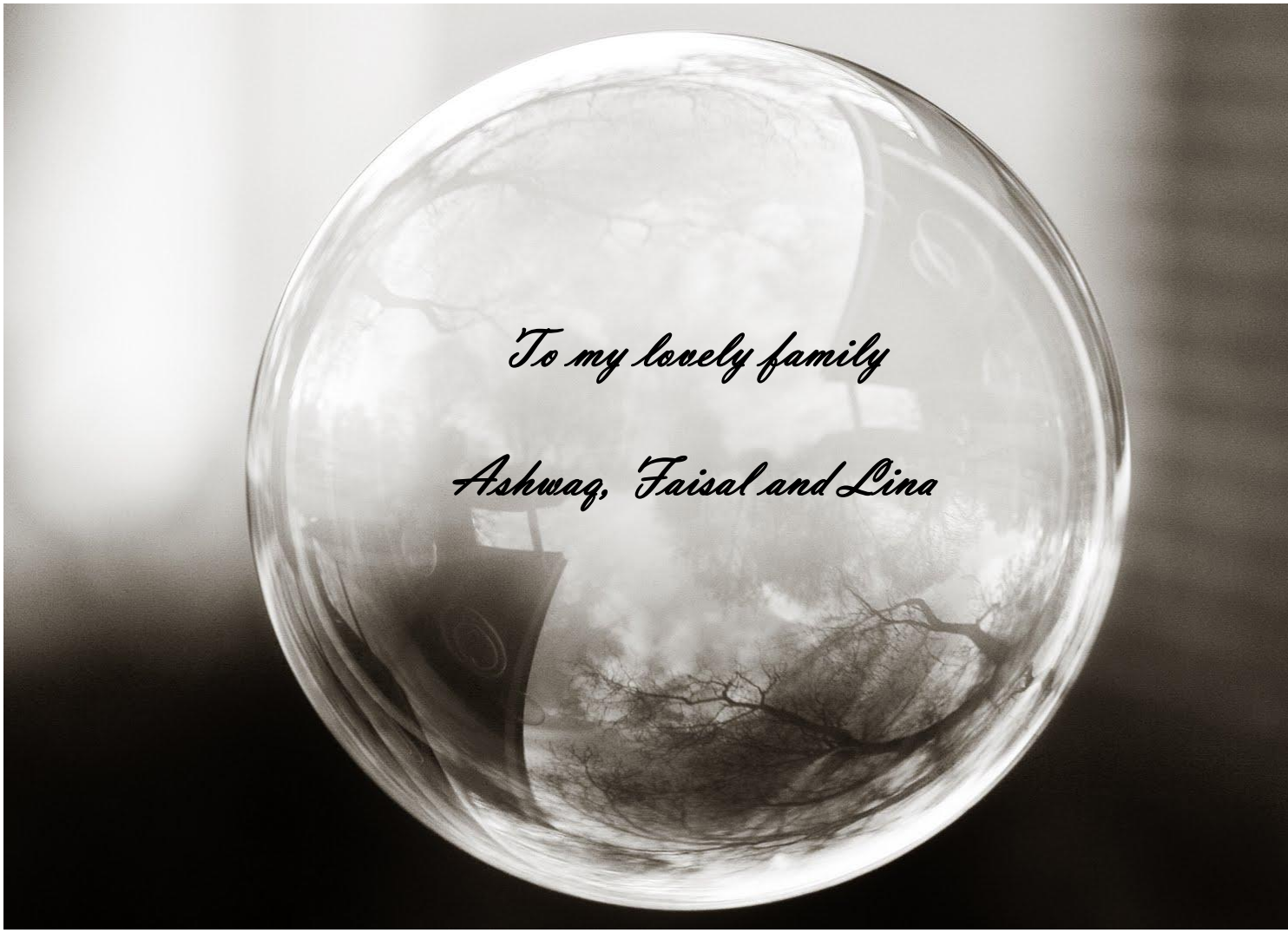
AN INVESTIGATION OF GAS VOID FRACTION AND TRANSITION CONDITIONS FOR TWO-PHASE FLOW IN AN ANNULAR GAP BUBBLE COLUMN

by

FAHD MAHBOOB ALOUFI

A Doctoral Thesis submitted in partial fulfilment of the requirements for the award of the degree of Doctor of Philosophy in Chemical Engineering

© by Fahd Aloufi (2011)


To my lovely family
Ashwaq, Faisal and Lina

ABSTRACT

Gas-liquid flow may be characterised in terms of the gas void fraction, α. This is an important variable in two-phase flow, used in predicting the occurrence of flow regimes, and the associated pressure drop, and mass and heat transfer. The gas void fraction transitions in a two-phase flow system from uniform bubble flow (homogeneous) to churn-turbulent bubble flow (heterogeneous) in an open tube bubble column (OTBC) and an annular gap bubble column (AGBC) have been investigated using a vertical column with an internal diameter of 0.102 m, containing a range of concentric inner tubes which formed an annular gap; the inner tubes had diameter ratios from 0.25 - 0.69. Gas (air) superficial velocities in the range 0.014-0.200 m/s were studied. Tap water and aqueous solutions of ethanol and isopropanol, with concentrations in the range 8 - 300 ppm by mass, were used as the working liquids.

Experimental results are presented to show that there are very significant differences in the mean gas void fractions measured in the OTBC and the AGBC, when operated at the same gas superficial velocity using a porous sparger. The mean gas void fraction decreases with increasing ratio of the inner to outer diameter of the annular gap column and the transition to heterogeneous flow occurs at lower gas superficial velocities and lower void fractions. Two reasons are proposed and validated by experimental investigations: (i) the presence of the inner tube causes large bubbles to form near the sparger, which destabilize the homogeneous bubbly flow and reduce the mean void fraction; this was confirmed by deliberately injecting large bubbles into a homogeneous dispersion of smaller bubbles. Moreover, (ii) the shape of the void fraction profiles changes with gap geometry, which affects the distribution parameter in the drift flux model.

Radial profiles of the local void fraction were obtained using a two- and four-point conductivity probe, and were cross-sectionally averaged to give mean values that were within 12% of the volume-averaged gas void fractions obtained from changes in aerated level. The presence of alcohol inhibited the

coalescence between the bubbles, and consequently increased the mean gas void fraction at a given gas superficial velocity in both the open tube and the annular gap bubble columns. This effect also extended the range of homogeneous bubbly flow and delayed the transition to heterogeneous flow. Moreover, isopropanol results gave slightly higher mean void fractions compared to those for ethanol at the same mass fraction, due to their increased carbon chain length. It was shown that the void fraction profiles in the annular gap bubble column were far from uniform, leading to lower mean void fractions than were obtained in an open tube for the same gas superficial velocity and liquid composition.

The chord length measurements in the OTBC for both the tap water and alcohol solutions exhibited two trends with respect to increasing j_g: (i) at low j_g, in the homogeneous flow, an increasing function was obtained; and (ii) with further increase in j_g, a reduction in the chord length was observed. In the presence of the orifice, the results concerning mean chord lengths show a decreasing function of the bubble size with increasing j_g; this was visually demonstrated using photographs. For the AGBC, the chord lengths obtained from the conductivity probe offered evidence of the bubble size decreasing as j_g increased in the heterogeneous regime, which agreed with the findings of the OTBC. This was also confirmed using the results obtained from photographs.

A novel approach for bubble size transformation was implemented to process the conductivity probe measurements. An analytical method was used as a forward transform to predict the chord length distribution from the bubble size distribution and an optimisation approach was applied as a backward transform method to obtain the bubble size distribution from the chord length distribution. The challenge was to consider a variable aspect ratio, φ, for the bubble shape, which depended on their size. The model gave excellent and reasonable predictions for the bubble sizes as their trends were identical to the trend of the chord length, and to the bubble size obtained from photographs.

ACKNOWLEDGEMENTS

First and foremost, I thank Almighty Allah (God) for blessing me with success and prosperity. I would like to thank all the people who have supported me in various ways throughout the period of this doctoral research. In particular, I would like to thank my supervisors, Prof. Chris Rielly and Dr. Cumming for their enthusiasm, guidance and continuous encouragement throughout the research. Special recognition is also paid to their incredible patience, their many fruitful discussions and excellent ideas.

I would like to take this golden opportunity to show my appreciation, gratitude and deep thanks to all those people who helped me in carrying out my research and provided all kinds of support in the Department of Chemical Engineering; from the administrative staff: Yasmin, Anna, Liz, Ann, Janey and Becky; from support and technical staff: Terry, Jim, Paul, Sean, Tony, and Dave. I would also like to thank the lab technicians, Graham, Monika and Kim for helping me with the fittings and connections. My thanks also go to Mark and Steve for doing a great job manufacturing the new equipment.

I would like to express my gratitude to my sponsor the Royal Commission of Jubail & Yanbu (RC); Yanbu Industrial College (YIC). My sincere thanks is extended to my friends in S158: Hakem Alshalaan, Dr. Redah Alsabei, Dr. Saleemi, Dr. Bahareh, Dr. Matthew and Alhajji for their support and encouragement.

Thanks and gratitude to my parents and my parents-in-law, who have been the greatest driving force behind my PhD, and I absolutely could not have finished without their support, love and prayers. To all my family; my brothers, sisters and cousins, especially my dear brother, Abdusalaam, and my dear cousin, Torky; you have inspired me to go far and get the PhD.

Last but not least, I would like to extend my sincere gratitude to my wife, my son and my daughter, you have always there for me and there is no way I can repay you, my thesis dedication is the smallest gesture I can offer.

TABLE OF CONTENTS

ABSTRACT ..... **i**

ACKNOWLEDGEMENTS ..... **iii**

LIST OF FIGURES ..... **xi**

LIST OF TABLES ..... **xxiii**

NOMENCLATURE ..... **xxiv**

CHAPTER ONE **1**

1 INTRODUCTION **1**

1.1 Background 1

1.2 Applications of bubble and airlift columns 3

1.3 Motivation 4

1.4 Research aims and objectives 6

1.5 Main contributions of the study 8

1.6 Structure of the Thesis 9

CHAPTER TWO **11**

2 LITERATURE REVIEW **11**

2.1 Introduction 11

2.2 Gas void fraction in bubble columns 12

2.2.1 Liquid height and column diameter 12

2.2.2 Gas distributor configurations 17

2.2.3 Water contamination 21

2.2.4 Influence of alcohol on gas void fraction 22

2.3 Annular gap bubble columns 25

2.4 Implementation of an impedance method in two-phase flow 29

2.4.1 Single-point conductivity probe 30

2.4.2 Two-point conductivity probe 31

2.4.3 Four-point conductivity probe 32

2.5 Bubble size and velocity 33

2.5.1 Bubble size 33

2.5.2 Bubble rise velocity 35

2.6 Image visualisation/analysis 39

2.7 Conclusion 40

CHAPTER THREE 42

3 MEASURING TECHNIQUES, SIGNAL PROCESSING AND BUBBLE SIZE TRANSFORMATION 42

3.1 Introduction 42

3.2 Aerated level technique 42

3.3 Setup and design of imaging experiments 43

3.4 Conductivity technique 49

3.4.1 Introduction 49

3.4.2 Conductivity experiment setup 49

3.4.3 Design and dimensions of the probe 51

3.4.4 Assessment of the exposed tip length 54

3.4.5 Conductivity measurement principles of a gas-liquid system 56

3.4.6 Visualisation of bubble interaction with the probe to understand the signal shape 57

3.4.7 Probe signal processing 63

3.4.8 Local and mean gas void fraction 68

3.4.9 Different sampling rates 70

3.4.10 Bubble velocity and chord size calculation 72

3.4.11 Transformation of chord length to bubble size 75

3.5 Conclusion 85

CHAPTER FOUR 87

4 OPEN TUBE BUBBLE COLUMN (OTBC) 87

4.1 Introduction 87

4.2 Experimental setup and design 87

4.3 Preliminary tests 89

4.3.1 Development of an experimental protocol to give repeatable results 90

4.3.2 Investigation of hysteresis effects in homogeneous and transition flow 91

4.3.3 Selection of the working fluid 93

4.3.4 Selection of sparger type 95

4.3.5 Selection of liquid height 97

4.3.6 Probe height selection 99

4.4 Conclusion from the preliminary experiments 102

4.5 Investigations on the addition of alcohol 102

4.5.1 Effects of alcohol concentration on gas void fraction profiles in the OTBC 105

4.5.2 Mean gas void fraction in an OTBC with tap water 109

4.5.3 Mean gas void fraction in the OTBC with aqueous alcohol solutions 111

4.6 Effects of alcohol concentration on flow regime transitions in the OTBC 114

4.7 Measurements of bubble size and velocity 117

4.7.1 Chord length in the OTBC 117

4.7.2 Bubble velocity in the OTBC 120

4.7.3 The Sauter mean diameter, d_{32},in the OTBC 123

4.7.4 The volume average mean diameter,d_{43}, in the OTBC 126

4.7.5 The standard deviation of the lognormal bubble size distribution 128

4.8 Conclusion 132

CHAPTER FIVE 134

5 DESTABILISATION OF HOMOGENEOUS FLOW BY INTRODUCTION OF LARGE BUBBLES 134

5.1 Introduction 134

5.2 Experimental setup and design 134

5.3 Local gas void fraction 138

5.4 Mean gas void fraction 143

5.5 The distribution parameter in the OTBCEO 144

5.6 The effect of the presence of orifices on the transition condition 146

5.7 Bubble size and velocity measurements 150

5.7.1 The effect of orifices on the chord length 150

5.7.2 The effect of orifices on the bubble velocity 152

5.7.3 The effect of orifices on the Sauter mean diameter 154

5.7.4 The effect of orifices on the volume average mean diameter, d_{43} 156

5.7.5 The effect of orifices on the standard deviation 160

5.8 Conclusion 162

CHAPTER SIX 164

6 ANNULAR GAP BUBBLE COLUMN (AGBC) 164

6.1 Introduction 164

6.2 Experimental setup and design 164

6.3 Preliminary tests 166

6.3.1 Inner tube height 166

6.3.2 Bottom end shape of the inner tube 168

6.3.3 Inner tube position.....170

6.3.4 Conclusions from the preliminary experiments.....171

6.4 Local and mean gas void fraction in AGBC 172

6.4.1 The local gas void fraction in an AGBC with tap water and aqueous alcohol solutions 172

6.1.1 Mean gas void fraction in an AGBC with tap water 175

6.4.2 Influence of alcohol on the mean gas void fraction in the AGBC.... 177

6.5 The distribution parameters in the AGBC 180

6.5.1 The effect of annular gaps with tap water on the distribution parameter 180

6.5.2 The influence of the alcohol aqueous solution on the distribution parameters in AGBC.....181

6.6 Flow regime transitions in the AGBC 182

6.7 Measurements of bubble size and velocity 185

6.7.1 Mean chord length in AGBC.....185

6.7.2 Mean bubble velocity in AGBC.....187

6.7.3 Sauter mean diameter in AGBC.....189

6.7.4 Mean diameter, d_{43}, in AGBC.....191

6.7.5 Bubble size distribution in AGBC 192

6.8 Conclusions.....194

CHAPTER SEVEN 196

7 CONCLUSIONS AND RECOMMENDATIONS 196

7.1 Conclusions 196

7.2 Recommendations and future work 199

REFERENCES 201

APPENDICES 216

Appendix A 216

Image analysis codes 216

Appendix B 223

LabView block diagram and interface 223

Appendix C 225

Sample calculation 225

Appendix D 231

Signal processing DEVELOPMENT 231

LIST OF PUBLICATIONS 247

LIST OF FIGURES

Figure 1.1 Mean void fraction for air-tap water with respect to gas superficial velocity. The mean gas void fraction was obtained from the change of level in the bubble columns (internal diameter, D_o = 0.102 m) on aeration by using a sintered plastic sparger (Al-Oufi, 2006).....3

Figure 1.2 Comparisons of measured gas void fractions for air-tap water in (i) an open tube (D_o = 0.102 m) and (ii) an annular gap bubble column (inner tube diameter, D_i = 0.051 m, D_o = 0.102 m). The mean gas void fraction was obtained from the change of level in the bubble columns on aeration; data from Al-Oufi (2006). 6

Figure 2.1 Effect of liquid height on transition velocity in air-water system, data reproduced from Sarrafi *et al.* (1999). 14

Figure 2.2 Effect of column diameter on the transition superfical velocity as proposed by Sarrafi *et al.* (1999).....16

Figure 2.3 Effect of aspect ratio H_L/ D_o on the transition superfical velocity (reproduced from Ruzicka *et al.,* 2001). 16

Figure 2.4 Mean gas void fractions for a variety of perforated plate spargers, provided by Zuber and Hench (1962). (See Table 2.2 for details of their perforated plate spargers.).....18

Figure 2.5 Influence of orifice diameter size on transition superficial velocity, data reproduced from Sarrafi *et al.* (1999). 20

Figure 2.6 Effect of liquid contamination on gas void fractions, according to Anderson and Quinn (1970). 22

Figure 2.7 Accumulation of alcohol molecules (hydrophilic and hydrophobic) at the air-liquid interface to form a non-coalescing solution. 24

Figure 2.8 Effect of the presence of alcohol; Wallis plot to determine transition parameters α_{trans} and $(j_g)_{trans}$ (Krishna *et al.,* 2000). 25

Figure 2.9 Void fraction data comparison for open tube and annular gap at the same superficial gas velocities (Al-Oufi, 2006). 26

Figure 2.10 Terminal rise velocity with respect to equivalent diameter, d_e, of a bubble (Gaudin, 1957). 38

Figure 3.1 Aerated level technique to measure the overall gas void fraction. 43

Figure 3.2 Setup of image experiments. 44

Figure 3.3 a) An image of the transparent test section shows the attached scale; b) A typical image produced by the camera of bubbles at low gas flow rate.....45

Figure 3.4 A typical image showing the steps used to determine data on bubble sizes, shapes and orientations. 46

Figure 3.5 Schematic diagram of a bubble showing the long axis *a*, short axis *b* and orientation *θ*. 47

Figure 3.6 The final appearance of an image after identifying more than 250 bubbles using the MATLAB imaging analysis codes. The image is for air-tap water flow in an open tube column with a porous sparger and j_g =0.144 m/s.48

Figure 3.7 Setup of the experimental probe rig. 50

Figure 3.8 An image of the probe setup designed to measure α, bubble velocity and chord size.....50

Figure 3.9 Probe design; top view sketch of the probe and flange ring shows the attached ruler. 51

Figure 3.10 Design and geometry of the two-point conductivity probe (not to scale); the inset shows the two-point conductivity probe. 52

Figure 3.11 A schematic of the four-point conductivity probe (not to scale); the inset shows the four-point conductivity probe alongside some typical bubbles. 53

Figure 3.12 Probe reaction test to the phase changes surrounding the probe tips. 55

Figure 3.13 Phase signals produced by immersing the tips in tap water. 56

Figure 3.14 Typical upstream raw signals (probe 1) 57

Figure 3.15 Probe response experiment: a) test section schematic diagram; b) top view (not to scale). 59

Figure 3.16 The probe (p1) signals show the de-wetting and re-wetting time and the time that the probe stays in the bubble; images confirm the signal output. 61

Figure 3.17 The raw signal of the four-point probe hit by the same bubble shown in Figure 3.16. 62

Figure 3.18 Raw signals showing a double bubble hitting probe I (p1), captured by frames in the matching assessment. 62

Figure 3.19 The bubble rise velocity: a comparison between image and probe methods. 63

Figure 3.20 The signal treatment steps flowchart. 64

Figure 3.21 A typical time history of the raw signals for air-water bubbly flow given using a four needle-probe 65

Figure 3.22 Histogram method used to determine the cut off line from the raw signal produced by probe 1. 67

Figure 3.23 A signal obtained from a single conductivity probe, p1: (a) raw signal with the liquid baseline and threshold and (b) the phase discriminated 0-1 signal, where 0 is the liquid phase and 1 is the gas phase. 68

Figure 3.24 Typical gas void fraction profile across the column for different gas superficial velocities in the OTBC. 70

Figure 3.25 Void fraction with respect to the different sampling rates. 72

Figure 3.26 Chord length distribution for air-tap water flow using a porous sparger at j_g=0.17 m/s measured by the conductivity probe in the OTBC. 75

Figure 3.27 Flowchart for the signal processing and the optimisation model. 78

Figure 3.28 The cumulative probability function for the pdf $P_p(R)$ to generate a random deviate; x is in the range [0,1]. 79

Figure 3.29 The pdf of $P_p(R)$ (Equation 3.21) and the histogram of the random deviates of R compared to $P_p(R)$. 81

Figure 3.30 A side and top view of a bubble of radius R_i is pierced at an eccentricity e. 82

Figure 3.31 Comparison of analytical and Monte-Carlo methods for a fixed aspect ratio, $\varphi=0.8$, the red lines represents the Monte-Carlo method. 84

Figure 3.32 The final output comparison of the measured and predicted chord length according to a variable aspect ratio. 85

Figure 4.1 The experimental setup for the open tube bubble column. 88

Figure 4.2 Repeatability tests for the initial experimental runs in the OTBC. . 91

Figure 4.3 Comparison between sequential and random methods of varying the gas flow rate. 93

Figure 4.4 Comparison of the gas void fraction results for contaminated water with results for high purity water in the OTBC. 94

Figure 4.5 Comparison of the experiments and Anderson and Quinn (A&Q) (1970) regarding gas void fractions for measured contaminated and high purity water in the OTBC. 95

Figure 4.6 Comparison of gas void fractions and transition rates between results for the sintered plastic and the sintered glass spargers in the OTBC. 96

Figure 4.7 Effect of liquid height on the gas void fraction and the transitional superficial velocity: a comparison of 0.8 and 1.0 m water heights. 98

Figure 4.8 Schematic diagram for the local $\boldsymbol{\alpha}$ and its profile in an OTBC; the probe is placed at the centre of the column. 100

Figure 4.9 Gas void fraction with respect to j_g; comparison between the aerated level method and results using three different probe heights. 101

Figure 4.10 Open tube bubble column specifications and experimental conditions. 103

Figure 4.11 Surface tension with respect to various of concentrations (ppm by mass) of ethanol. 104

Figure 4.12 Profiles of the local gas void fraction with the distance from the wall, y, across a diameter of the open tube bubble column, using a porous sparger, tap water and assorted alcohol concentrations. The legend gives the gas superficial velocity. 106

Figure 4.13 The ratio of centreline void fraction, α_c, to the wall void fraction, $\alpha_{w,}$ with respect to the j_g in the OBTC. 107

Figure 4.14 Hibiki and Ishii's (2002) model for exponent *z* with respect to j_g: a) tap water and b) assorted alcohol concentrations; the experiments were conducted in an OTBC using a porous sparger. 108

Figure 4.15 Mean gas void fraction in the OTBC from measurements obtained from changing the aerated level compared to measurements using the conductivity probe. 110

Figure 4.16 Mean gas void fractions for various ethanol concentrations compared to results using tap water, obtained from employing the aerated level method. 112

Figure 4.17 Cross-sectional mean gas void fractions obtained by using the two-point conductivity probe method (probe 1) with gas superficial velocities for a range of alcohol concentrations. 112

Figure 4.18 Mean void fractions of ethanol and isopropanol concentrations at 300 ppm; these data were produced using the aerated level (filled symbols) and four-point conductivity probe methods (open symbols). 114

Figure 4.19 Wallis plot to determine transition parameters, α_{trans} and $(j_g)_{trans}$, for different ethanol concentrations in an OTBC. 115

Figure 4.20 Wallis plot: comparisons of tap water, ethanol and isopropanol in an OTBC. 116

Figure 4.21 Two-point conductivity probe output; chord length profile of the tap water in the OTBC with a porous sparger. 118

Figure 4.22 Mean chord length for a low concentration ethanol solution with respect to j_g. 119

Figure 4.23 Influence of alcohol on mean bubble chord length: a comparison of various ethanol concentrations and 300 ppm IPA with tap water. 120

Figure 4.24 Mean gas velocity profile with the distance from the wall, y, across the diameter of the OTBC, using tap water and a porous sparger. 121

Figure 4.25 Mean bubble velocity with respect to j_g; low ethanol concentrations compared to tap water. 122

Figure 4.26 A comparison of the mean bubble velocities of 300 ppm IPA, assorted ethanol concentrations and tap water. 122

Figure 4.27 Sauter mean diameter profiles for various j_g with respect to the distance (y) across the column; data obtained from tap water experiments. 123

Figure 4.28 Predicted Sauter mean diameter at various j_g for tap water and low ethanol concentrations. 124

Figure 4.29 Predicted Sauter mean diameter with respect to j_g: high alcohol concentrations compared to tap water. 125

Figure 4.30 A comparison of the Sauter mean diameter obtained from the conductivity probe and the image methods. 126

Figure 4.31 The mean diameter profiles with respect to the distance, y, across a diameter of the OTBC, obtained from the transformation process for tap water system. 126

Figure 4.32 The mean bubble diameter, $d_{43,}$ as a function of j_g; tap water compared to the assorted low ethanol concentrations. 127

Figure 4.33 The mean bubble diameter of various high alcohol concentrations compared to tap water. 127

Figure 4.34 Relationship between the mean bubble diameter, $d_{43,}$ and j_g: a comparison between conductivity probe and image techniques. 128

Figure 4.35 Profiles of the local lognormal standard deviation with the distance from the wall, y, across a diameter of the OTBC. 129

Figure 4.36 Lognormal standard deviation with respect to j_g: tap water (labelled as porous sparger) compared to the solution with low ethanol concentration. 130

Figure 4.37 Relationship between lognormal standard deviation and the gas superficial velocity: a comparison between tap water and assorted high alcohol concentrations. 130

Figure 4.38 The lognormal standard deviation obtained from the image method compared to the conductivity probe method. 131

Figure 5.1 Schematic diagram of the sintered plastic sparger showing the orifice located at the centre of the sparger (not to scale). 135

Figure 5.2 Fractions of air flow rate and pressure drops for a porous sparger and relatively small orifices. 137

Figure 5.3 Fractions of air flow rate and pressure drops for a porous sparger and relatively large orifices. 138

Figure 5.4 Profile of the local gas void fractions for different orifice diameters across the diameter of an open bubble column. The data were obtained using a two-point probe; the legend gives the gas superficial velocity. 140

Figure 5.5 The correlation of the void at the centreline, α_c, to the wall, α_w, with respect to the range of j_g 141

Figure 5.6 Values of the exponent z as a function of j_g calculated from the local gas void fraction using Hibiki and Ishii's power–law equation for a porous sparger (no orifice), and a sparger with orifice diameters < 1mm. 142

Figure 5.7 Exponent z over a range of j_g: comparison between porous sparger and large orifice diameters, d_o >1 mm. 142

Figure 5.8 Mean void fraction variations with superficial gas velocity for the empty column equipped: with a porous sparger, with and without a single orifice of various diameters, a) d_o<1mm and b) d_o>1 mm diameter; closed symbols derive from change in the aerated level method and open symbols are a cross-sectional mean determined by the conductivity probe method (probe 1) 144

Figure 5.9 Void fraction-weighted mean gas velocity with respect to gas superficial velocity; the mean void fraction data for a porous sparger with 0.8 mm orifice in an open tube obtained using the conductivity probe method (p1). 145

Figure 5.10 Distribution parameter, C_o, and rise velocity, v_t, values with respect to the orifice diameter, d_o; data obtained from the drift-flux model. .146

Figure 5.11 Drift-flux velocity with respect to mean α for a porous sparger, with and without orifice diameters: a) small orifices, d_o < 1 mm and b) large orifices, d_o> 1 mm 148

Figure 5.12 Mean gas void fractions for the porous sparger and for the same sparger with different central orifice sizes: comparisons with Zuber and

Hench's (Z&H) (1962) results (see Table 5.2 for details of their perforated plate spargers) 149

Figure 5.13 Mean chord length obtained by the conductivity probe with respect to j_g; a comparison between small orifices and a porous sparger ... 151

Figure 5.14 A comparison of the chord length between the porous sparger and large orifices; the results were obtained by calculating the mean of the chord length across the column at different values of j_g 152

Figure 5.15 The mean bubble velocity,v_g, with respect to j_g: data for small orifices compared to data for the porous sparger as obtained using a two-point conductivity probe 153

Figure 5.16 Mean bubble velocity results using large orifices with respect to j_g 154

Figure 5.17 Sauter mean diameter obtained using the optimisation model with respect to j_g: the porous sparger compared to a) small orifices, d_o <1 mm and b) large orifices, d_o >1 mm. 155

Figure 5.18 The Sauter mean diameter with respect to the gas superficial velocity for the 3.0 mm orifice: a comparison between the image method and the probe at the wall. 156

Figure 5.19 The mean diameter, d_{43} , predicted from the optimisation model with respect to j_g: the porous sparger was compared to a) small orifices, and b) large orifices. 157

Figure 5.20 A comparison of the mean diameter, d_{43}, obtained from photographs and the conductivity probe at the wall. 158

Figure 5.21 The bubble size as a decreasing function with respect to increasing j_g; images were taken from the 3 mm orifice experiments with tap water 159

Figure 5.22 Standard deviation of the bubble size distribution for the porous sparger and the small orifices with respect to j_g 160

Figure 5.23 Standard deviation of the bubble size distribution were obtained using the optimisation model; a comparison the porous sparger and the large orifices. 161

Figure 5.24 Results for the 3 mm orifice obtained from the conductivity probe method at the wall compared to the image method. 162

Figure 6.1 Typical annular gap setup, created by placing an inner tube with a conical bottom inside the 0.102 m column. 165

Figure 6.2 An annular 0.070 m tube at different heights inside a 0.0102 m column (not to scale).....167

Figure 6.3 The effect of inner tube height on bubble formation from the sparger.....168

Figure 6.4 Different bottom shapes: a) rod-shaped, b) cone-shaped, c) flat (not to scale). 169

Figure 6.5 A comparison of mean α data with respect to j_g for different inner tube bottom end shapes and an open tube. The data were obtained using the aerated level technique. 170

Figure 6.6 Plan view of the position of the β =0.69 inner tube in 0.102 m column: a) eccentric and b) concentric tube (not to scale). 171

Figure 6.7 Mean α with respect to j_g, and the effect of inner tube position on α; data were obtained using the aerated level technique. 171

Figure 6.8 Radial profile of local gas void fraction for different geometries of the annular gap bubble column, with the porous sparger in tap water. The vertical dashed line indicates the centreline of the annulus. The legend gives the gas superficial velocity (m/s). 174

Figure 6.9 Radial profiles of local gas void fraction for different geometries of the AGBC for 300 ppm ethanol. The vertical dashed line indicates the centreline of the annulus. The legend gives the gas superficial velocity (m/s). 175

Figure 6.10 Mean gas void fraction in the AGBCs compared to the OTBC results with tap water from measurements: a) of the change of aerated height (Equation 3.1), and b) using the two-point conductivity probe. 177

Figure 6.11 Mean gas void fraction in the AGBC compared to the OTBC for 300 ppm ethanol from measurements using a) change of aerated height (Equation 3.1), and b) two-point conductivity probe. 179

Figure 6.12 The effects of annular gap geometry on the mean gas void fraction, with a comparison to the open tube results for 300 ppm IPA from measurements using a) change of aerated height (Equation 3.1), and b) two-point conductivity probe. 180

Figure 6.13 The distribution parameter and the rise velocity with respect to the gap ratio for tap water. 181

Figure 6.14 The distribution parameter and the rise velocity with respect to the AGBC diameter ratio for 300 ppm ethanol and IPA solution. 182

Figure 6.15 Wallis plot to determine transition parameters α_{trans} and $(j_g)_{trans;}$ the mean gas void fraction data were obtained using the aerated level method. 183

Figure 6.16 Flux model to predict the α_{trans} and $(j_g)_{trans}$ for different annular gap geometries in a) 300 ppm ethanol and b) 300 ppm IPA aqueous solution. ..184

Figure 6.17 The drift-flux velocity with respect to the β ratio; influence of alcohol (300 ppm ethanol and IPA) on the stability of the homogeneous flow in OTBC and AGBC. 185

Figure 6.18 Mean chord length with respect to j_g; a comparison between assorted annular gaps and a porous sparger. 187

Figure 6.19 A comparison of the mean bubble velocity between different annular gap columns and a porous sparger for tap water, 300 ppm ethanol and IPA solutions. 188

Figure 6.20 Sauter mean diameter for various annular gaps and a porous sparger. 190

Figure 6.21 The Sauter mean diameter of β= 0.50 for tap water obtained from photographs compared to the probe method at the wall of the column. 190

Figure 6.22 Mean diameter, d_{43}, of annular gaps with respect to j_g; legend is the same as in Figure 6.18. 191

Figure 6.23 The mean diameter d_{43} of β= 0.50 in tap water for the image and the conductivity probe method. 192

Figure 6.24 Standard deviation of the AGBC compared to the OTBC in tap water and alcohol aqueous solutions. 193

Figure 6.25 Standard deviation of the AGBC compared in tap water; a comparison between the image and probe methods. 194

LIST OF TABLES

Table 2.1 A summary of the effect of certain variables considered in this study on the flow regime transition 12

Table 2.2 Gas distributor (sieve plate) configurations used by Zuber and Hench (1962) 18

Table 3.1 Variables was obtained from the comparison of analytical and Monte-Carlo methods in Figure 3.31 83

Table 4.1 The experimental conditions for the preliminary tests in the OTBC (D_o=0.102 m). 89

Table 4.2 Alcohol concentrations used in the OTBC experiments. 103

Table 4.3 Summary of α_{trans} and $(j_g)_{trans}$ for tap water and alcohol aqueous solutions in an OTBC. 115

Table 4.4 α_{trans} and $(j_g)_{trans}$ for tap water, ethanol and isopropanol aqueous solutions in an OTBC. 116

Table 5.1 The transition point for various orifice sizes, d_o < 1 mm, obtained by Richardson and Zaki model 147

Table 5.2 Gas distributor configurations used by Zuber and Hench (1962) . 149

Table 6.1 The setup and output of preliminary tests conducted in AGBC. ... 166

Table 6.2 Transition point α_{trans} and $(j_g)_{trans}$ for tap water and alcohol aqueous solutions in the OTBC and AGBC 185

NOMENCLATURE

A	Cross sectional area of the column	(m^2)
A_a	Cross sectional area of the annular gap	(m^2)
A_i	Cross sectional area of the inner tube	(m^2)
A_o	Orifice Area	(m^2)
C	Bubble chord length	(m)
C_0	Distribution parameters in the drift-flux model	( )
C_D	Drag coefficient	( )
C_e	Cumulative function for e	(-)
$C_p(R)$	Cumulative probability of a bubble with radius R	(-)
D_i	Inner tube outside diameter	(m)
D_o	Open column internal diameter	(m)
Eo	Eotvos number	(-)
F_B	Buoyancy force	(N)
F_D	Drag force	(N)
H_L	Liquid height	(m)
H_o	Orifice coefficient	(-)
M	Morton number	(-)
N	Number samples in the time history	(-)
T	Total time	(s)

TL	Threshold levels	(V)
VL	Voltage of the liquid	(V)
Vg	Voltage of the gas	(V)
P_{atm}	Atmospheric pressure,	(N/m^2)
P_c	pdf of the chord length detected by the probe	(-)
$P_c fitted$	pdf of the chord length predicted by the model	(-)
P_e	Probability of piercing the bubble at e	(-)
$P_p(R)$	pdf of the of the bubble detected by the probe	(-)
$P_s(R)$	pdf of the bubble size distribution	(-)
$Q_{\ f}$	Corrected airflow rate	(L/min)
Q_g	Gas flow rate	(m^3/s)
Q_g	Gas flow rate	(m^3/s)
Q_o	Gas flow rate through orifice	(m^3/s)
R_l	Radius of the inside column	(m)
R_o	Radius of the outside column	(m)
T_g	Time of the probe in the gas phase	(s)
V_g	Volume of gas	(m^3)
V_l	Volume of liquid	(m^3)
V_{max}	Minimum voltage	(V)
V_{min}	Maximum voltage	(V)
d_{32}	Sauter mean diameter	(m)

d_{43}	Mean diameter	(m)
d_{BP}	Primary bubble size	(m)
d_{BS}	Secondary bubble size	(m)
d_e	Bubble equivalent diameter	(m)
d_{el}	Bubble equivalent diameter at laminar flow	(m)
d_{et}	Bubble equivalent diameter at churn-turbulent flow	(m)
d_o	Orifice diameter	(m)
h_g	Height of gas in the column	(m)
h_l	Height of liquid in the column	(m)
$(j_g)_{trans}$	Transition superficial velocity	(m/s)
j_g	Gas superficial velocity	(m/s)
j_{gl}	Drift-flux velocity	(m/s)
j_l	Liquid superficial velocity	(m/s)
l_{12}	Distance between the probe tips	(m)
p_a	Pressure before the sparger	(N/m^2)
p_b	Pressure above sparger	(N/m^2)
p_o	Orifice perforated pitch	(m)
q_m	Rotameter reading of the inlet air flow rate	(L/min)
v_G	*in-situ* gas velocity	(m/s)
v_t	Single bubble rise velocity	(m/s)
Δp	Pressure difference	(N/m^2)

Re	Reynolds number	(-)
a	Long axes of the bubble	(m)
b	Short axes of the bubble	(m)
d	Bubble diameter	(m)
e	Eccentricity	(-)
ft	Bubble flying time from one probe to anther	(s)
g	Gravitation acceleration	(m/s^2)
k	Permeability	(m^2)
n	Richardson and Zaki exponent	(-)
r	Radial position of the probe	(m)
tR	Residence time	(s)
v	Bubble volume	(m^3)
w	Width of the histogram bin	(-)
y	Distance a cross the column	(m)
z	Exponent used in Hibiki and Ishii equation	(-)

Greek Symbols

α_a	Void fraction annulus channel	(-)
α_c	Centreline void fraction	(-)
α_i	Void fraction inner channel	(-)
α_{transt}	Void fraction transition point	(-)
α_w	Wall void fraction	(-)

μ_g	Viscosity of gas	(N s/m^2)
μ_l	Viscosity of liquid	(N s/m^2)
ρ_g	Density of gas	(kg/m^3)
ρ_l	Density of liquid	(kg/m^3)
α	Void fraction	(-)
β	Diameter ratioD_i/D_o of the annular gap column	(-)
θ	Orientation angle of the bubble	(-)
σ	Standard deviation	(-)
φ	Axis aspect ratio; $b/\ a$	(-)

Abbreviations

AGBC	Annular gap bubble column
BSD	bubble size distribution
CFD	Computed Fluid Dynamics
CLD	Chord length distribution
CMOS	Complementary Metal-Oxide Semi-conductor
DAQ	Data acquisition device
ERT	Electrical Resistance Tomography
LDV	Laser Doppler velocity
NS	Normal sparger which has no orifice
OTBC	Open tube bubble column
OTBCEO	Open tube bubble column equipped with an orifice

p1	Probe number 1
p2	Probe number 2
p3	Probe number 3
p4	Probe number 4
PDF	Probability density function

CHAPTER ONE

INTRODUCTION

1.1 Background

Gas-liquid flow is an important phenomenon that occurs in a variety of flow geometries, such as evaporators, condensers, boilers, fermenters and other gas-liquid reactors. Chemical reactions, such as oxidation, chlorination, alkylation and many others, which are utilised in the chemical and bio-technological industries, often involve gas–liquid bubble contact in columns. These columns possess numerous advantages in terms of their simplicity, and absence of mechanical moving parts, as well as efficient heat and mass transfer characteristics, when compared to other types of multiphase reactors, such as stirred vessels (Vijayan *et al.*, 2007). Often these process applications involve cases where a gas is bubbled into a liquid and breaks up into a distribution of bubbles sizes, which rise at various velocities towards a free surface. Two-phase flow transitions can take place within the equipment as the fraction of gas increases; for example, in steam production (Coulson *et al.*, 1999) or as coalescence and breakage processes that alter the bubble size distribution.

The gas void fraction, α, is the volume of gas phase divided by the total volume of both gas and liquid phases. It is an important two-phase flow variable, as it may be used to define the occurrence of various flow regimes and is required for the prediction of, for example, the process pressure drop and the heat transfer coefficient; typically the hydrostatic pressure difference, which depends on α, is a significant term in the overall pressure drop. So, two-phase gas–liquid flow is distinguished by being of great utility, yet it is an area of significant difficulty because: (i) neither the bubble size, nor α, are known *a priori* and can vary significantly within a single flow geometry; (ii) a complex array of flow patterns can exist, which are in part determined by the containing flow geometry; and (iii) two-phase models have difficulty in capturing observed phenomena, such as large-scale eddies and back-mixing in bubble columns. In practice, a number of

factors, for example, the internal dimensions of the pipe work, the physical properties of the gas, and liquid phases and flow rates (or superficial velocities), exert considerable influence and determine the flow regime.

In bubble columns with no liquid flow, there are three basic flow regimes: homogeneous, transition, and heterogeneous (Deckwer, 1992; Kastanek *et al.*, 1993; Molerus, 1993; Zahradnik *et al.*, 1997). These flow regimes are illustrated in Figure 1.1 using data obtained from a 0.102 m diameter bubble column (open tube) using air–tap water (Al-Oufi, 2006). The homogeneous regime is characterised by having a uniform dispersion of small spherical or ellipsoidal bubbles; it generally occurs at low gas superficial velocities. With increasing gas superficial velocity (j_g), α increases, and hence there is an increased probability of coalescence, leading to a broader bubble size distribution. Under some circumstances, coalescence leads to the transition regime, where α decreases with increasing j_g. At still higher gas superficial velocities, the flow comprises large, irregularly shaped bubbles, which rise rapidly through a dispersion of smaller ellipsoidal bubbles (in air–water), and α increases once more with increasing j_g in the heterogeneous regime. Hills and Darton (1976) showed that the presence of small bubbles causes the large bubbles or gas slugs to rise much faster than they would do in isolation. In Figure 1.1, at j_g ≈0.12 m/s, the bubbles reach a maximum concentration at α =0.4 and then start to coalesce; with increasing j_g, the transition from homogeneous to heterogeneous flow occurs, and α falls.

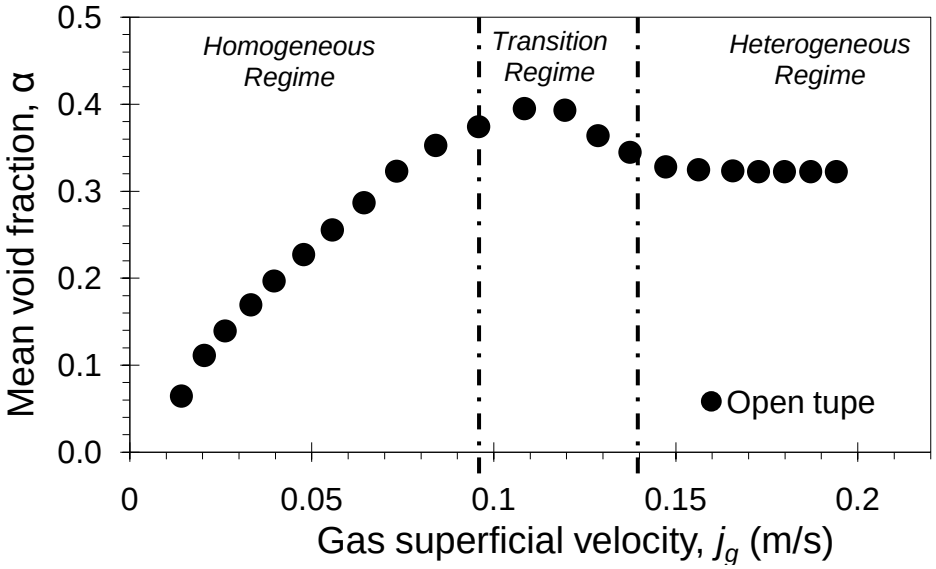


Figure 1.1 Mean void fraction for air-tap water with respect to gas superficial velocity. The mean gas void fraction was obtained from the change of level in the bubble columns (internal diameter, D_o = 0.102 m) on aeration by using a sintered plastic sparger (Al-Oufi, 2006)

1.2 Applications of bubble and airlift columns

Bubble-column reactors are used as an apparatus to achieve mass-transfer and/ or chemical reactions. In the past decade, bubble columns have been commonly used in biotechnological processes, such as the production of baker's yeast, antibiotics, citric acid fermentation, and wastewater treatment. The uses of bubble columns can be categorised according to their flow regimes. Due to high mass transfer rate, bubbly flow is preferable in most biochemical applications, such as the cultivation of bacteria, bio-mass processes, the production of single cell proteins, animal cell cultures and the treatment of sewage (Shaikh and Al-Dahhan, 2007). Additionally, bubble columns operating in bubbly flow are used in the hydro conversion of heavy oils and petroleum feedstocks, and coal hydrogenation. Due to high heat transfer rates, a churn turbulent flow regime is preferable for highly exothermic processes, such as liquid phase methanol synthesis, Fischer-Tropsch synthesis, and the hydrogenation of maleic acid (Deckwer, 1992; Blanch and Clark, 1996).

Whenever absorption or desorption of a gas is required in the context of industrial processes, gas–liquid reactors are typically found, including bioreactors for aerobic microbial and cell culture processes. The bubble column and airlift loop

reactor are two commonly encountered types of gas–liquid reactor. Gas injection is the sole means of mixing in these reactors, and a homogeneous bubble flow regime is required for the effective operation of these reactors due to the mass transfer requirements. This flow regime is characterised by a relatively uniform size of ellipsoidal bubbles (Kantarci *et al.*, 2005). In contrast to larger spheroidal or spherical cap bubbles, uniform small-size bubbles exhibit a greater specific interfacial area for gas-liquid mass transfer. In churn-turbulent or heterogeneous flows, the large bubbles coexist with small bubbles. In bubble columns and airlift reactors, the transition from bubble to churn-turbulent flow begins at somewhat low gas injection rates. The flow transition contributes to a number of adverse effects; e.g. poor contact in gas and liquid phases, broad residence time distribution in the gas phase, and reduced efficiency of gas–liquid mass transfer. Hence, it is an objective to extend the favourable bubble flow regime through suitable reactor designs at higher gas flow rates than is currently the case for bubble columns and airlift reactors (Fadavi and Chisti, 2005).

1.3 Motivation

There are several variables, which affect the void fraction and the position of the flow regime transition. These include liquid height (e.g. Ruzicka *et al.*, 2001), liquid purity (e.g. Anderson and Quinn, 1970), column geometry (e.g. Jamialahmadi *et al.*, 2000), and sparger configuration (e.g. Sarrafi *et al.*, 1999). The majority of previous studies of α, and homogeneous to heterogeneous flow transitions, have been conducted for open-tube bubble columns of circular cross-section. In the current contribution, annular gap bubble columns are discussed and α data are compared with those from open-tube bubble columns. These flow geometries commonly occur in the outer annulus of an internal loop air-lift bubble column (albeit with an additional upward velocity), formed by concentric tubes; alternatively, the inner tube could be the downcomer and the outer tube could be the riser of a plunging jet bubble column; see, for example, Cumming et al. (2002).

Figure 1.2 shows the void fraction, α, resulting from an open-tube bubble column and an annular gap geometry with respect to gas superficial velocities, j_g, where j_g is given by

$$j_g = \frac{Q_g}{\mathrm{A}} \qquad 1.1$$

where Q_g is the gas flow rate (m^3/s), and A is the cross sectional area of the column (m^2). At the same gas superficial velocities, j_g, there is a very significant difference between the measured mean α for the annular gap geometry; the mean value of α can be 50% lower than in the open tube, and there is no obvious evidence of a change in flow pattern from homogeneous through transition to heterogeneous flow. The data in Figure 1.2 have been fitted according to Zuber and Findlay's (1965) drift-flux model, which has often been used to correlate α across a range of flow regimes.

$$\alpha = \frac{j_g}{C_o j_g + v_t} \qquad 1.2$$

The model contains two adjustable parameters: a velocity, v_t, and the distribution coefficient, C_o. Both parameters depend on the radial distributions of gas & liquid velocity and void fraction, as given below:

$$C_o = \frac{\langle \alpha (j_g + j_l) \rangle}{\langle \alpha \rangle \langle j_g + j_l \rangle} \qquad 1.3$$

$$v_t = \frac{\langle \alpha j_{gl} \rangle}{\langle \alpha \rangle} \qquad 1.4$$

where j_{gl} is the drift-flux velocity of the gas with respect to the mixture, and the averages are taken over the cross-sectional area of the column (see Hibiki and Ishii (2002) for further details). The parameter, v_t, is typically close to the single bubble rise velocity and hence depends on the average bubble size in the flow, as well as the liquid physical properties.

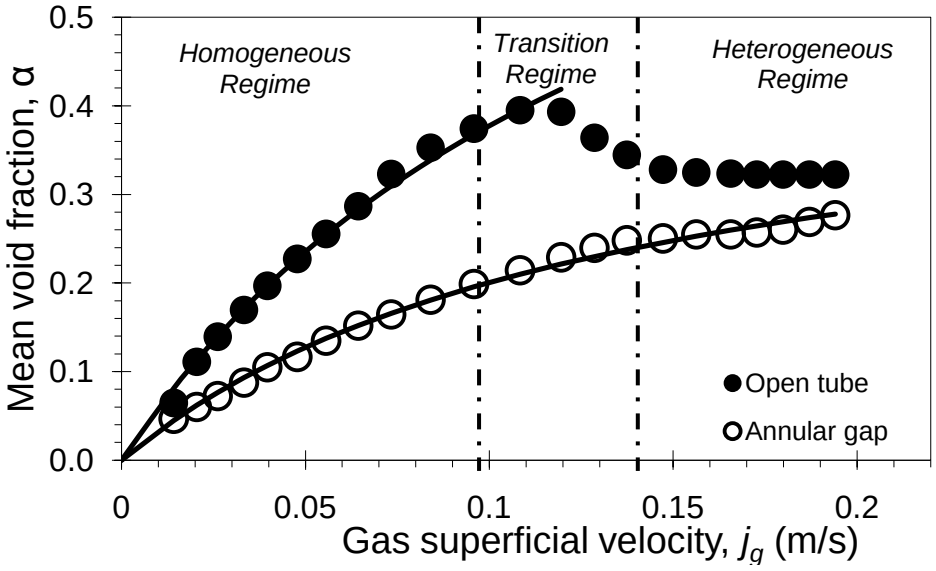


Figure 1.2 Comparisons of measured gas void fractions for air-tap water in (i) an open tube (D_o = 0.102 m) and (ii) an annular gap bubble column (inner tube diameter, D_i = 0.051 m, D_o = 0.102 m). The mean gas void fraction was obtained from the change of level in the bubble columns on aeration; data from Al-Oufi (2006).

Two reasons are postulated for the differences in α between the annular gap and open-tube bubble columns: (1) large bubbles form near the sparger at the bottom of the inner tube in the annular gap system, and these destabilise the flow, such that a flow transition occurs earlier than in the open tube experiments; (2) there are significant differences in the local void fraction and velocity radial profiles, which affect the distribution parameter, C_o, and hence affect the mean α. Both these effects have been studied using a range of annular gap geometries.

1.4 Research aims and objectives

The overall objective of the present study is to carry out further experiments to develop an improved understanding of the main features of bubble columns. The following objectives were identified for the research:

a. To achieve a full understanding of an air-liquid system in a vertical bubble column by studying the effect of liquid height, liquid purity, column geometry and sparger configuration on α and the position of the flow regime transition.
b. To study and implement, according to their simplicity of application and their cost effectiveness, the appropriate measuring techniques to predict

the air-water hydrodynamics parameters in an open tube and annular gap bubble column.

c. To determine the local α, velocity and size of the bubbles by designing and employing two- and four-point conductivity probes for use in bubble column.
d. To develop a signal treatment technique, by specify the liquid baseline and threshold level of the measured voltages correctly, by using a histogram method, and identifying the mean and standard deviations of the liquid baseline, in order to predict the void fraction, velocity and chord size of bubbles.
e. To understand the air-water system flow in a vertical bubble column. This will be achieved by conducting experiments to measure air-water hydrodynamic parameters, e.g. void fraction, size and velocity of bubbles in both open-tube and annular gap columns.
f. To define the homogeneous and heterogeneous regimes and investigate the factors that lead to the destabilisation of the homogenous flow in an air-liquid system.
g. To discuss annular gap bubble columns, and compare α data with those from an open tube bubble column.
h. To establish a relationship between α and the annular gaps by introducing different inner tube sizes in the open tube bubble column.
i. To determine a scientific answer for the difference in α data between open tube and annular gap bubble columns.
j. To study the effect of orifice presence on a homogeneous flow by employing different orifice sizes to generate large bubbles.
k. To investigate the influence of alcohol on α in the open tube and annular gap, as well as in orifice experiments.

1.5 Main contributions of the study

The main contributions of the work presented in this thesis can be summarised as follows:

a. The provision of a comprehensive literature review on air-liquid systems in open-tube and annular gap bubble columns. This includes a compilation of methods from the literature of the effect of liquid height, liquid purity column geometry and sparger configuration on α, bubbles and the position of the flow regime transition. In addition, the work offers a review of the behaviour of α and bubbles in an air-aqueous solution system.
b. The aims of this study were achieved by implementing image analysis of photographs, and two- and four-point conductivity probe methods, to investigate the variation in α between open tube and annular gap bubble columns.
c. A voltage signal treatment technique has been developed to give the local α, velocity and chord size of the bubbles. The raw voltage measurements were converted in a MATLAB program by identifying the liquid baseline of the measured voltages using a histogram method. Threshold levels were also identified by specifying the mean and standard deviations of the liquid baseline.
d. The LabVIEW interface and MATLAB codes were systematically designed to collect and analyse the two- and four-point probe data in order to extract the desired results of α, bubble velocity and chord size.
e. A novel approach was developed to calculate the bubble size from the chord length distribution obtained from the conductivity probes. Practical comparisons were also made between calculated bubble size data, obtained using probe methods, and predicted bubble size data taken from image technique data.
f. Improvements to experimental design were made to investigate the effect of the presence of alcohol on α and bubble behaviour in open-tube and annular gap bubble columns.

1.6 Structure of the Thesis

Chapter 2 contains a review of the published literature which is relevant to void fractions and the variables considered in this study that may affect void fractions. These variables include: liquid height, column geometry, liquid purity and sparger configuration. The main findings of previous studies on the use of annular gaps are also introduced. The benefits of employing conductivity probes and image visualisation to measure the void fraction (α), velocity and size of bubbles are described.

Chapter 3 describes the techniques: aerated level, image and conductivity methods, which were used in the study. Two- and four-point conductivity probe experiments are implemented and described in this section. Issues such as the probe design, calibration and signal assessment are also discussed. The chapter considers the theory related to conductivity measurement in detail; signal processing and piercing phenomena are also discussed. The technique, implemented to treat the raw signal according to the base line, and the specification of the threshold level is also discussed, and the calculation of void fraction (α), bubble velocity and chord size from the probe signal are explained. Similarly, void fractions and bubble velocity profiles are predicted and described. Finally, a novel transformation method is proposed to convert the bubble chord length to the bubble size using a forward analytical transformation and an optimisation model.

Chapter 4 gives full descriptions of the Open Tube Bubble Column (OTBC) experimental apparatus and methods used during the void fraction experiments in an air-water system. The chapter is divided into two parts: (i) preliminary experiments which were conducted to ensure that the results are reproducible. Other tests were conducted to select the most appropriate fluid, sparger type, liquid and probe height from the sparger. The preliminary results are presented and discussed here and finally a conclusion is drawn from the preliminary experiments; (ii) local, mean α, chord length, size, the velocity of bubbles for tap water and alcohol (ethanol and IPA) aqueous solution experiments in the OTBC are described and the results, discussions and conclusion are also presented.

Chapter 5 in this chapter, the Open Tube Column Equipped with an Orifice (OTBCEO) experiments are described. The rig setup and design are presented and the local, mean α, size, velocity of bubbles in the OTBCEO are described, together with the results, discussion and conclusion.

Chapter 6 describes the Annular Gap Bubble Column (AGBC) experimental setup, design and conditions. Similar to Chapter 4, this chapter is divided into two parts: (i) preliminary experiments which were conducted to test the effect of inner tube height, bottom end shapes and the position of α. The preliminary results are presented and discussed. Finally, a conclusion is drawn from the preliminary experiments. (ii) Local, mean α, chord length, size, the velocity of bubbles for tap water and alcohol (ethanol and IPA) aqueous solutions experiments in the AGBC are described and the results, discussion and conclusions are presented.

Chapter 7 presents a set of conclusions, which were drawn from all the experimental results and observations. Recommendations for future work and modifications to the present work are also proposed.

CHAPTER TWO

LITERATURE REVIEW

2.1 Introduction

A vital and quite common operation in the process industries, whether petrochemical, biochemical or mineral, is that involving gas-liquid contact. The equipment used in processes such as absorption, distillation and froth flotation, is specifically developed to achieve the optimal hydrodynamic states necessary for the performance required. In this context, calculating the mass transfer coefficients requires the transport processes at the interface between the two phases, i.e. gas and liquid, to be known. Furthermore, precise predictions must be made regarding the discrete phase in terms of volume, residence time, and contribution to mixing. In addition, the chemical and physical properties of the liquid phase (e.g. density, viscosity and surface tension), and those of the discrete phase (such as bubble sizes and rise velocity), must also be defined. These properties are important, as they define the hydrodynamics and flow within the process. Smaller bubble size lead to lower bubble rise velocity, and hence higher residence time.

Gas-liquid systems exhibiting gas void fraction behaviour have been studied extensively; the performance of system components has been assessed and improvements have been introduced to such systems. In addition, these studies have widened considerably in scope, to include various flow area types, including annular gaps. The present review focuses principally on the variables considered in this study that may affect gas void fractions in bubbly flow, e.g. liquid height, gas distributor configuration, water contamination, column geometry and the presence of a surface active agent such as an alcohol. The review has also been extended critically to include studies which deal with annular gaps, the use of electrical conductivity probes, and photographic methods for gas void fraction measurement in a gas-liquid flow.

2.2 Gas void fraction in bubble columns

The parameters that might affect gas void fractions and the position of the flow regime transition are illustrated in Table 2.1; each variable is discussed in a separate section.

Table 2.1 A summary of the effect of certain variables considered in this study on the flow regime transition

Variable	Effect on flow regime transition	Reference
Liquid height	An increase in liquid height reduces the void fraction	Sarrafi *et al.* (1999); Ruzicka *et al.* (2001)
Sparger (perforation pitch)	Void fraction increases with perforation pitch	Sarrafi *et al.* (1999); Jamialahmadi *et al.* (2000)
Sparger (hole size)	Void fraction decreases with an increase in hole size up to a certain size	Sarrafi *et al.*(1999); Jamialahmadi *et al.* (2000); Zuber and Hench (1962)
Liquid phase contamination	Void fraction increases with contaminated water	Anderson and Quinn (1970)
Column geometry	An increase in column diameter decreases void fraction at the same gas superficial velocity	Ohki and Inoue (1970); Sarrafi *et al.* (1999); Jamialahmadi *et al.* (2000); Urseanu (2000) Zahradnik *et al.* (1997); Ruzicka *et al.* (2001)

2.2.1 Liquid height and column diameter

The gas void fraction, α, is reduced as the liquid column height is increased (Yamashita, 1985). However, this is only true until a certain height is reached, after which the gas void fraction is unaffected (Wilkinson, 1991). Gas void fraction is independent when the ratio of liquid height, H_L to column internal diameter, D_o is greater than 5 (Wilkinson *et al.,* 1992). For a H_L/D_o ratio of less than 5, a decrease in gas void fraction with an increase in static liquid height has also been observed by other researchers; this is justified by the three region concept (Wilkinson *et al.,* 1992; Yamashita, 1998). Yamashita (1995) used a manometer to measure the gas void fraction at different points along a vertical bubble column. The test section was a rectangle, 0.05 x 0.10 m., with a height of 1.10 m. Yamashita (1995) divided the bubble column into three regions:

(i) The entrance region.

(ii) The bulk region.

(iii) The foam region.

Millies and Mewes (1999) divided the areas that appear within any bubble column into four regions:

(i) The primary bubbles region formed at the sparger.
(ii) The secondary bubbles region, resulting from the breaking up of the primary bubbles.
(iii) The dynamic equilibrium region, resulting from the secondary bubbles coalescing and breaking up.
(iv) The separation region at the top of the column.

The gas void fraction is dependent on the bubble size, while the latter may be dependent on H_L (Hughmark, 1967). This is reasonable, since the bubble size relies on a balance between the coalescence and breakup rates. If H_L is small, no effect is expected on the bubble size, since it seems to be determined by the formation of bubbles at the sparger (Akita and Yoshida, 1974).

Yang *et al.* (2007) reviewed the previous literature related to bubble formation in gas-liquid solid fluidisation and concluded that the local pressure varies along the bubble path. Changes in local pressure may affect the density of the gas and may also affect the bubble size which in turn affects the gas void fraction in the bubble column.

Collating data reported in the literature, as well as data from their own work, Sarrafi *et al.* (1999) concluded that, up to a height of 4 m for the static liquid height, the transition velocity was reduced accordingly. However, after 4 m, the transition velocity was no longer affected by height of the liquid; see Figure 2.1. The data covered column diameters, D_o, of 0.14-0.16 m; sparger orifice diameters, d_o, of 0.001-0.002 m; and perforation pitches, p_o, of 0.02 m. The work of Ruzicka *et al.* (2001) on air-water two-phase flow, which related to column diameters of 0.14, 0.29 and 0.4 m, agreed with the conclusion of Sarrafi *et al.* (1999); the transition velocity is generally reduced by greater liquid height in a bubble column.

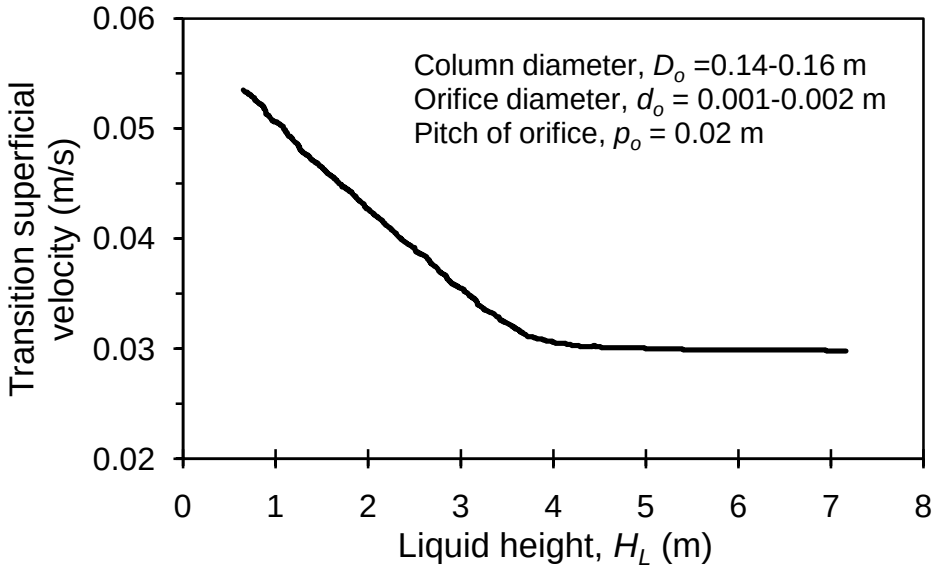


Figure 2.1 Effect of liquid height on transition velocity in air-water system, data reproduced from Sarrafi *et al.* (1999).

Many studies agreed that the column diameter, D_o has a significant effect on α. Thorat *et al.* (1998) studied, in depth, the effect on α of column diameter. They used a vertical bubble column of D_o= 0.385 m and a column height of H = 3.2 m and employed different sieve plate geometries. They used three systems: air-water, an air-aqueous solution of 1% CMC (Sodium salt) and an air-electrolyte solution (NaCl). The range of ratio H_L/D_o was between 1 to 8 and the j_g range between 0 to 0.3 m/s. Thorat *et al.* (1998) concluded that α decreased as the H_L/D_o ratio increased when multi-point sieve plates, with an orifice diameter of < 3 mm, were used. However, α was found to increase for single-point sieve plates. On the other hand, in both cases, the values of α remained constant beyond H_L/D_o ratio values. The value of α is independent as the H_L/D_o ratio values were in the range of 4 - 5 for the air-water system, greater than 8 for the air-electrolyte system, and 3 for the air-aqueous system.

Thorat *et al.* (1998) proposed that the effect of the H_L/D_o ratio on α can be identified by the relative proportion of the sparger region to the total column height. If the sparger region is large, the effect of the H_L/D_o ratio on α is a maximum and vice-versa. However, the height of the sparger region depends on: (i) the difference between the primary bubble size (d_{BP}) and the secondary

bubble size (d_{BS}); (ii) the coalescence nature of the liquid phase; and (iii) the liquid circulation in the bubble column.

The physical reason for the drop in α with an increase in D_o is the increase in movement of liquid circulation and turbulent circulation in larger containers. The effect of D_o is regularly linked to wall friction (Tinge and Drinkenburg, 1986), backmixing (Deckwer, 1992), turbulence scale (Zahradnik *et al.,* 1997), turbulent viscosity (Ueyama and Miyauchi, 1979), the intensity of circulation (Krishna *et al.,* 2000), and axial dispersion (Van Baten and Krishna, 2001).

In general, D_o has no effect on α if the aspect ratio H_L/D_o is larger than a certain minimum value. These studies specified the critical value of H_L/D_o where beyond this value, D_o has an insignificant effect on α. Wilkinson *et al.* (1992), Zahradnik *et al.* (1997) and Thorat *et al.* (1998) recommended that H_L/D_o should be greater than 5.

Sarrafi *et al.* (1999) studied the effect of D_o on the transition superficial velocity $(j_g)_{trans}$. They conducted experiments in two cylindrical bubble columns with diameters of 0.08 and 0.155 m and variable H_L. The gas distributor was a circular metal plate of the same diameter as the column with 55 orifices of 1 mm diameter, on a 15 mm triangular pitch. Quick-closing valve and manometric methods were used to obtain α over a range of j_g. Figure 2.2, which represents $(j_g)_{trans}$ with respect to D_o, is reproduced from the work of Sarrafi *et al.* (1999), who also provided the literature data concerning air-water systems. They observed that $(j_g)_{trans}$ increased sharply as D_o increased up to 0.15 m. Beyond this value, $(j_g)_{trans}$ remained constant at about 0.06 m/s; they offered no explanation for this.

Ruzicka *et al.* (2001) carried out experiments using three different column diameters (0.14, 0.29 and 0.4 m) and a range of H_L values between 0.1 – 1.2 m. The columns were equipped with 3 mm thick brass plates with 0.5 mm orifices, and a 10 mm pitch with a plate-free area of 0.2%. Aerated level and manometric methods were used to measure α. The researchers used a drift-flux plot method to obtain the critical void fraction transition, α_{trans}, and $(j_g)_{trans}$ (as explained in §

2.2.4). Figure 2.3 illustrates α_{trans} with respect to H_L/D_o at different column diameters and shows decreases in α_{trans} values as the H_L/D_o increases in all three diameters. However, comparing H_L/D_o for all the studied diameters offered no firm conclusions.

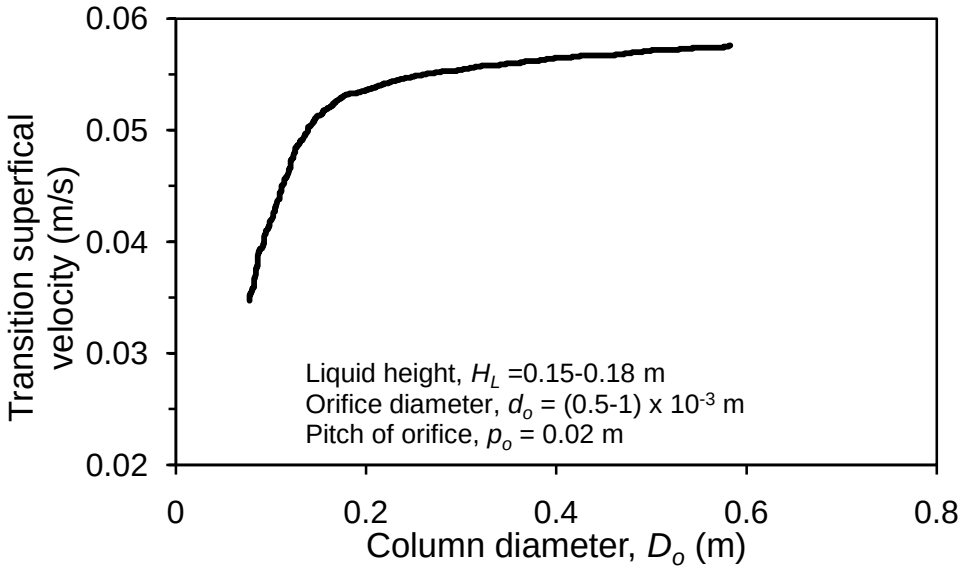


Figure 2.2 Effect of column diameter on the transition superfical velocity as proposed by Sarrafi *et al.* (1999).

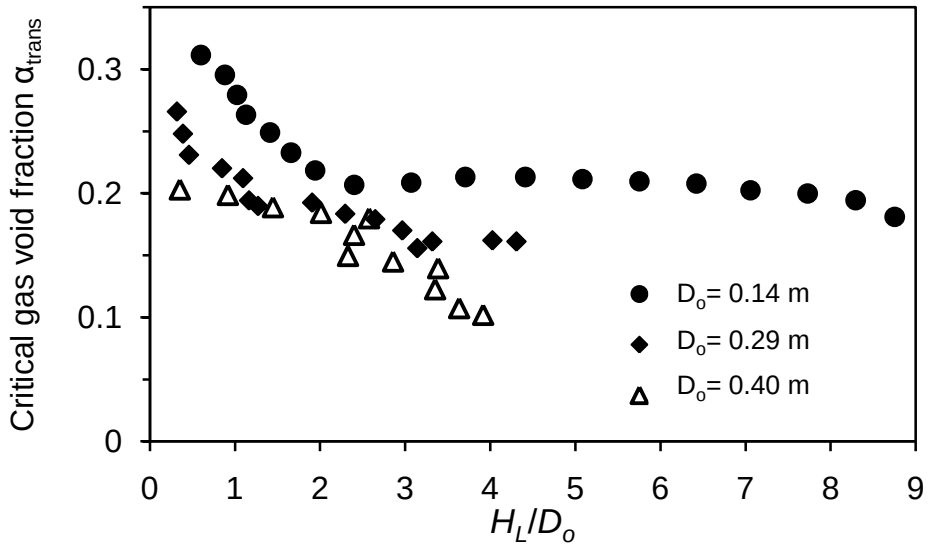


Figure 2.3 Effect of aspect ratio H_L/D_o on the transition superfical velocity (reproduced from Ruzicka *et al.*, 2001).

From the studies presented, it seems that there are conflicting results for the effect of D_o on the transition superficial velocity $(j_g)_{trans}$. Ohki and Inoue (1970), Sarrafi et al. (1999), Jamialahmadi et al. (2000), and Urseanu (2000) stated that

as D_o increased, $(j_g)_{trans}$ values also increased. In contrast, Zahradnik *et al.* (1997) and Ruzicka *et al.* (2001) noted a decrease in $(j_g)_{trans}$ values as D_o increased. Based on these studies, the question is still open regarding whether D_o increases or decreases $(j_g)_{trans}$.

2.2.2 Gas distributor configurations

The stability of the homogeneous two-phase flow regime is influenced by a variety of factors, including surfactants, the viscosity of the liquid phase, column designs, and the distributor geometry (Zahradnik *et al.,* 1997). A homogeneous, two-phase regime results from using a gas distributor consisting of many small and closely-sited orifices, providing the gas flow velocity is not too high (Shollenberger *et al.,* 2000). In this case, small and almost spherical bubbles, that are non-coalescing and approximately the same size, can be seen to form. Under these conditions, the flow is relatively stable, with the bubbles travelling almost vertically upwards, entraining with them a significant amount of liquid and carrying it to the upper part of the column. Since a batch liquid column was considered, liquid carried upwards by the bubbles must, by necessity, flow down again at the walls (Varma and Al-Dahhan, 2007).

The heterogeneous, two-phase flow regime is also referred to as turbulent and churn-turbulent. This turbulent flow regime can be achieved by using high gas flow through perforated gas distributors or, alternatively, by increasing the orifice size. Using a large orifice size of d_o>1 mm, results in a heterogeneous flow regime, irrespective of gas velocity, which is termed pure heterogeneous (Tsuchiya and Nakanishi, 1992). Passing gas at high velocities through a small orifice gas distributor causes an unstable homogeneous flow regime after a transition. Regardless of the conditions which result in their formation, both transition and pure heterogeneous regimes are virtually indistinguishable (Kazakis *et al.*, 2007). In both cases, relatively large and non-uniformly sized bubbles, which tend to coalesce, can be observed. However, the pure heterogeneous two-phase flow regime acts as a useful reference for the transition from a homogeneous regime.

Zuber and Hench (1962) carried out experiments over the same range of gas flow rates using a variety of perforated plates as air dispersers. Figure 2.4 illustrates the mean α with respect to j_g for two types of gas distributor; the configurations are shown in Table 2.2. From Zuber and Hench's (1962) results, as the hole size in the gas distributor plate was decreased (and the number of orifices was increased), higher gas void fractions were generated. An initially homogeneous regime was obtained at low superficial velocities when the hole size was 0.41 mm, as is shown in Figure 2.4; larger orifices gave heterogeneous flow over a much wider range of gas superficial velocities. This is because the small orifice, 0.41 mm, produced small-sized bubbles compare to a larger orifice size, which generated large bubbles. These large bubbles would rise much faster than the smaller spherical bubbles. The large bubbles would sweep the smaller bubbles into their wake, causing coalescence and hence transition to heterogeneous regime occurring. So, the orifice diameter plays an important role in determining the gas void fraction by destabilising the homogeneous regime.

Table 2.2 Gas distributor (sieve plate) configurations used by Zuber and Hench (1962)

No. of orifices	Diameter (mm)	Square array spacing (mm)
49	4.06	6.25
289	0.41	6.25

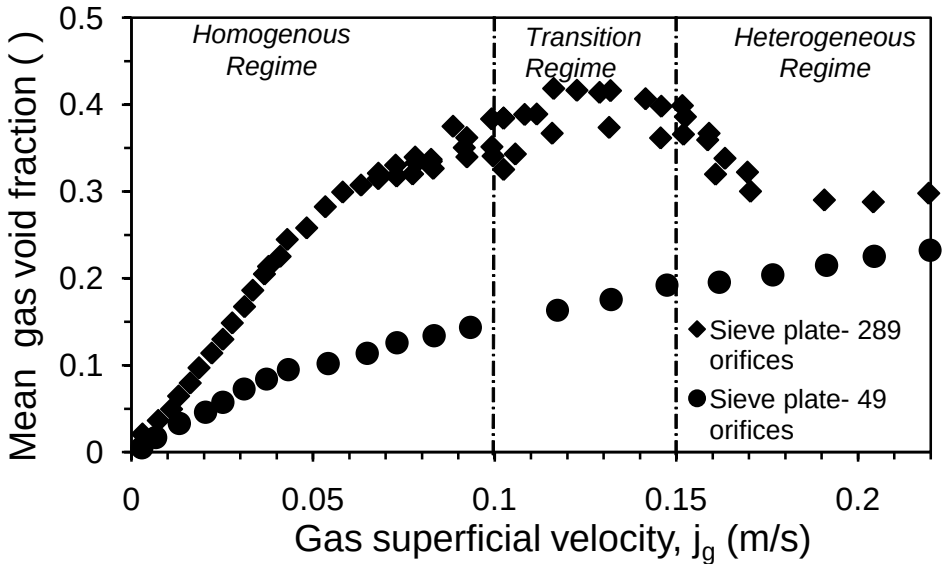


Figure 2.4 Mean gas void fractions for a variety of perforated plate spargers, provided by Zuber and Hench (1962). (See Table 2.2 for details of their perforated plate spargers.)

From the gas distributor, significant and powerful non-uniformities, relating to variations in buoyancy, cause convective liquid flows (water circulations) throughout the column; these are significantly strong and large-scale (Ruzicka *et al.*, 2001). Regions within the column have high void fractions and are thus advected and pushed rapidly to the upper part of the column. At the top, the gas bubbles are able to escape and so the bubble-free liquid then flows along the walls towards the bottom of the column. These central upward flows of liquid help bubbles to rise and so reduce the mean gas void fraction. With quite short intervals of time, liquid (water) circulations are observed to be very non-stationary (Chen *et al.,* 1994; Devanathan *et al.,* 1995). Moreover, the two-phase homogeneous flow regime is observed to be stable at low void fractions and with low velocity disturbances. Hence, the transition from such a stable regime to a heterogeneous one does not occur suddenly. Rather, transition takes place slowly, with a number of indicative features, which grow in magnitude and intensity, including flow circulations and vortices inside the column's bubble bed.

Ong *et al.* (2009) investigated the effect of sparger design on α radial profiles in a bubble column. They used six different spargers with different orifice sizes and numbers, and with various perforated arrangements. A non-invasive γ-ray computed tomography technique was used to measure the time-averaged cross-sectional distribution of α. Their main findings were that for all the sparger configurations used, α always increased as j_g increased. Moreover, the perforated sparger with the smallest orifice size, 0.4 mm, gave higher α compare to the other types of sparger. This might be due to the sparger configuration, the 0.4 mm orifice size and the arrangement of perforations; these may have discouraged the bubbles' coalescence, yielding a higher α.

Merchuk *et al.* (1998) studied the influence of sparger design on α in a concentric tube air-lift bioreactor using sea water as the liquid phase. Their results emphasised that both sparger geometry and sparger porosity had a strong effect on the behaviour of the system when a non-coalescing solution, such as sea water, was used. A small orifice size, 6 µm, produced high α compared to the largest orifice size, 0.03 m, for the same range of j_g. The differences in α can be accounted for in both spargers by the differently sized bubbles they produced.

Sarrafi *et al.* (1999) used columns with diameters of 0.14–0.16 m and heights of 1.5–1.8 m. They concluded that the transition superficial velocity decreased significantly as the size of the sparger hole was increased because the design of the sparger strongly affected the bubble size. The effect of orifice size on the transition superficial velocity is shown in Figure 2.5. The results proposed by Sarrafi *et al.* (1999) show that the transition superficial velocity decreases sharply as the orifice diameter increases to about 1.5 mm. With an orifice size greater than 2 mm, the transition superficial velocity stays constant at about 0.035 m/s.

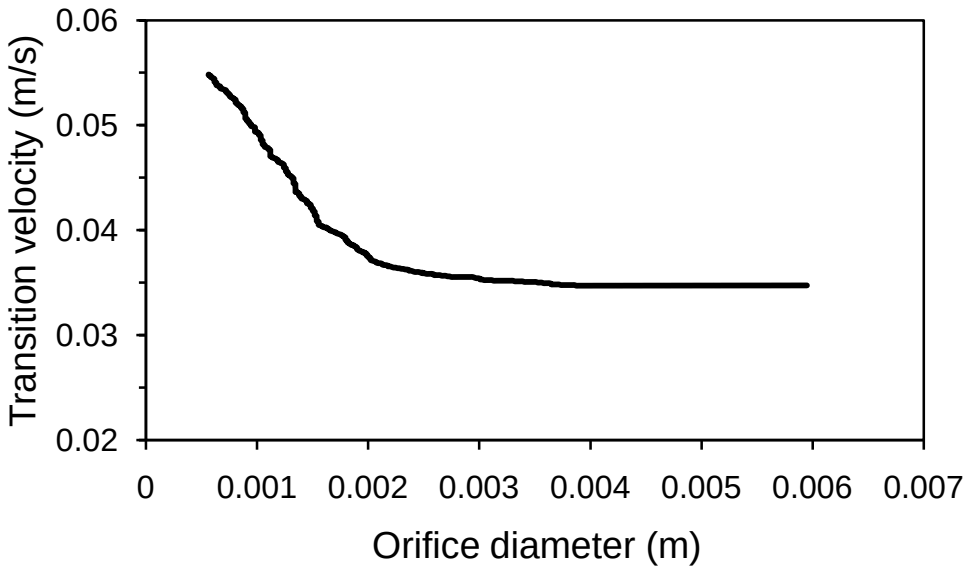


Figure 2.5 Influence of orifice diameter size on transition superficial velocity, data reproduced from Sarrafi *et al.* (1999).

Zahradnik *et al.* (1997) studied the effect of sparger design on transition velocity. They used four spargers of different materials and geometries: (i) perforated plastic plates with 0.5 and 1.6 mm. orifice diameters; (ii) perforated rubber plates with 2 and 10 mm orifice diameters; (iii) sintered glass plates with pore sizes of 100-160 and 160 -250 µm; and (iv) a sintered metal plate. Their experiments were performed using an air-water system in a bubble column reactor 0.14 m in diameter and with an aspect ratio of H_L/D_o =7. Their results confirmed that the transition superficial velocity was affected by the geometry of the sparger. As the orifice diameter decreased for ≤1 mm, the transition superficial velocity increased and led to greater stability in the homogeneous regime for maximum α. The findings of Zahradnik *et al.* (1997) agreed with the results of Shnip *et al.* (1992), and Ohki and Inoue (1970).

2.2.3 Water contamination

It is usually assumed that the properties of air and water are unchanging and therefore, the results obtained in air–water systems are reproducible. However, in a review of the literature relating to the gas void fractions in clean and contaminated air-water systems, Anderson and Quinn (1970) compared gas holdup in a 0.021 m (i.d.) semi-batch bubble column using distilled water and tap water. They found that contaminants in tap water caused small, uniformly sized bubbles to form, which led to high gas void fractions. In contrast, distilled water in similar circumstances tended to produce large bubbles. The resulting flow was highly turbulent and adopted large, random circulation patterns with low gas void fractions. They also found that solutions made from mixing varying quantities of tap and distilled water also gave different gas void fraction results, at the same superficial gas velocities. Tap water may contain trace amounts of substances such as salts, chloramines and microorganisms (Ingram, 2006). The presence of impurities in tap water might affect the size of bubbles in the bubble column. By using the same gas distributor in a bubble column, smaller bubbles would be produced in tap water compared to those produced in distilled water at the same j_g. Small bubbles rise more slowly than large ones in an air-water system (Clift *et al.*, 2005). Therefore, as the large bubbles rise more quickly, this encourages the coalescence phenomenon, and thus produces a low α. Figure 2.6, presented by Anderson and Quinn (1970), illustrates the effect on α of increasing the concentration of contaminants in distilled water. The researchers used tap water as a source of contaminants and found that pure (100%) distilled water gave low α readings compared to those found using tap water. This is due to the formation of large bubbles, which rise quickly and increase the coalescence of bubbles. In contrast, smaller bubbles form in tap water and provide high α readings.

Maruyama *et al.* (1981) used tap water and air from a compressor. They noticed that different gas holdups were obtained in each of the three experiments repeated using the same semi-batch bubble column without filtering the air or changing the water. They credited this difference to the accumulation of trace impurities, such as oil from the compressor, in the tap water.

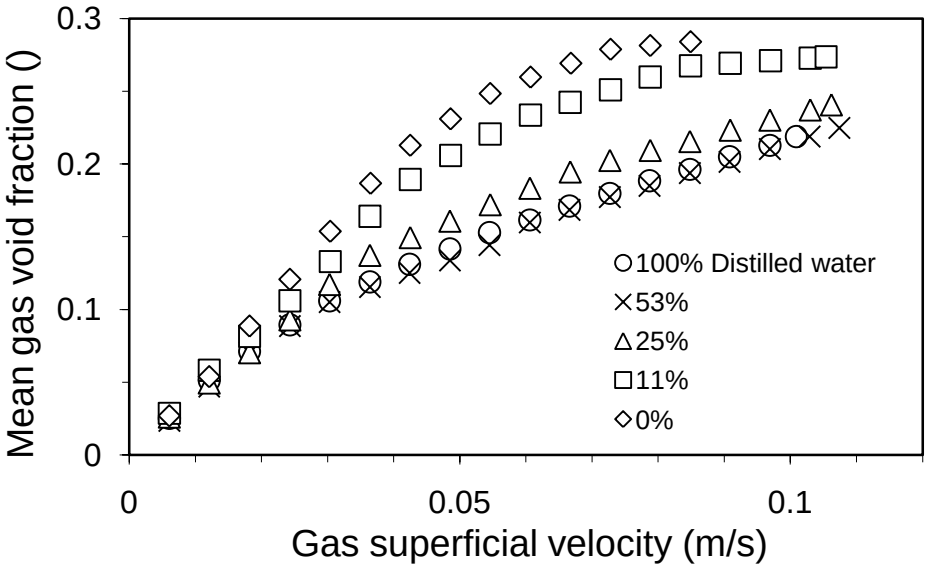


Figure 2.6 Effect of liquid contamination on gas void fractions, according to Anderson and Quinn (1970).

In other experiments, Anderson and Quinn (1970) found that impurities of 10 wt% glycerol-water and 0.075 wt% acetic acid solutions could increase and decrease the α in bubble columns respectively. This is because the acetic acid solution has sufficient active surface agents to inhibit bubble coalescence. Ueyama *et al.* (1989) discovered that the type of water (tap water or ion-exchange water) and gas (compressed air or N_2) could change both α and flow behaviour in a semi-batch bubble column. They proposed that some coalescence-inhibiting impurities were present in the water, and that the concentrations were higher in tap water than in ion-exchange water. Ueyama *et al.'s* (1989) results agreed well with the findings of Anderson and Quinn (1970) as ion-exchange water is similar to distilled water in terms of purity. Ueyama *et al.* (1989) inferred that the presence of a mist in the air, assumed to be oil droplets, inhibited bubble coalescence as the mist accumulated in the water. They assumed that the coalescence-inhibiting impurities in the tap water, together with the coalescence-weakening mist in the compressed air, caused the rather different α values observed in the bubble column.

2.2.4 Influence of alcohol on gas void fraction

In many bubble column and airlift reactors, the liquid phase consists of a mixture of organic and inorganic compounds as, for example, in the case of bubble

column bioreactors, where inorganic salts, sugars and metabolic products, such as alcohols and organic acids, are present in significant quantities in the culture medium (Schugerl *et al.*, 1977; Jamialahmadi and Muller-Steinhagen, 1992). In such units, bubble behaviour, the hydrodynamics and mass transfer rates are strongly affected by the properties of the liquid phase. It is well known that the most significant difference between air-water and air-aqueous solution systems is that, in the former, bubble coalescence rates are high, whilst, in the latter, the coalescence rates are low (Schugerl *et al*., 1977). Little detailed analysis has been carried out on annular gap systems, and consequently, the mechanisms underlying these different behaviours remain poorly understood (Miyahara and Nagatani, 2009).

The addition of alcohol to the liquid phase can be used to simulate the liquid phase behaviour in coal liquefaction and in bioreactors due to the presence of non-coalescing organic mixtures in the bed (Kelkar *et al.,* 1983). VAZQUEZ Vazquez *et al*. (1995) found that the only property of these solutions that differed considerably from water was their surface tension. They also concluded that the surface tension of aqueous solutions decreased as the alcohol concentration increased. The decrease of surface tension in the presence of alcohol results in a smaller average size of bubbles, and consequently, lower bubble rise velocities due to the prevention of bubble coalescence. In addition, the presence of relatively small amounts of alcohol increases the gas void fraction in aqueous solutions in bubble columns (Camaras *et al.,* 1999; Sijacki *et al*., 2010). Anastasiou *et al*. (2010) related this increase in α to the composition of the alcohol molecules, which consist of hydrophilic and hydrophobic parts; the former represents the polar group, while the latter the carbon chain. These substances can accumulated at the air-liquid boundary with the carbon chains (hydrophobic) pointing inwards towards the centre of the bubble; see Figure 2.7. As bubbles approach, a thin liquid film forms between them. As film thinning proceeds, the surface area of this element is greatly increased. Accordingly, the surface concentration of alcohol around the bubble's surface becomes high compared to the remainder in the liquid film. An increase in the surface tension of the liquid film is produced as a result of low alcohol concentration. Therefore, surface

tension gradient forces are generated and separate the gas–liquid interface so that coalescence is inhibited.

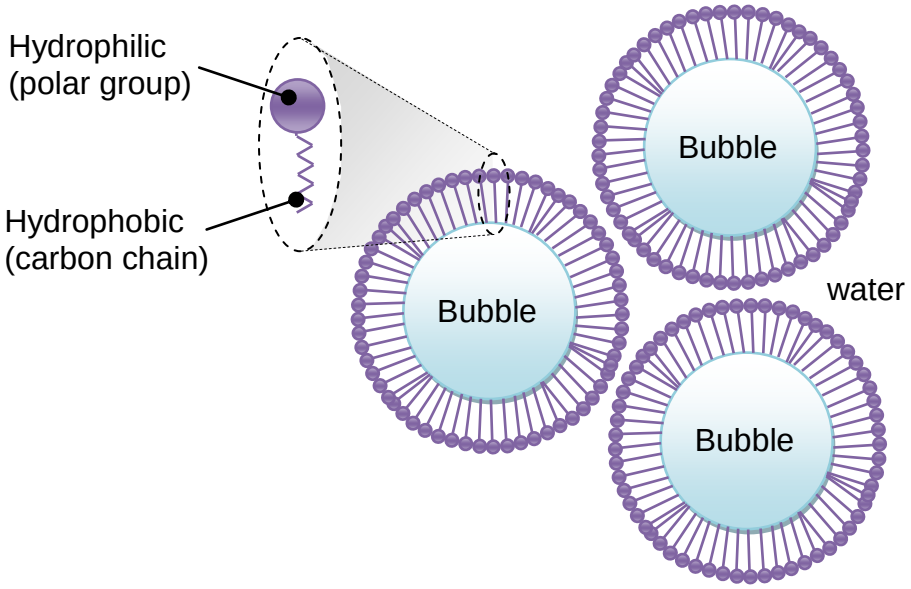


Figure 2.7 Accumulation of alcohol molecules (hydrophilic and hydrophobic) at the air-liquid interface to form a non-coalescing solution.

Krishna *et al.* (2000) studied the effect of the presence of alcohol on the transition regime. They used a Wallis plot (Wallis, 1969) to predict the regime's transition point: α_{trans} and $(j_g)_{trans}$. Figure 2.8 shows the relation between the "drift-flux" velocity, $j_g(1-\alpha)$, and the gas void fraction, α; the smooth curve represents the Richardson and Zaki (1954) equation:

$$j_g(1-\alpha) = v_t \alpha (1-\alpha)^n \qquad 2.1$$

where n is an empirical index and v_t is the rise velocity of a single bubble. For the air–water system in the homogeneous regime, n = 2 (Krishna *et al.,* 2000) and for the rise velocity, v_t = 0.24 m/s (Wallis, 1969). In Figure 2.8, the point where the data deviate from the curve is taken to indicate the regime's transition point; Krishna (2000) commented that the transition point is often difficult to characterise. However, Krishna *et al.* (2000) concluded that, in the air-liquid system, tap water clearly deviates from the Richardson and Zaki curve mentioned earlier (α_{trans}= 0.12), compared with the 0.1% water/ ethanol solution (α_{trans}=0.32) and the 1% water/ ethanol solution (α_{trans} = 0.40). In other words, the void fraction increases with an increase in alcohol concentration.

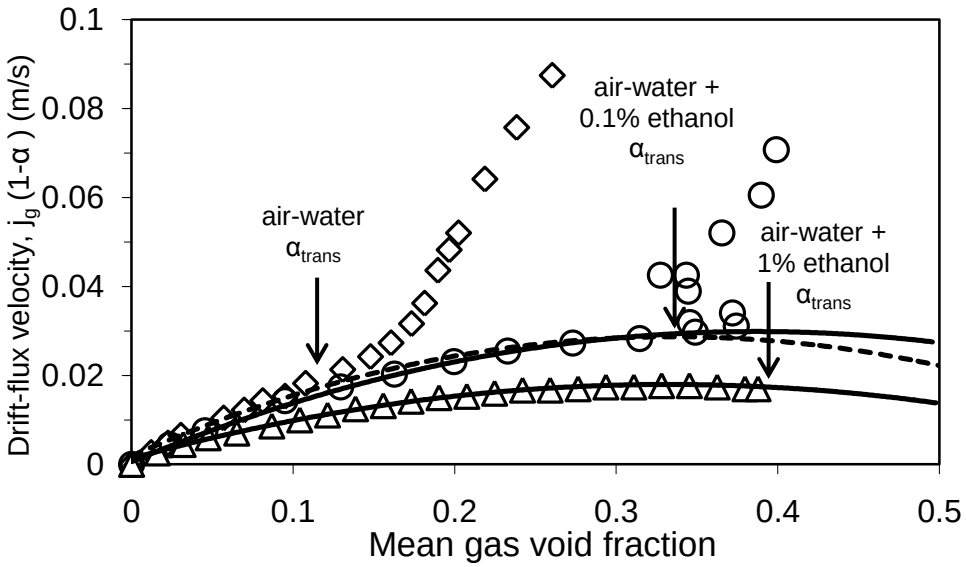


Figure 2.8 Effect of the presence of alcohol; Wallis plot to determine transition parameters α_{trans} and $(j_g)_{trans}$ (Krishna *et al.,* 2000).

2.3 Annular gap bubble columns

For decades, scientists and engineers have made numerous attempts to understand two-phase flow systems by carrying out experimental investigations (e.g. Serizawa *et al.,* 1975; Lucas *et al.,* 2005), and to model them by developing appropriate mathematical theory (e.g. Ishii, 1975; Drahos *et al.,* 1991). The majority of such studies considered two-phase flow using circular tubes; the reason for this stems from the widespread use of circular geometry in engineering applications. Nevertheless, flow through an annular gap of a circular cross-section also occurs frequently, and this is of great interest to those involved in the exploration and extraction of oil and natural gas. Double-pipe heat exchangers, different cooling channels, various gas lifting devices are examples where two-phase flow occurs through a concentric circular annulus. Accordingly, the flow of a two-phase mixture through an annular gap has been studied by several authors such as Sadatomi *et al.* (1982), Caetano (1984), Hasan and Kabir (1992), Caetano *et al.* (1992), Sun *et al.* (2004), and Das and Das (2010).

Al-Oufi (2006) compared data concerning gas void fractions using annular gap columns with those obtained when using open tube (circular cross-section) bubble columns (Figure 2.9). In this figure, the void fraction is plotted as a function of the superficial velocity in a vertical column with an internal diameter of

D_o=0.102 m and an open column equipped with a concentric 0.051 m inner tube. Figure 2.9 shows a least squares fit of the drift-flux model (as discussed in § 1.3) for two experimental data sets: (i) an open tube, and (ii) an annular gap bubble column. Typical values for the parameter v_t could fall in the range 0.15 – 0.25 m/s for bubble sizes in the range 3 – 8 mm (Shamlou *et al.,* 1994; Whalley, 1996; Shen and Finch, 1997); the larger fitted value of v_t for the annular gap column may indicate that larger bubbles than those in the open tube were present.

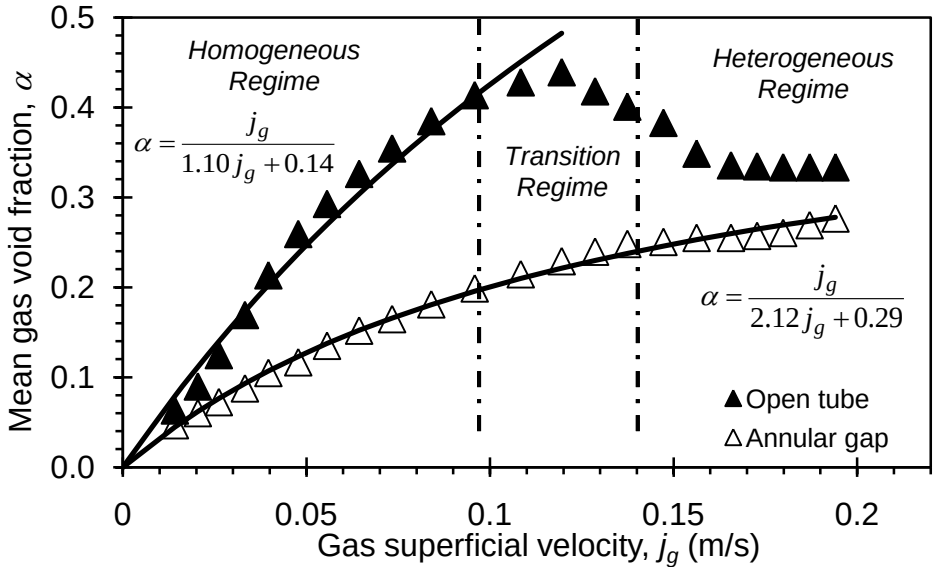


Figure 2.9 Void fraction data comparison for open tube and annular gap at the same superficial gas velocities (Al-Oufi, 2006).

The distribution parameters, C_0, for the two data sets are also significantly different and outside the normally expected range of 0.9–1.3 reported by Hibiki and Ishii (2002). This may indicate that the bubble size is increasing with increasing superficial gas velocity. (The values of these fitted parameters are rather sensitive to the exact range of superficial gas velocities used for data regression).

Hasan and Kabir (1992) reported that C_0 did not change with the ratio of inner to outer column diameter, given by:

$$\beta = \frac{D_i}{D_o} \qquad 2.2$$

for an annular gap bubble column; it remained close to the value of 2.0 that they had previously obtained for large diameter pipes (D_o > 0.1 m). Clearly C_0=2.0 has been reported in the past, and hence the range 0.9–1.3 that was proposed by Hibiki and Ishii (2002) is too narrow. In contrast, Hasan and Kabir (1988a, b) found that an increase in β led to a slight increase in C_0, but offered no explanation. The data in Figure 2.9 show that the diameter ratio, β, has a much larger effect on the distribution parameter. Furthermore, Hasan and Kabir (1992) found that for annular gap bubble columns, v_t remained unchanged from its value in an open tube, which would indicate rather similar bubble sizes in these two cases. Observations of an annular gap column in Al-Oufi's (2006) work show that at low j_g, small bubbles were produced. Increasing j_g caused these bubbles to merge and form bigger bubbles, which destabilised the flow at much lower void fractions and superficial gas velocities than in the open tube bubble column.

Hasan and Kabir (1992) used three different annular gap geometries by introducing 0.048, 0.057 and 0.087 m (o.d.) inner tubes into a 0.127 m (i.d.) column. They used batch stagnant water and a j_g range between 0.0066 to 0.2 m/s. The pressure drop method (manometer) was used to measure α in the bed. The bubble rise velocity was measured by determining the time required for bubbles to travel along a 3 m section of the column. They investigated the effect of annular gaps on two-phase hydrodynamics, and used the drift-flux model to obtain the average α. The drift flux model was implemented to model the *in-situ* gas velocity, v_G, by:

$$v_G = \frac{j_g}{\alpha} = C_o\, j_g + v_t \qquad 2.3$$

Harmathy (1960) presented the terminal rise velocity, v_t, depending on the surface tension σ, and the densities of gas, ρ_g, and liquid, ρ_l.

$$v_t = 1.53\left(g\sigma\left(\frac{\rho_l - \rho_g}{\rho_l^2}\right)\right)^{0.25} \qquad 2.4$$

They assumed that C_o is equal to the ratio of the velocity at the centre to the cross-sectional average velocity, and hence found that C_o=1.2 for circular

channels. Nevertheless, Hassan *et al.* (1988) and others reported a value of 2.0 for C_o for batch liquid columns with large diameters (> 0.10 m) due to liquid circulation. They reported that the terminal rise velocity, v_t, for bubbly flow was unaffected by annular gap geometries. The transition from bubbly to slug flow was found to occur at α=0.25 for both annular and cylindrical (open tube) geometries.

Kelessidis and Dukler (1989) studied air-water flow through vertical concentric and eccentric annuli of β = 0.67 (D_i= 0.0508 m and D_o= 0.0762 m). They identified the flow regimes from their conductivity probe signals by using probability density function analysis (PDF). They divided the time scale into equal increments of width, Δt=1 ms, and divided the voltage scale into equal increments of width, w. They expressed the PDF, $p(v)$, for time T and n_i times as follows:

$$p(v) = \lim_{w \to 0} \frac{1}{w} \left(\lim_{T \to \infty} \frac{n_i \Delta T}{T} \right) \qquad 2.5$$

The PDF gave a single peak near the maximum voltage value for the bubbly flow. This was because the probe tip was exposed primarily to liquid and little gas. On the other hand, the PDF demonstrated two peaks for slug flow: one at zero voltage and another at maximum voltage. This was because the probe tip encountered either all gas or the bubbly mixture with the presence of liquid. A regime map for transitions of different flow patterns has been established based on this analysis.

PDF analysis was also used by Das *et al.* (1999) to investigate transition conditions in an annular gap column. They conducted experimental observations of air–water up-flow through concentric annular gaps using three different geometries and column diameters: A (D_o= 0.508 m, D_i= 0.254 m, β= 0.5), B (D_o=0.381 m, D_i= 0.127 m, β=0.33) and C (D_o= 0.254 m, D_i= 0.127 m, β= 0.5). A parallel plate-type conductivity probe was used to identify the distribution of the void fraction in different flow regimes. The main finding was that the bubble-slug transition was distinguished by an increase in the peaks in the probe signals and a maximum voltage peak in the PDF curve, rather than the area between the two

peaks. This indicates that the growth of cap bubbles, rather than the coalescence of the spherical bubbles at an increased j_g, results in a slug flow regime arising from the bubbly flow. For flow through the concentric annular gaps, the researchers found that an average α value of 0.2 was predicted at the bubble to slug transition regime; this agreed well with the findings of Kelessidis and Dukler (1989).

2.4 Implementation of an impedance method in two-phase flow

Among the methods used to experimentally measure bubble velocity and size, electrical methods, which exploit the measurable differences in the conductivity of liquid and gas phases, are widely used (Azzopardi *et al.*, 2010; Luo *et al.,* 1997; Steinemann and Buchholz, 1984). When using an electrical probe in two-phase flow, the first requirement is that the phases have significantly different electrical conductivities (Jones and Delhaye, 1976). Impedance methods, using one or more electrodes, are popular techniques to measure local void fractions, and have been used by many researchers to study different two-phase flow regimes. The electrical conductance of the gas–liquid region surrounding the tips of the electrodes is measured; when the probe tip has penetrated a bubble there is no conductance, whereas when the probe tip is immersed in liquid, there is high conductance. The probe then behaves effectively as a local phase discriminator and the probability (the fraction of time) that the probe is immersed in a bubble is assumed to be equal to the void fraction (Angeli and Hewitt, 2000). From the time history of a two-phase flow at a given position (x), the gas void fraction, α, can be obtained:

$$\alpha(x) = \lim_{T\to\infty} \sum_i \frac{T_{gi}}{T} \qquad 2.6$$

where T_g and T are the time the probe indicates the gas phase and the total time of the run respectively.

2.4.1 Single-point conductivity probe

Many studies have used a single-point conductivity probe to measure local void fraction and bubble velocity in two-phase flow. Herringe and Davis (1976) described methods to analyse data from single-point conductivity probes for gas–liquid flows. They used a single-point conductivity probe to discriminate between the gas and liquid phases. They predicted the α profile for an air-water system in a vertical column 0.0508 m in diameter. They proposed a method to calculate the bubble size by assuming that bubbles are spherical, move in the same direction and have the same bubble rise velocity, v_t , and by knowing the residence time, t_R, which is the time that the probe tip is in the gas phase. Therefore, the bubble chord length, C, of a detected bubble is given by:

$$C = v_t t_R \qquad 2.7$$

Their analysis to calculate the bubble chord length is restricted to spherical bubbles; this is assumed to be the mean shape of bubbles in bubbly or dispersed flow. Furthermore, the assumption that the bubbles move in the same direction is not true since bubbles in the bed rise in different directions, even at low j_g.

Teyssedou *et al.* (1988) studied the implementation of a single-point conductivity probe in an air-water system to measure the local α. The test section was a vertical Plexiglas tube, 0.019 m in diameter and 1.105 m in height. They used two sensor tip geometries (long at 2 mm and short at 0.5 mm in length) and compared α data with those obtained using a quick-close valve method. They found that the short tip sensor gave better α results, particularly when the probe was close to the tube walls. They attributed this to the reduction in the deformation of the electrical field around the short sensor tip, which improved α measurements.

Angeli and Hewitt (2000) used this technique to detect flow regimes and to measure volume fractions in an oil–water flow in a horizontal pipe. They showed that the impedance method has advantages over visual observation, photographic and video methods in clarifying the boundaries of the various flow regimes. However, these techniques are inadequate for giving a clear description

of the flow pattern, as the view is obscured by complex interfacial structures, resulting in reflections and refractions.

2.4.2 Two-point conductivity probe

A two-point probe can be used to predict both local void fractions and bubble velocity. The bubble rise velocity, v_t, can be calculated from the known values of the distance between the probe tips and the time it takes for a bubble to be detected by both sensors. The two-point probe also yields information about the chord length distribution of bubbles intercepted by the probe from which the true bubble size may be inferred. (See for example Liu and Clark, 1995). Van der Welle (1985) used a two-point probe to measure the void fraction, bubble velocity and bubble size in air-water flow. Lucas *et al*. (2004) described the use of a two-point tip probe to obtain the local gas volume fraction and the local gas velocity in low volume fraction, vertically upward, bubbly air–water flows.

Panagiotopoulos (2009) used a two-point conductivity probe to validate Electrical Resistance Tomography (ERT) in measuring the local volume fraction, axial bubble and oil droplet velocity of dispersed phase air-water and water-oil systems. Experiments, which were conducted in a 0.08 m. (i.d.) vertical and inclined column, showed that the local conductivity probe gave more accurate measurements of the volume fraction, and the bubble and oil droplet velocity profiles compared to those obtained using the ERT method. However, ERT was found to be useful in determining the mean α and bubble velocity. Panagiotopoulos (2009) also used a conductivity probe to validate data produced by Computational Fluid Dynamics (CFD) simulations.

Recently Bao *et al.* (2010) used a two-point conductivity probe in a stirred air-water tank to measure the local α and bubble size distribution. The probe consisted of two stainless steel needles, 0.2 mm in diameter and insulated with varnish except for a very short length at the tip of the needles. The vertical distance between the two tips was 0.34 mm. They used a time-averaged quantity (Equation 2.6) to measure the local void fraction in the tank. They noticed that the α predicted by needle 2 was about 20% smaller than that obtained by needle 1. They reported that, as the bubble was pierced by the leading sensor (needle 1), it

disturbed the movement and the shape of bubbles; these then hit needle 2 and hence, needle 1 was used to measure the local α.

2.4.3 Four-point conductivity probe

A further development in using the probe technique was introduced by employing a four-point probe: e.g. Mishra *et al.,* 2002; Zhao *et al.,* 2009. The purpose of using a four-point probe was to collect more information about the bubble: e.g. the local axial, radial and azimuthal velocity components of the gas bubbles.

Lucas and Mishra (2005) used a four-point probe to characterise the flow distribution across the cross section, both with and without swirling, bubbly air-water flow, in terms of the mean local axial, radial and azimuthal velocity components of the gas bubbles. Experiments were carried out in a vertical column with the water superficial velocity within the range of 0.41 – 0.91 m/s; j_g was in the range of 0.037 – 0.081 m/s. The probe was fitted to a pipe and used to measure void fraction, bubble velocity and chord size. The sharply tapered sensor tips reduce the number of missed bubbles, as well as the deformation of passing bubble interfaces. Overall, this conductivity probe provides great flexibility in measuring a wide range of two-phase flow regimes. The researchers found that the radial velocity of the gas bubbles was always close to zero and the presence of swirl increased the azimuthal velocity of the gas bubbles in the direction of the swirl. Moreover, they reported, on the introduction of swirl, a very slight effect on the distribution of the local axial velocity of the gas bubbles. The distribution of the local α in the flow across was unaffected by the presence of swirl.

Luther *et al.* (2004) proposed an algorithm to recreate bubble shape, aspect ratio and velocity from signals obtained from a four-point fibre-optic probe. The conductivity technique and measurements of void fraction, bubble velocity and chord are discussed in detail in §3.4.

2.5 Bubble size and velocity

2.5.1 Bubble size

Bubble size is an important variable in the design and scale-up of industrial units, such as bubble columns, since it enhances the understanding of mixing as well as heat and mass transfer properties. It can also be used for validation, or often as a tuning variable in process simulations using CFD. Bubble formation is affected by many operating parameters (e.g. gas flow rate through the gas distributor), system properties (such as the gas distributor geometry), and also physico-chemical properties, such as liquid viscosity and liquid surface tension, which decide the mode of bubble formation and subsequently reflect on the bubble size. The main forces acting on a moving bubble are gravity, buoyancy, drag, viscous forces, added mass force, and the lift force. In many cases, the gas-liquid properties, gas distributor dimensions, and the material of construction govern these forces. The flow rate of gas through the distributor and the distributor's dimensions mainly decide the bubble frequency and thus the detachment time. Kulkarni and Joshi (2005) carried out a comprehensive review of earlier works, particularly those relating to the measurement of bubble size. They reported those factors that might affect bubble size, i.e. liquid viscosity, density, surface tension and velocity, gravitational acceleration, gas density and flow rate, diameter, submergence, contact angle, orientation, and the material of construction of the gas distributor. In this section, only the relevant factors, sparger geometry, gas flow rate and surface tension, which might affect bubble formation, according to the conditions current in an air-water system, are discussed.

The sparger configuration seems to play an important role in the initial bubble size close to the entrance region. Kazakis *et al.* (2008) studied the effect of the pore size of the sparger for a number of liquids covering a wide range of surface tension and viscosity values, on the bubble formation by implementing nominal pore sizes of both 40 and 100 μm. They observed that, for the same j_g, the bubbles' mean Sauter diameter produced using a sparger with a pore size of 40 μm was 15-30% smaller than that of the 100 μm sparger.

When the bubble is generated very slowly at an immersed orifice placed horizontally in water, the bubble grows until its buoyancy force exceeds the surface tension force holding it on the orifice tip. A chain of bubbles become independent from the solid-liquid-gas boundary and rise in the liquid. For a spherical bubble, formed by a perfectly wetted orifice diameter, d_o, from the liquid, the bubble equivalent diameter, d_e, at laminar flow in the orifice can be derived by equating the two forces:

$$d_e = \sqrt[3]{\frac{6 d_o \sigma}{g(\rho_l - \rho_g)}} \qquad 2.8$$

For an air-water system at 20°C acceleration due to gravity, g = 9.81 m/s^2, with a surface tension, σ = 0.07274 N/m, and density difference, $(\rho_l - \rho_g)$ = 997 kg/m^3, Equation 2.8 can be rearranged to be:

$$d_e = 0.0355 \sqrt[3]{d_o} \qquad 2.9$$

Jamialahmadi and Muller-Steinhagen (1993) and others studied, in an air-water system, the effect of the gas flow rate on bubble sizes formed at the orifice. They concluded that, as the gas flow rate increased, the bubble size also increased. For an airlift column with j_g in the range from 0.0059 to 0.0737 m/s, Wongsuchoto et al. (2003) reported a reduction in the bubble size as j_g increases in the riser section. They used a vertical airlift column with a height of 1.2 m and a diameter of 0.137 m equipped with a perforated ring sparger with 1 mm orifices. An image technique was implemented for the bubble size measurements. At high values of j_g, they noted a reduction in the number of large bubbles, and an increase in the number of smaller size bubbles. They proposed that this reduction in the bubble size was due to the increase in the liquid velocity at high j_g, which might be responsible for the development of turbulent strength. Prince and Blanch (1990) attributed this to the bubble breakage, which was caused by the energy from the turbulent swirls of appropriate size obtained from the contact between bubbles. It can be concluded that an increase in j_g could generate large and small bubbles simultaneously; however the number of small bubbles might be greater than the large bubbles, which leads to a reduction in average bubble size.

In a churn-turbulent flow and in an air-water system at 20°C, Jamialahmadi and Muller-Steinhagen (1993) proposed that the bubble diameter is mainly affected by the j_g and by the α:

$$d_{et} = 0.45 j_g^{0.87} \alpha^{0.85} \qquad 2.10$$

where d_{et} is the bubble diameter in churn-turbulent flow.

Therefore, in an air-water system, the bubble size, d_e, at a j_g range of 0-0.12 m/s can be determined by combining Equations 2.9 and 2.10 to give the following term:

$$d_e = \sqrt[3]{d_{el}^3 + d_{et}^3} \qquad 2.11$$

Jamialahmadi and Muller-Steinhagen (1993) confirmed the reliability of Equation 2.11 for air-water systems at 20°C.

As mentioned earlier in §2.2.4, the addition of a relatively small amount of alcohol inhibits the bubble coalescence, and hence produces smaller sized bubbles. The organic and inorganic substances act as surface-modifying agents, and reduce the surface tension. Jamialahmadi and Muller-Steinhagen (1992) studied the effect of the concentration of alcohols (e.g. ethanol), organic acids (e.g. ethanoic acid) and potassium chloride on bubble size. By using a perforated plate of d_o= 0.001 m and for a constant j_g of 0.1 m/s, the addition of both organic and inorganic solutions seems to decrease the diameter of the bubbles. A similar effect was reported by Nahara and Kamotani (2003). They also concluded that, as the liquid surface tension decreased, the bubble size decreased, and at the same d_o and j_g. It is obvious from Equation 2.7 that the surface tension, σ, has a significant effect on the bubble size. As the surface tension, σ, decreases, the bubble diameter decreases.

2.5.2 Bubble rise velocity

It is important to understand the bubble motion mechanism in gas–liquid operations. Bubble rise velocity is one of the parameters, which influences the

residence time of the gas phase and hence the contact time for the interfacial transport; this subsequently affects the performance of the equipment. In a stagnant liquid, a bubble is moving due to the buoyancy force. Once the bubble is generated by the gas distributor (e.g. the orifice), it rapidly reaches its terminal velocity, v_t, as obtained through drag, F_D, and buoyancy, F_B, forces.

$$F_B = \frac{1}{6}\pi d_e^3(\rho_l - \rho_g)g = \frac{1}{2}\frac{\pi d_e^2}{4}\rho_l v_t C_D = F_D \qquad 2.12$$

By rearranging Equation 2.12, the terminal bubble rise velocity, v_t, can obtained:

$$v_t = \sqrt{\frac{4gd_e(\rho_l - \rho_g)}{3C_D\rho_l}} \qquad 2.13$$

For spherical bubbles in laminar flow, the drag coefficient, C_D, is given by Stokes law:

$$C_D = \frac{24}{Re} \qquad 2.14$$

where Re is the Reynolds number defined as:

$$Re = \frac{\rho_l d_e v_t}{\mu_l} \qquad 2.15$$

Many researchers have investigated bubble rise velocity in water. Clift *et al.* (2005) introduced a figure from Gaudin (1957) which illustrates terminal velocity with respect to the bubble size for an ellipsoidal regime, with adjacent parts of the spherical and spherical-cap regimes for pure and contaminated water. In the spherical regime for both pure and contaminated water, it shows that, as the bubble size increases, the terminal velocity also increases. Kulkarni and Joshi (2005) in their review paper on bubble formation and calculating the bubble rise velocity, stated that, for air-Newtonian liquids, the correlation proposed by Clift *et al.* (1978) can be used to calculate v_t:

$$v_t = \left(\frac{\mu}{\rho_l d_e}\right) M^{-0.149}(J - 0.857) \qquad 2.16$$

where

$$J = 0.94\, H_o^{0.747} \qquad for\ 2 < H_o \leq 59.3 \qquad 2.17$$

and

$$J = 3.42 H_o^{0.441} \qquad for\ H_o > 59.3 \qquad 2.18$$

where H_o is the orifice coefficient, which can be calculated based on the Eotvos number, Eo, and the Morton number, M:

$$H_o = -\frac{4}{3} Eo M^{-0.149} \left(\frac{\mu}{\mu_l}\right)^{-0.14} \qquad 2.19$$

$$Eo = \frac{g d_e^2 (\rho_l - \rho_g)}{\sigma} \qquad 2.20$$

and

$$M = \frac{g \mu_l^4 (\rho_l - \rho_g)}{\rho_l^2 \sigma^3} \qquad 2.21$$

Clift *et al.* (2005) recommended this correlation to predict the bubble terminal velocity, v_t, when surfactant contamination is present in the liquid, and when the data meets the criteria:

$$M < 10^{-3}, \quad Eo < 40, \quad Re > 0.1 \qquad 2.22$$

The approach modified by Jamialahmadi *et al.* (1994) to predict v_t, was based on the wave analogy theory proposed by Mendelson (1967). He assumed that bubble interfacial disturbances, whose dynamics are similar to those of waves on an ideal fluid, can be correlated in terms of the fluid properties and bubble size (d_e) for the terminal rise velocity of a bubble as:

$$v_t = \frac{v_{t1} + v_{t2}}{\sqrt{v_{t1}^2 + v_{t2}^2}} \qquad 2.23$$

where

$$v_{t1} = \sqrt{\frac{2\sigma}{d_e(\rho_l - \rho_g)} + \frac{g d_e}{2}} \qquad 2.24$$

and

$$v_{t2} = \frac{g d_e^2(\rho_l - \rho_g)}{18\mu}\left(\frac{3\mu_l + 3\mu_g}{2\mu_l + 3\mu_g}\right) \qquad 2.25$$

Kulkarni and Joshi (2005) concluded that both correlations yield excellent results when compared with the experimental data for various liquids. However, the correlation of Clift *et al*. (1978) gives good accuracy for bubble diameters, d_e< 5 mm, and the correlation of Jamialahmadi *et al.* (1994) is reliable for bubble diameters, d_e, ranging from 5 – 30 mm.

The terminal velocity, v_t, of air bubbles in water depends on water purity, especially in the spherical and ellipsoidal region. Figure 2.10 shows v_t with respect to the bubble equivalent diameter, d_e, presented by Gaudin (1957). The v_t varies in pure and contaminated water at the same d_e. This could be because bubbles in pure water are freely movable. However, the presence of impurities leads to the adsorption and collection of surfactants at the bubble surface, which hinders its mobility.

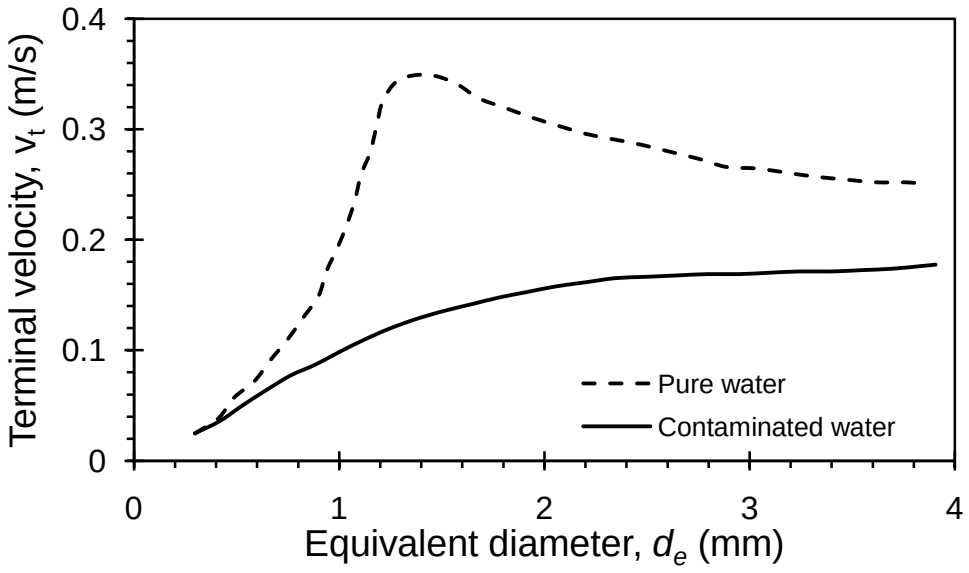


Figure 2.10 Terminal rise velocity with respect to equivalent diameter, d_e, of a bubble (Gaudin, 1957).

2.6 Image visualisation/analysis

Using transparent enclosures, imaging is preferred over other techniques to give a direct measurement of the velocity, size and shape of the bubbles. The aspect of the flow is an important feature and taking pictures through the wall is often reported in the literature (e.g. Miyahara *et al.,* 1986; Junker, 2006). However, the disadvantages of the imaging technique are noticeable: only the surrounding area of the wall can be observed, and a transparent liquid and a transparent wall are required. The use of such a method is tied to bubble coalescence properties and photography speed. In addition, it is well suited to transparent systems in two dimensions and may be extended to three dimensions, provided a small number of bubbles are being studied in a stagnant or slow flowing liquid phase. However, where the enclosures or liquid are not transparent, image visualisation/analysis techniques cannot be applied. In a transparent cylindrical column, a square box filled with water may be attached to the column to eliminate optical distortion during the photography of the bubbles (Camarasa *et al.,* 1999). A back source of light may also be placed in line with the camera, with tracing paper being placed between the lamp and the column to eliminate reflection (Wang and Dong, 2009).

Lage and Esposito (1999) implemented the image technique to obtain the size and distribution of bubbles in a transparent bubble column, which was operated in a homogeneous flow using an air-aqueous isopropanol solution. Three isopropanol concentrations, 0.5, 1 and 2% by volume at different j_g values, were used. The researchers measured the bubble diameter directly from the images with the help of a scale, which was attached to the wall of the column and was at the same focal distance as the measured bubbles. They then measured a range of between 50 to 100 bubbles per picture for each experimental condition. The experimental measurement error was estimated to be in the range of 10 to 15% based on error in the measurement of bubble axes and optical error. Lage and Esposito (1999) presumed that, as the column operated under homogeneous flow conditions, the bubble size distribution obtained in the test section shown in the image was approximately similar to that in the whole column. As the flow regime was characterised by a relatively uniform bubble size distribution, Lage and Esposito (1999) concluded that the photographic method provided a good

approximation of the mean bubble diameter. They also observed that the bubble size distributions were closer to a log normal distribution than a normal distribution.

Recently, Rakoczy and Masiuk (2009) studied the effect of a rotating magnetic field on the bubble size distributions by implementing digital photo cameras (Olympus µ500 digital) in order to obtain the bubble size distribution in a cylindrical Plexiglas column where D_o= 0.1 m. Tap water, synthetic wastewater (mainly containing peptone, urane, detergent, ammonium-chloride and magnesium sulphate) and an aqueous solution of NaCl brine. A rectangular container was attached to the column to eliminate distortion and the light source was located on the opposite side of the camera near the rectangular containers. MATLAB's Image Tool was used to process the images; 250 bubbles can be measured from the images for the various liquids and the operating conditions. The bubbles were observed to have an ellipsoidal shape and the equivalent diameter, d_e, can be obtained using the following term:

$$d_e = \sqrt[3]{a^2 b} \qquad 2.26$$

where a and b are the long and short axes of the ellipsoid respectively, and the bubble is assumed to have a depth equal to a. The researchers concluded that the application of a rotating magnetic field led to an increase in the diameter of the bubbles and that the bubble size increased with increased gas flow rate.

2.7 Conclusion

From the literature presented and discussed in the preceding subsections, it can be concluded that liquid height, gas distributor geometry, flow area and water contaminants play a major role in affecting void fraction in a gas-liquid system. Therefore, an increase in liquid height reduces the void fraction only up to a point: α is independent when the ratio of liquid height, H_L, to the internal diameter of the column, D_o, exceeds 5, as Wilkinson *et al.* (1992) reported. Additionally, a perforated gas distributor produces small and uniform bubbles to give a high void fraction in homogeneous flow, while a low void fraction (i.e. heterogeneous flow) forms as the size of the gas distributor hole increases. The presence of

contaminants in the water causes the formation of small and uniform bubbles, which lead to a high gas void fraction; moreover, the gas void fraction increases with increases in alcohol concentration and chain length, and so it was necessary to study their effect in the current study. In general, it was found that the void fraction decreases with increases in the column diameter, D_o, and the ratio H_L/D_o. On the other hand, the void fraction decreases with an annular gap column, as many authors have reported. However, from all the literature, no study, with the exception of that of Al-Oufi (2006), has investigated deeply the cause of low void fraction and compared it, at the same superficial gas velocity, with an open-tube void fraction. All the three methods (aerated level, conductivity and image visualization) were chosen for their simplicity, their cost effectiveness and their level of appropriateness to the current air-water system. Initially, a two-point conductivity probe was designed to collect information about void fraction, velocity and the chord size of bubbles. Later, it was decided to design a four-point conductivity probe in order to decrease the number of missed bubbles. In contrast, a photographic technique was implemented to predict the bubble size in order to compare its results with those obtained using the probe. Finally, it was observed that there is a firm relation between the gas void fraction and the size of bubbles; small, uniform and well distributed bubbles probably give a high gas void fraction whereas large and unevenly distributed bubbles probably produce a low gas void fraction. Thus, whatever factor affects gas void fraction, also affects bubble formation.

CHAPTER THREE

MEASURING TECHNIQUES, SIGNAL PROCESSING AND BUBBLE SIZE TRANSFORMATION

3.1 Introduction

The chapter mainly focuses on discussing the techniques that were used in this study to measure the variables of air-liquid flow, e.g. the mean and local gas void fraction, α, and the velocity and size of the bubbles. The conductivity probe technique was designed to measure all the variables, the aerated level technique was used to measure the mean α, and the imaging technique was designed to determine the bubble size distribution at the column wall. The aerated level and imaging techniques were designed to compare their results with those using the conductivity probe technique. From the point of view of simplicity, the design and setup of the aerated level and the imaging techniques are described in the first few pages, whereas the rest of the chapter describes the design and approach of the conductivity probe technique in depth.

3.2 Aerated level technique

The aim of the current technique is to measure the overall gas void fraction, α, in an air-water system. Overall, α (a volume average for the whole aerated column) values may be obtained by recording the volume change following aeration at a given gas superficial velocity, j_g, using:

$$\alpha = \frac{V_g}{V_g + V_l} \qquad 3.1$$

where V_g is gas volume and V_l is liquid volume. The cross-sectional area of the column is the same throughout and hence, height measurements were used in place of volumes, so liquid and aerated levels were conveniently read from a scale on the wall of the column; see Figure 3.1.

$$\alpha = \frac{h_g}{h_g + h_l} \qquad 3.2$$

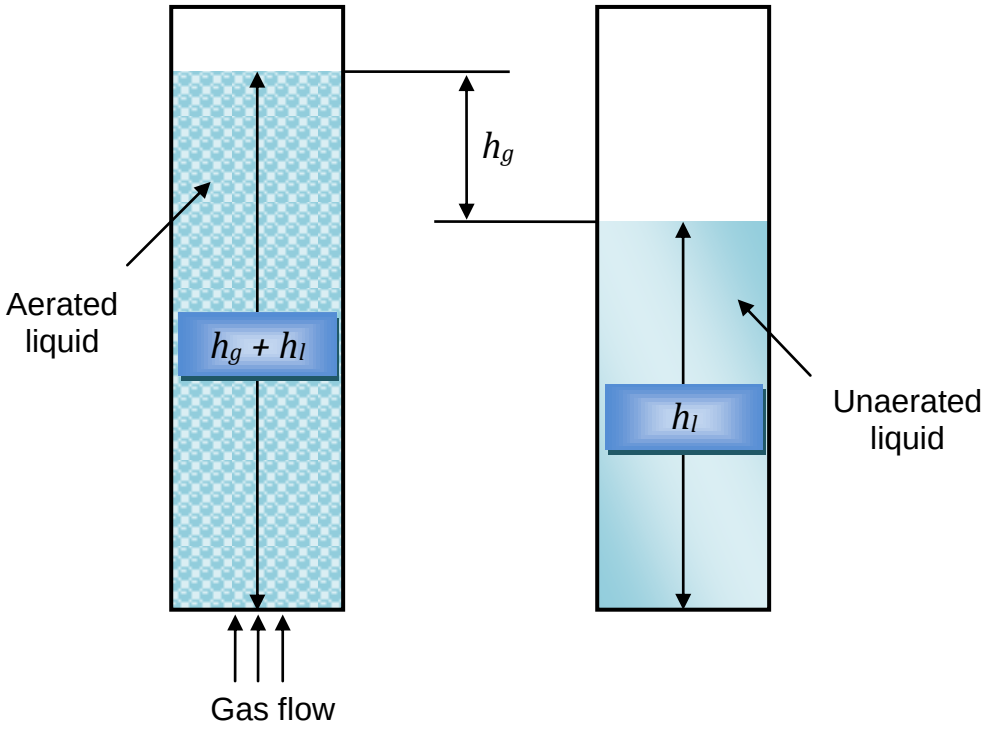


Figure 3.1 Aerated level technique to measure the overall gas void fraction.

3.3 Setup and design of imaging experiments

Imaging techniques are widely used for measuring bubble size because of their simplicity, ease of implementation and low cost compared to other methods such as X-ray and MRI (Acuna and Finch, 2010). However, it should be pointed out that an imaging method gives reliable results only in a bubbly flow regime at the wall of the column. This is because, at high gas flow, churn-turbulent flow could occur and it would then be difficult to capture an image of the edge of the bubbles. The aim of implementing this technique in an air-water system is to measure the size of the bubbles, and compare these with the size distribution deduced from the chord length distribution obtained using the probe method (see § 3.4.11).

Figure 3.2 shows a schematic diagram of the setup of the image experiments. A transparent box filled with water was mounted around the rig in order to eliminate optical distortion, and a ruler was attached to the wall of the column for use as a reference scale; see Figure 3.3 a. The tap water level in the column was set at

1.0 m and a sintered plastic sparger was used as the gas distributor. The air flow rate was measured by a rotameter, which was introduced from the bottom of the column.

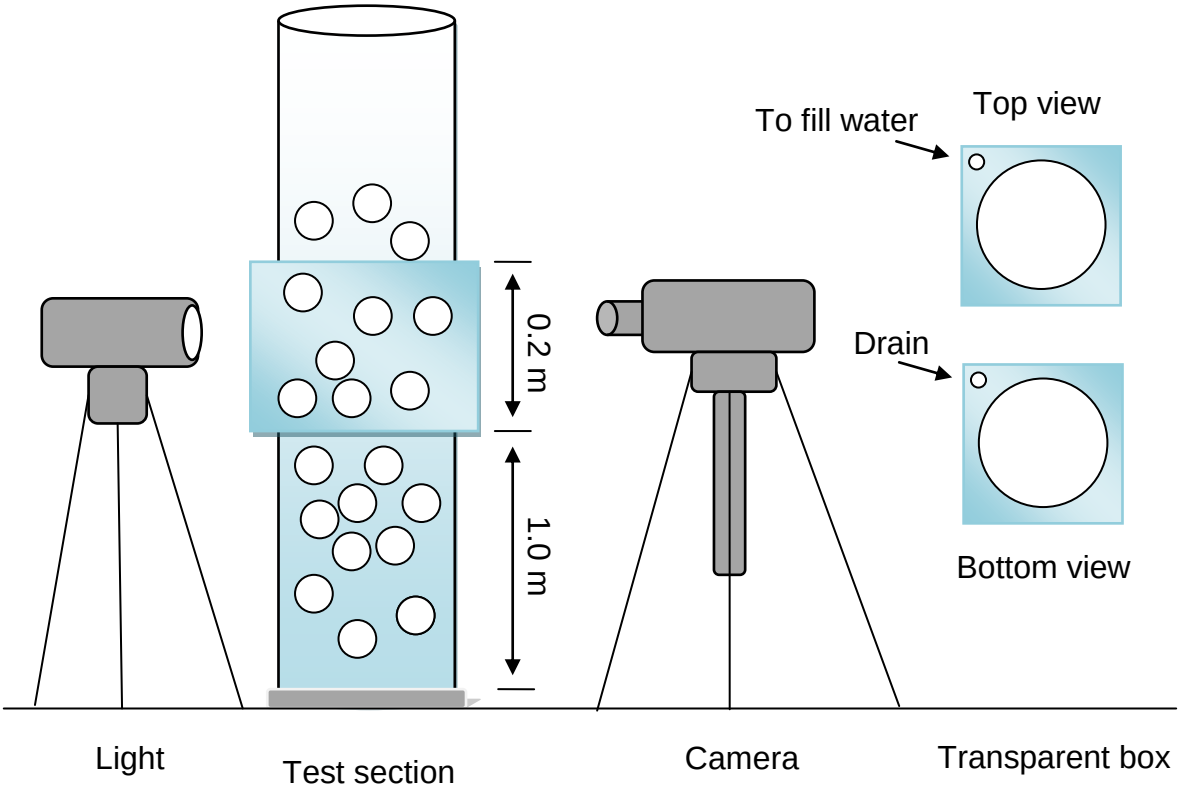


Figure 3.2 Setup of image experiments.

The image technique was implemented in an open tube bubble column (OTBC), an annular gap bubble column (AGBC) and in an open tube bubble column equipped with an orifice (OTBCEO) to carry out experiments to measure the bubble size distribution. A Canon EOS 350 SLR CMOS digital camera was used for taking images and a light source, covered with tracing paper to eliminate light reflections, was placed behind the test section. An EF-S 60mm f/2.8mm Macro USM lens was used to capture the bubbles; a typical image captured by the camera is illustrated in Figure 3.3 b.



Figure 3.3 a) An image of the transparent test section shows the attached scale; b) A typical image produced by the camera of bubbles at low gas flow rate.

The images of the captured bubbles were analysed using a MATLAB program to perform a quantitative analysis of the images in order to obtain data on the sizes, shapes and orientations of the bubbles. Figure 3.4 illustrates a typical image, captured by the camera, which was uploaded onto the MATLAB program to obtain information regarding size from the image. The process is described in the following steps (Figure 3.4) while the MATLAB codes used can be found in Appendix A :

1. Calibrating pixels: mm with the help of the scale on the image and to improve the quality of the image by using contrast, brightness etc. and also to magnify the field of view.
2. Selecting six points on the surface edges of bubbles. From analytic geometry, an ellipse can be defined by a specific set of five points: (x,y) to obtain parameters a, b, c, d and e in the ellipse equation:

   $$ax^2 + bxy + cy^2 + dx + ex + 1 = 0 \qquad 3.3$$

3. Six points in the bubble edge were taken and a best fit of the 5 parameters was conducted to represent the ellipse.
4. The analysis yielded the long, a, short, b, axes and orientation angle, θ.

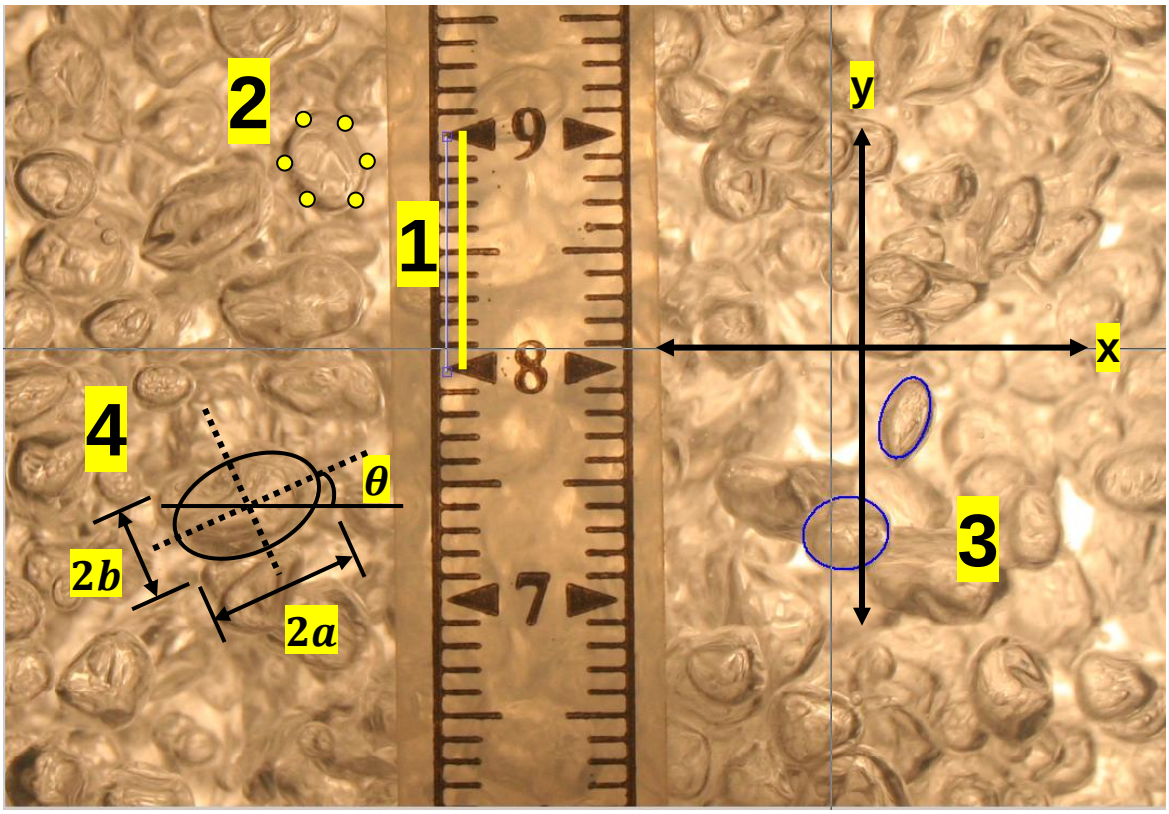


Figure 3.4 A typical image showing the steps used to determine data on bubble sizes, shapes and orientations.

Figure 3.5 illustrates schematically the long axis a, the short axis b and the orientation angle θ. The aspect ratio, φ, can be calculated by:

$$\varphi = \frac{short\ axis, b}{long\ axis, a} \qquad 3.4$$

The aspect ratio, φ, value can be used as a bubble shape discriminator, where φ (the value of the spherical bubble) is equal or close to 1; φ <1 would indicate an ellipsoidal bubble.

The volume-equivalent diameter approach was used to calculate the bubble diameter. It was assumed that the bubble depth was equal to the long axis, a, so the bubble volume equation might be expressed as follows i.e. an oblate spheroid.

$$v = \frac{4\pi}{3} a^2 b \qquad 3.5$$

Thus, the volume – equivalent diameter, d_e, is:

$$d_e = 2\sqrt[3]{a^2 b} \qquad 3.6$$

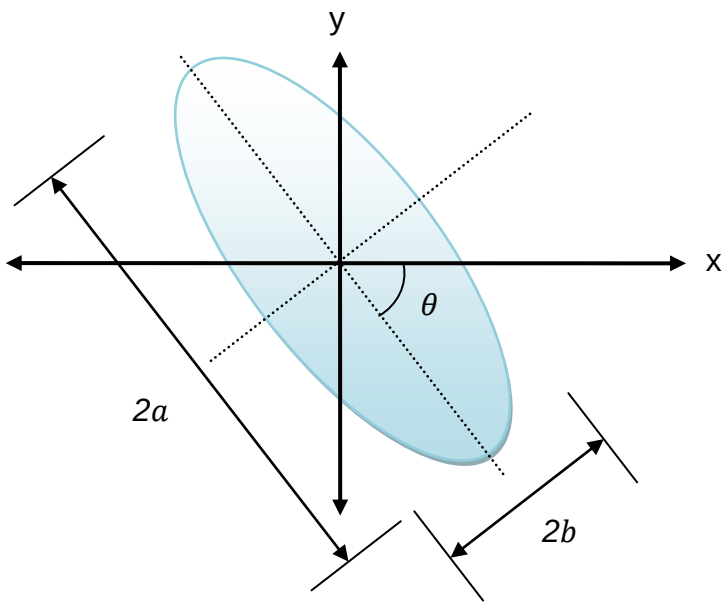


Figure 3.5 Schematic diagram of a bubble showing the long axis *a*, short axis *b* and orientation *θ*.

In the literature, the number of sampled bubbles required to obtain the bubble size distribution is yet an open subject: Wongsuchoto *et al.* (2003) and Rakoczy and Masiuk (2009) counted 250 bubbles, Hanselmann and Windhab (1999) counted 300 bubbles per one image and others more than that, but over more than one image.

The number of sampled bubbles was chosen according to the maximum number of bubbles per image that might be identified at the lowest gas superficial velocity, j_g. At the same time, this number of bubbles should give a reasonable bubble size distribution. The number of sampled bubbles per image was set to be between 250 to 300 bubbles/ image.

Figure 3.6 shows an image that was processed by the MATLAB codes to identify more than 250 bubbles in order to obtain the bubble size distribution. The scale is shown in Figure 3.6 in the middle of the image, which was used to calibrate the pixels. With the help of the image tools (e.g. zooming in and out), tiny bubbles at the bottom right of the image were identified. At a gas superficial velocity of j_g = 0.144 m/s, it was difficult in some parts of the image to identify the edge of the bubble because of their fast movement. Another disadvantage of the imaging analysis is that, with the bubbles close to the wall of the column, only the edge of the bubbles can be captured. Therefore, the bubble size distribution produced by the imaging technique should be compared with the bubble size distribution obtained using the conductivity probe technique, when the probe is positioned at the wall of the column.

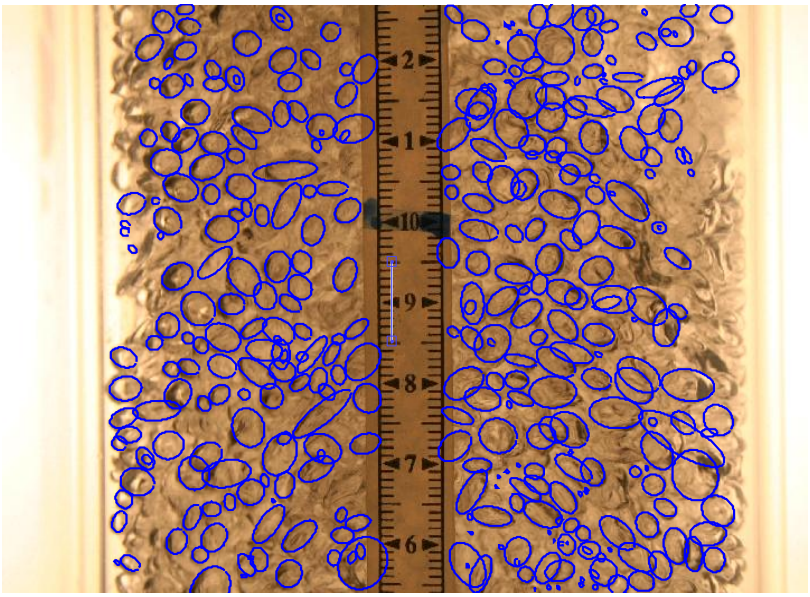


Figure 3.6 The final appearance of an image after identifying more than 250 bubbles using the MATLAB imaging analysis codes. The image is for air-tap water flow in an open tube column with a porous sparger and j_g =0.144 m/s.

3.4 Conductivity technique

3.4.1 Introduction

It is well known that the conductivity technique has advantages over the aerated level and image techniques, since it gives more detail about local α, bubble velocity and chord size distributions. The purpose of introducing the conductivity probe was to obtain radial profiles of local α and to study the air-water system in depth by detecting the local bubble velocity and chord size distribution. The average α over a diameter of the column obtained from using the conductivity technique can be compared with α measured by the aerated level method. In this part of the thesis, the rig setup, the probe design, dimensions and calibration are described.

3.4.2 Conductivity experiment setup

Conductivity probes represent one of the few point-wise measuring techniques in two-phase flow. The general principle of operation for such a probe is that two- or four-point probes should be immersed within the air-liquid flow. Figure 3.7 shows the setup and connection of the probe to the OTBC. The column wall is made from glass sections, joined by plastic flanges. A PVC plastic ring can be inserted between the glass sections and is held in place by the flange connections. The probe can be inserted through a hole in the PVC ring, as shown in Figure 3.8. The probe was connected to a conductivity meter, which was designed in the workshop of the Chemical Engineering Department at Loughborough University (the electrical circuit is shown in Appendix B). The conductivity meter was connected to a data acquisition device, DAQ (Model: USB6210), which converts the analogue voltage into a digital signal. The output signals were recorded digitally at 4 kHz using LabVIEW software.

LabVIEW 8.1 software was used as an interface program to collect and display the probe data and save them as a text file for further analysis. The LabVIEW flowchart and the interface are illustrated in Appendix B. Furthermore, the raw voltage measurements were converted in a MATLAB program to give local α, as well as bubble sizes and velocities.

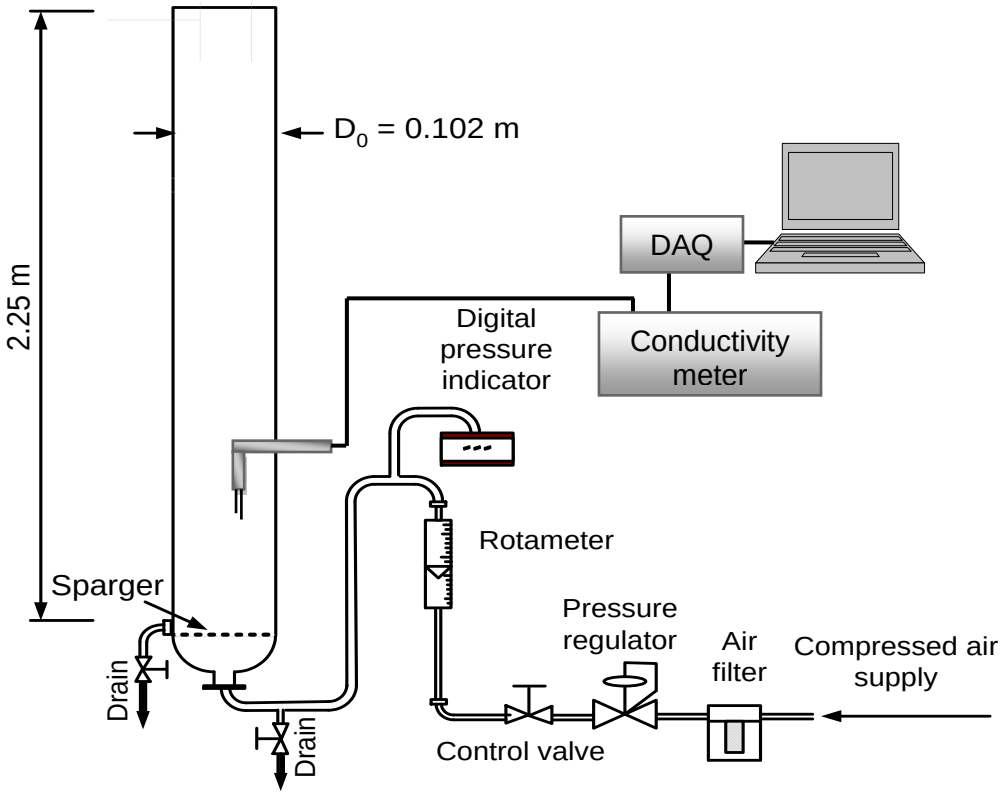


Figure 3.7 Setup of the experimental probe rig.

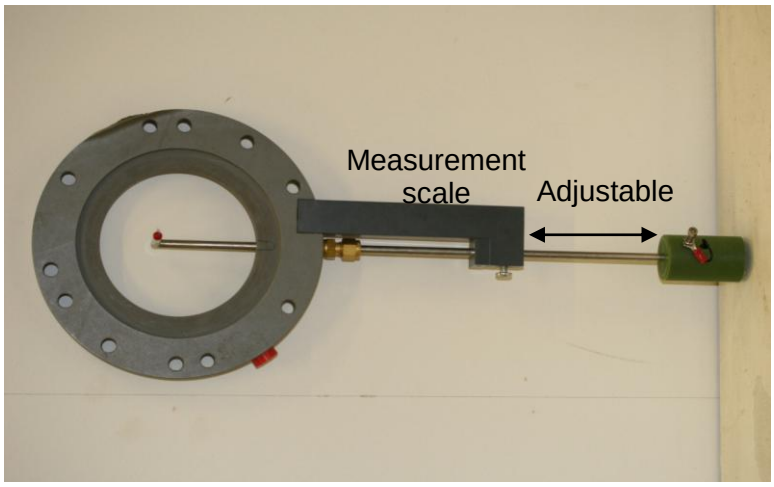


Figure 3.8 An image of the probe setup designed to measure α, bubble velocity and chord size.

3.4.3 Design and dimensions of the probe

The probe was designed to be directed vertically downwards opposite to the flow direction, as it was necessary to detect bubbles across the column and near walls. Therefore, the probe was designed to be able to traverse the column; it also had a tight radius, and a right angled bend to allow the probe to take measurements close to the walls; (see Figure 3.9). A PVC bar, to support the case of the probe, was attached to the flange to adjust the position of the probe across the column. This allowed the probe to traverse 95 mm from the close wall to the far wall across the column. A ruler was attached to the PVC bar to measure the distance that the probe travelled, as shown in Figure 3.9.

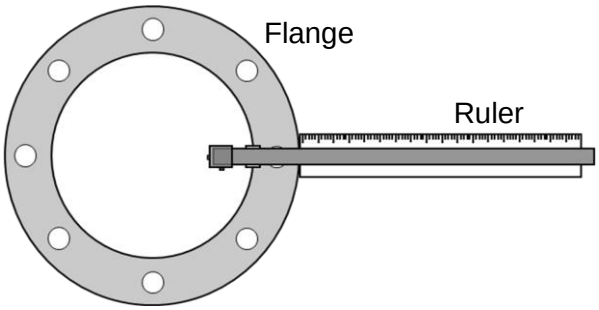


Figure 3.9 Probe design; top view sketch of the probe and flange ring shows the attached ruler.

Two-point conductivity probe

Initially, a two-point probe was designed and constructed. This conductivity probe consisted of two electrodes and a common earth, which is the outer stainless steel sheath of the probe body; see Figure 3.10. The two probes were made from stainless steel acupuncture needles that were electrically insulated and rendered non-wetting by the application of a varnish, except at the tips, which were gold-plated to stabilise the response and to prevent corrosion. Each needle tip was able to pierce, with minimum deformation, the fast-moving small bubbles at the point of impact, leading to a sharp signal response, which indicated the passage of a bubble–liquid interface. By using a travelling microscope, the exposed tips were set to be around 0.8 mm long and the axial probe tip separation was about 5.67 mm, whilst the lateral probe tip separation was about 2.00 mm. The distance between tips had to be adjusted, depending on the bubble sizes and velocities in

a two-phase flow system; in these experiments, an axial separation of around 5.67 mm was selected to measure the velocity of bubbles with reasonable accuracy. The probe operated like an electrical switch: when the tip was in contact with the liquid phase, the circuit was closed and, during the gas phase, the circuit was open. In this circuit, the tip is the live (+ve) electrode and the outer sheath is the earth. In addition, the probe yields information about the chord length distribution of bubbles intercepted by the probe, from, which the true bubble-size distribution may be inferred.

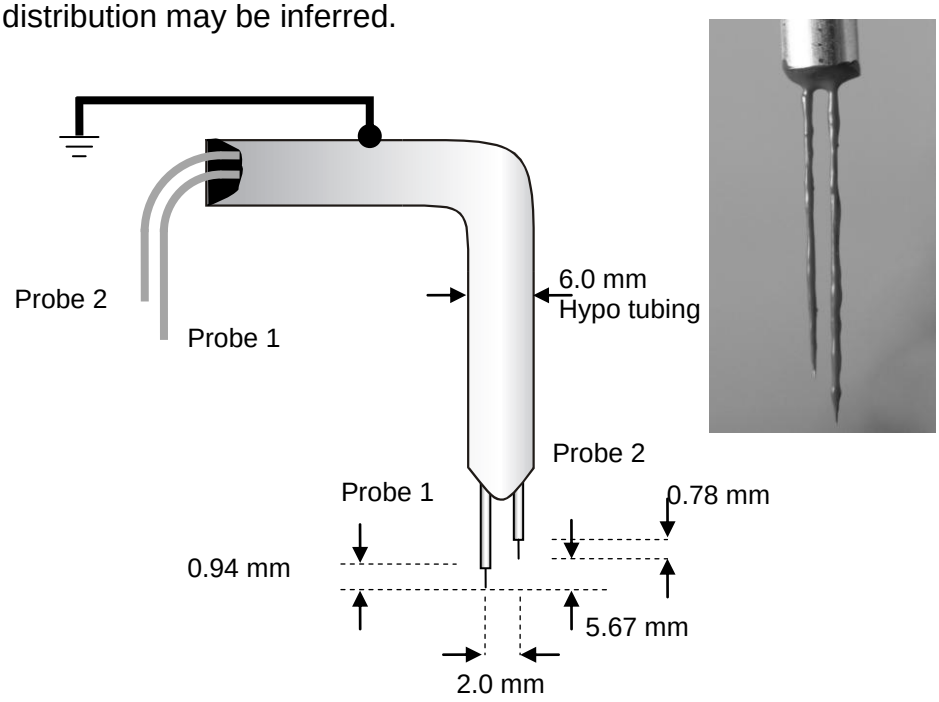


Figure 3.10 Design and geometry of the two-point conductivity probe (not to scale); the inset shows the two-point conductivity probe.

Four-point conductivity probe

A four-point probe has advantages over the two-point probe or other measurement methods, e.g. photographic. The purpose of using a four-point probe was to give more chances for bubble interception by a second probe. It was observed that bubbles would travel upward or downward, making contact with the probe at different angles, which leads to bubbles being missed; using a four-point probe decreased the number of missed bubbles. Figure 3.11 illustrates the design and geometry of the four-point probe.

In principle, the four-point probe operates in a similar way to the two-point probe, the only differences being the number of tips and the geometry. The four-tip

probe was made from four stainless steel acupuncture needles, which were around 0.3 mm in diameter. Each needle tip was able effectively to pierce, with a minimum deformation, an oncoming bubble; this leads to a sharp signal response, which indicated the passage of a bubble–liquid interface.

The acupuncture needles were mounted inside a stainless steel tube sheath with an outer diameter of 6.0 mm, as shown in Figure 3.11. The tip was the live (+ve) electrode and the stainless steel tube sheath was used as a common earth electrode for the four tips. To minimise the effect of deformation, fragmentation of bubbles and the possibility of missed bubbles because of signal quality, the exposed tip, together with the axial and lateral tip dimensions, were modified compared to the two-point probe. Each acupuncture needle was gold- plated to stabilise the response and to prevent corrosion; they were coated with insulating varnish but 0.4 mm was exposed at the very tip of the needle. Thus, the four tips of the probe were located at the very tips of the acupuncture needles. The probe dimensions were measured using a digital macro method. Probe 1, p1, was set to be the reference and the longest probe. The distances between tip 1 and tips 2, 3 and 4 were 1.63 mm, 1.41 mm and 1.57 mm respectively. Probes 2, 3 and 4 were fixed at a distance of 0.5 mm from p1, as shown in the bottom view in Figure 3.11.

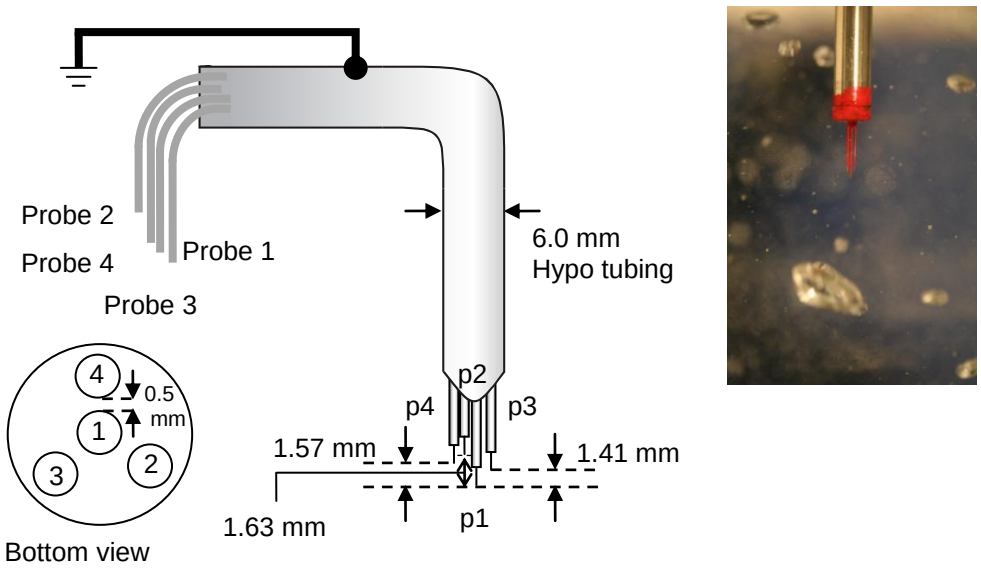


Figure 3.11 A schematic of the four-point conductivity probe (not to scale); the inset shows the four-point conductivity probe alongside some typical bubbles.

3.4.4 Assessment of the exposed tip length

The length of the probe tip has an effect on the signal resolution. A small exposed tip gives smooth signal transitions showing the re-wetting, de-wetting and residence time of a single bubble's signals from which α, chord size and the velocity of bubbles may be obtained. In addition, an overlapping signal might be produced by a large exposed tip, as the possibility of more than one bubble hitting the probe at the same time is high. According to the expected range of bubble sizes (2-4 mm) that might be produced, Zhao *et al.* (2005) used electrodes with exposed tip-lengths of about 0.2 mm, while Lucas *et al.* (2004) and Wu *et al.* (2001) used the sharp head of the tip only.

Therefore, the initial assumption regarding the specification of the length of the exposed tip was based on the range of bubble sizes that might be produced from the sparger. The expected range of bubble sizes was 2-5 mm; hence, the exposed tips had to be smaller than the bubble diameters; these were therefore set to be less than 1 mm. A travelling microscope was used to measure the exposed tips of the two-point probe; the exposed dimensions of the two-point probe were 0.94 mm and 0.78 mm for probe 1 (p1) and probe 2 (p2), respectively; see Figure 3.10. However, the exposed tip length in the four-point probe was about 0.4 mm in all four tips in order to improve the signal quality, as stated in the design of the four-point probe (§3.4.3).

Figure 3.12 shows a simple experimental setup to test the probe's response to the change in phase surrounding the tips. The probe was immersed in a beaker full of tap water and held by a retort stand and clamp. The sheath of the two electrodes represents the earth, while the tips represent the live current in the electric circuit. A strip of metal was connected to the sheath and was immersed in tap water to complete the circuit. A travelling microscope was used to observe the moment that the tips were immersed in the tap water. The probes were connected to a two-channel conductivity meter and the output signals were recorded digitally at 4 kHz using LabVIEW software. At the beginning of the current experiment, the tips were in the gas phase (i.e. at high voltage) and were

gradually immersed in tap water. Once the head of the tip touched the water surface, the signal suddenly decreased (see Figure 3.13).

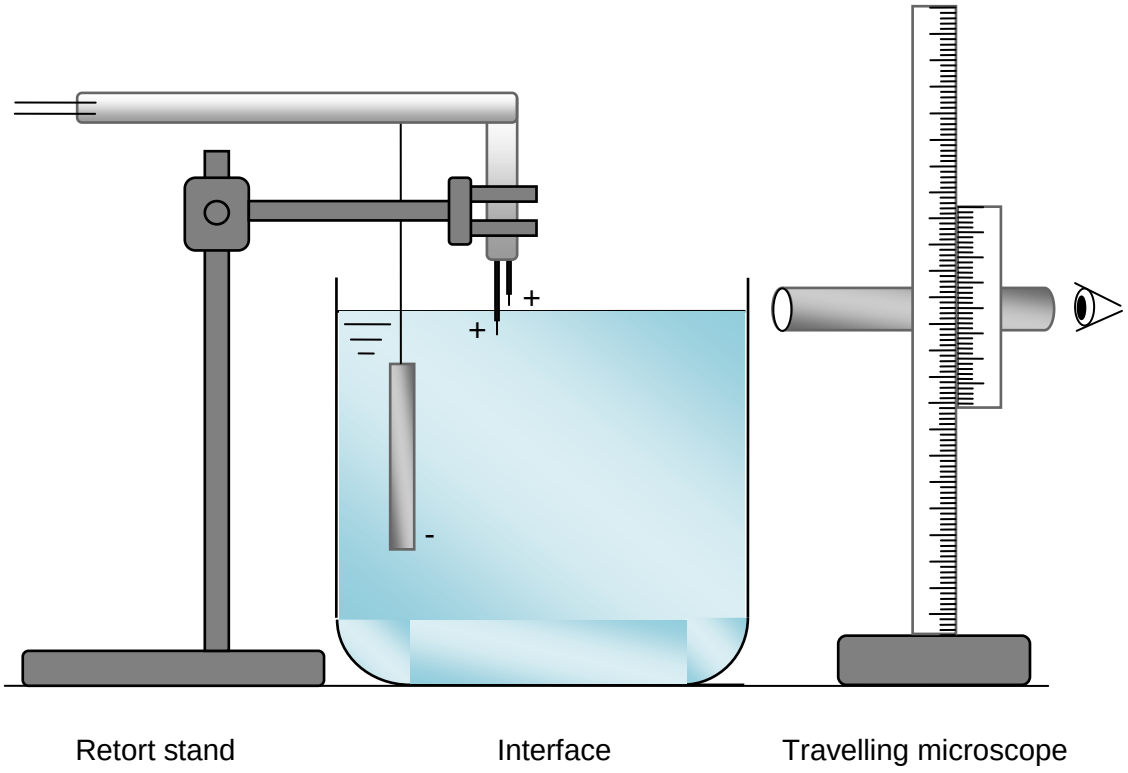


Figure 3.12 Probe reaction test to the phase changes surrounding the probe tips.

Figure 3.13 shows the probe's response in an experiment where the probe was moving up and down through the interface. The top voltage signal level represents the gas phase (around 9 V) and the bottom one represents the liquid phase. Both probes were initially in the gas phase. As the probe's tip was gradually immersed in tap water, p1 touched the liquid surface first and hence the voltage dropped rapidly to the liquid phase level. At this time, p2 was still in the gas phase and was emitting a high voltage. By continuing to lower the probe, p2 touched the liquid level and the signal dropped down to the lower voltage level. Conversely, as the probes were pulled out of the tap water, p2 left the tap water first and then the voltage went back to the gas phase level (i.e. the high voltage). The experiments give an indication of the rapid change in voltage as the phase changes around the tips.

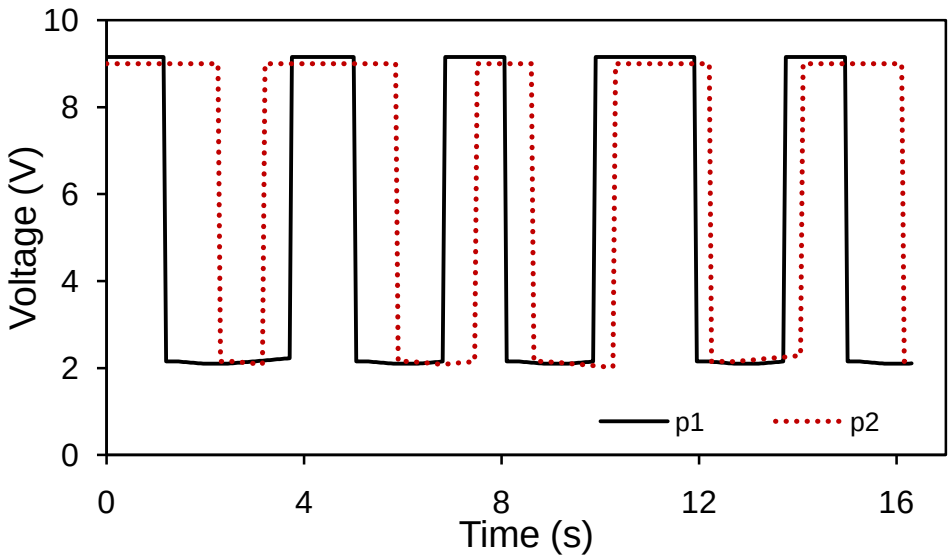


Figure 3.13 Phase signals produced by immersing the tips in tap water.

3.4.5 Conductivity measurement principles of a gas-liquid system

The use of conductivity probes in studying two-phase bubble flow helps in overcoming the critical problem of properly identifying the phases. This requires the probe responses to be properly interpreted before processing the parameters in a two-phase flow; in turn, this is helped by having knowledge of the probe responses at the liquid–bubble interface. This is characterised by a gradual rise in voltage due to the interaction between the bubble and the probe (de-wetting), as well as a sharp drop in voltage when liquid–probe interaction (re-wetting) occurs; the signal thus presents an asymmetric profile. The form and amplitude of the phase variation signal are also affected by factors such as flow conditions, bubble size and probe performance. Figure 3.14 shows a typical conductivity probe signal for a single bubble demonstrating the de-wetting, re-wetting and both phases (gas and liquid). Figure 3.14 also illustrates the threshold and the base line, which are discussed in §3.4.7.

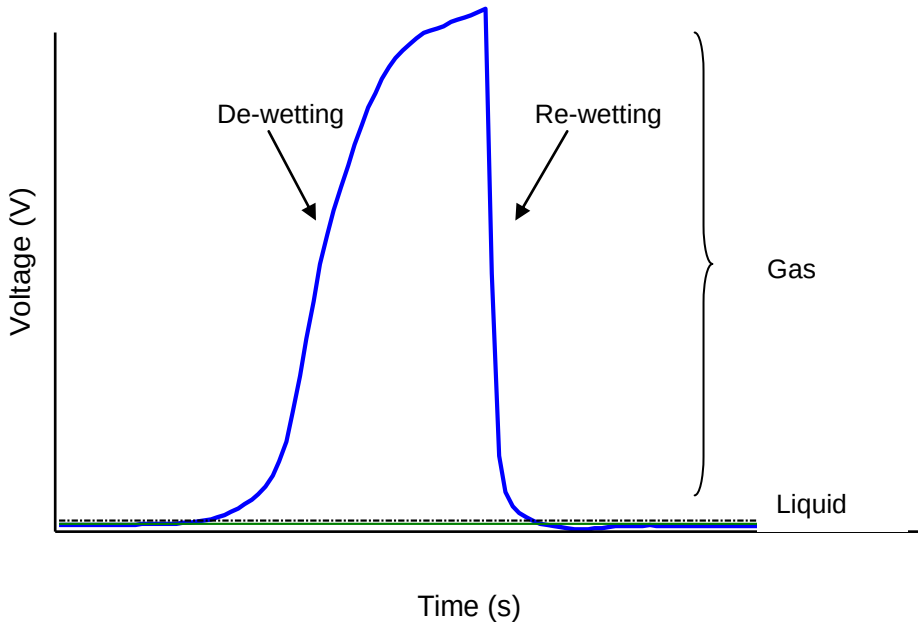


Figure 3.14 Typical upstream raw signals (probe 1)

As was stated previously, two- and four-point conductivity probes were used in the study. The design and dimensions of these two- and four-point conductivity probes are described in § 3.4.3. The long needle, p1, was used to calculate the local α and was used as a reference to calculate the chord and velocity of the bubble. Each signal yields information on the number of bubbles that have touched the probe tip, the interval during which the probe tip was exposed to the gas, and the time that elapsed between a bubble registering on the tip of p1 and then p2 (in the case of the two-point probe) or the tips of p2, p3 and p4 (in the four-point probe).

3.4.6 Visualisation of bubble interaction with the probe to understand the signal shape

The aim of these experiments was to test the probe's response to the impact and detachment of bubbles. The difference between this experiment and that involving the assessment of the exposed tip length is that the latter was conducted by moving the electrode in and out of stagnant tap water starting from the gas phase, whereas the present experiment more realistically simulated the bubble column. The test section consisted of a vertical tube of internal diameter

(i.d.) D_i=0.102 m, made of transparent QVF® glass, with a height of about 0.50 m (see Figure 3.15 a). A transparent box filled with water was attached around the rig to eliminate optical distortion and to allow photographs to be taken of bubbles hitting the probe tips. The tube bottom was sealed with a rubber plug through, which a 1.0 mm (i.d.) tube was introduced to generate small bubble diameters of between 3-5 mm. The tube was connected to a spherical rubber bulb that could be squeezed to produce bubbles as needed (see Figure 3.15 a). A high speed camera, an Olympus i-speed 3 CMOS (complementary metal-oxide semi-conductor) with a 1280 x 1024 sensor, was used to capture the images of bubbles hitting the probe tips. The frame rate and shutter speed were set, based on the expected bubble velocity, to 300 fps and 1/4000 respectively; a gigabit ethernet connection was used to connect the camera to a computer. Two light sources, covered with tracing paper, were used to give better image quality; one was placed 0.10 m behind the test rig in line with the camera, whereas the other was placed at 0.5 m and approximately 45° with respect to the transparency box wall to avoid light reflection (see Figure 3.15 b). As stated in §3.4.2, the probe electrodes were connected to the conductivity meter and then to a data acquisition device, DAQ. Finally, the latter was connected to a computer running LabVIEW software, which was used to monitor and collect the signal for further processing. This experiment was conducted by filling the 0.5 m tube with tap water, leaving about 0.10 m head space to avoid overflow when bubbles were introduced into the tube. The four-needle probe was put in place from the top and was positioned close to the tube's wall for high image clarity, as shown in Figure 3.15. While bubbles were generated by the rubber bulb, the camera and signal recording programme were operated simultaneously. A matching process was applied to the signal data and frames to match each bubble signal with its corresponding image frame.

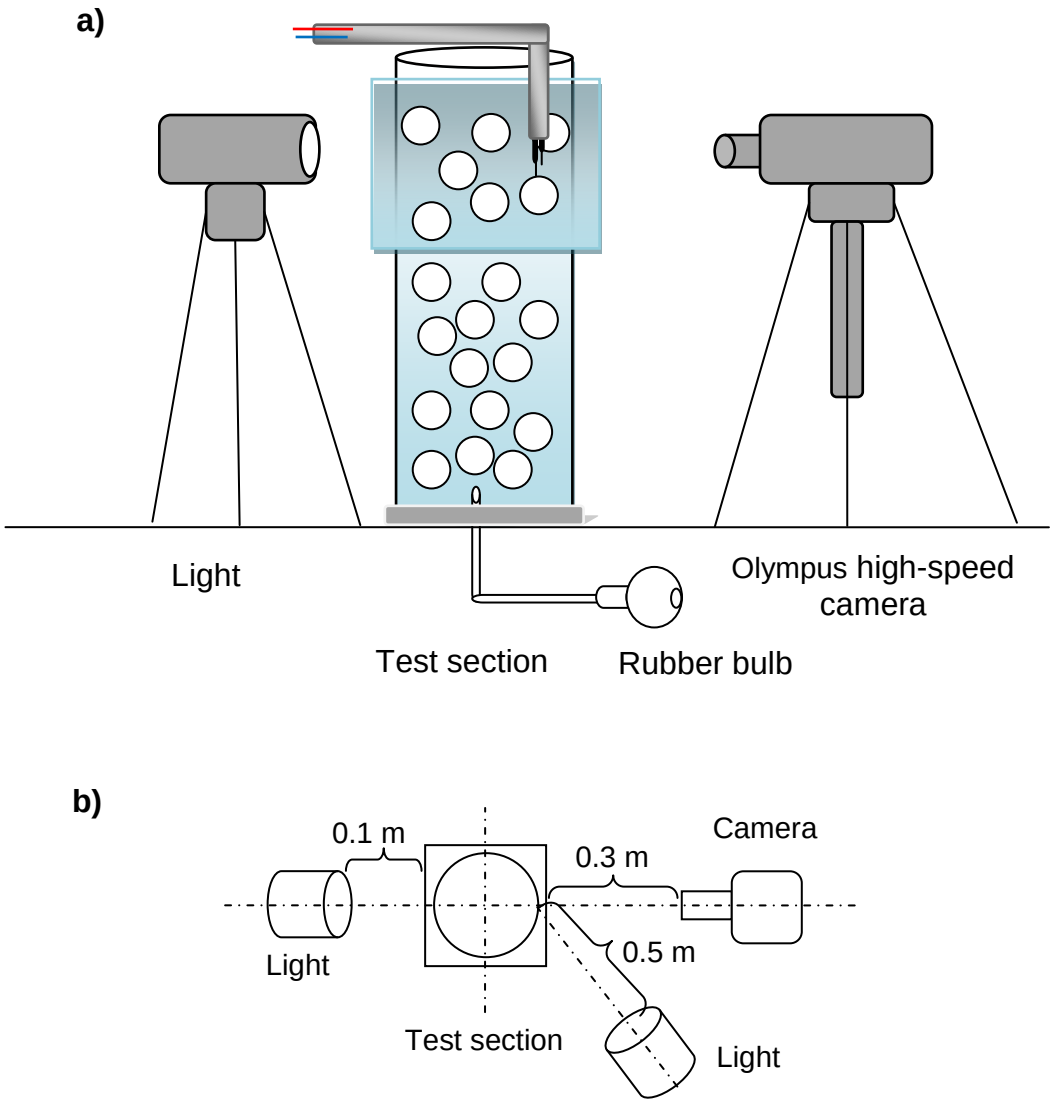


Figure 3.15 Probe response experiment: a) test section schematic diagram; b) top view (not to scale).

In order to test the probe's response to the phase change around the tips, the signal was matched with the assessment of the corresponding image frames. In order to match the frames with their corresponding signals by knowing the frame rate (f/s), two methods were proposed: converting the number of frames to signal time or vice versa. The former method was used in this study because of its accuracy and simplicity. Therefore, frames were analysed to create a list of frame numbers when the long probe (p1) just touched the bubble; subsequently the penetration time (s) could be calculated by dividing the frame's number (f) by the frame rate (f/s). Thus, the interval between the frames was calculated to be around 0.0033 s. The penetration time was compared to the rise time, which was

obtained using MATLAB by processing the raw signal. A period when no bubble signals were generated was considered deliberately in the signal's time history for use as a benchmark in matching progression.

It is clear from Figure 3.16 that the probe signals are not ideal state square-waves. This is due to the probe tip having a finite size, thus causing flow disruption. Moreover, there is possible deformation of the interface as the probe tip enters one phase from another. The trailing edge of the signal can be seen to be steeper than the leading edge. This is probably due to the probe tip being wetted by residual liquid when the probe tip enters the bubble. Since the probe is fixed, while bubbles are travelling upward at a velocity, v_t, the phenomenon of piercing can be observed. Figure 3.16 shows the following piercing phenomena from the visualisation of bubble interaction with the probe (p1):

1. The needle is in the liquid phase so the electric circuit is closed; voltage is below the baseline. The bubble moves towards the needle but the probe does not penetrate the bubble at this point.
2. When the bubble is in the proximity of the probe needle, the bubble surface is deformed due to the pressure of both the probe and the liquid. The thin film between the needle and the boundary is exhausted. The bubble velocity, v_t, the needle diameter, and fluid type determine the extent of the deformation. Once the film has become very thin, because of side film draining, the bubble bursts due to the pressure of the contact between the probe needle and the bubble interface. The voltage then slightly increases, indicating that the phase around the needle has started to change from liquid to gas (de-wetting).
3. The needle is inside the bubble and is almost dry.
4. When the probe needle makes contact with the other side of the bubble, liquid rapidly moves in along the needle and a new deformation occurs due to surface tension. Then the bubble leaves the probe. As a result, the conductivity signals drop to liquid level (de-wetting).
5. The probe is surrounded by liquid and the voltage is below the baseline.

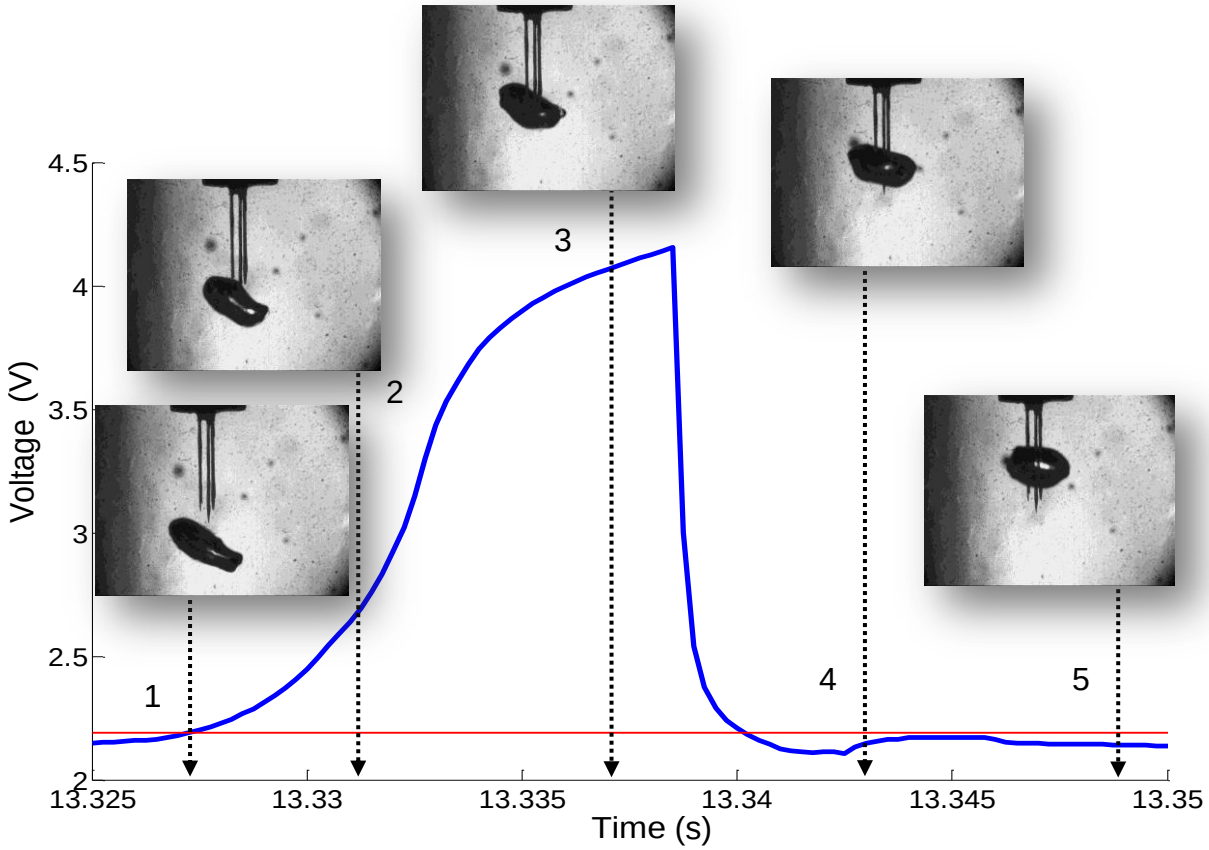


Figure 3.16 The probe (p1) signals show the de-wetting and re-wetting time and the time that the probe stays in the bubble; images confirm the signal output.

The raw signal of the four needles intercepted the same bubble shown in Figure 3.16 is illustrated in Figure 3.17. The bubble seems to hit the leading probe (p1), probe 3 (p3) and just touched the probe 2 and 4. This case confirms the advantage of using four-point probe, as the possibility of detecting the bubbles is high compared to the two-point probe.

On some occasions, two or more bubbles might hit the probe at the same time, which makes the treatment of the raw signal even more complicated. Figure 3.18 shows closely joined bubbles being detected as one single bubble. The probe (p1) is in the liquid phase and the voltage is low (1 and 2). The bubble's surface is deformed by the probe but the probe does not penetrate the bubble (3). The probe is inside the first bubble and is in the de-wetting stage (4). The first bubble is leaving the probe; simultaneously the second bubble hits the probe to form another spike and the probe is completely dry (5). The second bubble leaves the probe; the voltage is low, which indicates the liquid phase (6). The probe is completely wet by liquid (7).

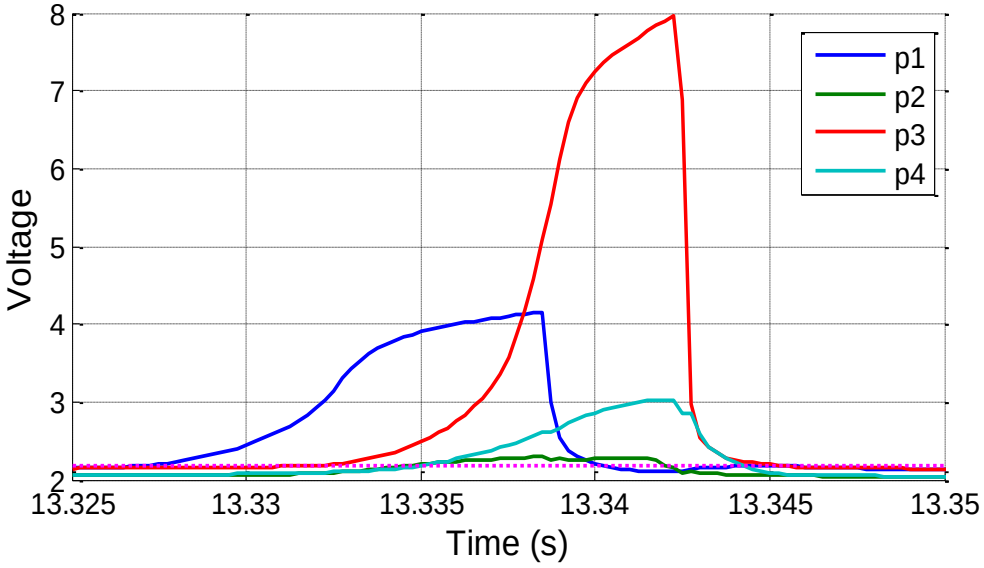


Figure 3.17 The raw signal of the four-point probe hit by the same bubble shown in Figure 3.16.

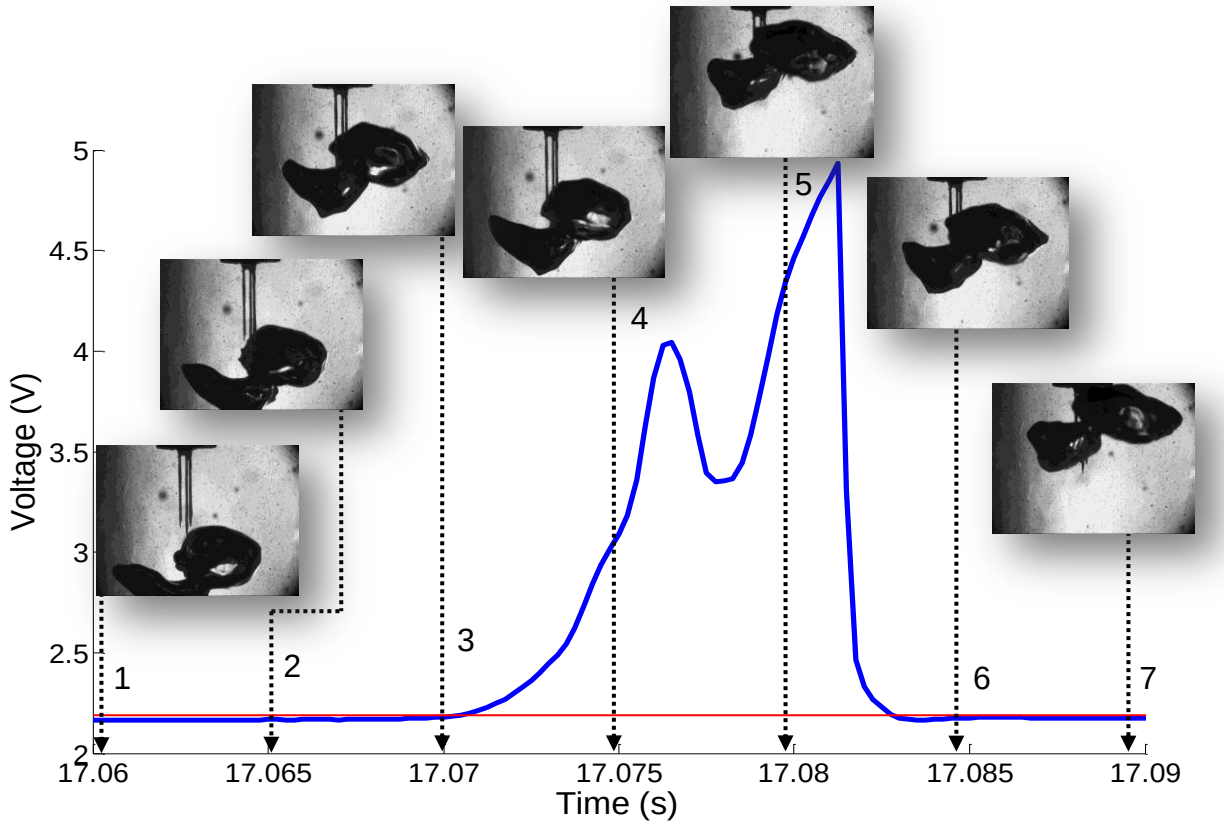


Figure 3.18 Raw signals showing a double bubble hitting probe l (p1), captured by frames in the matching assessment.

Figure 3.19 shows a comparison between the bubble rise velocity of the image and probe methods. The probe bubble rise velocity was predicted using Equation 3.16. On the other hand, the image bubble rise velocity was predicted by

averaging velocities of the bubble from the images. The bubble rise velocity was calculated by dividing the distance that the bubble moves up between two images by the frame rate (0.0033 s/f). Figure 3.19 shows the results of an assorted bubbles considered in the matching experiment. The results validate the conductivity probe method as almost the same bubble rise velocities were obtained by the two methods.

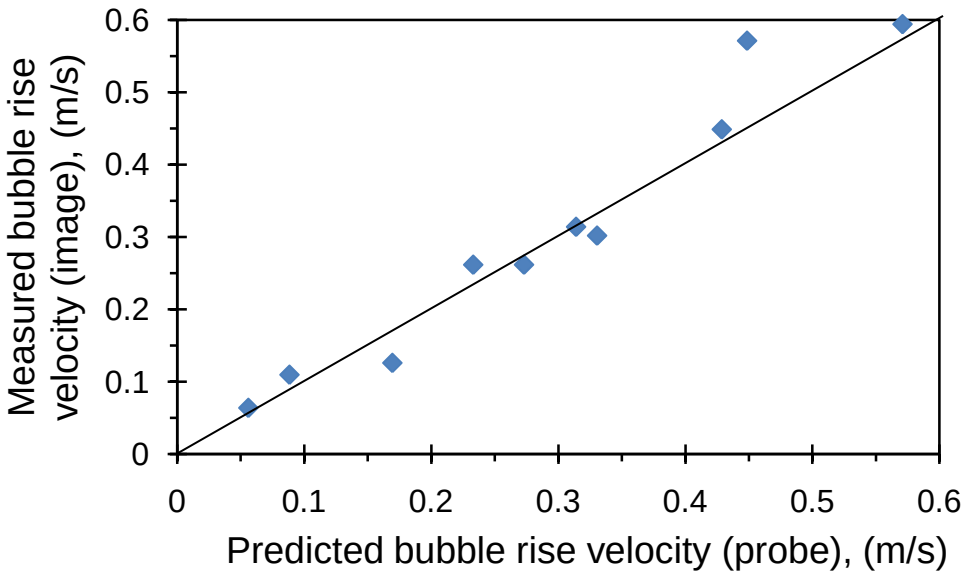


Figure 3.19 The bubble rise velocity: a comparison between image and probe methods.

3.4.7 Probe signal processing

In principle, the impedance probe technique relies on measuring the instantaneous local electrical resistance of the two-phase mixture by means of an electrode. In an air-water system, air acts as an electrical insulator, while water is a conductor. In simple terms, when the probe tip contacts liquid, the circuit is closed and no current flows. However, when the probe tip contacts a bubble, the circuit is open and current flows. This results in a voltage signal that alternates between minimum voltage, V_{min}, and maximum voltage, V_{max}, when the probe tip is in contact with liquid or gas respectively. In the two and four-tip probes, each probe tip and earth electrodes are connected to separate measuring circuits; hence, each probe tip is an independent phase-identifying device. The time that has elapsed during the change in voltage between V_{min} and V_{max} is recorded as the time taken by the gas-liquid interface to traverse the probe tip. This time could

be useful in defining the film thickness and contact angle. Therefore, two vital pieces of parallel and independent information are gained, pertaining to identifying the phases and transit time of the gas-liquid interface. The signal processing steps are summarised in Figure 3.20.

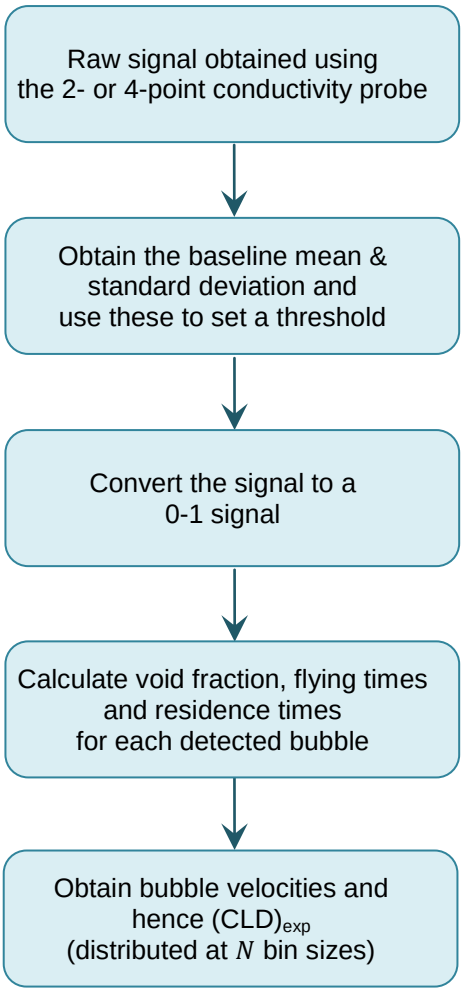


Figure 3.20 The signal treatment steps flowchart.

A typical raw time history was produced on LabVIEW from the raw signals given by the two- or four-tip conductivity probe in bubbly flow. Figure 3.21 shows the time history of the four-point conductivity probe for air-water bubbly flow, where j_g= 0.12 m/s. As stated earlier, the shape of the raw signal is not a square-signal; therefore more information can be gathered about the de-wetting and re-wetting durations. The shapes of the rising and falling edges of the signals are slightly different; this is due to differences in the de-wetting and re-wetting processes

while passing from phase to another. These transients depend on the dynamics and the geometry of the interaction process, i.e. the bubble velocity, the tip geometry and the contact angle (Hamad *et al.*, 1997). Figure 3.21 gives an impression of the complexity of the movement of bubbles inside the bed; even though the axial tip distance does not exceed 2 mm, some bubbles hit only one or a part of a tip. This makes the treatment of the signal even more difficult.

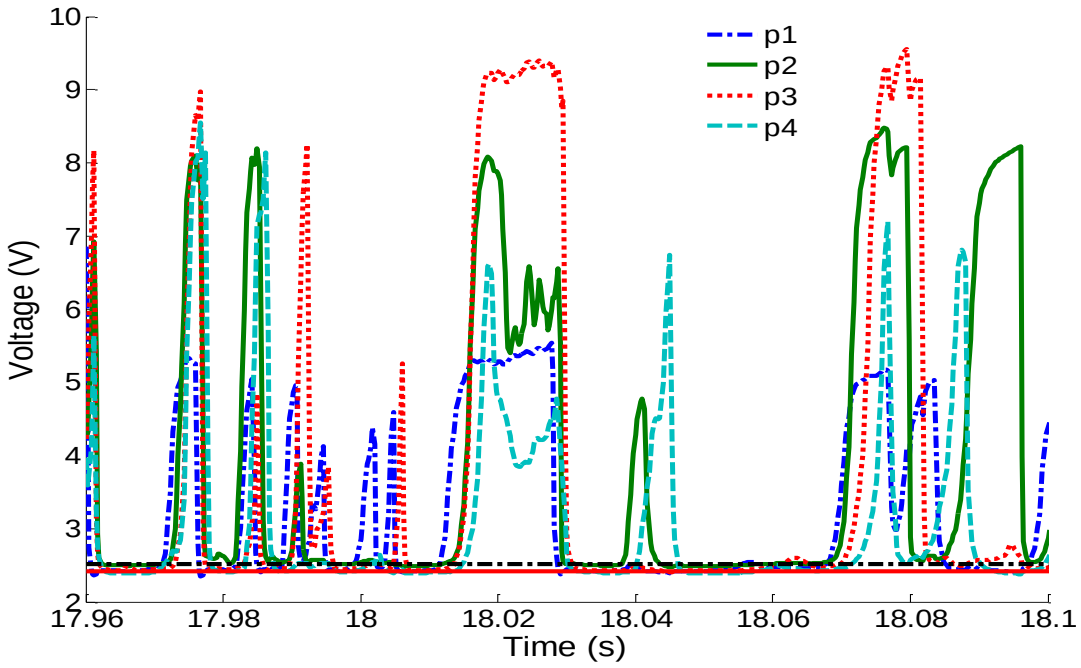


Figure 3.21 A typical time history of the raw signals for air-water bubbly flow given using a four needle-probe.

Signal processing in impedance-based measurement probes requires a threshold voltage to be set for raw voltage data interpretation. This threshold serves to identify the phase by acting as a trigger criterion. Hence, the phase indicator function is defined as the original signal transformed into a square wave by the threshold voltage trigger. Many techniques have been applied to treat the probe's raw signal: Van Der Welle (1985), and Angeli and Hewitt (2000) used an electrical switch that was triggered whenever the voltage exceeded a preset level. However, a disadvantage of using such a method is that signals below the trigger threshold are undetected. This can be overcome by digitally acquiring the signal using an analogue-to-digital converter. The resulting digital signal is then compared with two self-adjusting trigger threshold levels (TL). Dais *et al.* (1999) and Julia *et al.* (2005) used an equation, where:

$$TL = VL + \left(0.1(Vg - VL)\right) \quad 3.7$$

and where VL and Vg are the voltages of liquid and gas respectively. Their approach worked well with low-noise voltage signals. The threshold technique is a signal processing method typically used to process the raw signals and extract the required information. It is an important factor in establishing an appropriate threshold.

The present study used the histogram method (Hong *et al*., 2004) to set up the threshold to treat the raw signal produced from the probe (see Figure 3.22). Typically, a histogram of the voltage from a single probe contains two modes: the low voltage mode, which corresponds to the liquid baseline, and the high voltage mode, which corresponds to the gas level. The number of intensity bins determines two things: (1) how good the statistics will be in reflecting the ideal, continuous distribution, and (2) the effective fidelity of the intensities. It has been shown (Scott, 1979) that the optimal histogram bin size, which provides the most efficient, unbiased estimation of the probability density function, is achieved when:

$$w = 3.49\delta N^{1/3} \quad 3.8$$

where w is the width of the histogram bin, δ is the standard deviation of the whole signal and N is the number of available samples in the time history.

Figure 3.22 shows a histogram plot for the raw signal produced by probe 1 to define the signal cut off line; this can be identified by the value of the 2 bins past (right) to the maximum frequency bin (in this figure, the cut off line is about 2.3 V).

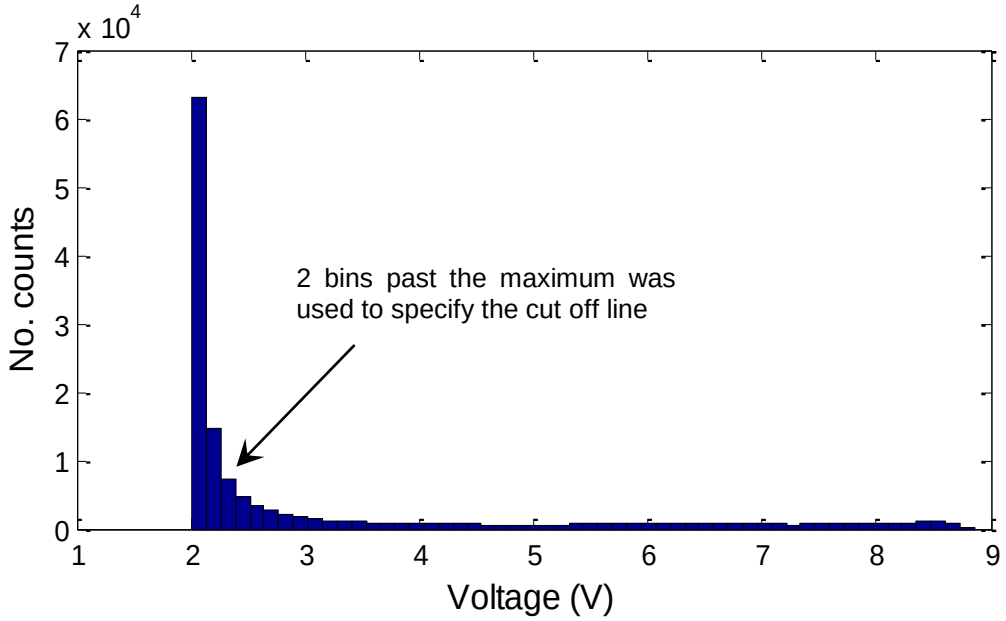


Figure 3.22 Histogram method used to determine the cut off line from the raw signal produced by probe 1.

The baseline is basically the mean of the base noise signal, which is below the cut off line (2.3 V in the case of Figure 3.22). The threshold was set by a multiple of the standard deviation value σ, of the base noise signal above the baseline. A set of σ values was investigated in order to choose the most appropriate value of σ that would give comparable results, with respect to the mean α obtained using the aerated level technique and by looking at the signal time history in detail (see Appendix D). In this study, the threshold level was set to be 2 σ above the mean value of the liquid baseline. A low number of < 2 σ, leads to the noise at the liquid level being picked up; however, a high number of > 2 σ, leads to real bubble signals being missed if they are weakly defined. The raw signal was then compared with the threshold level to determine the beginning and end of the equivalent rectangular wave (0-1 signal). Therefore, any voltages more than 2 σ above the baseline were taken to be in the gas phase. Figure 3.23 shows a time history for the raw and the rectangular wave signals obtained from probe 1. The threshold and the baseline shown here are for probe1. Each probe (sensor) was treated with a different threshold and baseline.

The gas void fraction, α, can be obtained simply by calculating the mean value of the rectangular wave signal. The residence time, velocity and size of the bubble are discussed in § 3.4.10.

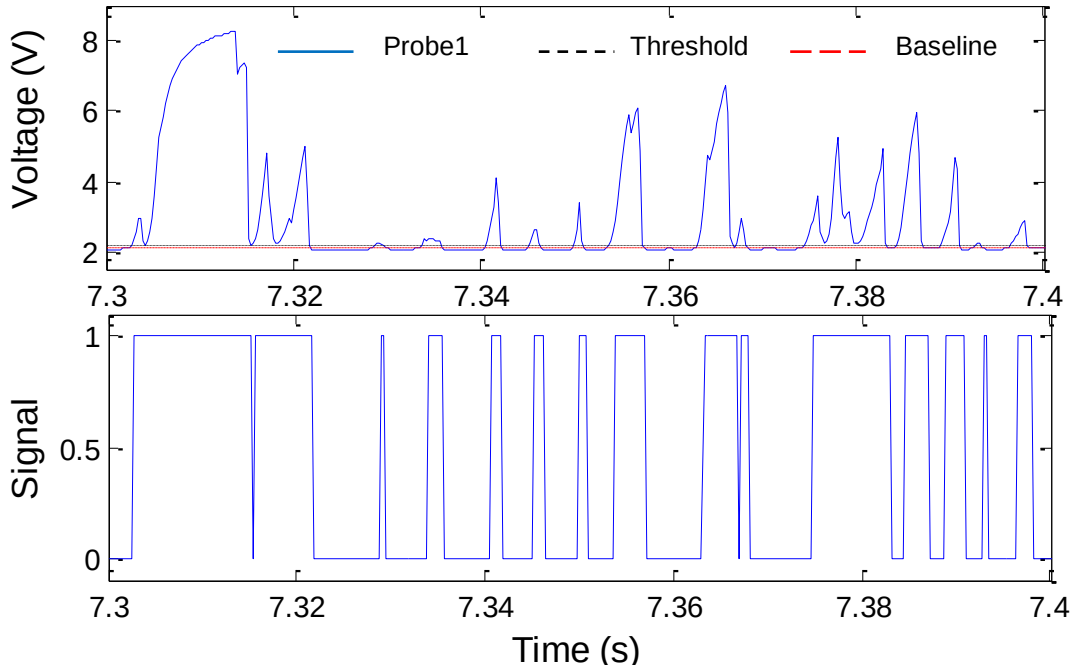


Figure 3.23 A signal obtained from a single conductivity probe, p1: (a) raw signal with the liquid baseline and threshold and (b) the phase discriminated 0-1 signal, where 0 is the liquid phase and 1 is the gas phase.

3.4.8 Local and mean gas void fraction

Obtaining the local α measurement is one of the important methods for investigating the behaviour of the bubbles travelling along the column. The advantage of the conductivity probe method is that it is able to determine local α, and by traversing the probe, α profiles can be measured. This method was used in the OTBC, AGBC and OTBCEO experiments to compare the mean α, which was calculated from the profile obtained from the measurements, gained from using the conductivity probe; the overall α was obtained from the measurements of changes of aerated height (Equation 3.2). Air flow rates were controlled by a rotameter to obtain the desired gas superficial velocities: 0.014 to 0.2 m/s.

A MATLAB program was used to treat the signal and calculate the two-phase flow variables: α, bubble velocity and chord length. The local α can be obtained by counting the fraction of time the electrode stays in the gas phase divided by the total time; it can also simply be calculated from the time-average of the 0-1 signal. The distribution of the local α was obtained by traversing the probe across the column diameter for the open tube, or radially across the annular gap at a

height of 0.57 m above the sparger. Means of α were obtained by cross-sectionally averaging the local α measurements, assuming (1) axisymmetric profiles and (2) a nearest neighbour points (two points) extrapolation of the local α profile to obtain the value at the wall.

For the open tube bubble column, OTBC:

$$\langle\alpha\rangle = \frac{\int_0^{R_o} 2r\alpha(r)dr}{R_o^2} \qquad 3.9$$

and for the annular gap bubble column, AGBC:

$$\langle\alpha\rangle = \frac{1}{R_0^2 - R_i^2}\int_{R_i}^{R_0} 2r\alpha(r)dr \qquad 3.10$$

where $\langle\alpha\rangle$, r, R_i and R_0 are the mean α, radius of OTBC, inside and outside the inner tube column.

Figure 3.24 shows the α profile obtained by traversing the probe across the diameter of the open tube bubble column at a height of 0.57 m above the sparger; due to the radius of the bend in the probe body, it is not possible to measure closer than 7 mm from the near wall of the column, whereas measurements can be made at a distance of only 4 mm from the far wall.

The profiles are axisymmetric about the line y =0.0508 m on the centre-line of the bubble column, justifying the use of Equation (3.9) to calculate the mean α. At low j_g the results show almost uniform distributions of the local void fraction across the column; in the homogeneous flow regime (j_g<0.1 m/s), the void fraction profiles become increasingly non-uniform with increasing gas superficial velocities: the ratio of the centreline void fraction, α_c, to the wall void fraction, α_w, increases significantly. Hibiki and Ishii (2002) fitted their void fraction profiles with a power-law equation:

$$\frac{\alpha - \alpha_w}{\alpha_c - \alpha_w} = 1 - \left(\frac{r}{R_o}\right)^z \qquad 3.11$$

Here the exponent z defines the shape of the non-dimensionalised profile. Hibiki and Ishii (2002) showed that z affects the value of the distribution parameter, C_0 , in the drift-flux model (Equation 1.2), more discussion is provided in § 4.5.1.

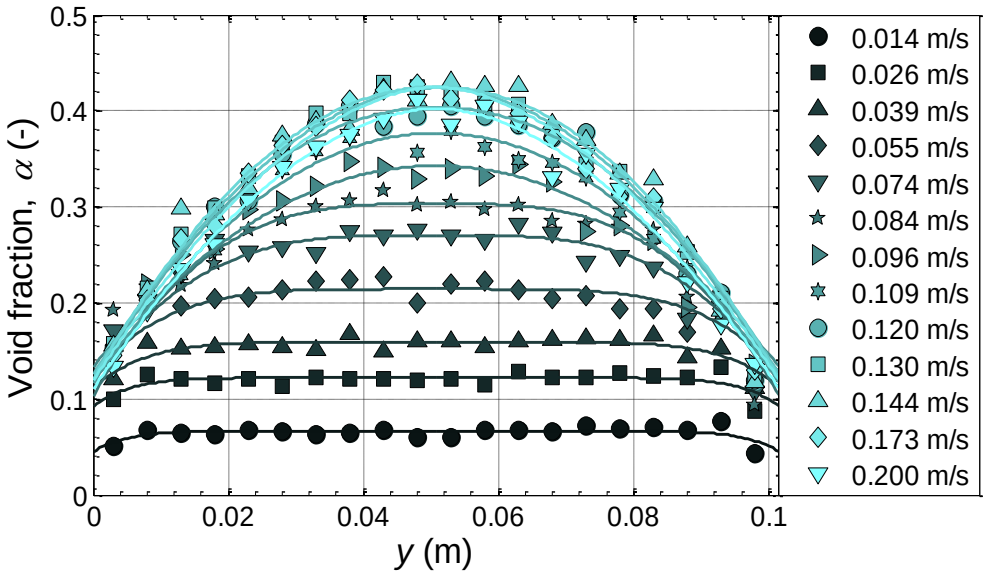


Figure 3.24 Typical gas void fraction profile across the column for different gas superficial velocities in the OTBC.

Ozar et al. (2008) measured and correlated a void fraction profile in annular gaps, albeit with a small outer column (0.038 m) and over ranges of gas superficial velocities 0.15 – 3.86 m/s. Furthermore, their experiments involved large upward superficial velocities of liquid (1.11–2.00 m/s).

They proposed power-law equations to represent the void fraction profiles according to:

$$\frac{\alpha}{\langle\alpha\rangle} = \frac{z+1}{z}\left(1 - \left|1 - \frac{2(r - R_i)}{R_o - R_i}\right|^z\right) \qquad 3.12$$

and showed that the distribution parameter, C_0, was related to the exponent z; more discussion is provided in §6.4.1.

3.4.9 Different sampling rates

The reason for carrying out these experiments was to test the effect of the sampling rate on the reproducibility of the data. The probe detects the change in the phase around the tip as electric signals that travel to a conductivity meter,

which amplifies them. The amplified signals are measured by a data acquisition device, DAQ, (NI USB-6210). Finally, the signals are transferred to a computer with the LabVIEW programme. LabVIEW works as an interface for the user, which treats the signals according to the time and the sample rate. The signals can be displayed on a monitor, and are saved in text format for further analysis. The experiments were carried out in the OTBC column with a 1.0 m tap water level at a constant gas superficial velocity of 0.11 m/s. The probe was placed at the centre of the column and the probe height was 0.57 m from the sparger. The sampling rate is defined as the frequency of sampling per unit of time and five different sampling rates were investigated: 2, 4, 6, 8 and 10 kHz. The sampling rate experiment was repeated five times, with each run lasting for about 30 s to take the average.

The large bubbles travel faster than the small ones in the air-water system (Gaudin, 1962). The largest bubble diameter size in a pure air-water system would be expected to be 10 mm; this would rise at a velocity of 0.22 m/s (Clift *et al.,* 2005). Therefore, the estimated time that the bubble might be in contact with the probe tip would be above 0.05 s. The examined sample rates gave a range between 0.0005 to 0.0001 s for the sampling time; hence, the lowest sampling rate, 2 kHz, gathered a sufficient number of samples relative to bubble velocity. Figure 3.25 illustrates the result of the local α with respect to the inspected sampling rates. At a gas superficial velocity, j_g, of 0.11 m/s, α was about 0.38 in all sampling rates. Therefore, at constant j_g, the results show that there is a negligible effect of the sampling rate on α. The estimated % error in the measurements for these data is 0.3%. In conclusion, 4 kHz was used for the remaining results.

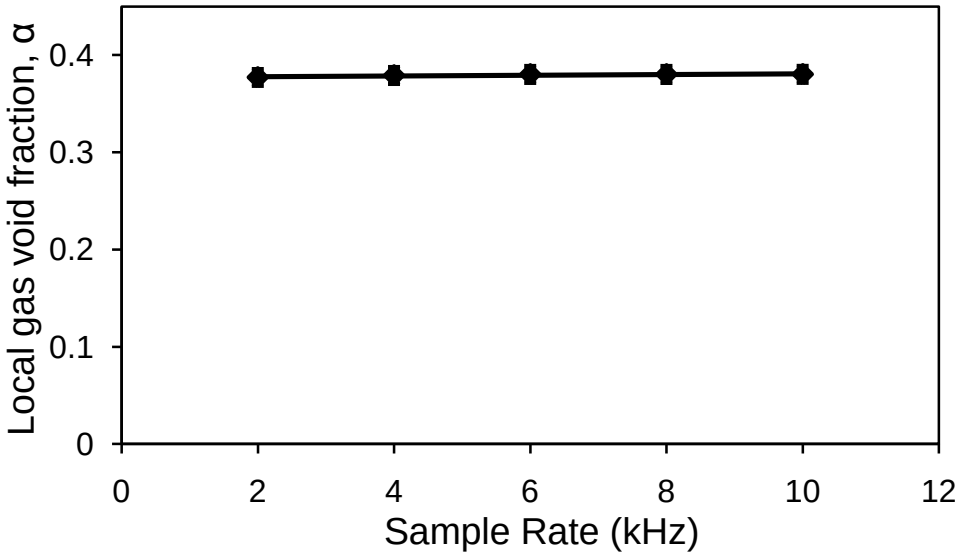


Figure 3.25 Void fraction with respect to the different sampling rates.

3.4.10 Bubble velocity and chord size calculation

One of the advantages of using a two- or four -tip conductivity probe is its ability to obtain bubble velocities and sizes. In this section, both probe tips should be used to calculate the velocity and then the chord length of the bubble. The flying time, ft, is that time taken by the bubble to traverse the probe tips. In practice, ft represents the time between the rises or falls from both probe tip signals for the same bubble:

$$ft = Rise\ 2 - Rise\ 1 \tag{3.13}$$

or

$$ft = Fall\ 2 - Fall\ 1 \tag{3.14}$$

while the residence time, tR for a single bubble is the time taken by the probe tip to stay in the gas phase. This can be obtained mathematically as follows:

$$tR_1 = Fall\ 1 - Rise\ 1 \tag{3.15}$$

The bubble velocity, v_g (m/s), is calculated from the known values of ft (s) and the distance between the probe tips l_{12} (m):

$$v_{gi} = \frac{l_{12}}{ft_i} \tag{3.16}$$

The velocity profile can be generated using the same approach that was used to obtain the gas void fraction profile; see § 3.4.8.

Since velocities have been calculated and the bubble residence time, tR_i, is known, the bubble chord lengths, C (m) are given by:

$$C_i = v_{gi} tR_i \qquad 3.17$$

The treatment of the two- and four-point probe signals was performed using MATLAB codes, which were created to obtain air-water flow variables, such as the void fraction, α, bubble velocity, v_g, and chord length, C of the bubbles. The signal treatment and the model are illustrated in Figure 3.27. As described earlier, the experimental data were obtained in the form of a voltage signal as a function of time from each sensor in the probe. The threshold was used to discriminate between the gas and the liquid phases. From this, a set of the times for rises (t_r) and falls (t_f) of the signal from each of the sensors was obtained, and the residence times (tR) of bubbles were calculated for each sensor.

The signals from the sensors were matched with the corresponding bubbles, as described in § 3.4.6, in order to validate the signal. However, this was not sufficient as some bubbles hit one sensor and deviated from the others. In order to validate the signal, therefore, the following conditions must be met:

1. It was assumed that the bubbles rise up to hit the leading sensor (p1) and then the other sensors. Therefore, the times of the rises and falls of p1 are smaller than the times of the other sensors:
   $t_{fi} > t_{ri}$, $t_{r2} > t_{r1}$ and $t_{f2} > t_{f1}$
2. If the first condition is fulfilled , the signal should also show that the residence times of a bubble is of comparable length for all the sensors:
   $$\frac{tR_1 - tR_2}{tR_1} > 0.05$$
   The 5% difference in the length of the bubble residence time is attributed to the effect of the probe on the bubble.
3. The terminal velocity of an air bubble in contaminated water can be calculated based on the Wallis (1974) correlation. Using the Eotvos number (Equation 2.20) and the Morton number (Equation 2.21) based on the

measured chord length (which is an underestimate of the true bubble diameter). Thus measured rise velocity must be greater than value calculated from Wallis' correlation, which provides a method to screen out incorrectly identified pairs of signals on adjacent probes. The tolerance of the calculated velocity from the time differences of rises $(t_{r2} - t_{r1})$, and falls $(t_{f2} - t_{f1})$ is $<$ 0.8, i.e. the Wallis (1974) correlation for terminal velocity of an air bubble in contaminated water.

4. The measured bubble rise velocity should be between V_{min} and V_{max} values, set by the user. This rise velocity range was investigated in Table D.1 in Appendix D.
5. Two modes were considered for each rise in the velocity range in order to match the bubble analysis: (i) find all matches ($Mode0$) and choose the best that satisfies all conditions, or (ii) take the first (fastest) match ($Mode1$).

The criteria were tested using data from the two-point conductivity probe in the open column using air-tap water and a porous sparger. According to the distance between the leading sensor and other sensors, either in the two- or four-point probe, it was assumed that the probe would measure bubbles with diameters of $\geq$ 1 mm, meaning the bubble rise velocity was at least 0.1 m/s (Clift *et al.*, 2005). However, for some criteria, the V_{min} value was set to be 0.05 m/s in order to include small bubbles with a diameter $<$ 1 mm. In order to test the criteria for large bubble diameters of $>$ 40 mm, V_{max} was set at 0.5, 0.8 and 0.9 m/s. The criteria with the mode, V_{min} and V_{max} were 0.1 and 0.8 m/s respectively were chosen to analyse the signal in this study, for further discussion see Appendix D.

The probability density function (PDF) of chord lengths can be obtained from the measured chord lengths from a frequency histogram method, using a method similar to that discussed in §3.4.7. Figure 3.26 shows an example of the chord length distribution (CLD) of the measurements obtained by the conductivity probe. The CLD can be statistically transformed into a bubble diameter distribution by assuming a spherical or ellipsoidal shape (Turton and Clark, 1989; Clark *et al.,* 1996), but a new method is proposed here which accounts for bubble shape effects. The next section describes a transformation method used to find the bubble size from the measured CLD. MATLAB codes were written to analyse

the signals, thus treating the signal and extracting the variables of interest to obtain the bubble size.

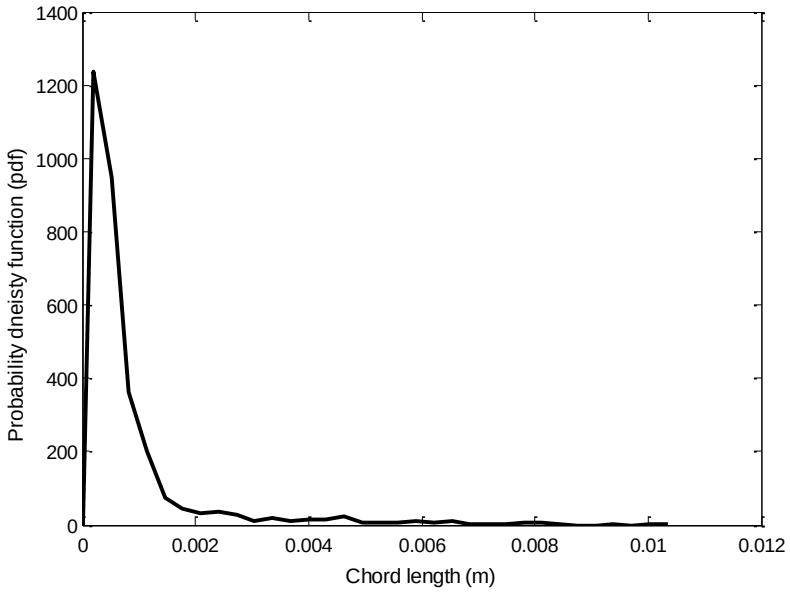


Figure 3.26 Chord length distribution for air-tap water flow using a porous sparger at j_g=0.17 m/s measured by the conductivity probe in the OTBC.

3.4.11 Transformation of chord length to bubble size

Deducing the bubble size distribution (BSD) from the pierced length distribution obtained from the conductivity probe measurements is not a straightforward transformation. The first analysis of the geometrical relationship between chord lengths and local bubble sizes using ellipsoidal bubble shapes, was addressed several years ago by Werther (1974 a,b). Clark and Turton (1988) proposed a numerical forward transformation to infer the chord length distribution (CLD) from the BSD for a range of bubble shapes (spherical and ellipsoidal with a constant shape factor φ=0.5). Hu *et al.* (2006) used the forward transform to obtain the CLD from the lognormal and uniform BSD. They recommended using the lognormal distribution, as the CLD deduced from the lognormal distribution BSD showed a higher probability at the large chords compared to the original BSD, reflecting the sampling bias, while for the system with a uniform BSD a parabolic CLD was obtained. A lognormal function for BSD was used by Lee et al. (1990) to evaluate the measurements of bubble chord lengths using optical fibre probes at different axial heights under steady-state operation, and obtaining a best fit using

the optimisation technique developed by Marquardt (1963). The forward transformation was considered first, where the CLD was obtained by randomly piercing a given BSD, and an optimisation technique was considered as a backward transformation.

For vertically rising bubbles of size R, which is defined in Figure 3.30, and of various shapes in a liquid operated in a bubble column, the lognormal distribution of these bubbles with respect to a mean, μ, and a standard deviation, σ, of the bubbles was considered. The BSD is going to be described by a distribution of R (semi-axis). The true BSD, $P_s(R)$, is given by the probability function (pdf):

$$P_s(R)dR = Pr(R, R + dR) \tag{3.18}$$

For the lognormal of the $P_s(R)$:

$$P_s(R)dR = \frac{1}{\delta\sqrt{2\pi}} exp\left(-\frac{\left(ln(R/\mu)\right)^2}{2\sigma^2}\right)\frac{dR}{R} \tag{3.19}$$

Bubbles with a large projected area (φR^2) are more likely to be detected by the probe. So given $P_s(R)$, the probe will be biased and will sample $P_p(R)$ where:

$$P_p(R) = \frac{R^2 P_s(R)}{\int_0^\infty R^2 P_s(R)dR} \tag{3.20}$$

The denominator of this expression simply ensures that $\int_0^\infty P_p(R)dR = 1$

In order to test the reconstruction algorithm, the bubble sizes from the distribution $P_p(R)$ should be randomly sampled and then randomly pierced at eccentricities $0 < e < R$, where e is a random variable (MATLAB command: *rand(n,m)* generates an *n* x *m* matrix of uniformly deviated, randomly distributed numbers between 0 and 1). By combining Equations (3.19) and (3.20), the following distribution would be generated:

$$P_p(R) = \frac{R^2 \frac{1}{\delta\sqrt{2\pi}} exp\left(-\frac{\left(ln(R/\mu)\right)^2}{2\sigma^2}\right)\frac{1}{R}}{\int_0^\infty R^2 \frac{1}{\delta\sqrt{2\pi}} exp\left(-\frac{\left(ln(R/\mu)\right)^2}{2\sigma^2}\right)\frac{dR}{R}} \tag{3.21}$$

Forward transform

A numerical method to calculate the CLD via the forward transform is presented (see Figure 3.27):

(i) Randomly select a bubble radius detected by the probe using Equation (3.21).
(ii) Calculate the aspect ratio, φ, from Equation (3.29).
(iii) Pierce the bubble at randomly selected eccentricities, and calculate chord length.
(iv) Repeat for very many sampled bubbles and collect the CLD.

Any probability distribution can be used to generate random deviates using the transformation method (Press *et al.*, 1992). The uniform deviate density function is:

$$P(x) = \begin{cases} 1 & 0 < x < 1 \\ 0 & otherwise \end{cases} \quad 3.22$$

A uniform deviate, x, is generated, from which the $R = R(x)$ function can be obtained from the transformation process. The probability of getting an R value in the range $(R, R + dR)$ is the same as getting an x in the range $(x, x + dx)$; see Figure 3.28.

$$P_p(R) = P(x)\left|\frac{dx}{dR}\right| \quad 3.23$$

The random deviate R can then be generated from $P_p(R)$, which is a known function with an integral of $\int_0^\infty P_p(R)dR = 1$, (positive values of R were considered); then, from Equations (3.22) and (3.23),

$$P_p(R) = \left|\frac{dx}{dR}\right| \quad 3.24$$

where x can be calculated by

$$x = C_p(R) = \int_0^R P_p(R)dR \quad 3.25$$

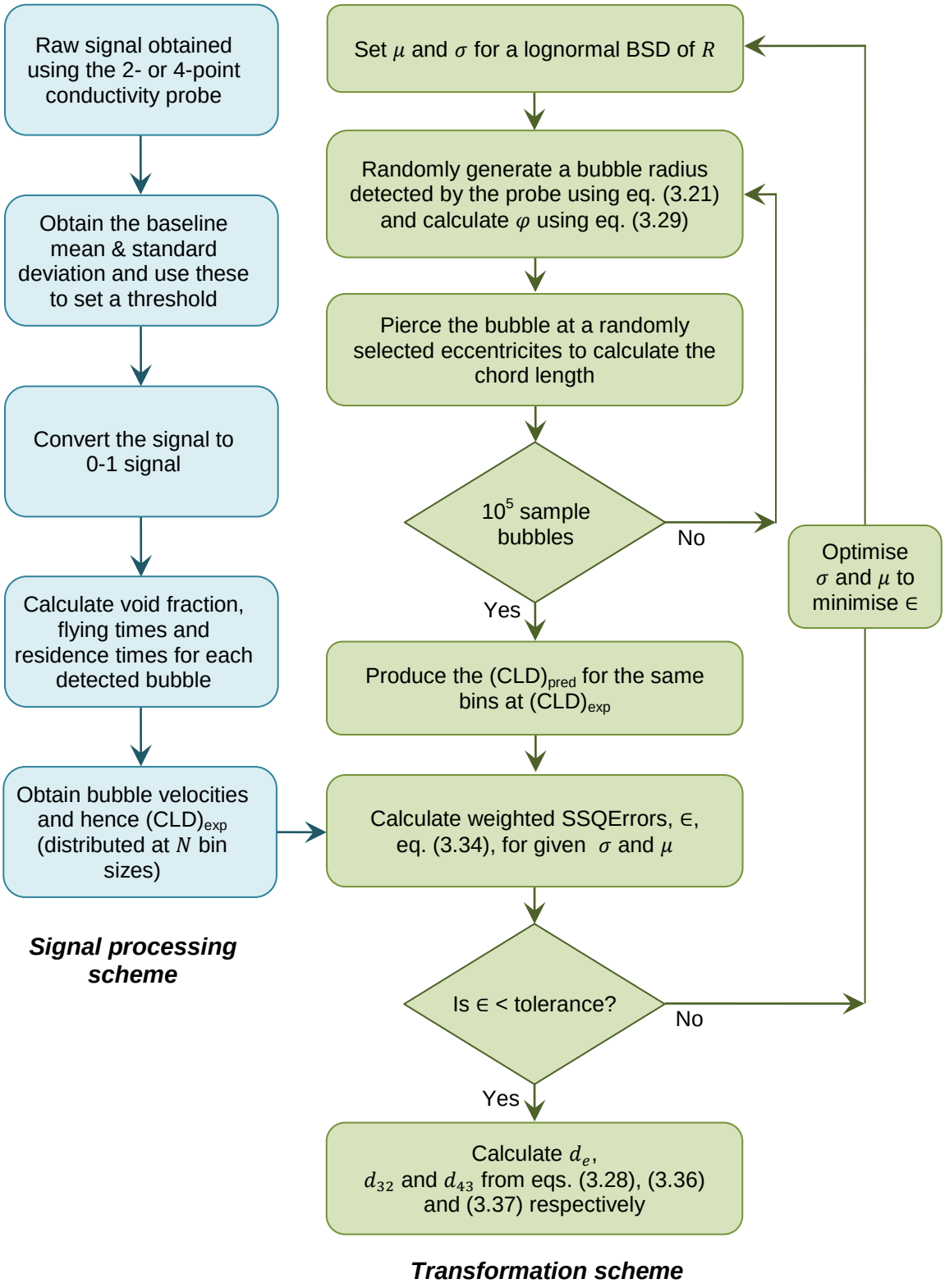


Figure 3.27 Flowchart for the signal processing and the optimisation model

The transformation, which takes a uniform deviate into one distributed according to $P_p(R)$, is then obtained by:

$$R(x) = {C_p}^{-1}(x) \qquad 3.26$$

where $R = {C_p}^{-1}$ is the inverse function of $x = C_p(R)$. The numerical approach was based on calculating $C_p(R)$ for a range of R values by numerical integration of Equation (3.25) using $P_p(R)$ from Equation (3.24). Interpolation of these data were used to obtain the inverse function $x = C_p(R)$.

The transformation method is illustrated in Figure 3.28. An input value of x was generated from the uniform deviate distribution (using the MATLAB command: *rand*) and finding the corresponding R as shown in the graph, i.e. using the inverse function ${C_p}^{-1}(x)$. If R is interpolated as a function of $C_p(R)$, then this is a convenient way to find the inverse relationship.

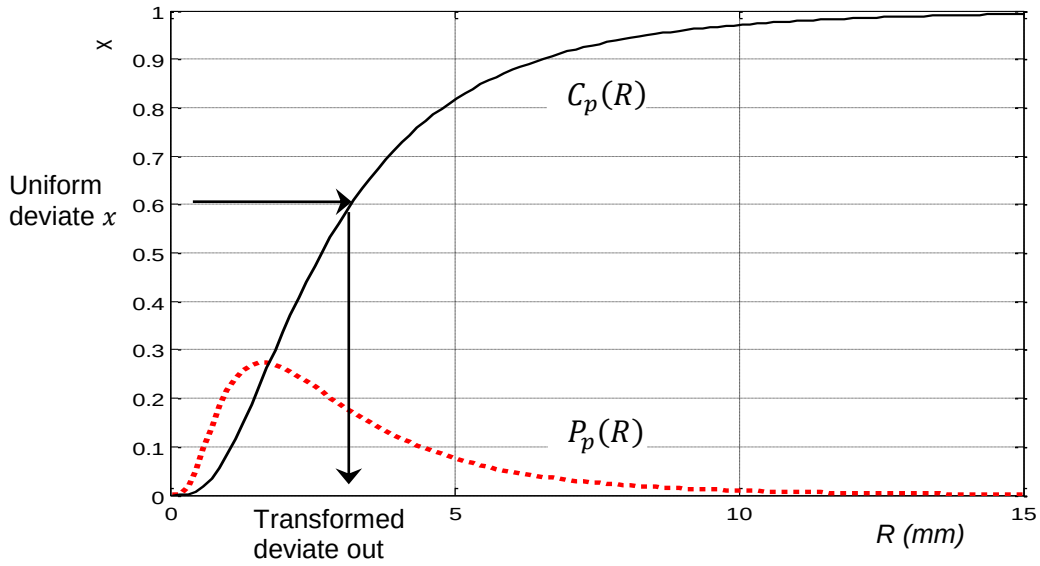


Figure 3.28 The cumulative probability function for the pdf $P_p(R)$ to generate a random deviate; x is in the range [0,1]. R_i

The aspect ratio, φ, can be defined as the ratio of the short to long axis, see Equation 3.4 and Figure 3.4. Wellek's (1966) equation was used to relate φ to the radius R through this transformation method, where:

$$\varphi = \frac{1}{1 + aEo^b} \qquad 3.27$$

and where a and b are constant values of 0.163 and 0.757 respectively, while Eo is the Eotvos number (Equation 2.20)

$$Eo = \frac{g d_e^2 (\rho_l - \rho_g)}{\sigma}$$

and the equivalent diameter, d_e , is given by

$$d_e = 2R\varphi^{1/3} \qquad 3.28$$

By substituting in Equation (3.27):

$$\varphi = \frac{1}{1 + a\left(\frac{g\Delta\rho 2R^2\varphi^{2/3}}{\sigma}\right)^b} \qquad 3.29$$

Referring to Equation (3.21), it is much easier to generate random variables R from a distribution function $P_p(R)$ numerically rather than analytically. The steps can be written as follows:

1. By considering the lognormal parameters mean, μ, and standard deviation, σ, and taking a range of R values, evenly spaced points can be calculated to represent the R domain. Then, the corresponding values of $P_s(R)$ can be obtained and plotted using Equation (3.19). In order to obtain $P_p(R)$, a numerical integration can be used to find the denominator of Equation (3.21). It is impossible to integrate between 0 all the way to infinity, but any large number is sufficient (see MATLAB command: quad). The values of $P_p(R)$ were calculated from the corresponding values of R; see the $P_p(R)$ curve in Figure 3.29.
2. The cumulative probability, $C_p(R)$, for various values of R shown in Figure 3.29, is calculated numerically by:

   $$C_p(R) = \int_0^R P_p(R)\, dR \qquad 3.30$$

   The values of $C_p(R)$ are a vector of the corresponding R values.

3. Returning to the method described in Figure 3.28, a random uniform deviate x in the range [0,1] can be generated and interpolated on the data set of R vs C_p to obtain the output sampled value of R_i.
4. Step 3 can be repeated to generate a further output vector of random deviates distributed according to $P_p(R)$.
5. A histogram based on 10^6 sampled values of R_i, which are converted to a pdf, can be compared with the original curve of $P_p(R)$. Figure 3.29 shows that the agreement between the calculated histogram and the original function is very good, proving that the transformation method has been implemented correctly using the numerical methods.

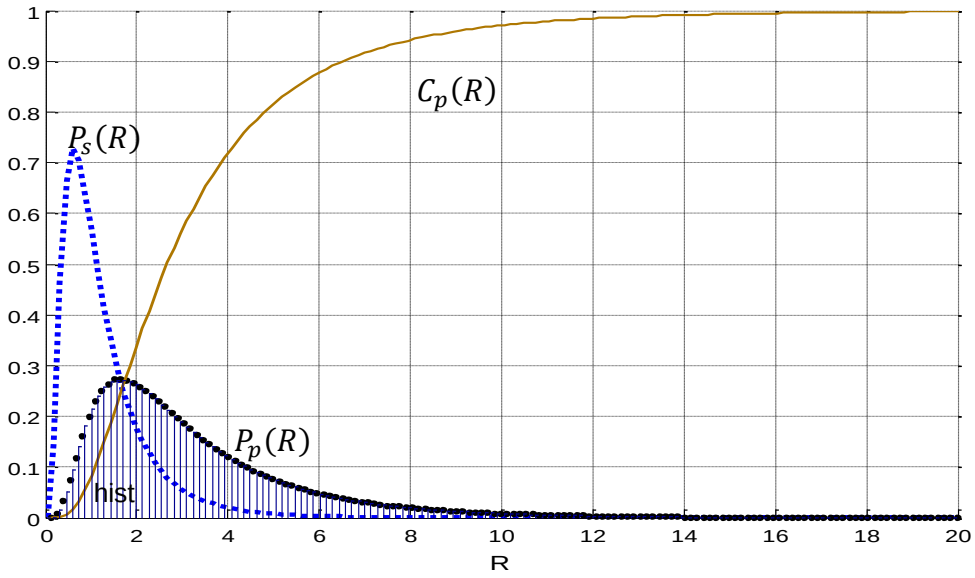


Figure 3.29 The pdf of $P_p(R)$ (Equation 3.21) and the histogram of the random deviates of R compared to $P_p(R)$.

Next the chord length distribution can be generated by cutting each synthetic bubble of size R_i at an eccentricity, which is a random deviate in the range $0 < e < R_i$. Figure 3.30 shows a front and top view of a bubble of radius R_i being pierced by a single point conductivity probe, at an eccentricity, e, from the centre of the bubble.

The probability of piercing a bubble at eccentricities in the range $(e,\ e + de)$ is proportional to the projected area $2\pi e\ de$ and can be expressed as follow

$$P_e(e|R_i)de = \frac{2\pi e\, de}{\pi R_i^2} \; or \; P_e(e|R_i) = \frac{2e}{{R_i}^2} \qquad for\ e \le R_i \qquad 3.31$$

where "$e|R_i$" means $P_e(e, e + de)$ for a given R_i.

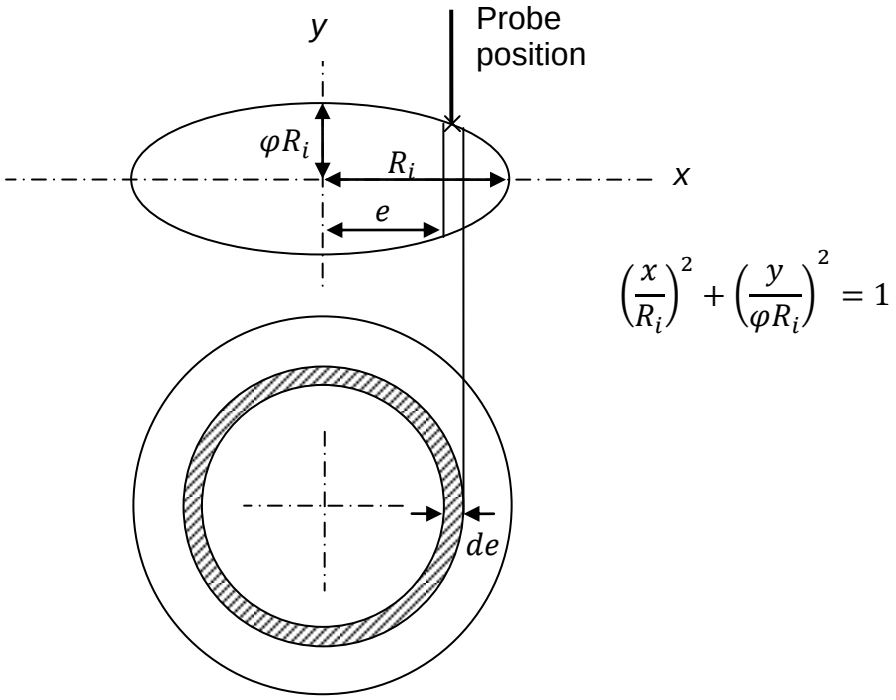


Figure 3.30 A side and top view of a bubble of radius R_i is pierced at an eccentricity *e*.

A technique similar to that described in Figure 3.28 was used to select the random values of e from the pdf of Equation (3.31). The cumulative function for e is given by:

$$C_e(e|R_i) = \int_0^e \frac{2e}{{R_i}^2} de \; = \frac{e^2}{{R_i}^2} \qquad for\ e \le R_i \qquad 3.32$$

If a random uniform deviate, x, is generated in the range [0,1], then the corresponding value of e is defined by:

$$e = R_i\sqrt{x} \qquad 3.33$$

and the chord length, C, is given by:

$$C = 2\sqrt{{R_i}^2 - e^2} \qquad 3.34$$

The open circle symbols in Figure 3.31 represent the C results after they were binned and converted to a pdf. P_p and P_s are the pdf of the probe and system bubble size distribution, and $P_c(C)$ is the distribution of the chord lengths detected by the probe; these were needed to test the reconstruction.

The existing analytical method only works for constant φ. However it can be used to check routines for the Monte-Carlo method at generation of $P_c(C)$. The analytical method was compared to the Monte-Carlo method at different constant values of φ, between 0.2 to 1. Figure 3.31 shows the comparison of the analytical to the Monte-Carlo methods at φ=0.8. Table 3.1 shows the fit parameters and the output from both methods. The results show good agreement between the two methods, which indicates that the analytical method works very well at constant φ. Nevertheless, the aim was to consider a variable aspect ratio, φ in the model to simulate the changes in the bubbles aspect ratio so the optimisation method was proposed to obtain the bubble size from the CLD.

Table 3.1 Variables was obtained from the comparison of analytical and Monte-Carlo methods in Figure 3.31.

Fit or output variable	Analytical Method	Monte-Carlo Method
Aspect ratio	0.80	0.80
Sq error	0.04	0.03
Fitted mu (mm)	0.52	0.48
Fitted sigma	0.72	0.71
Void fraction	0.45	0.45
d32 (mm)	2.68	2.76
d43 (mm)	3.69	3.78

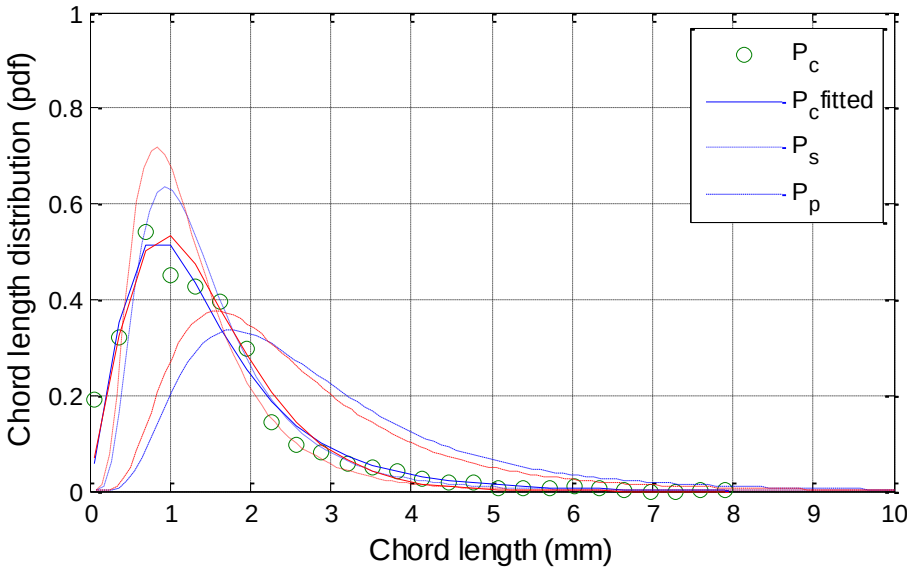


Figure 3.31 Comparison of analytical and Monte-Carlo methods for a fixed aspect ratio, *φ=0.8*, the red lines represents the Monte-Carlo method.

Backward transform

An optimisation method was implemented to predict the bubble size from the CLD. The idea was to compare the synthetic CLD, which was produced from the forward transform with the measured CLD, which was predicted by the conductivity probe. The chords from both methods should be distributed at the same bin sizes. The MATLAB function "fmincon" was used in the optimisation approach to minimize the sum of squares error (SSQError), $\in$, for the predicted and measured CLD subjected to μ and σ. The value of $\in$ was weighted equally to avoid the noise level in the data. The bounds of μ and σ were set to (-2.3 to 2.3) and (0.2 to 1.2) respectively. The error, $\in$, can be given by:

$$\in = \sum_{i=1}^{N_i} \frac{\left[\left(P_c(C_i)\right)_{pred} - \left(P_c(C_i)\right)_{exp}\right]^2}{C_i^2} \qquad 3.35$$

and is weighted to give a better bit for small chord lengths. Figure 3.32 shows good agreement between the pdf of the real measured chord length, P_c, and the pdf of the model chord length, $P_c fitted$. The curves P_p and P_s are the PDF of the probe and system bubble size distribution.

The equivalent diameter, d_e was calculated from the means of equivalent volume spheres corresponding to the lognormal distribution specified by μ and σ. Equation (3.28) shows that the d_e can be obtained from the φ and R. Where the lognormal inverse function "logninv" was used to predict R.

The Sauter mean diameter, d_{32}, is the ratio of the third to the second moment of bubble size distribution. The Sauter mean diameter is important in expressing the active surface area in the mass transfer process and is given by:

$$d_{32} = \frac{\sum d_e^3}{\sum d_e^2} \qquad 3.36$$

The mean diameter, d_{43}, is the ratio of the fourth to the third moment of bubble size distribution, which characterises large bubbles in the column. It can be obtained by:

$$d_{43} = \frac{\sum d_e^4}{\sum d_e^3} \qquad 3.37$$

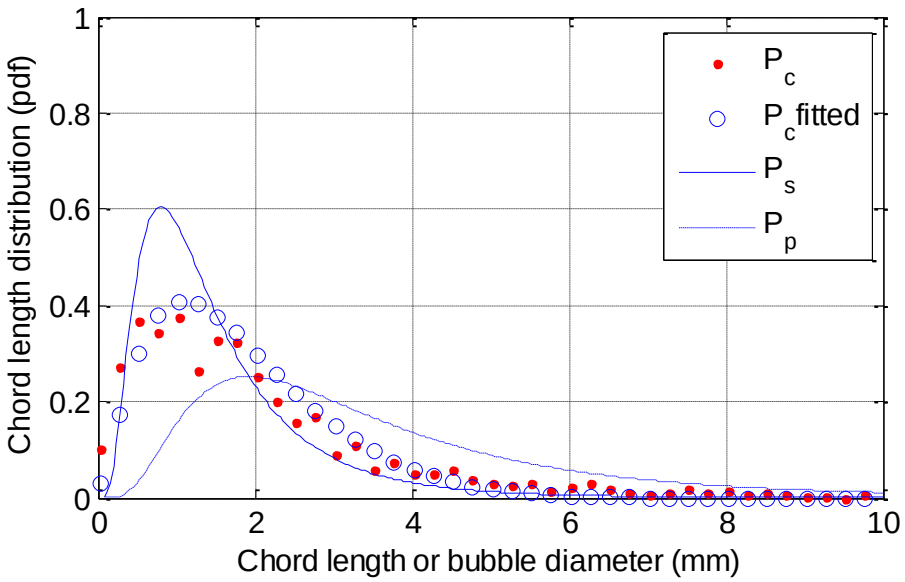


Figure 3.32 The final output comparison of the measured and predicted chord length according to a variable aspect ratio.

3.5 Conclusion

The design and experimental setup of the techniques used in this study were described in detail. The design of the two and four-point probe was described as

well as the estimation of the exposed tip length based on the expected bubble size and the raw signals. The shape of the probe signal was studied in order to treat the raw signal. In addition, the probe raw signal processing was described in detail together with base line identification, the threshold, local and mean void fraction. The bubble velocity and chord length calculations were also described. From all the three techniques and experimental developments, it can be concluded that the mean α measured by the aerated level technique can be used to validate the cross sectional mean α obtained by the conductivity probe technique. The bubble velocities, which were obtained by the image analysis technique, were used to validate those achieved by the conductivity probe technique. Moreover, the transformation of bubble size was implemented using the forward analytical method and the optimisation approach as a backward method. At a fixed φ, the analytical method was validated by the Monte-Carlo approach. The challenge was to consider a variable φ in the transformation method and yet the model fitted very well to the experimental results.

CHAPTER FOUR

OPEN TUBE BUBBLE COLUMN (OTBC)

4.1 Introduction

The main aim of the current study is to find the reason for there being different gas void fractions in open tube and annular gap columns. To achieve this objective, it was important to study the Open Tube Bubble Column (OTBC). Studying air-water flow variables (e.g. α) in an OTBC gives a better understanding of the behaviour of an air-water system in such a reactor ; this is required in order to compare these results with those from an AGBC over the same range of gas superficial velocities, and liquid compositions.

This chapter gives full descriptions of the OTBC experimental apparatus and the methods used during the void fraction experiments in an air-water system. The section is divided into two sub-sections. First, preliminary experiments are described, which were intended to ensure that the results were reproducible and self-consistent. Other tests were conducted to select the liquid, sparger type, depth of liquid, and distance of the probe from the sparger, that were most appropriate. The preliminary results are presented and discussed here; finally, some conclusions are drawn from these experiments. Second, experiments to measure the mean α, local α, size and velocity of bubbles in both water and in two alcohol solutions (Ethanol and IPA) in the OTBC are described; the results, discussion and conclusions are also presented for these experiments.

4.2 Experimental setup and design

The experimental setup for the OTBC is illustrated in Figure 4.1. The column consisted of a vertical tube of internal diameter (i.d.) D_o= 0.102 m and was made of transparent QVF® glass with a height of about 2.25 m. Compressed air was injected through a porous plastic sparger, which covered the whole of the column base. In the open tube experiments, the sparger had a permeability of 5.3 x 10^{-14} m^2 (see Appendix C), with a pore size of around 100 µm. At low gas superficial

velocities, j_g, the porous sparger produced a uniform distribution of bubbles and no large bubbles and slugs were observed moving up the open column. The compressed air supply was filtered to remove trace impurities and regulated through a rotameter to attain the desired j_g of 0.014 to 0.2 m/s. The rotameter Platon (A10), which was manufactured by Roxspur Measurement & Control Ltd, was connected to a digital pressure gauge and pressure correction was made to the rotameter reading, which had previously been calibrated at atmospheric pressure (see Appendix C). The non-aerated liquid level was set at 1.0 m above the sparger. Prior to the start of all the experiments, the air was passed through the column continuously for about 30 minutes in order to condition the water, and hence obtain reproducible results; this is discussed further in §4.3.1.

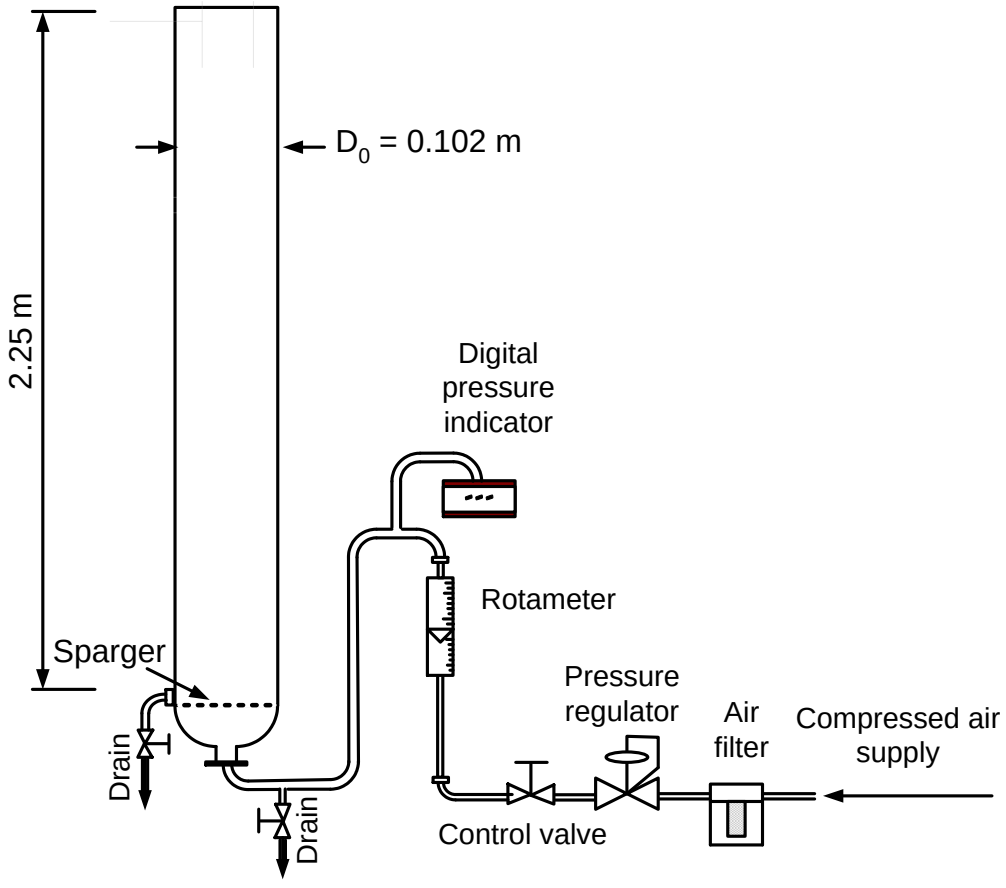


Figure 4.1 The experimental setup for the open tube bubble column.

4.3 Preliminary tests

Table 4.1 summarises the conditions for all the preliminary tests that were conducted in the OTBC. Apart from the probe height test, all runs used only the aerated level method to measure α, and were all conducted using the same range of j_g values. For the probe height tests, both the conductivity probe method and the aerated level method were used at five evenly spaced j_g values, between 0.0265 to 0.2 m/s. Tap water was used in all tests except for the liquid type test. In this test, both tap and distilled water were studied in order to select a suitable liquid for the study. Apart from the sparger type test, in which both plastic and glass spargers were used, all other tests used a sintered plastic sparger as the gas distributor. Liquid heights of 1.0 and 0.8 m were used in the liquid height test. Apart from this, all the tests used a liquid height of 1.0 m.

Table 4.1 The experimental conditions for the preliminary tests in the OTBC (D_o=0.102 m).

<table>
<tr><th>Test</th><th>j_g</th><th>Measuring method</th><th>Liquid type</th><th>Sparger type</th><th>Liquid height</th><th>discussed in section</th></tr>
<tr><td>Experimental protocols 1 & 2</td><td rowspan="5">0.014 – 0.2 m/s</td><td rowspan="5">Aerated level</td><td rowspan="2">Tap water</td><td rowspan="3">Sintered plastic</td><td rowspan="3">1.0 m</td><td>§ 4.3.1</td></tr>
<tr><td>Experimental procedure</td><td>§ 4.3.2</td></tr>
<tr><td>Liquid type</td><td>Tap and Distilled water</td><td>§ 4.3.3</td></tr>
<tr><td>Sparger type</td><td rowspan="3">Tap water</td><td>Sintered Metal, Glass and Plastic</td><td>§ 4.3.4</td></tr>
<tr><td>Liquid height</td><td rowspan="2">Sintered plastic</td><td>1.0 and 0.8 m</td><td>§ 4.3.5</td></tr>
<tr><td>The appropriate height of the probe from the sparger</td><td>0.026, 0.055, 0.098, 0.144 and 0.2 m/s</td><td>Aerated level + probe</td><td>1.0 m</td><td>§ 4.3.6</td></tr>
</table>

4.3.1 Development of an experimental protocol to give repeatable results

The purpose of conducting these experiments was to assess the reproducibility of the results concerning the mean gas void fraction, α, when tap water and compressed air were used. Tap water contains impurities such as salts, and compressed air may contain small oil droplets from the compressor, both of which could affect α. Maruyama *et al.* (1981) reported irreproducible results when they used tap water and air from a compressor. They noticed that different values of α were obtained in each of their three experiments repeated in the same semi-batch bubble column, without filtering the air or changing the water. With continuous experiments, it was noticed that run 3 gave the highest α compared to the two previous runs (1 and 2). However, the maximum α occurred at about the same j_g. They attributed the difference to the accumulation of trace impurities, such as compressor oil, in the tap water. In this study, the air was filtered before it was introduced to the tap water through a sparger from the bottom of the column. The air filter was placed so as to remove compressor oil and all impurities that came from the compressed air. Despite this precaution, the early experiments produced inconsistent results when they were conducted under the same conditions; e.g. in terms of the j_g ranges and type of sparger. Since Maruyama *et al*. (1981) said nothing about how to obtain repeatable results when tap water and compressed air were used, a set of experiments was proposed and designed with two protocols:

Protocol 1 (Prot 1): Fill the column, turn on the air flow and immediately start to make measurements of the mean α, based on changes in the aerated level.

Protocol 2 (Prot 2): Prior to the start of all experiments, pass the air through the column continuously for at least 30 mins. Then start to take measurements of α.

The experiments were conducted in the OTBC (see § 4.2), using a plastic sintered sparger. Two sets of experiments were carried out using Protocol 1 and Protocol 2; each protocol was repeated four times to test the consistency of the results. In Protocol 1, the same water was used for each of the four runs, while in

Protocol 2, a fresh batch of water was used for each of the four runs. In both protocols, the experiments were conducted using the same conditions of liquid height and range of j_g.

Figure 4.2 shows a comparison of the void fraction results with respect to j_g for Protocol 1 and Protocol 2 experiments. The first run (marked Run 1) gave low values of α in comparison with the second run (Run 2) and the third run (Run 3), which used the same batch of tap water. For the fourth and subsequent runs, the results became much more reproducible. Typically, each run took about 10 mins to perform. As a result, it was proposed in Protocol 2 to pass the air through the column 30 mins prior to the start of all experiments to condition the tap water and get consistent results for α. Figure 4.2 shows that Protocol 2 gave reproducible results for four repeat runs and was thus followed in conducting all subsequent experiments undertaken in this study.

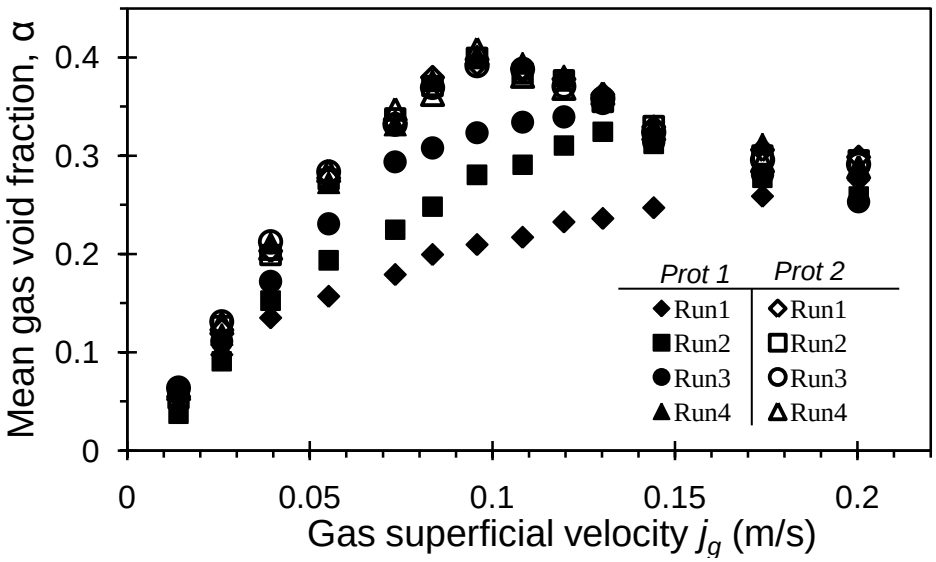


Figure 4.2 Repeatability tests for the initial experimental runs in the OTBC.

4.3.2 Investigation of hysteresis effects in homogeneous and transition flow

The purpose of these experiments was to test the consistency of the results, and check for any human bias in deciding the aeration levels. In addition, these experiments were conducted to check for any hysteresis; i.e. are the same values

of α obtained at the same j_g, when j_g is stepped up, stepped down, or randomly selected.

A set of three procedures was followed to control the air flow rate; this was undertaken to ensure that the data obtained from the experiments were independent of the way the changes at a particular aerated level were recorded.

(i) The experiment was conducted by increasing the air flow rate from a minimum to a maximum value in a sequence of evenly spaced steps.

(ii) The air flow rate was decreased from a maximum to a minimum value corresponding to the same values of j_g as in (i).

(iii) Random: the gas flow rate was changed randomly between the minimum and maximum values, but corresponding to the same values of j_g as in (i).

Figure 4.3 presents the results obtained from conducting experiments in the OTBC (see § 4.2) with a sintered plastic sparger. Initially the void fraction increased with increases in j_g, and uniform bubbly flow with small bubbles was generated. As the void fraction reached around 0.4, bubble coalescence occurred, causing the void fraction curve to drop by about 10%. The results of the three procedures showed high reproducibility of less than 3% run error in α values. The highest % error in repeat runs was found in the transition and heterogeneous regimes. At high j_g values (above 0.1 m/s), the bed becomes more turbulent, the aerated level fluctuated, and hence affected the α measurements. In general, no hysteresis and human bias were noted in the α results from the three procedures. It was observed that the method of manipulating the air flow rate had no affect on the α results. The increasing j_g procedure was followed in subsequent experiments.

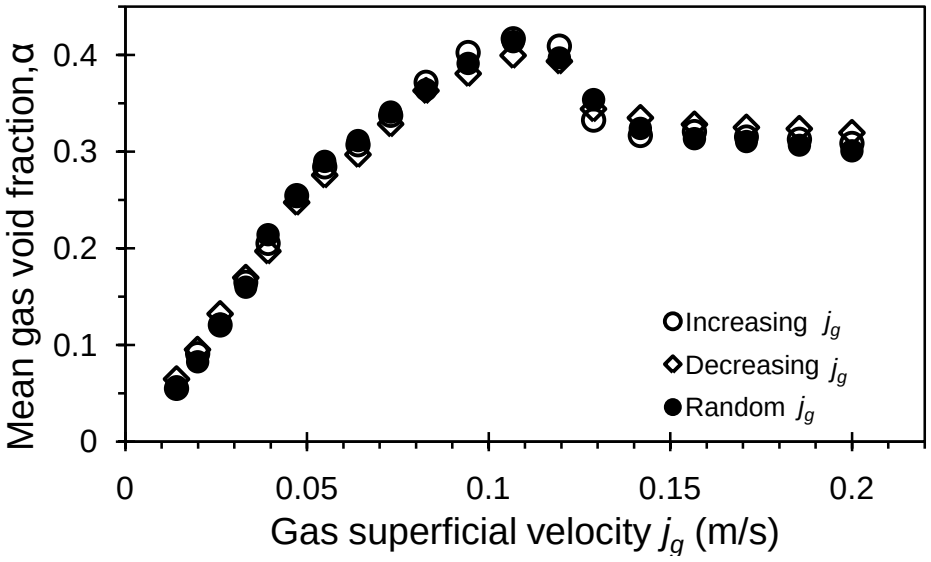


Figure 4.3 Comparison between sequential and random methods of varying the gas flow rate.

4.3.3 Selection of the working fluid

As was discussed in the Literature Review section (§2.2.3), Ueyama *et al.* (1989) and others reported that the purity of water affects both α and the transitional superficial velocity. Anderson and Quinn (1970) noticed that contaminants in tap water caused higher gas void fractions, while distilled water in similar circumstances tended to produce lower gas void fractions. Therefore, it was important to investigate this, regarding the purity of water (contaminated or water of high purity) to be used in this study. The reason for conducting these experiments was to study the effect of the presence of impurities in the water on the mean α and transition phenomena. The experiments were conducted in an OTBC column at the same conditions, sintered plastic sparger and liquid height described in § 4.2. Two types of water were employed: tap water (contaminated water) and high purity water. The conductivity probe method could not be used to obtain α due to the absence of ions in the high purity water, and therefore, the aerated level method was used to measure the mean α in both purities of water. Both types of water were conditioned using Protocol 2, which is described in §4.3.1.

Figure 4.4 illustrates α results for the tap and high purity water experiments. The tap (contaminated) water experiment gave higher void fractions compared to the

experiment using high purity water. According to the visual observation, up to a j_g of 0.08 m/s, uniform bubble flow was maintained in tap water. However, at only 0.02 m/s, bubbles coalesced to form spherical cap bubbles in the high purity water. The flow was highly churn-turbulent and exhibited random, large circulation patterns; coalescence occurred at locations between the sparger and the very top of the column. Trace impurities (e.g. salts and chloramines) are always present in tap water and their effect is to suppress coalescence (producing small bubble size and hence low rise bubble velocity), thus maintaining the state of homogeneous bubbly flow to larger j_g values than in high purity water. In the latter, coalescence occurs at low j_g, resulting in larger bubbles with greater rise velocities; hence the mean void fraction is lower than with contaminated water.

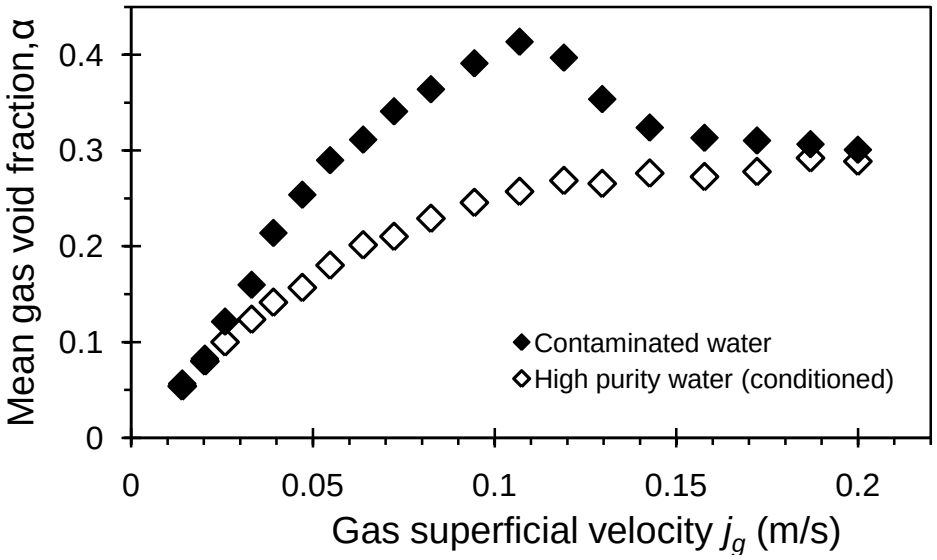


Figure 4.4 Comparison of the gas void fraction results for contaminated water with results for high purity water in the OTBC.

The results arising from this investigation are in good agreement with the conclusions of Anderson and Quinn (1970). They observed homogeneous flow with higher α in contaminated water, while high purity water gave lower void fractions in heterogeneous flow (see Figure 4.5). Coalescence is known to be promoted by surface-active materials, and a number of different mechanisms have been proposed as an explanation. Anderson and Quinn (1970) argued that such materials reduce surface tension and so increase the rate of thinning of the

film separating coalescing bubbles. As has been discussed, the presence or absence of impurities can lead to such differing behaviour, as is apparent from the work of Anderson and Quinn (1970). Tap water contains ions, which are essential for the conductivity method, so tap water was selected to be used as the liquid phase in all experiments in the current study. Moreover, it is difficult to maintain the water at high purity as it is gradually contaminated by the air. In addition, as shown in Figure 4.4, the contaminated water provides an obvious transition point in α data, while no transition point is observed in the high purity water data.

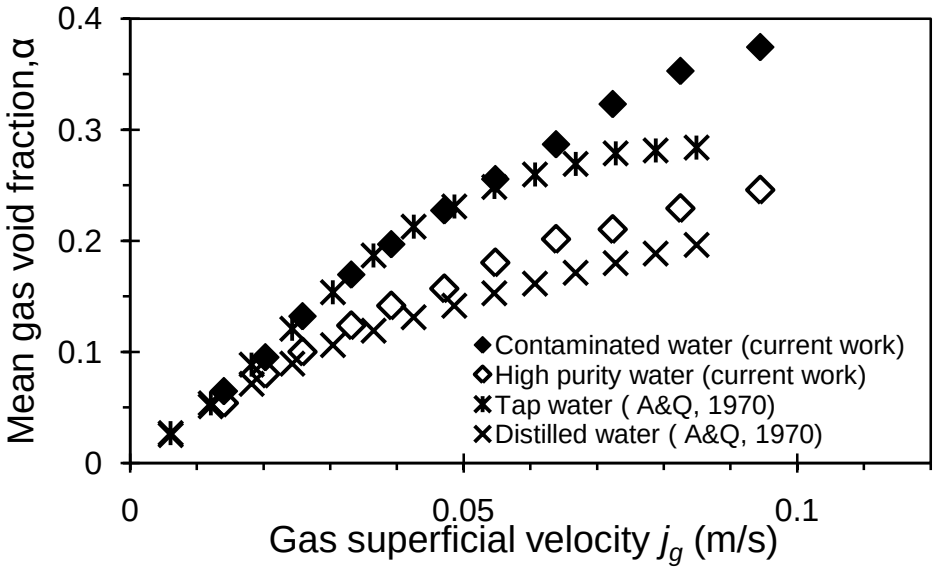


Figure 4.5 Comparison of the experiments and Anderson and Quinn (A&Q) (1970) regarding gas void fractions for measured contaminated and high purity water in the OTBC.

4.3.4 Selection of sparger type

In air-water systems, gas sparger configurations affect the superficial velocity of gas at the transition point. So, the purpose of conducting the present experiment was to investigate the effect of the sparger type on α, and the transition point. The conditions of the experiments are shown in Table 4.1. Two sparger materials were employed, sintered plastic and sintered glass. The pore size of the sintered plastic sparger was around 100 μm, as provided by Porvair Technology, whereas the sintered glass sparger had a nominal pore size of 40-100 μm, as provided by A1 Laboratory Supplies.

Figure 4.6 shows α measurements obtained with the sintered plastic and the sintered glass spargers. At low gas flow rates, both spargers produced small and uniform bubbles forming a homogeneous flow; then the flow changed towards the transition regime. This transition occurs at a point before the maximum α, when the bubble concentration is very high and there is a high probability of coalescence. Then α in the bed collapses and churn-heterogeneous flow follows. The flow produced using both plastic and glass spargers included homogeneous, transition and heterogeneous regimes. However, the flow transition occurred earlier when air was introduced to the rig through a sintered plastic sparger, rather than a sintered glass sparger. The maximum α = 0.42 occurred for the glass sparger at almost j_g = 0.11 m/s. compared to α = 0.39 at j_g = 0.10 m/s for the glass sparger. The dissimilarities in void fraction and flow transition are due to the difference in pore size or the material (wettability) of the spargers. Sada *et al.* (1986) observed that the bubble formation depends on the wettability of the gas distributor. Wettable spargers (glass) tend to produce smaller sized bubbles compared to non-wettable material (plastic).

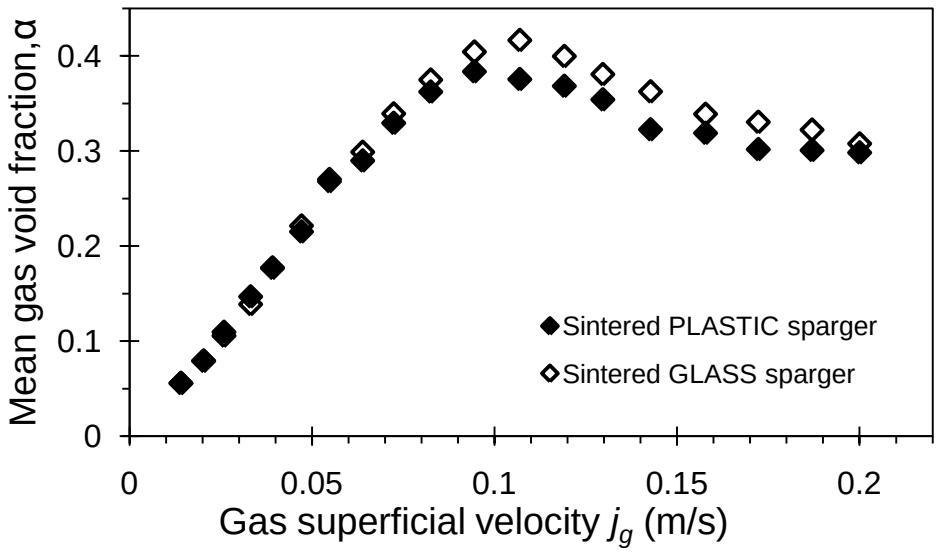


Figure 4.6 Comparison of gas void fractions and transition rates between results for the sintered plastic and the sintered glass spargers in the OTBC.

The sintered plastic sparger was selected for use in this study for two reasons:

(i) One of the aims of this study was to destabilise the homogeneous flow by generating large bubbles. The proposed method was to introduce orifices in the sparger and it would have been difficult to accurately drill differently sized orifices in sintered glass (see §5.2).

(ii) Another aim of this research was to study α and the transition position in an annular gap bubble column (AGBC) by placing different inner tubes in the open tube column. Therefore, a sintered glass sparger was not sufficiently strong to hold the weight of an inner tube filled with water; the weight was about 6 kg (see §6.2).

4.3.5 Selection of liquid height

In order to investigate the effect of water height, H_L, on α and the position of the transition regime, two different water levels were considered, 0.8 and 1.0 m above the gas distributor. The purpose of conducting these experiments was to choose a liquid height, which was sufficiently large to avoid end effects. The conditions of the experiments are shown in Table 4.1. First, the column was filled with tap water to the desired level, and was conditioned by passing the air through for about 30 mins (as discussed in §4.3.1). Then, gradually, the gas flow rate was increased by manipulating the rotameter valve. Figure 4.7 illustrates the effect of the liquid height on α and the transition point gas superficial velocity. The experiments were carried out over a range of gas superficial velocities, j_g, between 0.014-0.19 m/s; these yielded maximum void fractions of 0.44 and 0.41, for 0.8 and 1.0 m water levels respectively. At low gas flow rates, homogeneous flow was observed with small and uniform bubbles. The bubble concentration increased with increasing gas flow rates, up to a maximum value of α when bubbles started to coalesce, forming large bubbles. This signalled a transition of the flow from homogeneous to churn-heterogeneous. The gas void fraction at 0.8 m was larger than that at a 1.0 m water level; the transition occurred at a slightly lower j_g value for the greater liquid height, and hence there are significant differences in α at j_g > 0.12 m/s.

Wilkinson *et al.* (1992) reported that if the ratio of liquid height, H_L to column internal diameter, D_o is greater than 5, then α becomes independent. The H_L/D_o ratios in the current considered H_L of 0.8 and 1.0 m, are 8 and 10 respectively, as the D_o of the OTBC is about 0.1 m. Therefore the effect of H_L on the gas void fraction is negligible. On the other hand, the transition point gas superficial velocity is generally reduced by greater liquid height, as Sarrafi *et al.* (1999) reported without offering an explanation; α also decreases with increases in static liquid height, as Wilkinson *et al.* (1992) and Yamashita (1998) concluded for ratio H_L/D_o less than 5. In short columns, bubbles may undergo a process of coalescence as they rise, yielding a variation in bubble size with distance above the sparger. Therefore, the measured local α might change in line with the distance from the gas sparger; a similar conclusion was reported by Thorat *et al*. (1998) and Tse *et al*. (2003). In longer columns, this bubble size distribution should reach a state of equilibrium far from the sparger; therefore, reducing the effect of increased liquid height on the mean void fraction. A water height of 1.0 m above the gas distributor was selected for carrying out the experiments in this study.

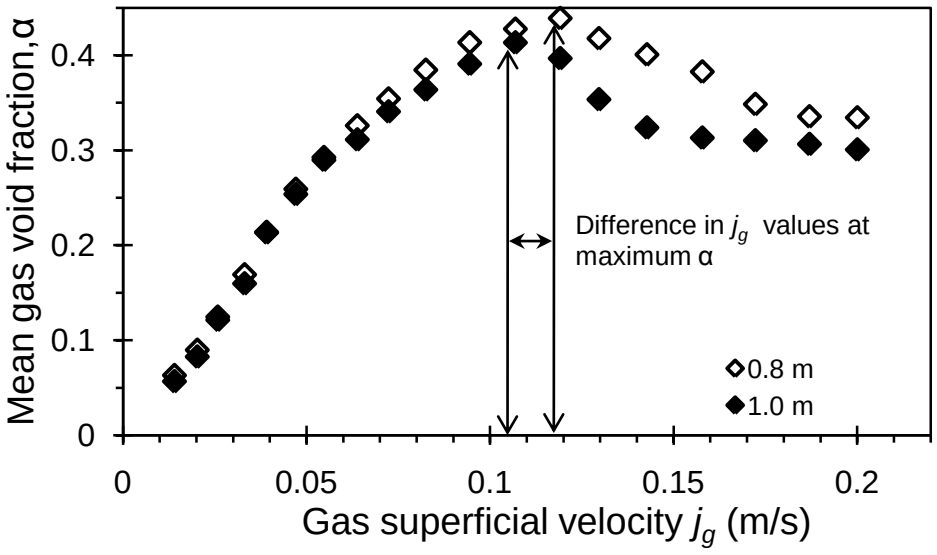


Figure 4.7 Effect of liquid height on the gas void fraction and the transitional superficial velocity: a comparison of 0.8 and 1.0 m water heights.

4.3.6 Probe height selection

The purpose of conducting these experiments was to investigate the effect on α of changing the height of the conductivity probe above the sparger. This was linked to the main aim of the research, which was to identify the most appropriate electrode height that would give similar measured results for a cross-sectional area averaged α compared to the volume-average gas void fraction results, which were obtained using the aerated level method. The distance between the sparger and the probe plays a critical role in identifying the value of the local distribution of α and this depends on understanding the equilibrium between the break-up of bubbles and the coalescence taking place in the bulk fluid. Millies and Mewes (1999) defined four regions of the flow in a bubble column:

(v) The primary region where bubbles form at the sparger.
(vi) The secondary region, resulting from the break up and coalescence of primary bubbles.
(vii) The dynamic equilibrium region, which results from the coalescence and break up of secondary bubbles.
(viii) The separation or disengagement region at the top of the column.

In a similar way, Wilkinson *et al.* (1992) and Yamashita (1998) divided the regions in the bubble column into, namely, the sparger, bubble and bulk regions. On the other hand, Thorat *et al*. (1998) divided the total column height that appears in the heterogeneous regime into two regions, the sparger and the bulk regions.

The description of Millies and Mewes (1999) is more satisfactory than others, because it recognises the region of equilibrium where bubble size and the local void fraction should be independent of height above the sparger. For longer columns, the cross-sectional area-averaged α should correspond more closely to the volume-averaged α value. Ideally, the conductivity probe should sit in the dynamic equilibrium region.

According to Thorat *et al.* (1998) and Tse *et al.* (2003), bubble size changes with respect to the probe's height from the sparger, depending on the nature of

coalescence in the liquid phase. Consequently, the measured local α might change with distance from the gas sparger.

The experimental conditions are illustrated in Table 4.1. The experiments were conducted in an OTBC column (see §4.2), equipped with a two-point probe. Only probe needle 1 (p1) was used to measure α over an evenly spaced range of five j_g values, which were between 0.0265 and 0.2 m/s. Figure 4.8 schematically shows the expected local α and its profile in an OTBC. The probe was placed in the centre of the column, which would give the highest local α compared with the other radial positions. Three different heights above the sintered plastic sparger, 0.265, 0.57 and 0.86 m, were considered. The LabVIEW program (see §Appendix B) was used to monitor and collect the data from the electrode with a sampling rate of 4 kHz. The MATLAB program (see §3.4.7) was used to analyse the findings. The raw data were processed using the threshold method and two standard deviations, σ, from the mean base line were used. (The data processing methods are described in detail in §3.4.7).

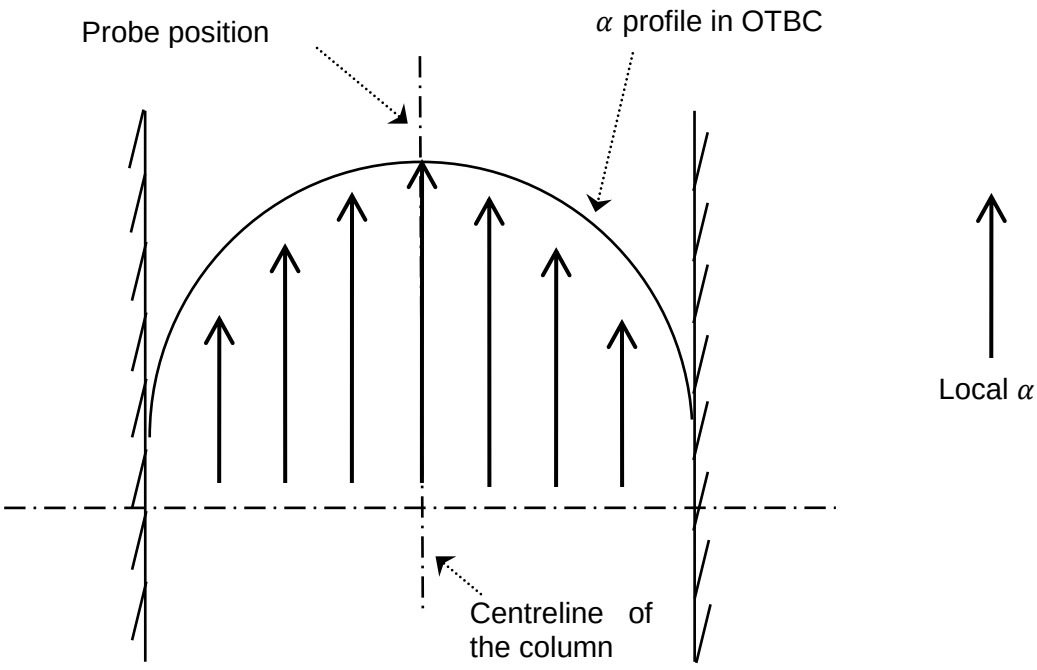


Figure 4.8 Schematic diagram for the local α and its profile in an OTBC; the probe is placed at the centre of the column.

Full radial profiles of the local void fraction distribution were not obtained at each probe height, and therefore no comparison of cross-sectionally averaged α (from probes) and volume averaged α (from aerated height differences) is possible. Instead centre-line measurement of the local α are compared at the three probe heights. For the typical shape of the α profile (Figure 4.8) the centreline value will be greater than the mean void fraction.

Figure 4.9 shows the results for local values of α using the conductivity probe, p1, at the centreline for the three probe heights. According to the description of Millies and Mewes (1999), the probe at a height of 0.265 m should be located in the sparger region; small bubbles, which had not coalesced to their equilibrium size, hit the probe and gave a high α value compared to other heights. On the other hand, with the probe at heights of 0.57 and 0.86 m, the bubble coalesced and may have reached their dynamic equilibrium size. However, the probe at a height of 0.86 m gave slightly lower α values compared with the height of 0.57 m. The values of α above that may be higher in the foam disengagement region. The difference between the cross-sectional α values at 0.57 and 0.86 m are small, about 3%. The probe with a height of 0.57 m was selected for use in the conductivity experiments in this study.

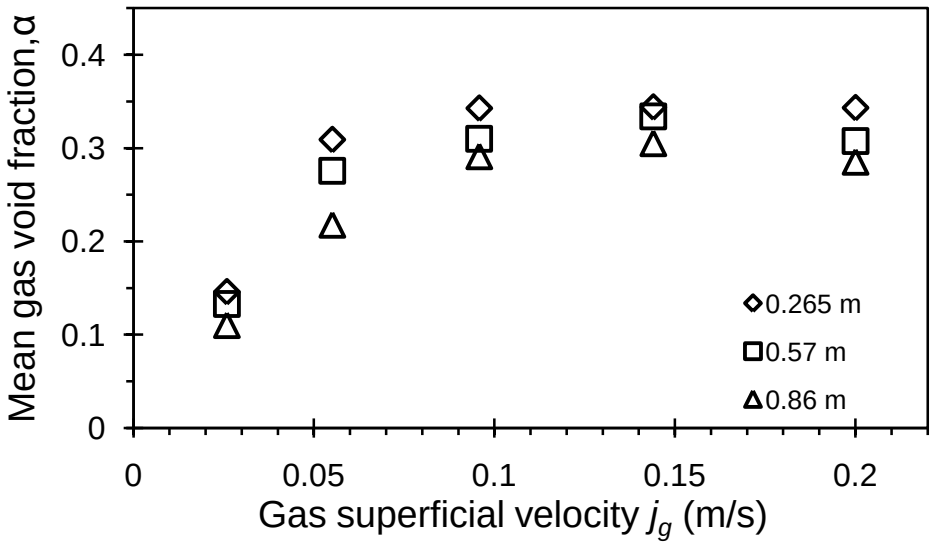


Figure 4.9 Gas void fraction with respect to j_g; comparison between the aerated level method and results using three different probe heights.

4.4 Conclusion from the preliminary experiments

A set of preliminary experiments were conducted to ensure that the results were reproducible and consistent. Prior to each run, it was recommended that the air should be switched on for at least 30 mins to condition the tap water, and hence, obtain consistent results. Also, tests were carried out to manipulate the air flow rate, in a sequence of steps from a minimum to maximum or vice-versa, or at random, following the same j_g steps. The test findings confirmed that the results were consistent; there were no effects of hysteresis and no human bias in the measured α results. It was suggested that tap water should be used, because it contains ions, which are important in applying the conductivity method used to predict α in the study. Moreover it was very difficult to maintain the purity of the high purity water over longer experimental runs. The sintered plastic sparger was also selected for use in this study, because it was strong enough to carry the heaviest inner tube and sufficiently flexible to be drilled with different orifice sizes. Liquid heights of 0.8 and 1.0 m above the sparger were considered, as the liquid depth affects α and $(j_g)_{trans}$, and as the liquid depth increases, both variables decrease. A water height of 1.0 m was selected in the subsequent experiments. Three probe heights above the sparger: 0.265, 0.57 and 0.86 m, were tested. The description of Millies and Mewes (1999) seems more reasonable than other proposals, because it distinguishes the region of equilibrium, where bubble size and the local void fraction should be independent of the height above the sparger. A probe height of 0.57 m in the dynamic equilibrium region was selected for use in all the conductivity experiments carried out in this study.

4.5 Investigations on the addition of alcohol

This investigation aims to offer a full understanding of the effect of surface active agents, present in aqueous solutions, on the gas void fraction in a bubble column reactor. In such units, the hydrodynamics and mass transfer rates are strongly affected by the properties of the liquid phase. The most important difference between air-water and air-aqueous solution systems is that, in the former, bubble coalescence rates are high whilst, in the latter, coalescence rates are low (Schugerl *et al*., 1977). The purpose of conducting the experiments in this research is to study the effect of the presence of a low concentration of an

alcohol in the bubble column on the gas void fraction and bubble size. Comparisons are made with results obtained in tap water with no alcohol added.

Experiments were conducted in the OTBC column (see §4.2). Apart from the addition of various alcohols, the experimental conditions and specifications of the column are listed in Figure 4.10.

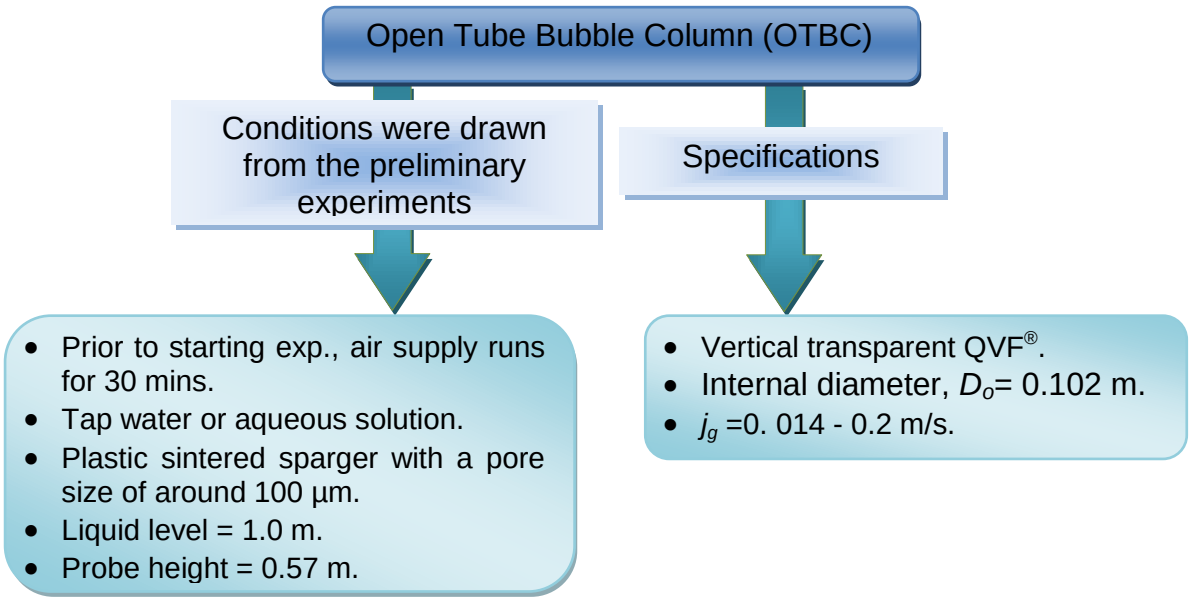


Figure 4.10 Open tube bubble column specifications and experimental conditions.

The liquid phase used in the experiments consisted of tap water to which ethanol and isopropanol were added in various concentrations. These OTBC experiments were carried out using ethanol concentrations of 0, 8, 16, 32, 75, 150 and 300 ppm by weight, while 300 ppm by weight was used for isopropanol (see Table 4.2).

Table 4.2 Alcohol concentrations used in the OTBC experiments.

System	*Ethanol conc. ppm/weight*	*Isopropanol conc. ppm/weight*
OTBC	0, 8, 16, 32, 75, 150 and 300	300

The surface tension, σ, of the tap water and various ethanol and IPA concentration solutions was measured using the digital surface tension balance (model 2ks, White Electrical Instrument Company Limited). For maximum

accuracy, the surface tension test was repeated five times, and an average value taken. The addition of alcohol would decrease the surface tension of the solution and consequently is expected to generate a smaller average size of bubble. Figure 4.11 illustrates the effect of the presence of ethanol on the tap water's surface tension, σ. At 20°C, the measured σ of the tap water was 74 mN/m; as a small amount of ethanol was added to the solution, the σ decreased. The lowest measured σ = 66.3 and 57.2 mN/m was reported at the highest concentration, 300 pp/mass, of ethanol and IPA solution respectively. The results are in good agreement with findings of Vazquez *et al.* (1995). Over the same range concentrations of ethanol and IPA, they found that IPA offered lower σ values compared to ethanol.

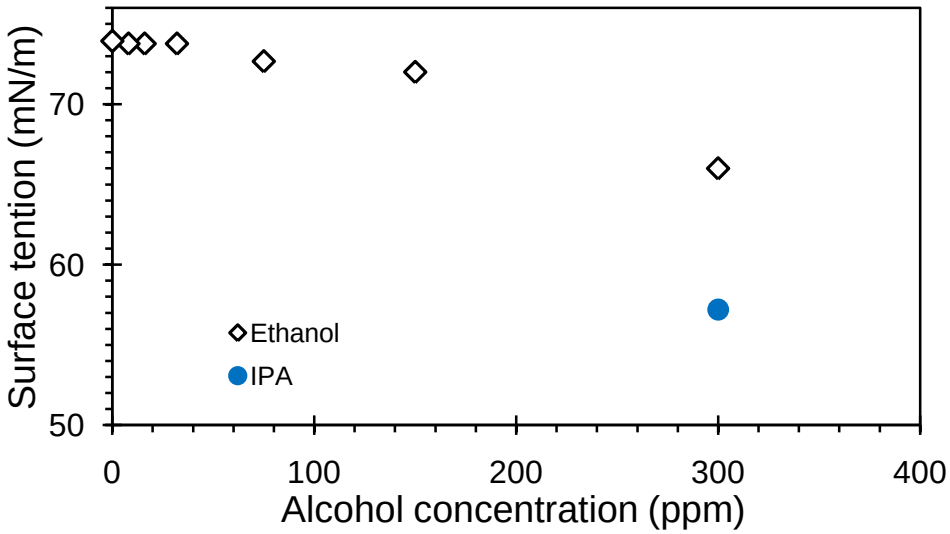


Figure 4.11 Surface tension with respect to various of concentrations (ppm by mass) of ethanol.

Mean and local gas void fractions, together with the size and velocity of the bubbles, are important hydrodynamic variables in the design of bubble column reactors. The experimental setup for the OTBC is presented in Figure 4.1 while a summary of the experimental conditions, which were drawn from the preliminary experiments and the OTBC specifications are shown in Figure 4.10. The purpose of conducting the next series of experiments was to measure the mean and local gas void fractions in the open tube bubble column. This geometry is the benchmark case for comparison with the Annular Gap Bubble Column (AGBC). Aerated level (see §3.2) and conductivity probe (see §3.4) techniques were used

to measure the volume-average and local gas void fractions respectively. The cross-sectional area-averaged gas void fraction was obtained from the local gas void fraction radial distribution by using the methods described in §3.4.8 and next §4.5.1 .

4.5.1 Effects of alcohol concentration on gas void fraction profiles in the OTBC

Figure 4.12 shows the α profile obtained by traversing the probe across the diameter of the open tube bubble column at a height of 0.57 m above the sparger. Regarding the radius of the bend in the probe body, it is not possible to measure closer than 7 mm from the near wall of the column, whereas measurements can be made at a distance of only 4 mm from the far wall. All of the profiles are axisymmetric about the line y = 0.052 m on the centre-line of the bubble column, justifying the use of Equation (3.9) to calculate the mean α. At very low j_g (homogeneous flow regime), the results show almost uniform distributions of the local void fraction across the column. At higher gas superficial velocities, in the transition flow regime (typically $j_g \approx 0.05\, m/s$ in tap water) the mean void fraction increases and the void fraction profiles become increasingly non-uniform. In tap water, the void fraction extrapolated to the wall, α_w increases in the homogeneous regime, but then remains constant for $j_g > 0.1\, m/s$. The ratio of the centre-line to wall void fractions, α_c/α_w, also increase significantly, from a value of 1 at low j_g (a flat profile) to a value of about 1.6 as shown in Figure 4.13 for the OTBC with tap water, and selected ethanol and IPA concentrations. Thus, the void fraction profiles change shape significantly with increasing j_g during the transition from homogeneous (bubbly) flow, but less quickly in the later stages of the transition, or heterogeneous flow regimes. In the case of 300 ppm IPA, the void fractions at the wall rise to around $\alpha_w \approx 0.4$, and the ratio α_c/α_w remains closer to unity.

The effects of the presence of alcohol concentrations on the void fraction profiles are evident even at 8 ppm of ethanol (Figure 4.12 (b)), where the centre-line void fraction is significantly greater than with tap water (Figure 4.12 (a)). Visually, the bubbles are much smaller in the ethanol solutions. With increasing ethanol

concentration, the centre-line void fraction increases, although the wall void fractions remain approximately the same $\alpha_w < 0.2$. The coalescence suppressing properties of the alcohol solutions allows higher centre-line void fractions to be obtained, without the formation of larger, fast-rising bubbles.

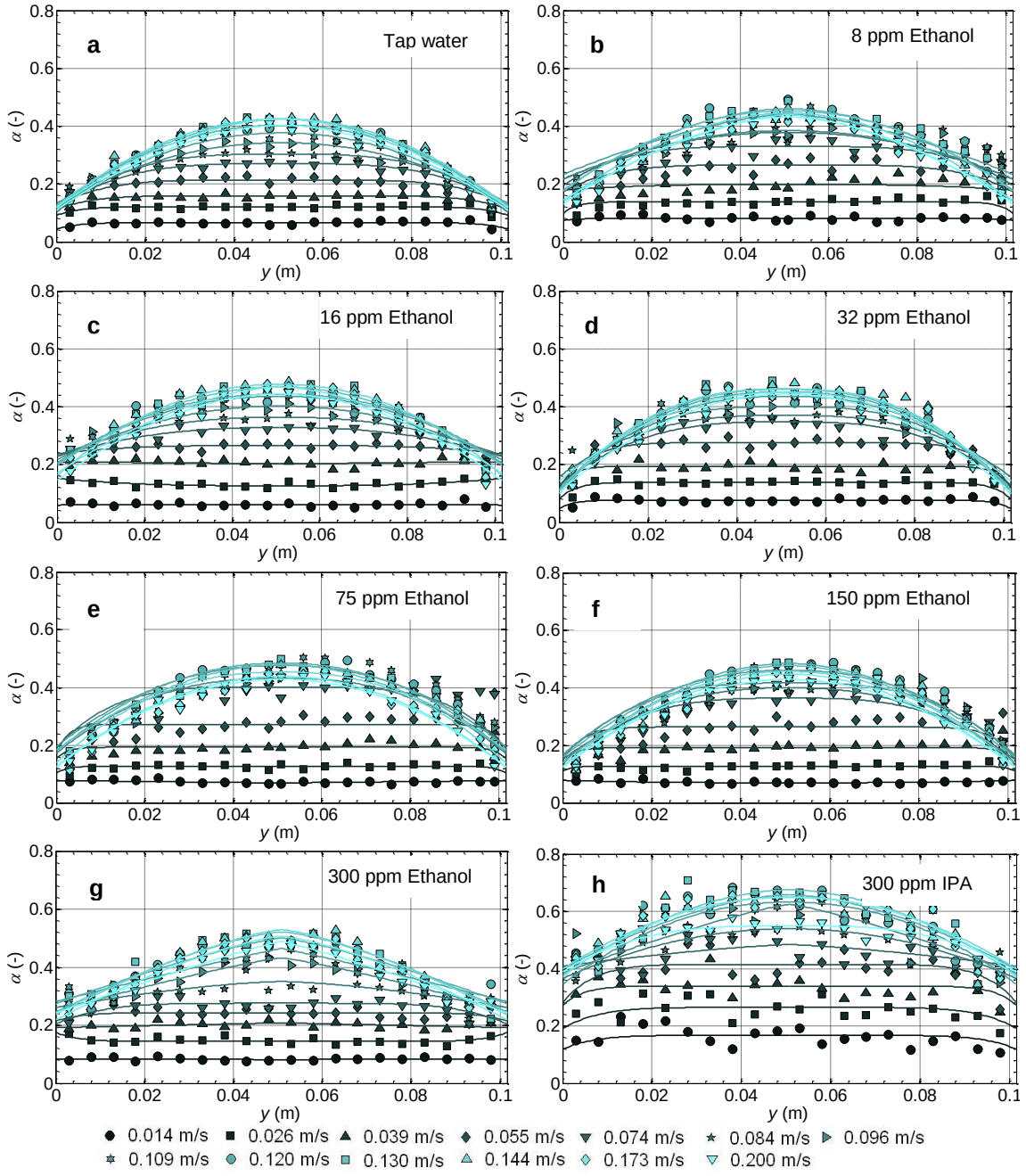


Figure 4.12 Profiles of the local gas void fraction with the distance from the wall, y, across a diameter of the open tube bubble column, using a porous sparger, tap water and assorted alcohol concentrations. The legend gives the gas superficial velocity.

The profiles of Figure 4.12 (g) and (h) indicate a significant increase in gas void fractions for IPA compared to ethanol at 300 ppm. Maximum void fractions of

$\alpha > 0.6$ are possible because of the increased degree of coalescence inhibition by the longer chain alcohol. The surface tension gradient (with respect to concentration) increases with increasing carbon chain length; hence the greater molecular weight alcohol provides a stronger effect on two-phase hydrodynamics (Albijanic *et al*., 2007).

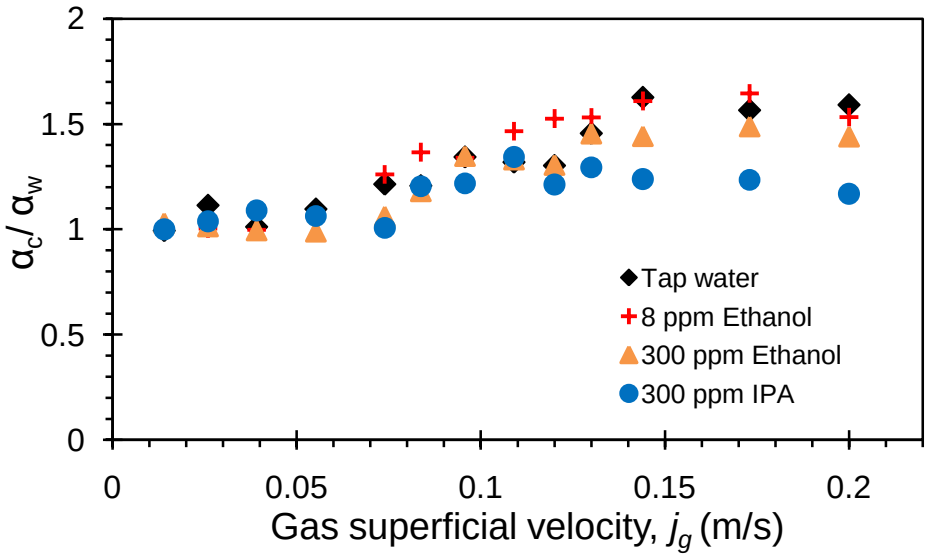


Figure 4.13 The ratio of centreline void fraction, α_c, to the wall void fraction, α_w, with respect to the j_g in the OBTC.

Hibiki and Ishii's (2002) equation (Equation 3.11)

$$\frac{\alpha - \alpha_w}{\alpha_c - \alpha_w} = 1 - \left(\frac{r}{R_o}\right)^z$$

was fitted to the void fraction profiles. Satisfactory fits of Hibiki and Ishii's equation to the measured void fraction profiles are shown by solid lines in Figure 4.12 (a)-(h), for tap water and the various alcohol concentrations, using z as the only adjustable parameter. The variation of z with j_g is shown in Figure 4.14. The latter shows that z falls sharply with increasing gas superficial velocity in the homogeneous regime and during the transition, whereas in the early parts of the heterogeneous regime $(j_g > 0.1\, m/s)$, the void fraction profiles almost collapse onto a single curve, and z decreases much more slowly, levelling off at a value between 1 and 2. Under these conditions, the majority of the bubbles tend to travel in the centre of the column and fewer bubbles travel close to the wall; coalescence is more likely to occur close to the centre-line of the column, giving

large, fast-rising bubbles. These are surrounded by small bubbles at the wall in the transition and heterogeneous flow regimes.

There is some scatter in the fitted values of z and Figure 4.14 shows little difference between the tap water and the low ethanol concentrations; hence, the profile shapes are approximately the same in each case and there should be little difference in the distribution parameter C_o. At the higher ethanol concentrations, slightly lower values of z were obtained than in tap water at the same j_g.

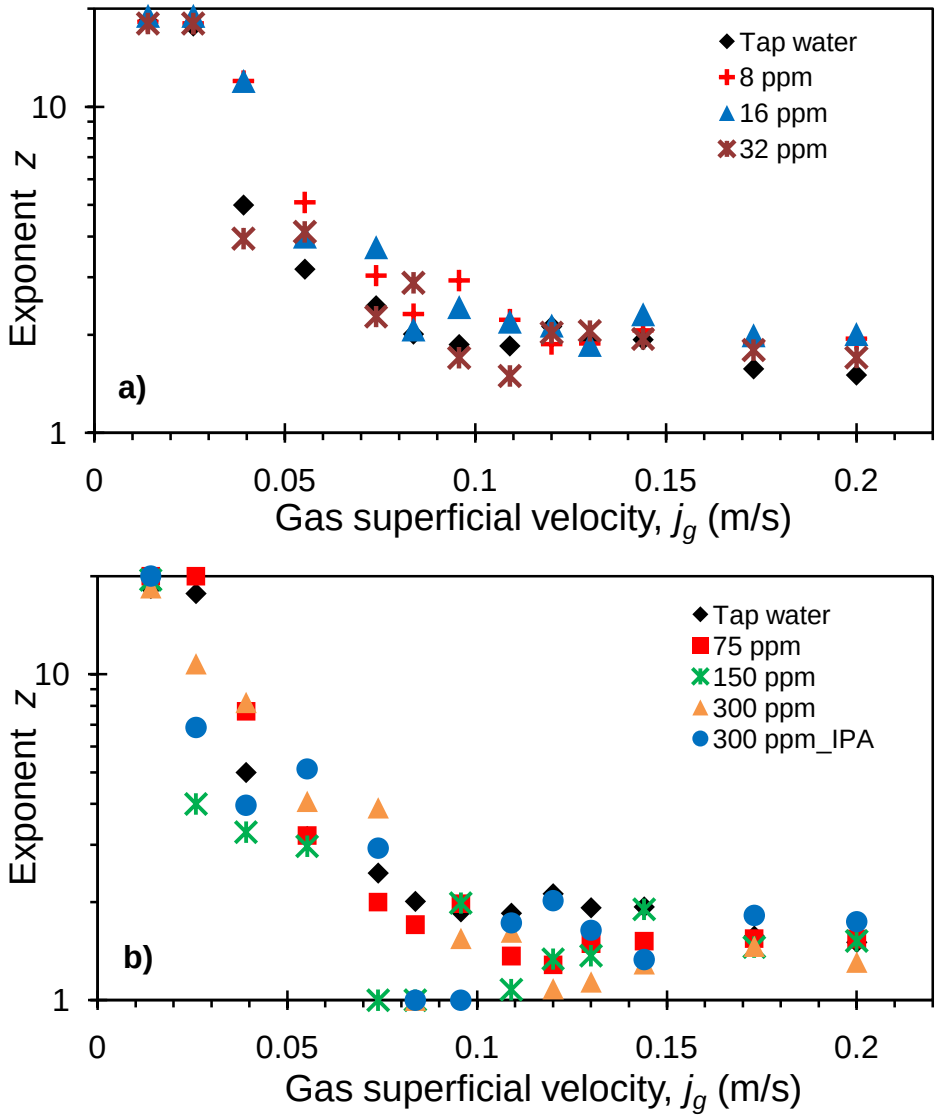


Figure 4.14 Hibiki and Ishii's (2002) model for exponent *z* with respect to j_g: a) tap water and b) assorted alcohol concentrations; the experiments were conducted in an OTBC using a porous sparger.

4.5.2 Mean gas void fraction in an OTBC with tap water

Figure 4.15 illustrates the gas void fraction data in an OTBC for a range of j_g values, which traversed the homogeneous, transition and heterogeneous regimes. The experimental conditions are shown in Figure 4.10. The homogeneous regime is characterised by having a uniform dispersion of small spherical or ellipsoidal bubbles; this generally occurs at low gas superficial velocities. With increasing gas superficial velocity, the gas void fraction increases and hence, there is an increased probability of coalescence, leading to a broader bubble size distribution. Under some circumstances, coalescence leads to the transition regime, where the gas void fraction decreases with increasing gas superficial velocities. At still higher gas superficial velocities, the flow comprises large, irregularly shaped bubbles, which rise rapidly through a dispersion of smaller ellipsoidal bubbles (in air–water) and α increases once more with increasing j_g in the heterogeneous regime.

Figure 4.15 also compares data obtained by measuring the changes in the aerated level from Equation (3.1), and from a two- and four-point probe (tip 1 of the conductivity probe). The former is a volume-average over the whole column, whereas, in the conductivity probe method, α is averaged across a horizontal cross-section, assuming an axisymmetric void fraction profile. The methodology is discussed in §3.4.8. The conductivity probes were located at a height of 0.57m above the sparger. With increasing axial height in the column, a small reduction in the void fraction was observed (due to bubble coalescence), as discussed in §4.3.6 indicating that there are some axial gradients of α; this is one reason for the discrepancy between the data from the two measurement methods, illustrated in Figure 4.15. In addition, it could be expected that very small bubbles, with diameters less than 1–2 mm, might not impact directly on the probe. Similarly, the probe might miss down-flowing bubbles, and hence their contribution to the locally measured void fraction would most likely not be included; this is a second reason why the probe-based method underestimates the mean void fraction. Cheng *et al.* (1998) compared measured mean void fractions (using manometers) with the cross-sectionally averaged void fractions obtained from using a two-point probe. They found reasonable agreement for co-current up-flow, but

underestimated α, by up to 25% for the zero liquid flow case, where bubbles could move down as well as up. This discrepancy was attributed to the down-flowing bubbles missing the down-facing needle probe. Figure 4.15 also shows that the four-point probe gives better results compared to the two-point probe. This improvement is because the acupuncture needles in the four-point probe were fully gold-plated instead of only the tips of the needles being plated with gold as in the two-point probe and the exposed tip length was reduced to 0.4 mm rather than 0.8 mm in two-point probe as the findings of Teyssedou et al. (1988).

The results, which were gathered using the two-point probe, underestimated α by 25% compared to the changes using the aerated level method, except at the very lowest gas superficial velocity where bubble impacts are at a low velocity and are infrequent. However, the four-point probe data improved the agreement with aerated level method; underestimations of the α values by 12% were obtained. The level of underestimation is better than reported in the literature e.g. Cheng *et al*. (1998); nevertheless, the conductivity probes provided useful information about the void fraction profiles within the column, which could not be obtained by using other measurement techniques. The errors are likely to be greater close to the walls of the column where down-flow of the bubbles is more likely to occur.

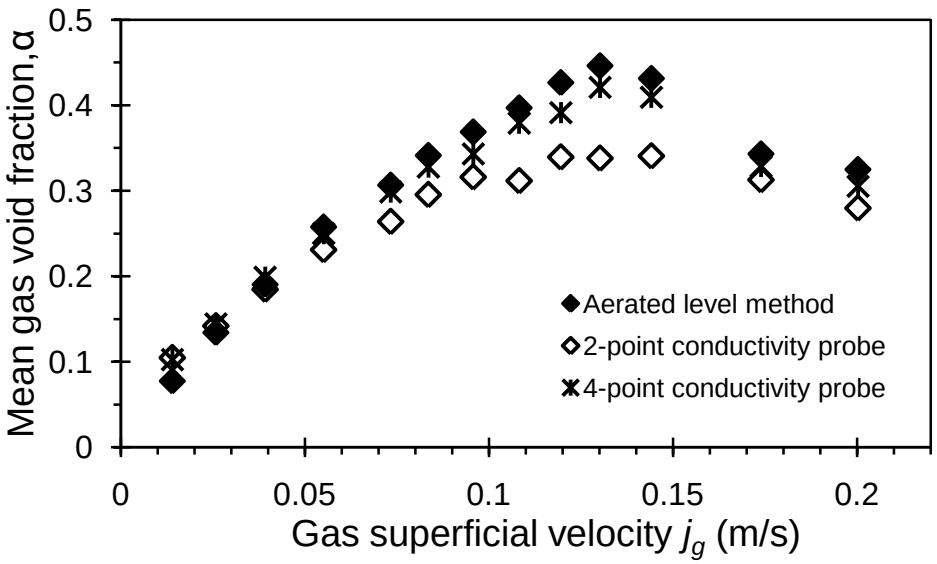


Figure 4.15 Mean gas void fraction in the OTBC from measurements obtained from changing the aerated level compared to measurements using the conductivity probe.

4.5.3 Mean gas void fraction in the OTBC with aqueous alcohol solutions

The presence of trace amount of an alcohol is expected to decrease the coalescence rate in the bed, producing a higher α. Figure 4.16 compares data obtained, using tap water and a range of alcohol concentrations, by measuring changes in the aerated level using Equation (3.2). The alcohol solution experiments gave higher values of α compared to the tap water experiments due to the presence of alcohol in the liquid phase. The highest α for the tap water results was about 0.43 at j_g = 0.12 m/s, whereas the highest α was about 0.66 at about j_g = 0.10 m/s for the 300 ppm alcohol concentration. In Figure 4.16, apart from the very lowest j_g, where bubble collisions with each other were at low relative velocities and coalescence is infrequent, the α of the 300 ppm ethanol concentration solution increased by about 45% compared to the tap water system. Figure 4.16 also compares α results for different alcohol concentrations. At j_g = 0.11 m/s, the aqueous solution with the lowest alcohol concentration, 8 ppm, gives $\alpha \approx 0.48$ and, at the highest concentration, 300 ppm, $\alpha \approx 0.63$ at the same j_g value. It was noticed that α increased as the alcohol concentration increased. These findings concur with the results of Krishna *et al.* (2000), who compared the void fractions obtained in air-tap water and air–tap water + two ethanol concentrations, 0.1% and 1%. They came up with the same conclusions, i.e. the presence of a relatively small amount of alcohol increased α in an aqueous solution.

Figure 4.17 illustrates the two-point conductivity probe mean α for the experiments using tap water and various alcohol concentrations with respect to j_g. The mean α was obtained by averaging the local gas void fraction across the column. The conductivity probe method, (see Figure 4.17), seemed to underestimate α by 25 % compared to the aerated level method (see Figure 4.16). Nevertheless, the conductivity probe method provided largely similar trends to the aerated level method. The alcohol seemed to increase the α and as the alcohol concentration increased, high values of α were produced.

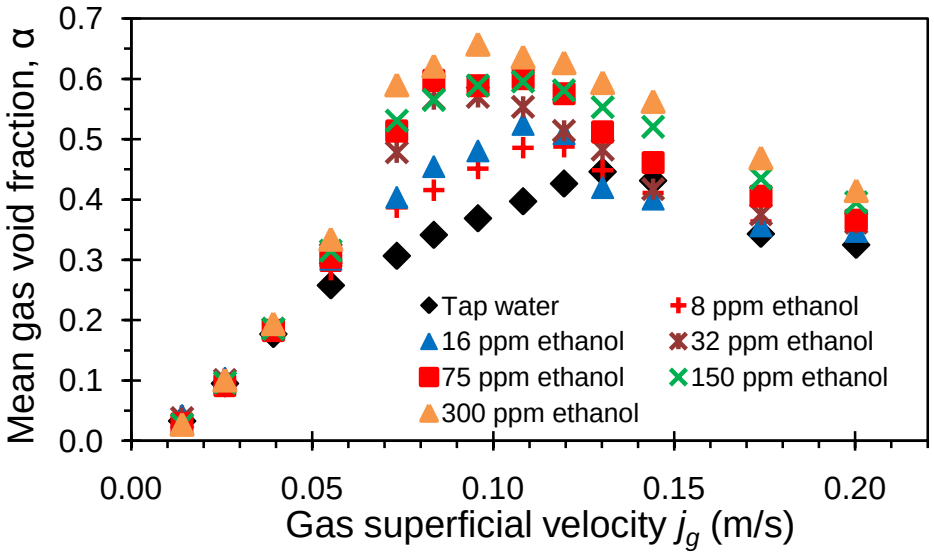


Figure 4.16 Mean gas void fractions for various ethanol concentrations compared to results using tap water, obtained from employing the aerated level method.

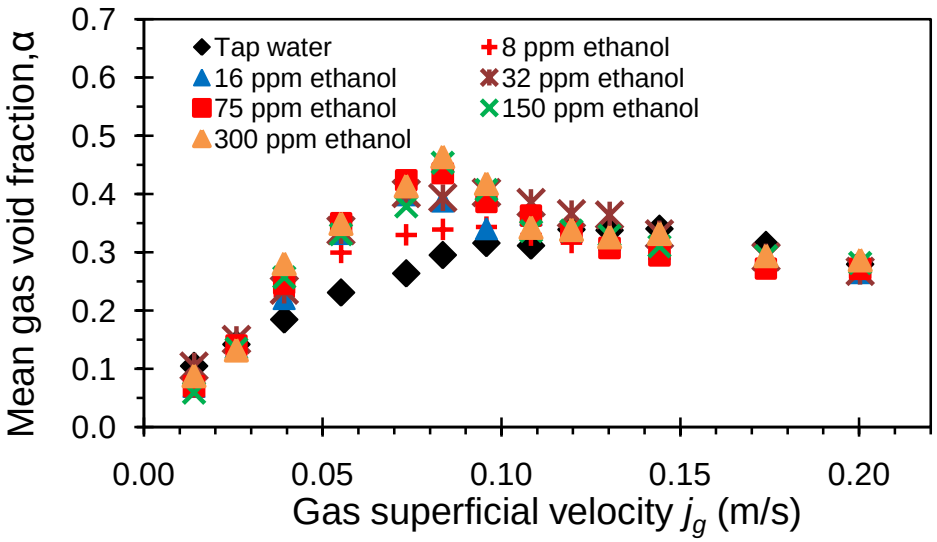


Figure 4.17 Cross-sectional mean gas void fractions obtained by using the two-point conductivity probe method (probe 1) with gas superficial velocities for a range of alcohol concentrations.

Figure 4.18 compares the measured mean void fractions for the ethanol and isopropanol aqueous solutions at 300 ppm. Two sets of data are shown for each solution: (1) a volume-averaged void fraction measured from the changes in aerated level (filled symbols), and (2) a cross-sectionally averaged void fraction from probe 1 (p1) of the four-point conductivity probe (open symbols). The latter makes use of the axisymmetric void fraction profiles to calculate the mean value. These two mean void fractions will only be equal if there are no axial gradients in

the bubble column, which is the case here since the column aspect ratio is H_L/D_o >10 and hence end effects should negligible (see §4.3.5). At low $j_g < 0.06\ m/s$, the void fractions obtained using the probe were slightly greater than the values obtained using the aerated level method; at higher j_g, the mean void fraction were underestimated by a maximum of 12% by the conductivity probe. The latter is due to the smallest bubbles not being intercepted by the needle tips and their contribution being missed in the mean void fraction. In all cases reported here, the difference between the two methods is small, confirming that conductivity probes provide an accurate measurement, even in the presence of the small bubbles obtained with the alcohol solutions.

Figure 4.18 shows that the 300 ppm IPA solution gives higher mean void fractions compared to the 300 ppm ethanol solution, which is in agreement with the results of Zahradnik et *al.* (1999) for the effect of carbon chain length. The hypothesis is that the IPA solution has a steeper surface tension gradient with respect to concentration than the ethanol solution, and hence the effect on void fraction is more significant.

As stated previously, alcohol influences the bubble size by preventing the phenomenon of coalescence. This is due to decreases in surface tension, which leads, in turn, to a decrease in the probability of bubble coalescence. Vazquez *et al*. (1995) concluded that surface tension decreases with increases in the carbon chain length. This was verified experimentally by measuring the surface tension of the tap water, and a range of ethanol concentrations between 8-300 ppm/mass (see Figure 4.11). The surface tension values for the 300 ppm/wt ethanol and isopropanol solutions were 66.3 and 57.2 mN/m respectively.

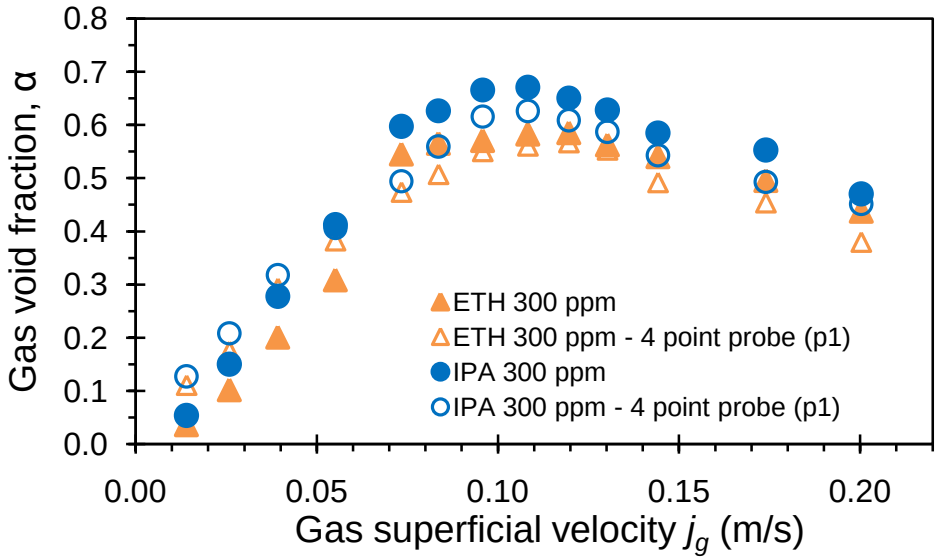


Figure 4.18 Mean void fractions of ethanol and isopropanol concentrations at 300 ppm; these data were produced using the aerated level (filled symbols) and four-point conductivity probe methods (open symbols).

4.6 Effects of alcohol concentration on flow regime transitions in the OTBC

Krishna *et al.* (2000) proposed the use of a Wallis plot (Wallis, 1969) to obtain information about the gas superficial velocity, $(j_g)_{trans}$ and void fraction α_{trans} marking the start of the transition from homogeneous to heterogeneous two-phase flow. Figure 4.19 shows the drift-flux velocity $j_g\,(1-\alpha)$ plotted against α, which was measured by the aerated level method. The smooth curve represents Richardson and Zaki's (1954) Equation (2.1), which is assumed to represent behaviour in the homogeneous bubbly flow regime and here uses n=2 (Krishna *et al.*, 2000) and v_t = 0.24 m/s (Wallis, 1969). The data fall close to the Richardson and Zaki curve at low gas superficial velocities, indicating that they indeed fall within the homogeneous bubbly flow regime. The points where the data deviate from the curve are taken to indicate the flow regime transition points, giving $(j_g)_{trans}$ and α_{trans}. Krishna *et al.* (2000) noted that it can be difficult to distinguish between the transition points for low alcohol concentrations. However, the largest ethanol concentration (300 ppm) clearly deviates from the Richardson and Zaki curve at much higher values of $(j_g)_{trans}$ = 0.06 m/s and α_{trans} =0.58, compared with the tap water experiments, where $(j_g)_{trans}$ =0.048 m/s and α_{trans}=0.26. Table

4.3 summarises the transition points obtained from Figure 4.19 for experiments using tap water and various ethanol concentrations in an OTBC. There is a consistent trend of the transition point moving to higher values of $(j_g)_{trans}$ and α_{trans} with increasing ethanol concentration (similar effects are found with IPA). Thus, the inhibition of coalescence by the adsorption of ethanol molecules at the air-water interface extends the homogeneous flow regime so that it remains stable at remarkably high void fractions, in agreement with the preliminary conclusions drawn from Figure 4.16.

Table 4.3 Summary of α_{trans} and $(j_g)_{trans}$ for tap water and alcohol aqueous solutions in an OTBC.

Solution	$(j_g)_{trans}$ (m/s)	α_{trans}
Tap water	0.048	0.26
Ethanol 8 ppm	0.050	0.28
Ethanol 16 ppm	0.053	0.31
Ethanol 32 ppm	0.062	0.48
Ethanol 75 ppm	0.062	0.51
Ethanol 150 ppm	0.062	0.53
Ethanol 300 ppm	0.060	0.58

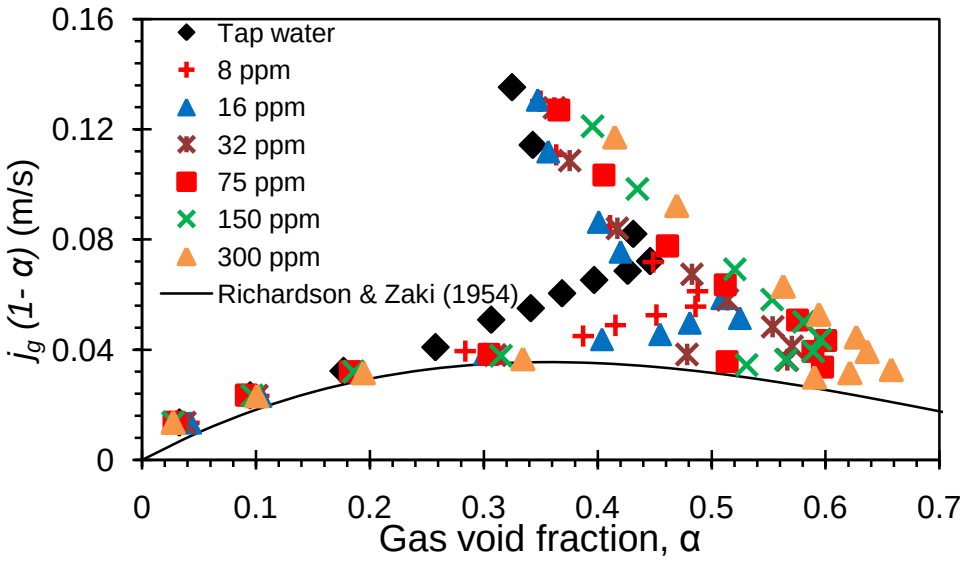


Figure 4.19 Wallis plot to determine transition parameters, α_{trans} and $(j_g)_{trans}$, for different ethanol concentrations in an OTBC.

It was known from the literature and from the previous experiments that the presence of alcohol would decrease the surface tension, which in turn would

inhibit the coalescence of the bubbles and hence delay the transition from homogeneous to churn-heterogeneous flow. Figure 4.20 shows a Wallis plot (discussed in §2.2.4) for the α data for tap water, ethanol and IPA solutions. The drift-flux velocity was plotted with respect to α. The concentration of both alcohols (ethanol and isopropanol) was 300 ppm/wt and the data were obtained from the aerated level method. The α data of the 300 ppm/wt isopropanol deviates from the Richardson and Zaki curve (n=1.8 and v_t = 0.22 m/s) later compared to the tap water and ethanol α data at the same concentration. As the length of the carbon chain increases, the homogeneous regime becomes more stable and the transition to heterogeneous regime is hindered. Table 4.4 emphasises the significant effect of the presence of alcohol on α_{trans} and $(j_g)_{trans}$ values.

Table 4.4 α_{trans} and $(j_g)_{trans}$ for tap water, ethanol and isopropanol aqueous solutions in an OTBC.

OTBC solution	$(j_g)_{trans}$ (m/s)	α_{trans}
Tap water	0.048	0.26
Ethanol 300 ppm	0.060	0.58
Isopropanol (IPA) 300 ppm	0.063	0.60

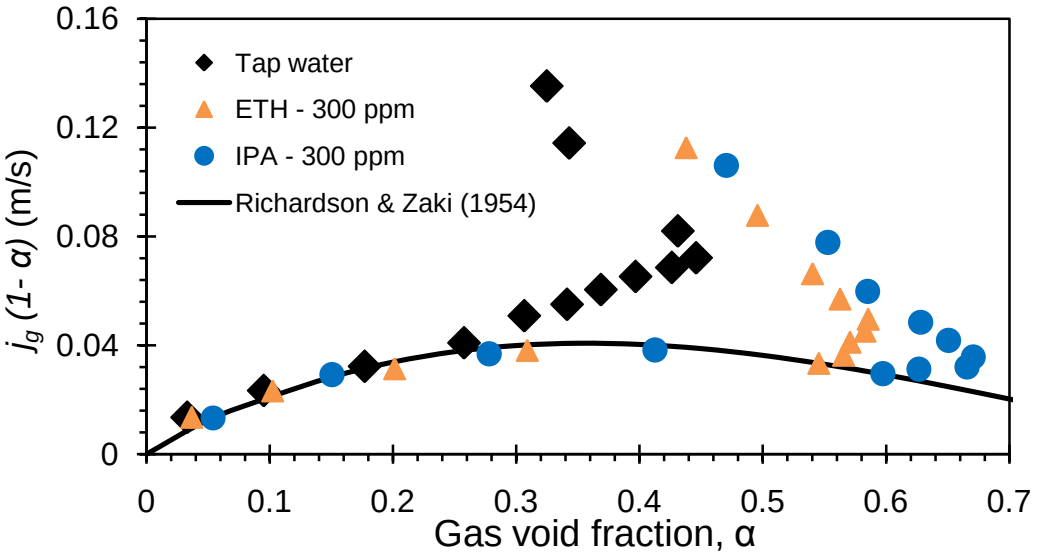


Figure 4.20 Wallis plot: comparisons of tap water, ethanol and isopropanol in an OTBC.

4.7 Measurements of bubble size and velocity

4.7.1 Chord length in the OTBC

The main advantage of using the two- or four-point conductivity probe was the capability to predict the local gas void fraction, as well as the size and velocity of bubbles. The gas void fraction was discussed in the previous section, whereas the purpose of the present section is to study the size of bubbles in the tap water and aqueous solutions. The effect of increasing j_g on the size and velocity of the bubbles is also considered. The chord length distribution, CLD, or chord length, C, give a more direct indication of size at least in a qualitative sense. On the other hand, the bubble size distribution, BSD, and bubble size require an inversion methodology, which is subject to some assumptions. The chord length was obtained from the conductivity probe using Equation 3.17, where the mean chord length, C, was obtained by averaging the local chord length across the column.

Figure 4.21 shows the profiles of the local chord lengths at various j_g , with the distance from the wall, y, across a diameter of the OTBC, and the porous sparger. Each point in the profile represents the time average of C at a specific j_g and radial position. At a first glance of Figure 4.21, the relatively large C seems to be concentrated at the wall of the column, whereas the small ones concentrate at the centre. It was difficult to distinguish between the profiles and study the effect of the increasing in j_g on C; therefore, a cross-sectional average of the profile was calculated to deduce the effect of j_g on bubble size (see Figure 4.21 and Figure 4.22).

$$\langle C \rangle = \frac{1}{\pi R^2} \int_0^{R_o} C(r)\, 2\pi r dr \qquad 4.1$$

A similar approach was used to obtain the mean bubble velocity,(v_t), the Sauter mean diameter (d_{32}), the volume average mean diameter (d_{43}) and the standard deviation (σ) in OTBC and in the orifice experiments, §5.7.

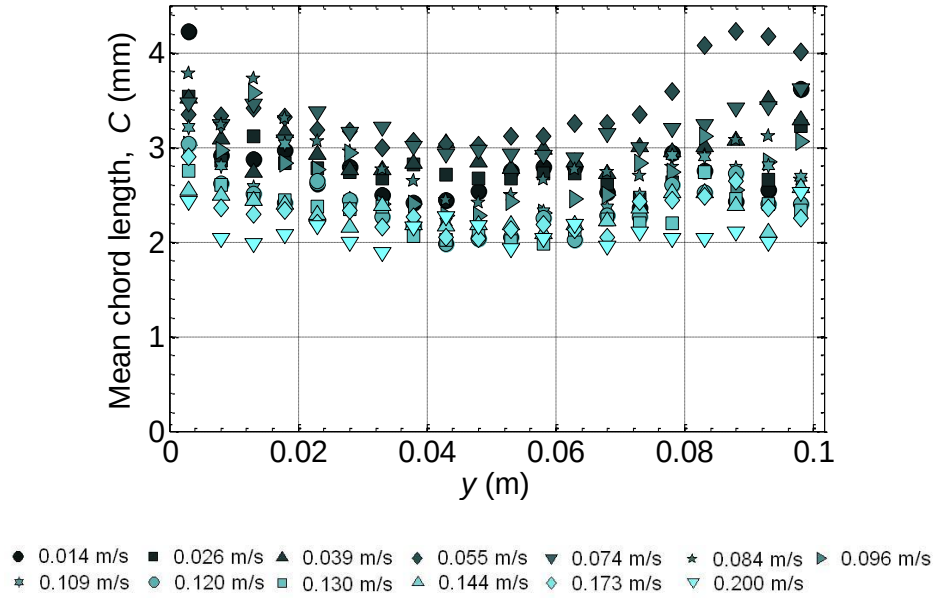


Figure 4.21 Two-point conductivity probe output; chord length profile of the tap water in the OTBC with a porous sparger.

The cross-sectionally averaged mean bubble chord lengths, $\langle C \rangle$, of the tap water, 300 ppm IPA and various ethanol concentrations operated in the OTBC with a porous sparger were plotted with respect to j_g. The mean bubble chord lengths were obtained from solutions where the alcohol was compared to the tap water. The alcohol chord lengths were divided into two groups, low and high alcohol concentrations. Figure 4.22 shows C for the low ethanol concentrations compared to C for tap water. The bubble chord lengths for low ethanol concentrations (8, 16 and 32 ppm) show a similar trend as for tap water. In general, C has two functions with respect to j_g : (i) an increasing function at low j_g and (ii) a decreasing function at high j_g. For j_g < 0.055 m/s, the mean chord length increased as j_g increased. This finding was in good agreement with results reported by Jamialahmadi and Muller-Steinhagen (1993). For j_g >0.055 m/s, C was a decreasing function as j_g increased; thus the flow might transit from homogeneous to churn-turbulent flow. The reduction in C at a high range of j_g indicated that bubble breakage was taking place in the system. As suggested by Wongsuchoto *et al.* (2003), the energy from turbulent eddies of appropriate size obtained from interactions between bubbles might be responsible for such bubble breakage. The liquid velocity might increase at high j_g and hence greater

turbulent intensity could exist, which then caused a reduction in the average C by increasing the breakage rate.

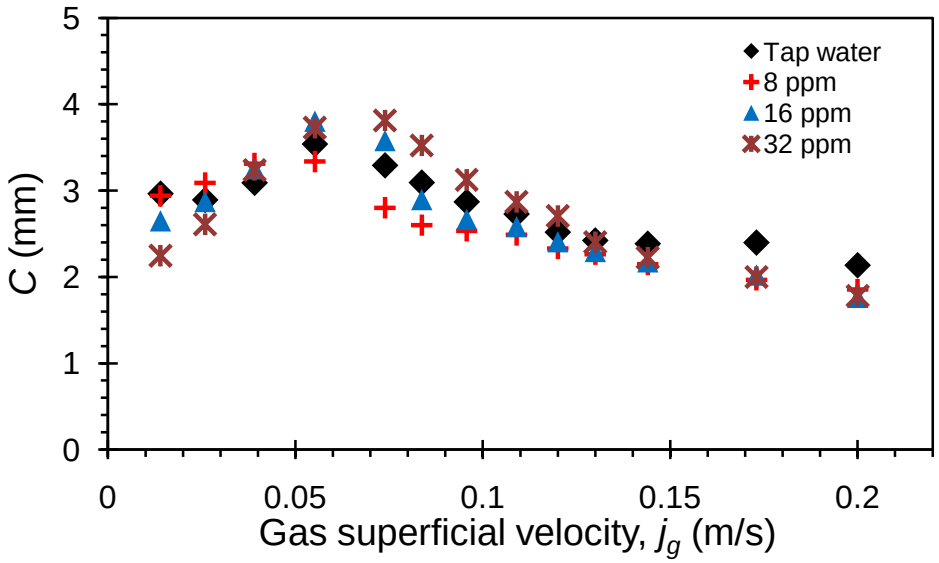


Figure 4.22 Mean chord length for a low concentration ethanol solution with respect to j_g.

The influence of alcohol on C became more significant as the concentrations increased. Figure 4.23 illustrates C at the higher ethanol and IPA concentrations compared to tap water. Higher alcohol concentrations provided similar trends to tap water; the bubble mean chord lengths were an increasing function at low j_g and a decreasing function at high j_g. Nevertheless, the maximum values of C were shifted at higher j_g compared to tap water. In other words, for the higher alcohol concentrations (e.g. 300 ppm ethanol and IPA), the bubble coalescence took place for the range of j_g<0.080 m/s instead of j_g< 0.055 m/s in tap water. Beyond these j_g values, the flow could become turbulent and hence more bubble breakup might occur. The presence of alcohol, however, is expected to increase the stability of bubbles and hence could inhibit the bubble coalescence. Similar findings were drawn using the Wallis plot method (§ 4.6) as the critical gas superficial velocities, $(j_g)_{trans}$, of the transition point in the α for the tap water and for 300 ppm of ethanol and IPA were 0.048, 0.060 and 0.063 m/s respectively (see Table 4.4). This provides further evidence that the transition from homogeneous to churn-heterogeneous flow is affected by the presence of alcohol. The influence of alcohol concentration on C was noted at high j_g > 0.120

m/s, as the tap water generally gave larger chord lengths values compared to the alcohol concentrations.

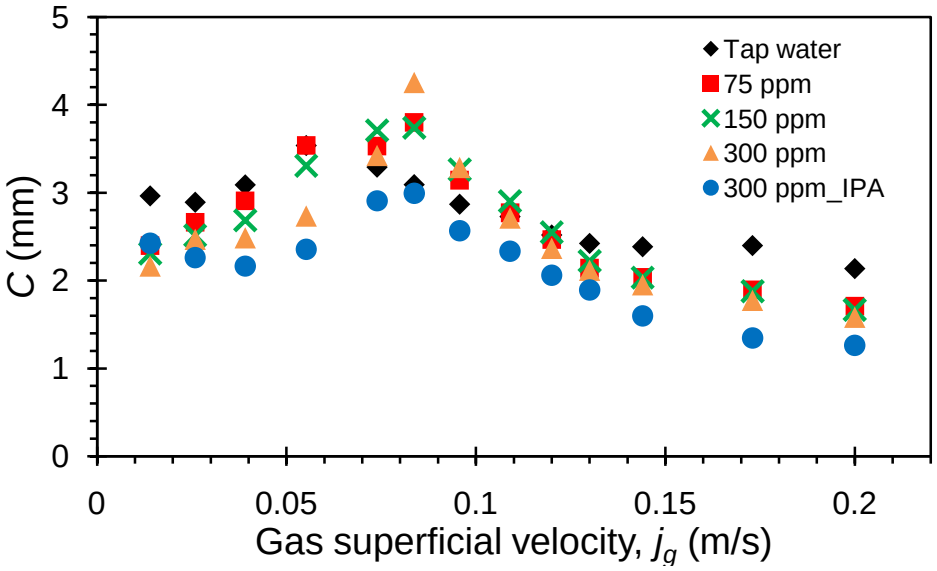


Figure 4.23 Influence of alcohol on mean bubble chord length: a comparison of various ethanol concentrations and 300 ppm IPA with tap water.

4.7.2 Bubble velocity in the OTBC

The bubble gas velocities, v_g, were also obtained using a conductivity probe and Equation 3.16. Figure 4.24 shows v_g profiles in tap water, which were obtained by traversing the probe across the diameter of the OTBC at a height of 0.57m above the sparger. The profiles are almost axisymmetric about the line *y*=0.052 m on the centre-line of the bubble column. At j_g ≤0.055 m/s, the distributions of the local v_g across the column are almost uniform; v_g has become increasingly more non-uniform at j_g >0.055 m/s. Each point in Figure 4.24 represents an average of the v_g data at a specific probe radial position and j_g.

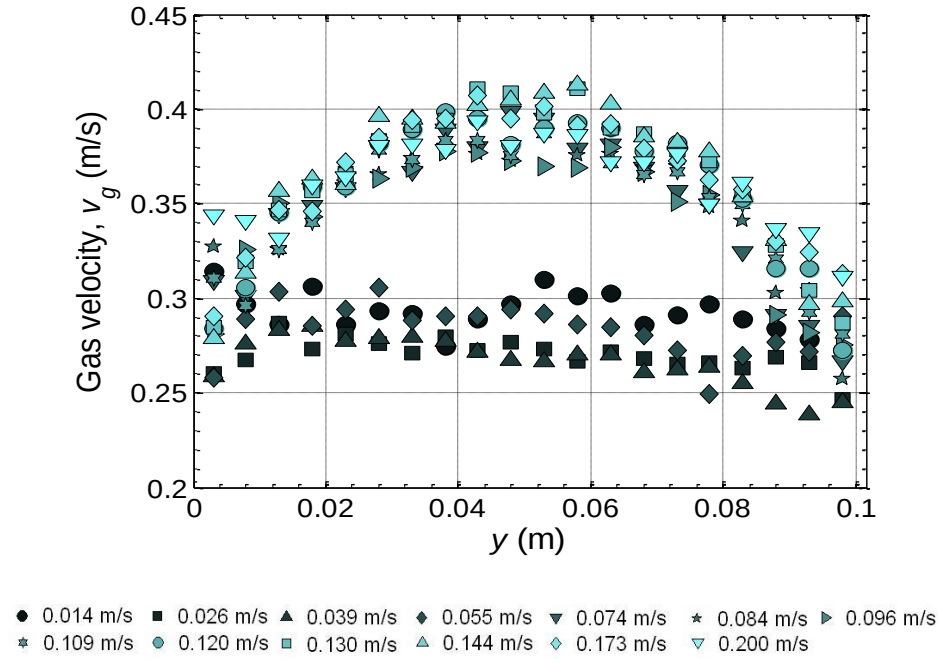


Figure 4.24 Mean gas velocity profile with the distance from the wall, y, across the diameter of the OTBC, using tap water and a porous sparger.

Figure 4.25 illustrates the mean v_g with respect to j_g for low ethanol concentrations (i.e. 8, 16 and 32 ppm) compared to tap water where the mean v_g calculated as mean C was calculated. For j_g < 0.055 m/s, a reduction from 0.29 to 0.26 m/s was noted in the tap water v_g as the j_g increased. The bubbles in the aqueous solution seemed to rise faster than the bubbles in the tap water. For j_g > 0.055 m/s, the v_g was an increasing function as the j_g increased. The centreline liquid velocity might increase with increasing the j_g and hence the liquid could lift up the bubbles at the same liquid velocity to hit the probe. Similar findings have been reported by many authors, such as Clift *et al.* (2005) and Jamialahmadi and Muller-Steinhagen (1993). Here the bubbles in the tap water are likely larger than the bubbles in the aqueous alcohol solutions and hence rose more quickly.

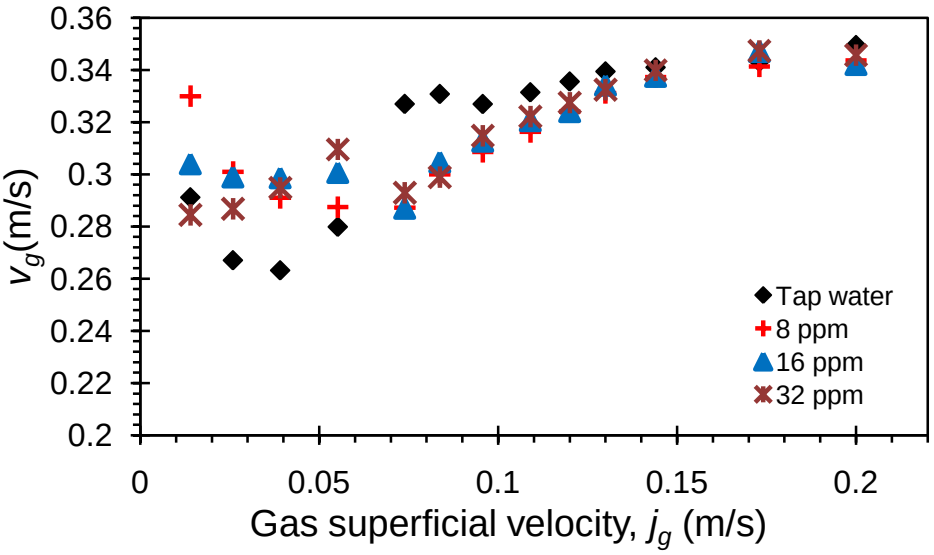


Figure 4.25 Mean bubble velocity with respect to j_g; low ethanol concentrations compared to tap water.

Figure 4.26 provides a comparison of the mean bubble velocity, v_g, in the tap water and the high concentration aqueous solution including 300 ppm IPA. The ethanol concentrations of 75, 150 and 300 ppm, showed a similar trend as the low concentration ethanol discussed in Figure 4.25. For j_g < 0.084 m/s, IPA (300 ppm) also showed a similar trend, but beyond this point, the increase in j_g seemed to have little effect on v_g.

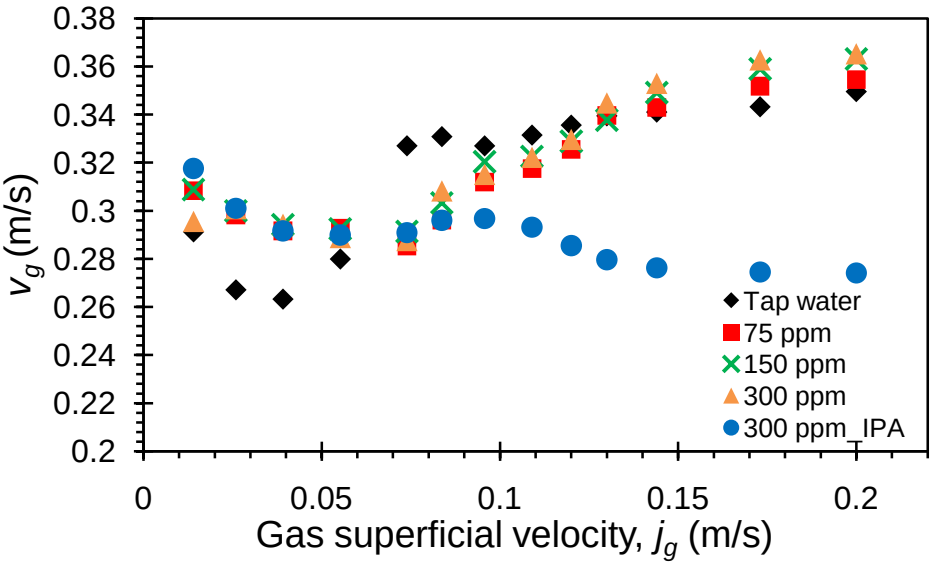


Figure 4.26 A comparison of the mean bubble velocities of 300 ppm IPA, assorted ethanol concentrations and tap water.

4.7.3 The Sauter mean diameter, d_{32},in the OTBC

Starting from an assumed bubble size characterised by a lognormal function with mean, μ, and standard deviation, σ, a forward transformation was used to obtain a predicted chord length distribution. The predictive values were then compared to the measured chord length distribution to form an objective function to be minimised by variation of μ and σ. An optimisation process was used as a backward transformation to minimise the sum of the squared differences between the predicted and the measured chord length distribution. When the optimisation had converged, the equivalent diameter, d_e, was calculated using Equation (3.28) where the Sauter mean diameter, d_{32}, could be found using Equation (3.36), (see §3.4.11). Figure 4.27 shows the profiles of d_{32} for different j_g, obtained by converting the local measured chord length using the transformation method for the air-tap water system. The profiles were plotted with respect to the distance from the wall, *y*, across a diameter of the OTBC. Due to difficulties in deducing the effect of the j_g on the bubble size, a cross-sectional average of each profile for each j_g was proposed.

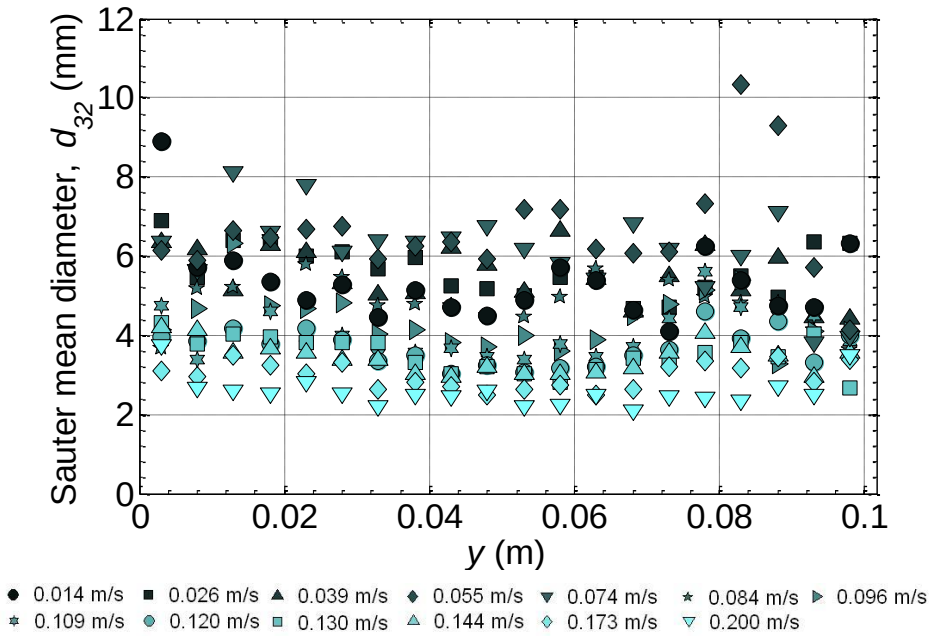


Figure 4.27 Sauter mean diameter profiles for various j_g with respect to the distance (y) across the column; data obtained from tap water experiments.

The transformation process seemed to yield physically sensible mean bubble sizes, which followed a similar trend to the mean chord lengths presented in Figure 4.22. The d_{32} for the low alcohol concentrations and tap water with respect

to the j_g are illustrated in Figure 4.28. Over the whole range of d_{32}, the tap water gave larger d_{32} values compared to the aqueous solutions. For tap water, as the j_g increased, the Sauter mean diameter, d_{32}, first remained approximately constant for j_g< 0.039m/s, then increased and finally decreased. At high j_g, turbulent flow is likely to occur and hence the breakage rate will increase, which would decrease the bubble size from 6 to 3 mm. This trend agrees well with the findings reported by Wongsuchoto *et al.* (2003) and Miyahara and Hayashino (1995). The lowest ethanol concentrations, 8 and 16 ppm, showed the same trend as the tap water, but only with small bubble sizes. For j_g <0.084 m/s, and with an increase function in the ethanol concentration (32 ppm), the bubble size increased from 5 to 2.8 mm as the j_g increased. This increase, at low j_g, could be due to an increase in the coalescence rate in the homogeneous regime. It was noticed that the transition point in the bubble size for tap water, and for 8 and 16 ppm ethanol was at $(j_g)_{trans}$=0.055 m/s. However, $(j_g)_{trans}$ increased when the ethanol concentration increased to become about 0.084 m/s.

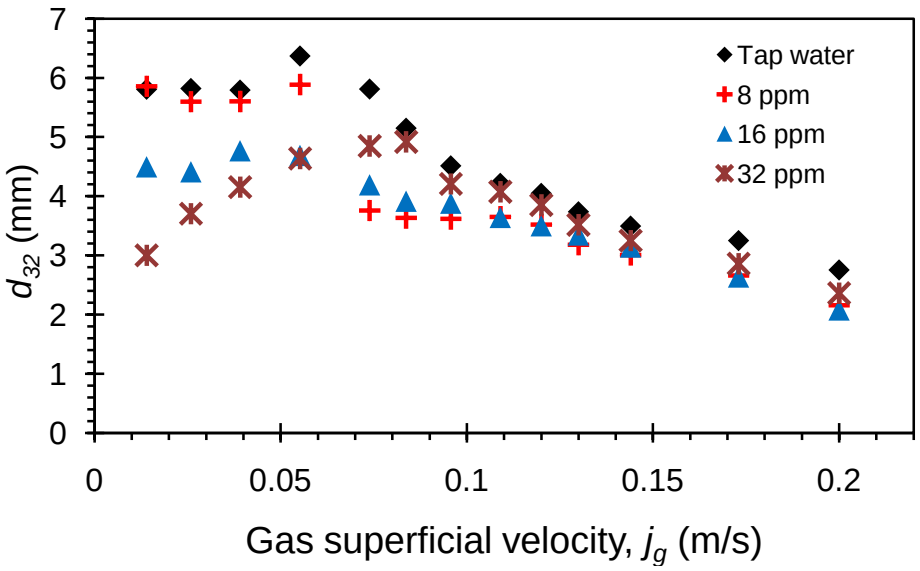


Figure 4.28 Predicted Sauter mean diameter at various j_g for tap water and low ethanol concentrations.

Figure 4.29 shows a comparison between assorted concentrations of ethanol, IPA and tap water. In general, as the concentration of alcohol increased, the bubble size decreased, because the presence of alcohol could inhibit the coalescence of the bubbles. The trend in terms of bubble size in the solution with

a high ethanol concentration was similar to that in the 32 ppm ethanol concentration previously discussed. The bubble size in the 300 ppm IPA solution was small; about 1 to 4 mm, compared to the tap water and various ethanol concentrations. As stated earlier, the hypothesis is that IPA solution has a steeper surface tension gradient with respect to concentration than the ethanol solution, and hence the effect on d_{32} is more significant.

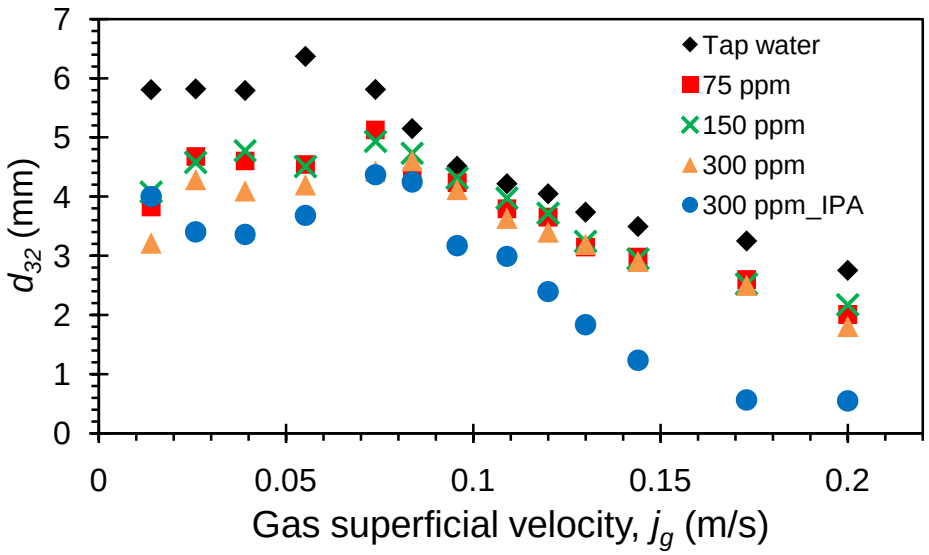


Figure 4.29 Predicted Sauter mean diameter with respect to j_g: high alcohol concentrations compared to tap water.

Figure 4.30 illustrates the d_{32} at the wall of the column obtained by the transformation process compared to the d_{32} measured by the image technique; this is discussed in §3.3. Two types of liquid were considered in this comparison: tap water and an ethanol solution of 75 ppm. Both techniques produced the same trends in d_{32}: an increased function at low j_g and a reduction as j_g increased. It should be emphasised that the image technique considered only those bubbles close to the wall to calculate the d_{32}, so for the conductivity probe technique, the d_{32} at the wall of the column should considered in the comparison. The image technique validates the transformation method as the d_{32} produced from the transformation method is in good agreement with the image method. The image results confirmed that even a relatively small amount of the ethanol alcohol solution (75 ppm) produced smaller bubbles compared to tap water.

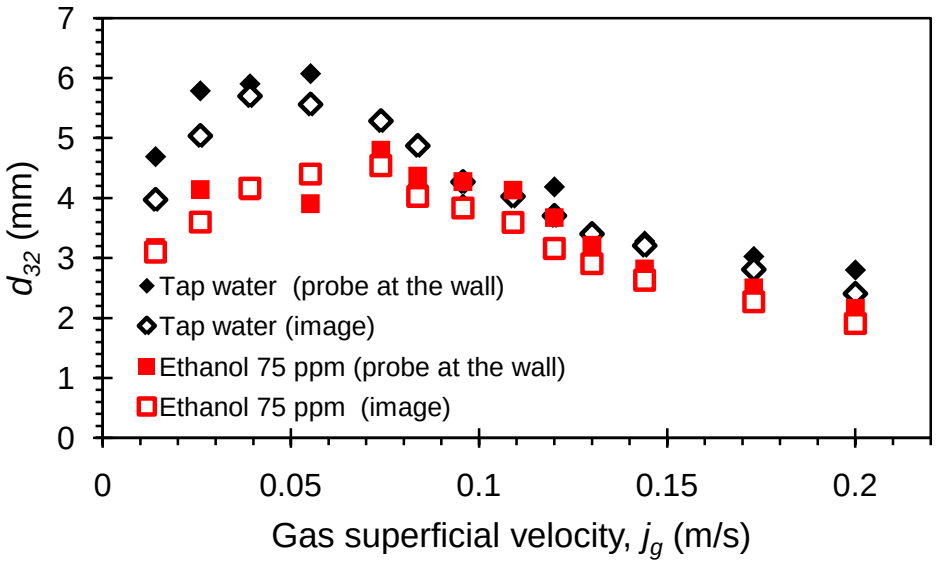


Figure 4.30 A comparison of the Sauter mean diameter obtained from the conductivity probe and the image methods.

4.7.4 The volume average mean diameter, d_{43}, in the OTBC

The volume average mean diameter, d_{43}, profiles of tap water, shown in Figure 4.31, were obtained from the transformation process and using Equation (3.37) (see §3.4.11). It is difficult to calculate the effect of j_g on d_{43} from the profiles and therefore it was proposed to cross-sectionally average the profiles across a diameter of the OTBC.

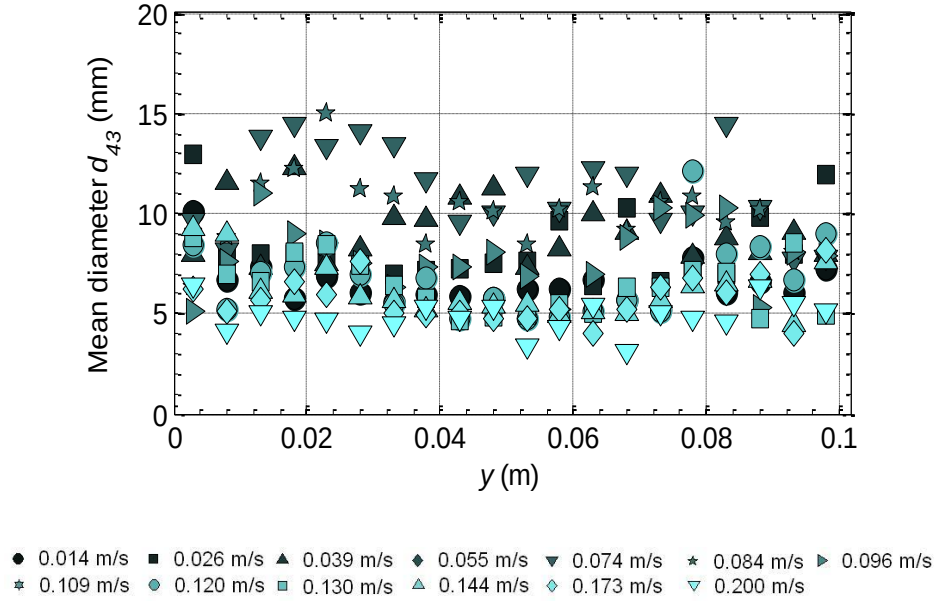


Figure 4.31 The mean diameter profiles with respect to the distance, y, across a diameter of the OTBC, obtained from the transformation process for tap water system.

The mean bubble diameter, d_{43}, of tap water is compared to that at low ethanol concentration in Figure 4.32, and to the assorted high alcohol concentrations in Figure 4.33. The d_{43} of tap water with respect to j_g can be categorised into two trends: an increasing function for j_g<0.074 m/s and a decreasing function beyond this point. Tap water offered larger d_{43} values compared to the aqueous solutions; bubble coalescence might be inhibited by the addition of alcohol. Figure 4.33 shows that the alcohol chain length led to small sized bubbles, while the IPA 300 ppm offered small d_{43} compared to the same concentration of ethanol, particularly at high j_g.

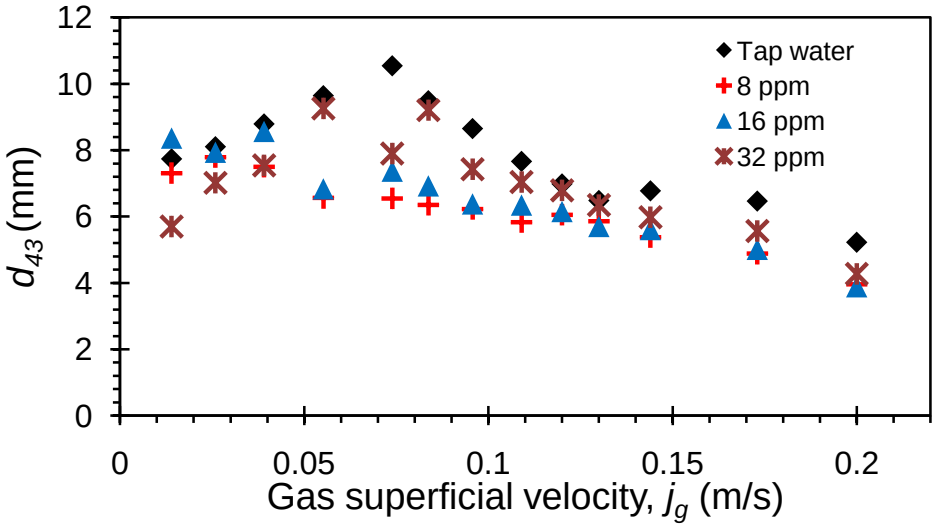


Figure 4.32 The mean bubble diameter, d_{43}, as a function of j_g; tap water compared to the assorted low ethanol concentrations.

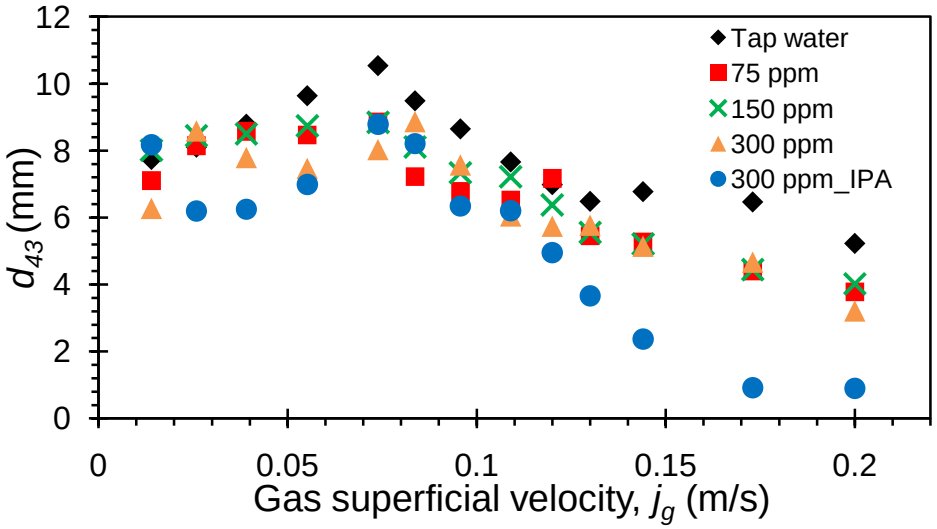


Figure 4.33 The mean bubble diameter of various high alcohol concentrations compared to tap water.

Figure 4.34 illustrates a comparison between conductivity probe and image methods. The data validate the transformation process as the image method gave a similar d_{43} trend as the probe method. However, the image method provided small d_{43} compared to the probe method. As stated before, this could be because of the limitations of the image method. Figure 4.34 also verifies that the bubble size in the ethanol solution (75 ppm) was smaller than in tap water, even when a relatively small amount of alcohol was added to tap water.

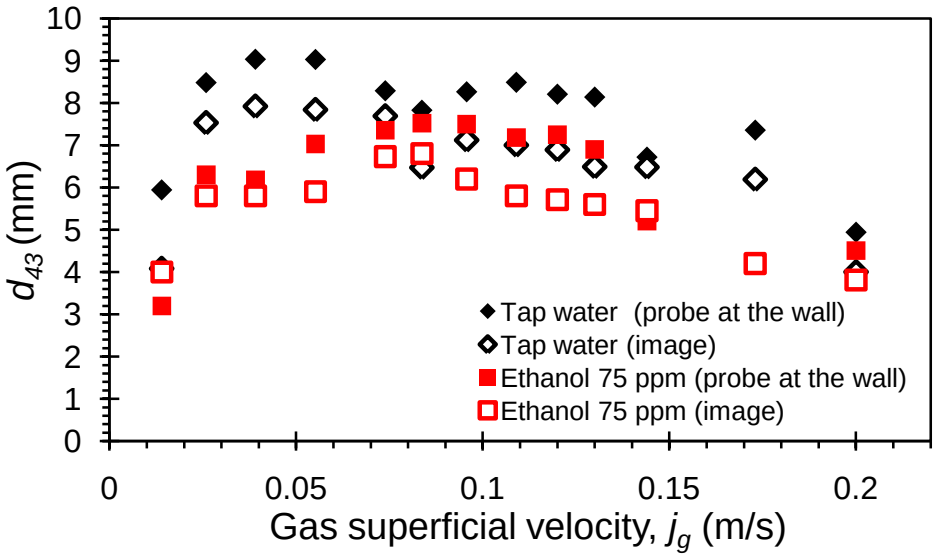


Figure 4.34 Relationship between the mean bubble diameter, d_{43}, and j_g: a comparison between conductivity probe and image techniques.

4.7.5 The standard deviation of the lognormal bubble size distribution

The standard deviation, σ, of the lognormal bubble size distribution gives an indication of the distribution of the bubble size around the mean. A low σ indicates a narrow bubble size distribution, whereas high σ indicates that the bubble sizes are spread out over a large range of values. In other words, σ is the standard deviation of the log of the bubble size, small changes in σ result in quite a large change in the spread of bubble size. It is quite important to consider the σ of the bubble size in this study, as the mean bubble size is insufficient to characterise the real bubble size distribution.

Figure 4.35 shows the profiles of the local lognormal standard deviation, σ, with distance across a diameter of the OTBC. The σ profiles presented in Figure 4.35

are for the bubble sizes in tap water. The range of σ is between 0.3 to 1.2 over all the studied levels of j_g due to the upper and lower bounds for the optimisation method. At low j_g (< 0.055 m/s), tap water seemed to provide a broader distribution due to coalescence of some bubbles, i.e. the flow contains both large and small bubbles. The effect of increasing the j_g is unclear in Figure 4.35, so averaging the profiles across the column was proposed.

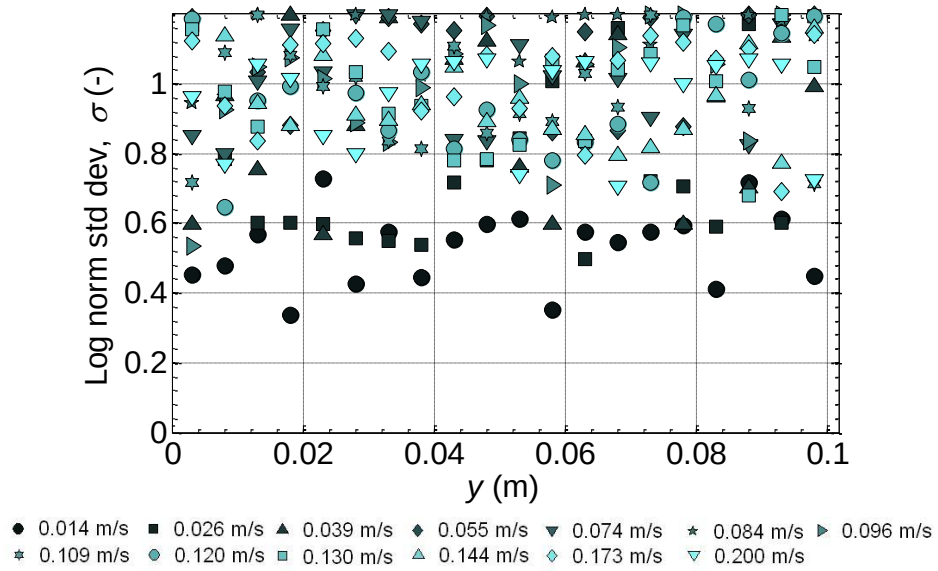


Figure 4.35 Profiles of the local lognormal standard deviation with the distance from the wall, y, across a diameter of the OTBC.

Figure 4.36 represents the relationship between the cross-sectionally mean σ and the j_g for the low ethanol concentrations compared to tap water. As stated previously, for j_g < 0.055 m/s, the σ of tap water was small compared to the ethanol solutions, verifying that the relatively small amount of alcohol concentration produces small bubbles, and results in a narrow bubble size distribution. At high j_g (> 0.055), the range of σ became similar, between 0.8 to 1.1, for both solutions.

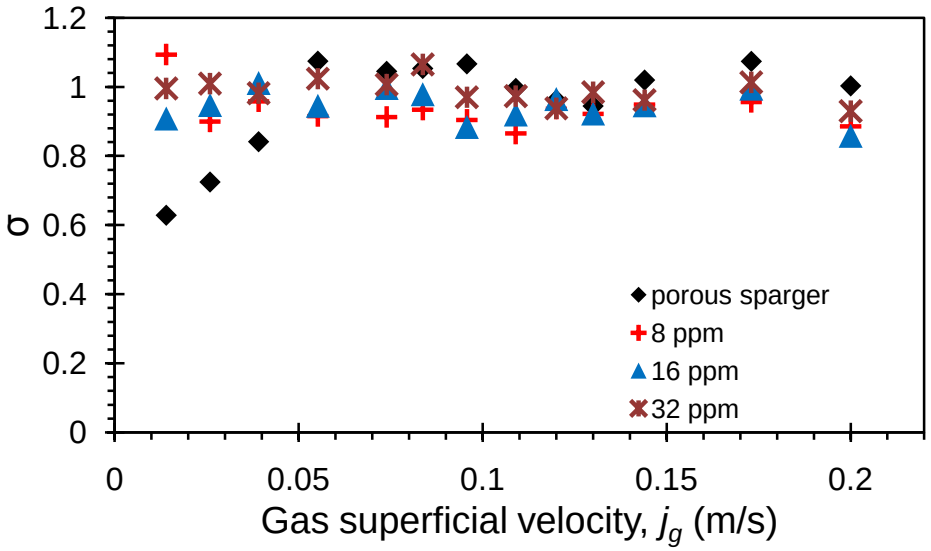


Figure 4.36 Lognormal standard deviation with respect to j_g: tap water (labelled as porous sparger) compared to the solution with low ethanol concentration.

Figure 4.37 illustrates σ for high alcohol concentrations (ethanol at 75 to 300 ppm and IPA at 300 ppm) and tap water with respect to j_g. The bubble size distribution of the high ethanol concentrations and IPA (300 ppm), for j_g < 0.12 m/s, was broader with increasing j_g compared to tap water. However, for j_g > 0.12 m/s, the alcohol solutions and tap water provided a broader bubble size distribution. The bubble breakup and inhibition of bubble coalescence at high j_g are likely responsible for the high σ values.

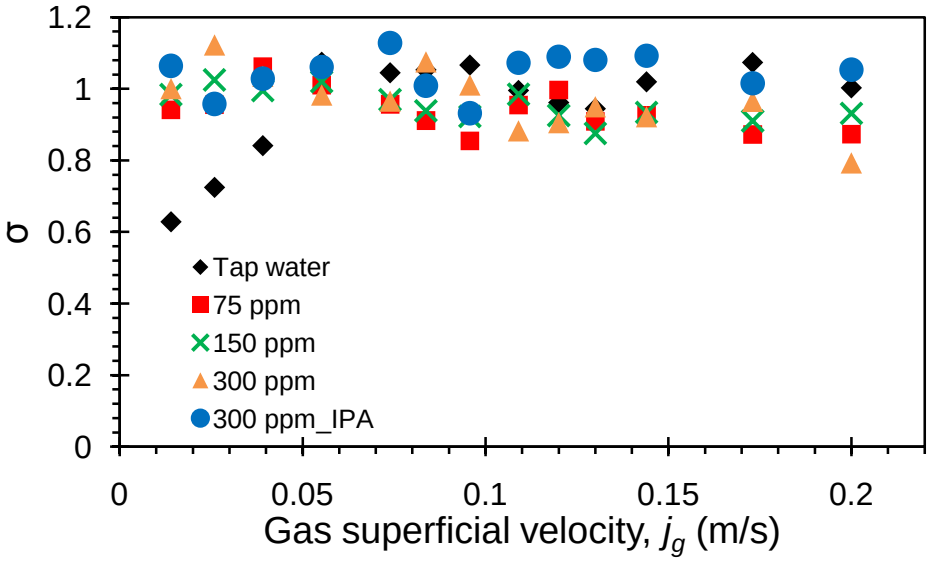


Figure 4.37 Relationship between lognormal standard deviation and the gas superficial velocity: a comparison between tap water and assorted high alcohol concentrations.

Figure 4.38 shows a comparison of the σ data between the conductivity probe and image methods. The σ data are presented with respect to the increase in j_g, where two sets of data are considered, tap water and the ethanol (75 ppm) solution. The image method confirms that the addition of alcohol narrows the bubble size distribution. Looking at the tap water and ethanol (75 ppm) solution data in both methods, the image method gave higher σ values compared to the conductivity probe method. The presence of relatively large and small bubbles (< 1 mm) across the column width might be responsible for the broader bubble size distribution. The image method might include the whole range of bubbles, whereas the conductivity probe method, due to the probe design, considers the bubbles at > 1 mm in the calculations. The ethanol solution (75 ppm) shows contradictory results as the conductivity probe method provided broader bubble size distribution compared to the image method. Two reasons might be responsible for the narrow bubble size distribution in the image method: (i) only the bubbles close to the wall were considered and (ii) the presence of the ethanol inhibited the bubble coalescence, where the relatively small bubbles were observed at the wall.

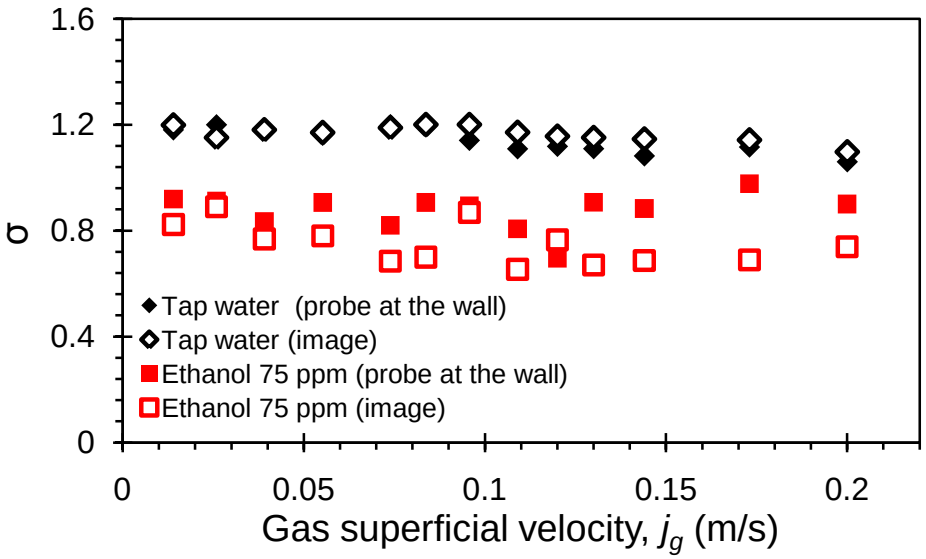


Figure 4.38 The lognormal standard deviation obtained from the image method compared to the conductivity probe method.

4.8 Conclusion

Two measurement methods were implemented in an OTBC to obtain mean α: (i) changing aerated levels and (ii) the conductivity probe method. The two-point conductivity probe underestimated the mean α data by 25% compared to the changing aerated level method. This discrepancy was discussed, and attributed to: (i) the down-flowing bubbles missing the down-facing needle probe; and (ii) probes underestimating the chord lengths of bubbles that were pierced eccentrically from their centre, which would also lead to underestimations of α. A four-point conductivity probe gave more promising data by reducing the difference in the mean value α compared to the changing aerated level method to only 12%. However, useful information was provided by both conductivity probes about α profiles within the column.

Measurements of local void fractions in an OTBC showed that the profiles changed shape with increasing gas superficial velocity, particularly in the homogeneous and early transition regimes. The changing shapes of the profiles were analysed by fitting Hibiki and Ishii's (2002) radial distribution to the data, demonstrating that these effects would alter the value of distribution parameter C_0 in the homogeneous regime. With the alcohol solutions, there were similar changes to the void fraction profiles and very large centre-line values could be obtained without significant bubble coalescence. Mean void fractions were up to 150% of tap water values with low concentrations of ethanol or IPA and even the smallest addition of 8 ppm ethanol produced a noticeable effect on coalescence. IPA had a stronger effect on the two-phase hydrodynamics in the OTBC, because of its greater carbon chain length than ethanol. Transition point void fractions and gas superficial velocities were obtained, which demonstrated that the OTBC homogeneous flow regime could be significantly extended with small additions of ethanol or IPA; the transition was delayed until the void fraction exceeded $\alpha > 0.6$ in the highest alcohol concentrations.

The chord length results showed the $(j_g)_{trans}$ values for tap water, which were similar to the values those were obtained using the Wallis plot method. The presence of alcohol seemed to generate small bubbles, which keep the

homogeneous flow more stable, and this agreed well with the findings from the Wallis plot method. In general, the chord length values of both tap water and alcohol solutions were divided into trends with respect to increasing j_g: (i) at low j_g, an increasing function was seen; and (ii) with further increasing in j_g, a reduction in the chord length was observed.

The transformation process was found to be capable of calculating the bubble size distribution from the measured chord length distribution; the bubble sizes followed similar trends to the chord lengths. The image method also validated the transformation process by providing similar bubble sizes and trends. The bubble size results from both methods confirmed that the addition of alcohol would decrease the diameter of bubbles.

CHAPTER FIVE

DESTABILISATION OF HOMOGENEOUS FLOW BY INTRODUCTION OF LARGE BUBBLES

5.1 Introduction

The previous chapter investigated an OTBC, in terms of gas void fraction, α, bubble size and velocity, when operated in tap water and various aqueous alcohol solutions. Referring to the motivation of the study in § 1.3, the first mechanism by which the mean gas void fraction might be lowered in an annular gap bubble column (AGBC) will be investigated in Chapter 6; namely, that the formation of large bubbles destabilises the flow, and forces an early transition to the heterogeneous regime. Chapter 5 studies the effect of the presence of large bubbles on the stability of a homogeneous flow, and investigates the distribution and mean of α, the bubble size and velocity in an open tube bubble column equipped with an orifice (OTBCEO).

5.2 Experimental setup and design

The purpose of the current experiments was to investigate the effect of large bubbles on the stability of a homogeneous bubbly flow. Larger bubbles were deliberately introduced into the flow through a single orifice drilled in the centre of a porous sparger (see Figure 5.1). The diameter and thickness of the sintered plastic sparger were 0.102 and 0.004 m, respectively. The OTBC was used for this set of experiments and the rig setup is presented in §4.2. Various orifice diameters, 0.4, 0.6, 0.8, 1.6, 2.0, 2.4 and 3.0 mm, were investigated; each generated a stream of large bubbles, which rose rapidly through the dispersion of more uniformly sized bubbles produced by the surrounding porous plate sparger. The OTBCEO rig setup, the procedure and conditions were the same as for the OTBC; these are described in §4.5. The only difference was that different orifice diameters were drilled in the plastic sparger. The experiments were carried out over a similar range of j_g that would exhibit homogeneous flow as in OTBC experiments.

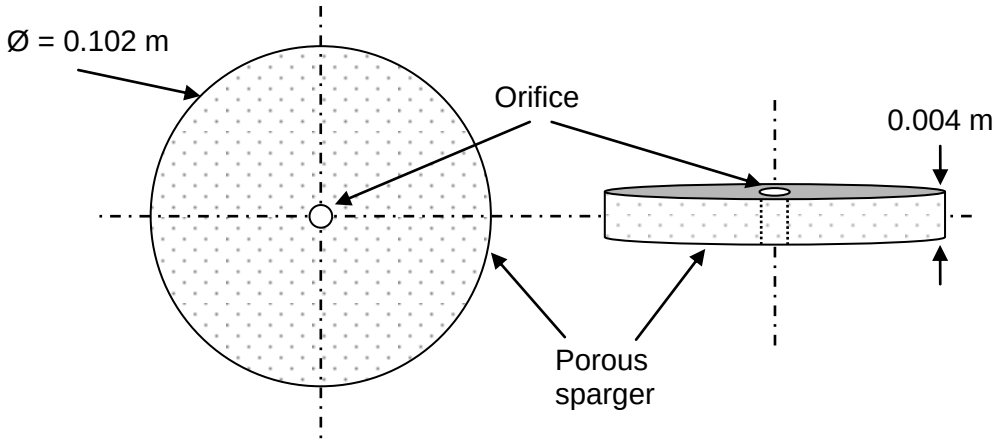


Figure 5.1 Schematic diagram of the sintered plastic sparger showing the orifice located at the centre of the sparger (not to scale).

The approach that was adopted to calculate the flow rate through the orifice for the same pressure drop across the sintered sparger is described below. The analysis describes the calculation of the permeability of the porous sparger to deduce the relationship between the pressure drop and the flow rate.

Darcy's law may be used to calculate the air flow rate through sparger, Q_s, (m^3/s)

$$Q_s = \frac{-kA_s(p_b - p_a)}{\mu_g L} \qquad 5.1$$

where the sparger permeability, k (m^2) is equal to 5.2 x 10^{-14} m^2 (see Appendix C), A_s is the area of sparger (m^2) (the sparger diameter, d_s, is similar to the column diameter, 0.102 m), p_b is the pressure above the sparger (N/m^2), p_a is the pressure below the sparger (N/m^2), μ_g is the viscosity of gas (N s/m^2) and L is the thickness of the sparger (m). The pressure, p_b, applied above the sparger is given by:

$$p_b = \rho_l g h_l \qquad 5.2$$

where ρ_l, g, and h_l are the density of water (kg/m^3), the acceleration due to gravity (m/s^2) and the height of liquid in the column (m) respectively.

The gas flow rate through an orifice can be calculated by the orifice equation:

$$Q_o = C_d A_o \sqrt{2\frac{\Delta p}{\rho_g}} \quad 5.3$$

where Q_o is the air flow rate through the orifice (m^3/s), C_d is the discharge coefficient (0.6), A_o is the orifice area (m^2), ρ_g is the air density (kg/m^3) and Δp is the pressure difference, $p_b - p_a$, (N/m^2), as in Equation (5.1).

The total gas flow rate is the sum of the sparger and orifice flow rates.

$$Q_{tot} = Q_s + Q_o \quad 5.4$$

and by rearranging Equations (5.1), (5.3) and (5.4):

$$Q_{tot} = Q_s + C_d A_o \sqrt{2\frac{Q_s \mu_g L}{A_s k \rho_g}} \quad 5.5$$

This analysis was performed to calculate the fraction of air that flows through various orifice sizes relative to the total air flow rate introduced in the column. A sample of this calculation is provided in Appendix C.

Figure 5.2 shows the fractions of air flow through the porous sparger, Q_s/Q_{tot}, as well as the pressure drops, Δp, with respect to the total air flow rate, Q_{tot} introduced to the column. The figure illustrates, using the same scale, the results using a porous sparger and relatively small orifice sizes. In the case of the porous sparger, the introduced air flows through the porous sparger as Q_s/Q_{tot}=1 over the whole range of Q_{tot} simultaneously; a high pressure drop was noticed as the air flow rate increased. In the case of the 0.4 mm orifice size at a low air flow rate, most of the air flows through the orifice due to the low pressure applied on the sparger. However, as air flow rate increases, the pressure increases as well, and then more air flows through the porous sparger. In general, as the orifice size increases, the air will flow through the orifice more than through the porous sparger and hence the pressure difference will decrease.

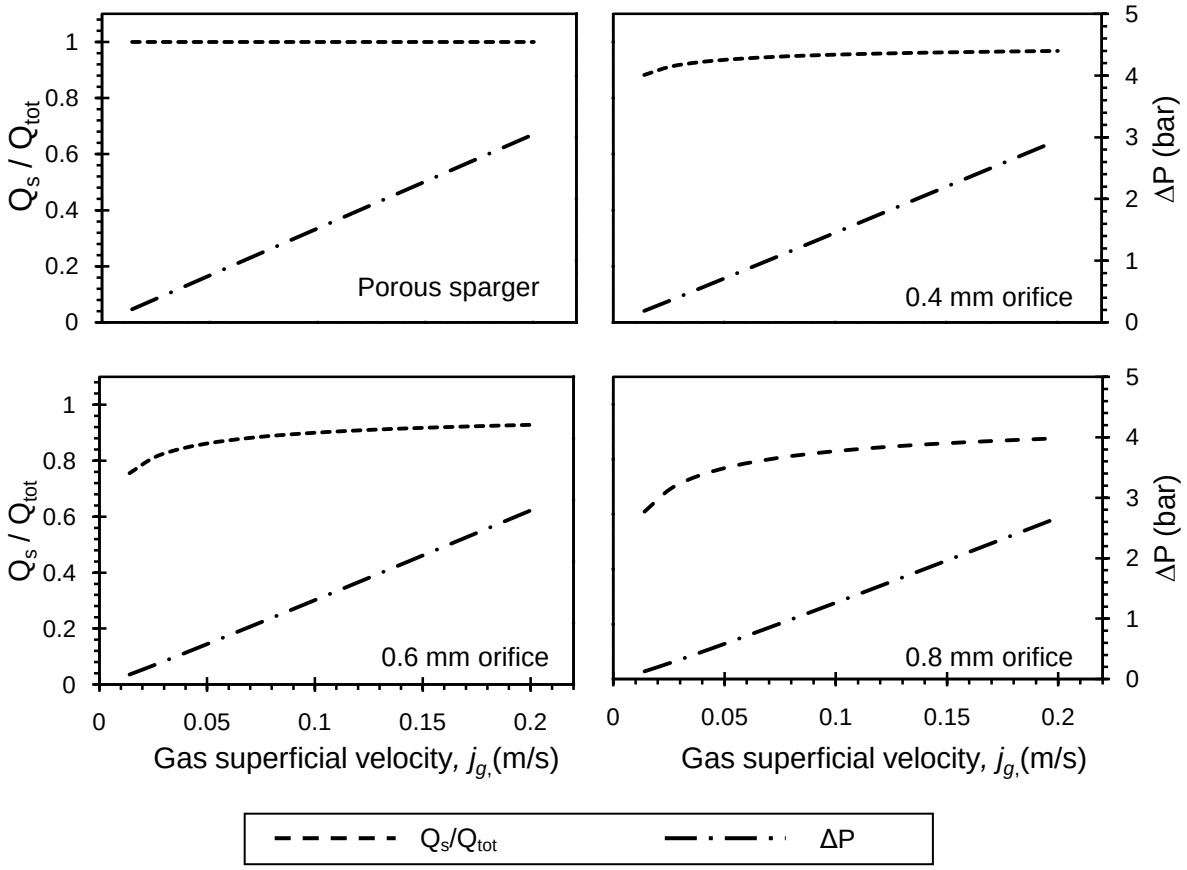


Figure 5.2 Fractions of air flow rate and pressure drops for a porous sparger and relatively small orifices.

Similarly, Figure 5.3 illustrates the effect of increasing the orifice size on the amount of air flowing through the porous sparger, and on the pressure drop at the sparger. The large orifice sizes were plotted using the same scale, confirming that the majority of inlet air is flowing through the orifices rather than through the porous sparger. The highest flow rate through the orifice was obtained using the largest orifice (3 mm), which was used in the experiments. This also gave the lowest pressure drop around the sparger.

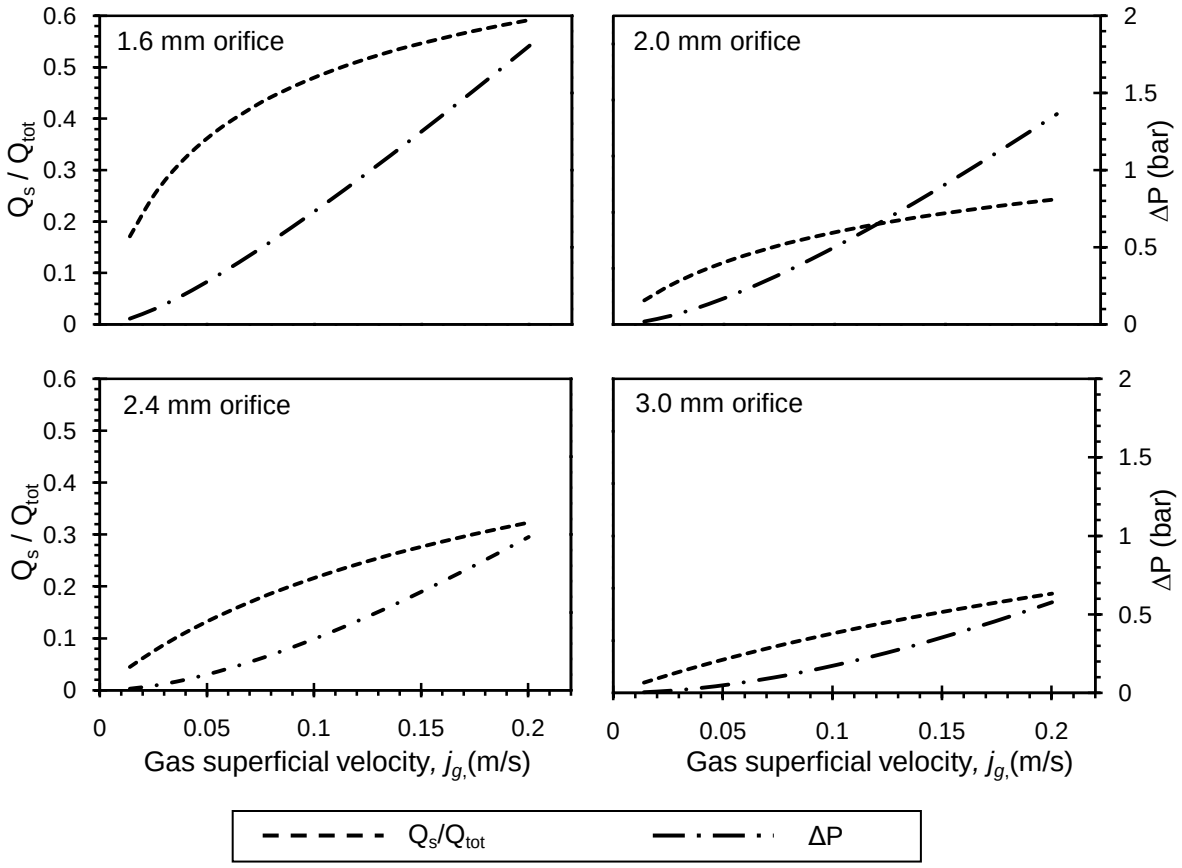


Figure 5.3 Fractions of air flow rate and pressure drops for a porous sparger and relatively large orifices.

5.3 Local gas void fraction

Measuring the void fraction profile is one of the most important methods used to investigate the distribution of the bubbles rising in the column. Void fraction profiles were obtained using two and four-point conductivity probes implemented in the OTBCEO. Electrodes were used to measure the void fraction, α, by measuring changes in the conductivity between the water and the air around the electrode tip as discussed in §3.4.

Figure 5.4 shows the radial profiles of the local gas void fraction for different orifice diameters with respect to the distance from the wall. The profiles are approximately symmetric about the centreline, y = 0.052 m, of the bubble column, justifying the use of Equation (3.9) (explained in § 3.4.8) to calculate the mean α.

$$\langle \alpha \rangle = \frac{\int_0^{R_o} 2r\alpha(r)dr}{R_0^2}$$

The void fraction profiles were fitted, using MATLAB's nonlinear least square optimisation (ffit function), to Hibiki and Ishii's (2002) power-law equation (Equation 3.11 is explained in § 3.4.8)

$$\frac{\alpha - \alpha_w}{\alpha_c - \alpha_w} = 1 - \left(\frac{r}{R_o}\right)^z$$

where the exponent, z, defines the shape of the non-dimensionalised profile and α_c and α_w are the centreline & wall void fraction respectively. Figure 5.4 shows the void fraction profiles for the porous sparger and various orifice sizes where they fitted to Hibiki and Ishii's equation. The value of α_w was obtained by extrapolating the data from both sides to the column wall. Hibiki and Ishii's equation fits very well with the void fraction profile of the porous sparger and various orifice sizes. As the z value increases, an almost flat profile would be expected, and as the z value approaches 2, a parabolic shape profile is formed. It is clear from the void fraction profiles in Figure 5.4 (e.g. for the 0.6 mm orifice) that z would be a decreasing function of gas superficial velocity in the homogeneous regime. In contrast, in the transition and in the early parts of the heterogeneous regime (j_g>0.1 m/s), z would remain almost constant at about 2. However, the local void fraction is not the same over a range of j_g, as it gives different mean void fractions.

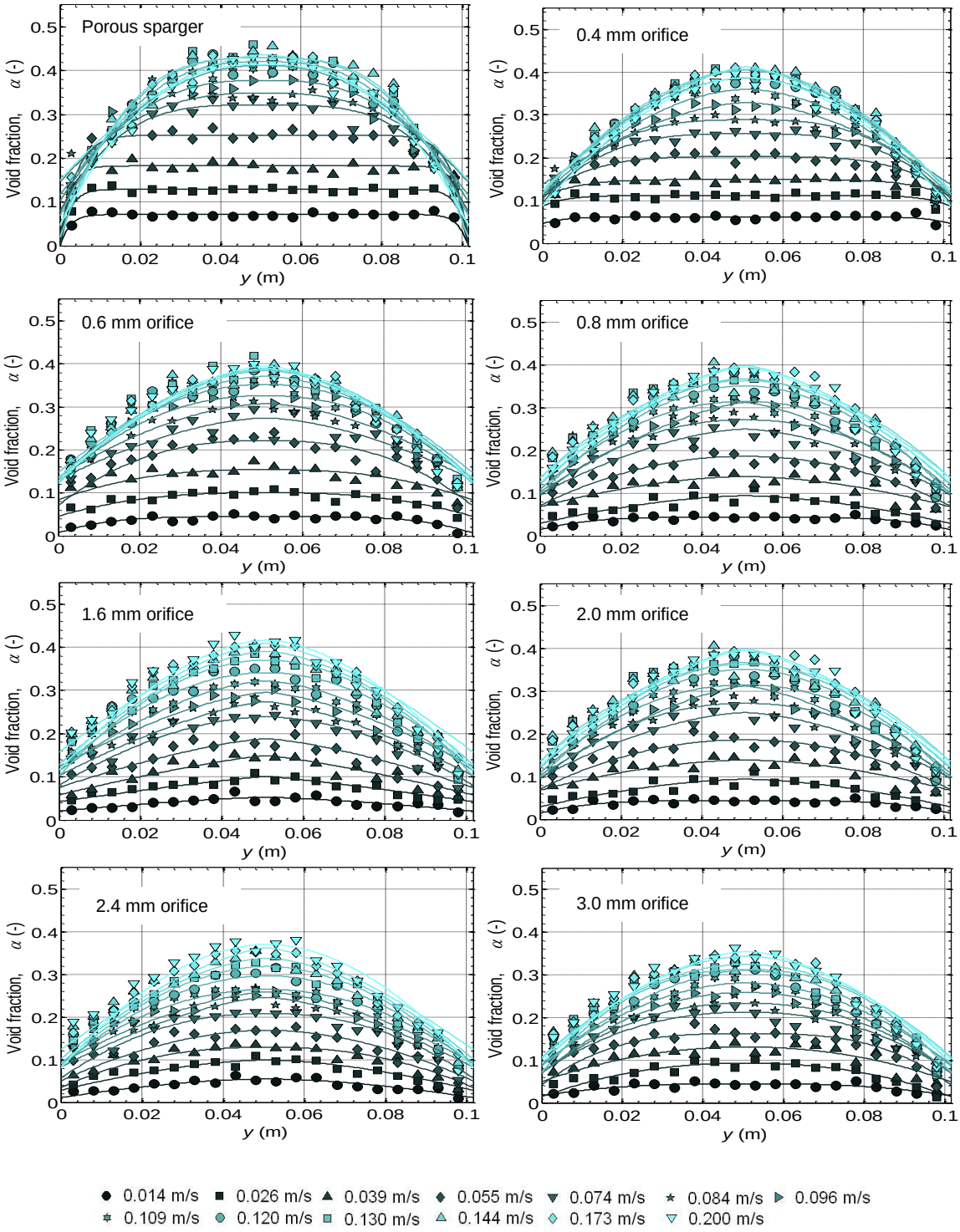


Figure 5.4 Profile of the local gas void fractions for different orifice diameters across the diameter of an open bubble column. The data were obtained using a two-point probe; the legend gives the gas superficial velocity.

At low j_g, the results show almost uniform distributions for the local void fractions across the column with the porous sparger (with no orifice) and also with the different orifice diameters. As j_g increases, the void fraction profiles become

increasingly non-uniform, and the ratio between the void fraction at the centreline of the column, α_c, to the wall void fraction, α_w, increases significantly, as shown in Figure 5.5. At low j_g, the value of the ratio α_c/α_w is about 1, which indicates that the void fraction at the centreline is almost equal to the void fraction at the wall of the column; however, this ratio increases as j_g increases. The α_c seems to increase with increasing orifice diameter, d_o, whereas α_w remains in the same range. The data presented in Figure 5.5 show that the 3 mm orifice gave high ratio, α_c/α_w, values compared to the porous sparger. As shown in Figure 5.2 and Figure 5.3, more gas flows through the orifice as d_o increases indicating that more gas flows up the centreline of the column.

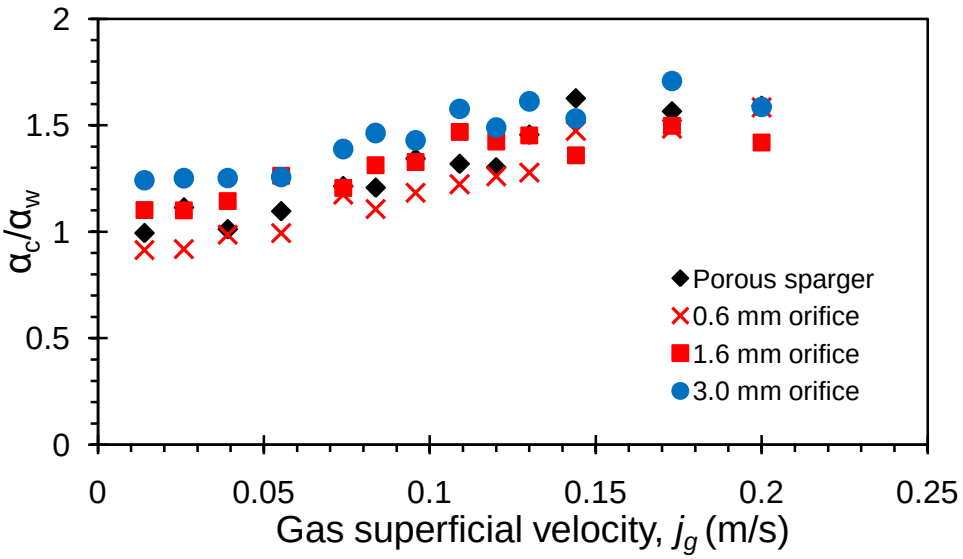


Figure 5.5 The correlation of the void at the centreline, α_c, to the wall, α_w, with respect to the range of j_g .

The values of the fitted parameter z were plotted with respect to j_g for a porous sparger and different orifice diameters; Figure 5.6 is for d_o <1mm, whereas Figure 5.7 is for d_o >1m. In Figure 5.6, for low j_g, the z values are very large because profiles are almost flat. The value of z is sensitive to errors and noise in the data in this region. As j_g increases, the exponent z seems to be decreasing towards about 2.

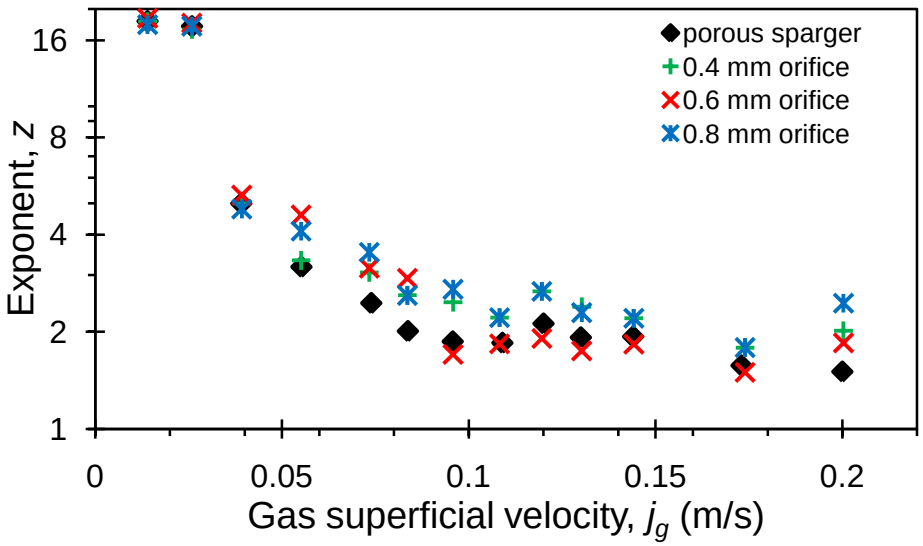


Figure 5.6 Values of the exponent *z* as a function of j_g calculated from the local gas void fraction using Hibiki and Ishii's power–law equation for a porous sparger (no orifice), and a sparger with orifice diameters < 1mm.

For the large orifice diameters illustrated in Figure 5.7, the results clearly confirm that large values of z correspond to flat profiles. Figure 5.7 shows fairly clearly that there is a stronger radial gradient in the column with large orifices.

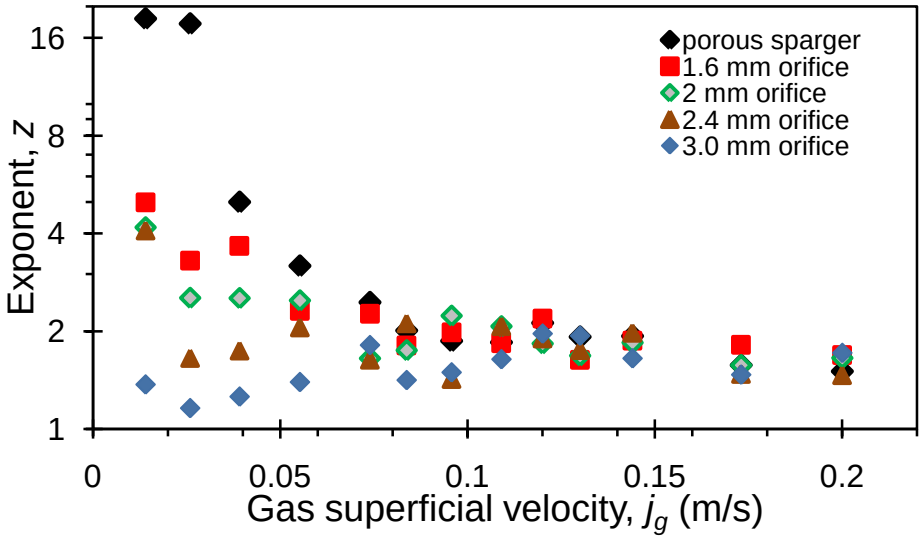


Figure 5.7 Exponent z over a range of j_g: comparison between porous sparger and large orifice diameters, d_o >1 mm.

5.4 Mean gas void fraction

Figure 5.8 presents a comparison between the mean void fraction data for the porous sparger and various orifice sizes; Figure 5.8a shows data for the small orifices, d_o < 1 mm, and Figure 5.8b is for the larger orifices, d_o > 1 mm. The presented results were obtained using the difference in the aerated level and conductivity probe methods; for the latter, mean gas void fractions correspond to a volume-averaging of the local α distributions, using Equation (3.9). As mentioned previously, Figure 5.8 shows that the conductivity probe's mean gas void fractions agree fairly well (to within 12%) with the aerated level results; certainly, qualitatively consistent behaviour is observed using both measurement methods. From the porous sparger (no orifice) experiments, it was observed that, at low j_g, small and uniform bubbles in homogeneous flow were generated; these observations are confirmed here in the results shown in Figure 5.8. The results shown in Figure 5.8a illustrate that the small orifices, d_o < 1 mm, have no significant effect on the mean gas void fraction; this was confirmed by both the aerated level and conductivity probe methods. At about $j_g \approx$ 0.10 m/s, a swarm of bubbles, rising rapidly through the column, triggered the flow into the transition regime. As j_g increased further, the coalescence rate also increased, resulting in the appearance of a mix of small and relatively large bubbles; this significantly decreased the mean α and signified the presence of heterogeneous flow. The bubble size is discussed in § 5.7.

It was observed from the orifice experiments that large bubbles start to become visible at an orifice diameter of 1.6 mm; these bubbles, with a mean chord size of 5 mm (see § 5.7), rise much faster than the smaller spherical bubbles produced by the porous plate. With increasing j_g, an increasing fraction of the gas flow is transported as large bubbles and consequently, the measured gas void fraction is reduced compared to the porous sparger. Figure 5.8b confirms that the effect of the orifice on the mean void fraction starts to take place at d_o > 1 mm. This outcome agrees well with the literature (e.g. Zuber and Hench, 1962), which suggests that the orifice size has to be greater than 1mm to generate heterogeneous flow at all levels of j_g.

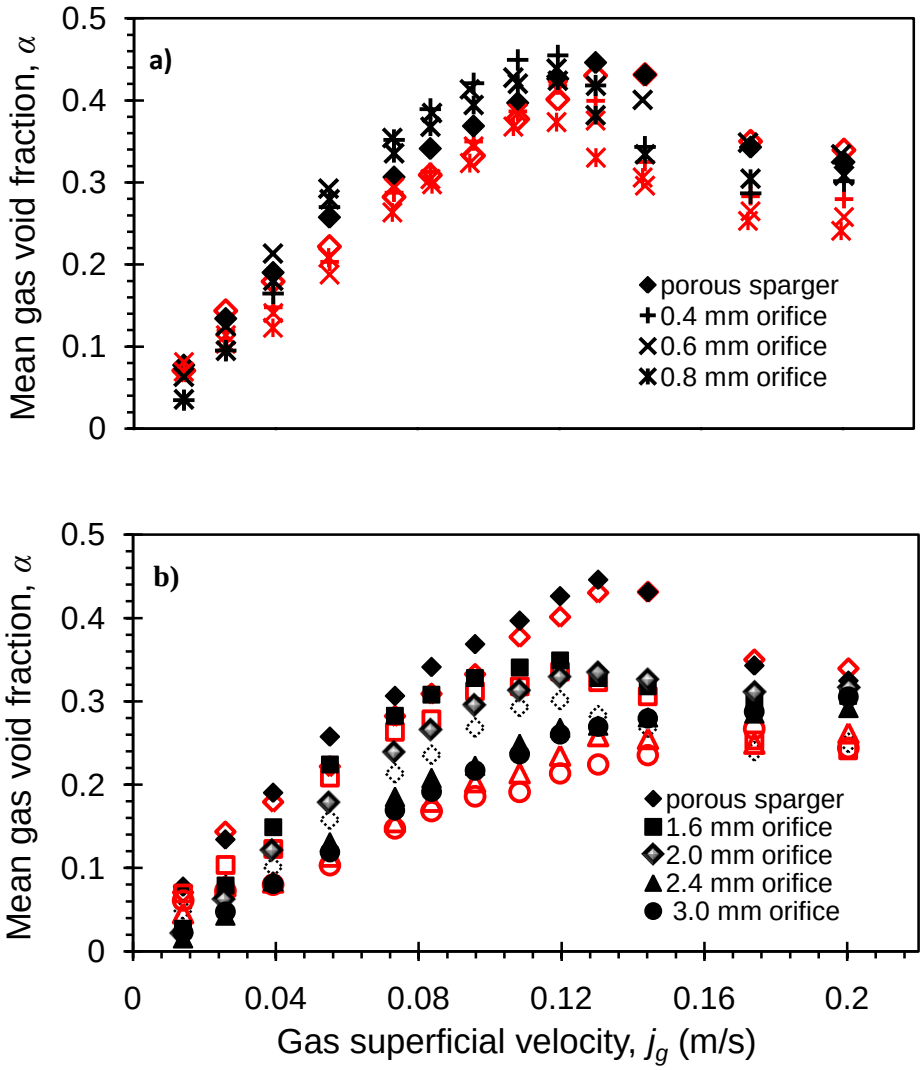


Figure 5.8 Mean void fraction variations with superficial gas velocity for the empty column equipped: with a porous sparger, with and without a single orifice of various diameters, a) d_o<1mm and b) d_o>1 mm diameter; closed symbols derive from change in the aerated level method and open symbols are a cross-sectional mean determined by the conductivity probe method (probe 1)

5.5 The distribution parameter in the OTBCEO

From the drift-flux model proposed by Zuber and Findlay (1965), (Equation 1.2),

$$\langle\alpha\rangle = \frac{j_g}{C_o\, j_g + v_t}$$

Hibiki and Ishii (2002) suggested that the value of the distribution parameter, C_o, can be obtained by plotting $j_g/\langle\alpha\rangle$ with respect to j_g, $\frac{j_g}{\langle\alpha\rangle} = C_o j_g + v_t$, where C_o is

the slope of the line and the intercept of this line with $j_g/\langle\alpha\rangle$ axis is the void-fraction-weighted mean local drift velocity, v_t.

Figure 5.9 shows an example of the technique that was suggested by Hibiki and Ishii (2002), which was used to gather the data for C_o and v_t. The data shown in Figure 5.9 are for an open tube with tap water and with a 0.8 mm orifice drilled into the porous sparger, where the mean void fraction, $\langle\alpha\rangle$, is the average of the local void fraction obtained using the conductivity probe method (p1). Only the first 7 points were considered to obtain the values of C_o and v_t, as the drift-flux model has been fitted in the flow at j_g<0.1 m/s. Figure 5.9 shows the slope value of the data, C_o =1.25 and the intercept value, v_t=0.093 m/s.

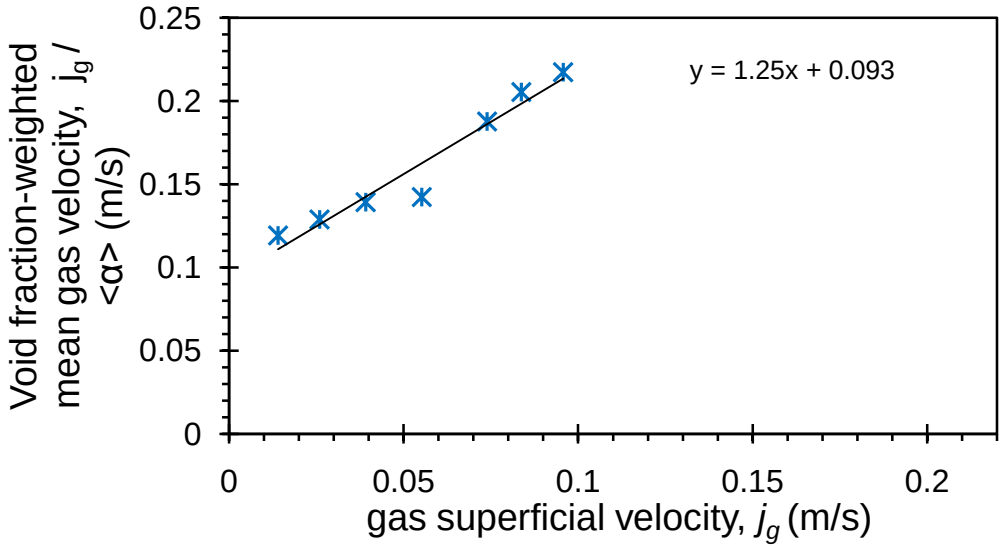


Figure 5.9 Void fraction-weighted mean gas velocity with respect to gas superficial velocity; the mean void fraction data for a porous sparger with 0.8 mm orifice in an open tube obtained using the conductivity probe method (p1).

Figure 5.10 illustrates the distribution parameter, C_o , and the rise velocity, v_t, with respect to various orifice sizes, where the porous sparger is represented by a 0 mm orifice size diameter. From the profiles represented in Figure 5.4, the void fraction decreases with the increasing the orifice size, so C_o is likely to increase above unity. As stated earlier in this study, the porous sparger, in the homogeneous regime, produces small bubbles that rise at almost the same velocity and distribute uniformly in the bed to form a flatter profile, and hence $C_o \approx 1$. The small orifices, d_o < 1 mm, have an insignificant effect on the mean

void fraction (to be discussed in § 5.4). However, both the C_o is slightly increased whereas v_t is almost unchanged. For the large orifices, d_o > 1 mm, C_o and v_t are increasing functions of the orifice size. This indicates that the orifice is able to produce large bubbles that rise quickly and accelerate the coalescence, which destabilises the homogeneity of the flow to form a heterogeneous regime.

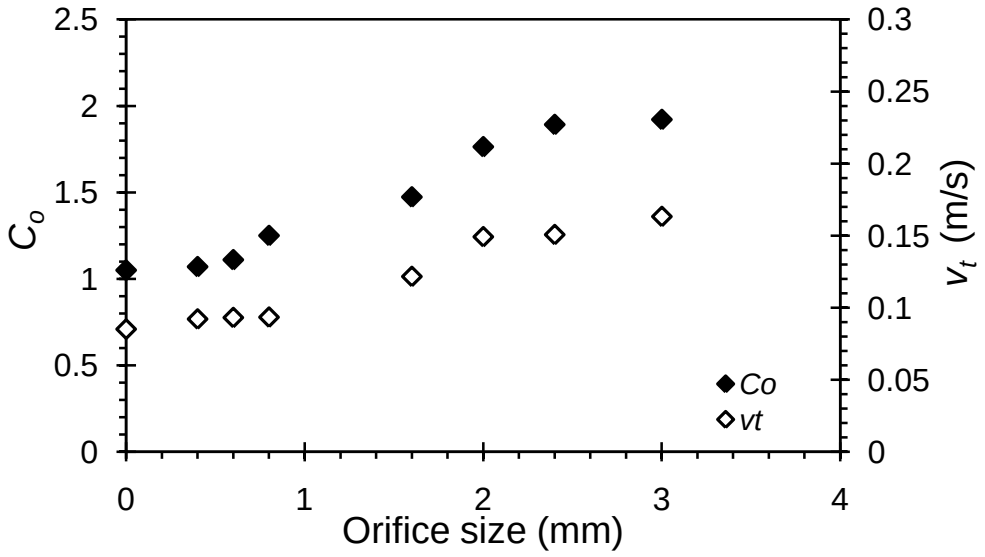


Figure 5.10 Distribution parameter, C_o, and rise velocity, v_t, values with respect to the orifice diameter, d_o; data obtained from the drift-flux model.

5.6 The effect of the presence of orifices on the transition condition

Krishna *et al.* (2000) used the Wallis plot (Wallis, 1969) to predict the regime transition point, α_{trans}, and the critical gas superficial velocity, $(j_g)_{trans}$ by using the Richardson and Zaki model (1954), shown in Equation (2.1). The point where the data deviate from the Richardson and Zaki curve is taken to indicate the regime's transition point, α_{trans}, where the critical gas superficial velocity, $(j_g)_{trans}$, can be calculated from Equation (2.1). Figure 5.11 illustrates the drift-flux velocity with respect to the mean void fraction, which was obtained by using the aerated level method. The smooth curve represents the Richardson and Zaki equation and, for air-water homogeneous flow, the values of the exponent, n, and rise velocity, v_t, were 2 and 0.24 m/s respectively, as suggested by the literature

(e.g. Krishna *et al.*, 2000). The Richardson and Zaki curve is flattened by increasing the n value and moves up as v_t increases.

Figure 5.11a and b show data for small orifices, d_o < 1 mm, and large orifices, d_o > 1 mm. When the porous plastic sparger was drilled with small orifice diameters, d_o<1mm, the bubbles produced from these small orifices were not sufficiently different from those produced by the porous sparger (data is shown in Figure 5.11); hence there was no effect on the flow stability or void fraction so a homogeneous flow was observed at low gas superficial velocity, j_g.< 0.06 m/s.

For the small orifices, d_o < 1 mm, it is difficult to distinguish between the transition points of the porous sparger and various orifices. This indicates that these orifice sizes are not sufficient to generate large bubbles, which affect the mean void fraction and deviate early from the Richardson and Zaki model. Table 5.1 summarises the regime transition point, α_{trans}, and the critical gas superficial velocity, $(j_g)_{trans}$, extracted from Figure 5.11a.

Table 5.1 The transition point for various orifice sizes, d_o < 1 mm, obtained by Richardson and Zaki model

sparger type	$(j_g)_{trans}$ (m/s)	α_{trans}
Porous sparger	0.048	0.26
d_o =0.4 mm	0.047	0.27
d_o =0.6 mm	0.049	0.29
d_o =0.8 mm	0.048	0.28

The large orifices, d_o > 1 mm, illustrated in Figure 5.11b, show clearly the effect of the presence of the large orifice on the mean void fraction. As the Richardson and Zaki model is only valid for the homogeneous flow, it is difficult to detect exactly when the transition occurs, even at low j_g. This indicates that these orifices are able to generate large bubbles, which destabilise the homogeneous flow to form a heterogeneous flow for the whole range of j_g.

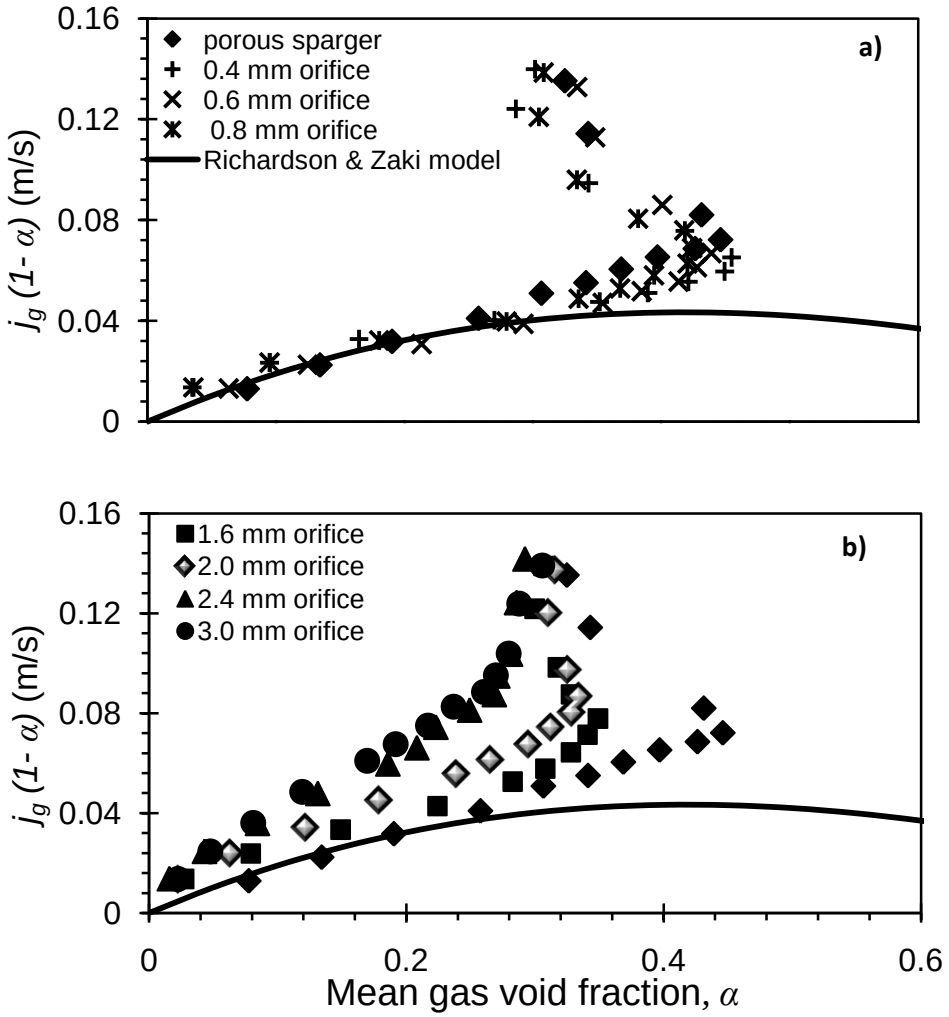


Figure 5.11 Drift-flux velocity with respect to mean *α* for a porous sparger, with and without orifice diameters: a) small orifices, d_o < 1 mm and b) large orifices, d_o> 1 mm

Zuber and Hench (1962) (see §2.2.2) carried out experiments over the same range of gas flow rates using a variety of perforated plates, as air dispersers; see Table 5.2. From their experiments, as the orifice diameter, d_o, in the gas distributor plate was increased (and the number of orifices was decreased), higher gas void fractions were generated; an initially homogeneous regime was obtained at low superficial velocities when the hole size was 0.41 mm. As is shown in Figure 5.12, larger orifices gave heterogeneous flow over a much wider range of gas superficial velocities. So, the orifice diameter plays a role in determining the gas void fraction by destabilising the homogeneous regime. Figure 5.12 shows the void fraction with respect to j_g. Since the small orifice, d_o < 1 mm, gave the same void fraction as the porous sparger, only the porous sparger and the large orifice sizes, d_o > 1 mm, were compared with the results of Zuber and Hench (1962). There is good agreement for the porous sparger (no

orifice) with Zuber and Hench's (1962) results for their perforated plate with a 0.41 mm diameter orifice. The magnitude of the reduction in the mean gas void fraction with increasing orifice size is greater in Zuber and Hench's results. This could be because they used an orifice plate, where only the air flow through the orifice generates large bubbles. However, in the current study, the orifice in the porous sparger was used where the air is split between the orifice and the porous sparger; so a mix of large and small bubbles could be generated. Nevertheless, the effects are qualitatively similar: larger orifice sizes generate large bubbles, which sweep the smaller bubbles into their wake, causing coalescence and hence an early transition to the heterogeneous regime.

Table 5.2 Gas distributor configurations used by Zuber and Hench (1962)

Orifice diameter, d_o (mm)	No. of orifices	Square array spacing (mm)
0.41	289	6.25
1.52	100	9.5
4.06	49	6.25

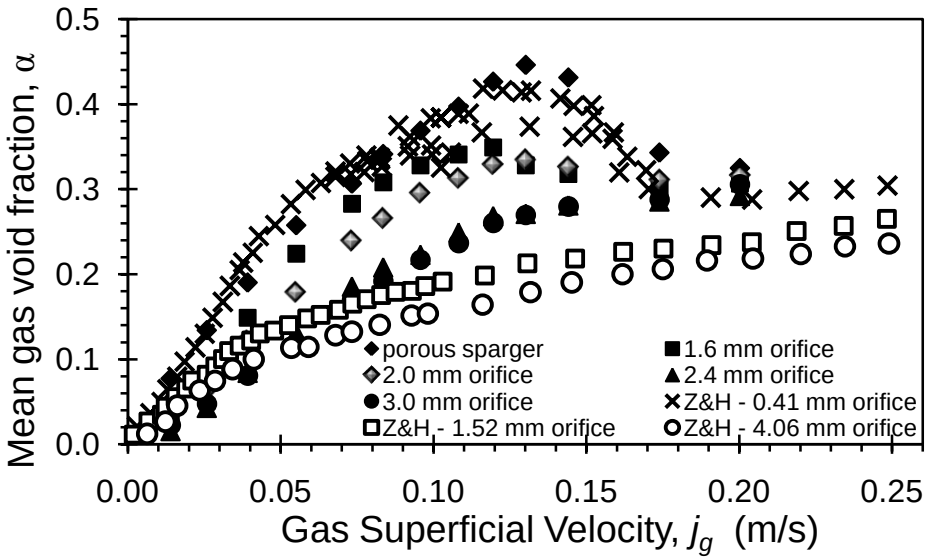


Figure 5.12 Mean gas void fractions for the porous sparger and for the same sparger with different central orifice sizes: comparisons with Zuber and Hench's (Z&H) (1962) results (see Table 5.2 for details of their perforated plate spargers)

5.7 Bubble size and velocity measurements

5.7.1 The effect of orifices on the chord length

The chord length was obtained from the conductivity probe, while the mean chord length, C, was obtained by averaging the local chord lengths across the column. Two trends can be observed from Figure 5.13 regarding the effect of increasing j_g on the bubble size: (i) an increasing function up to j_g = 0.06 m/s and (ii) a decreasing function beyond this j_g value. This follows the same general trend as Jamialahmadi and Muller-Steinhagen's (1993) findings, see §2.5.1. However, they reported that bubble sizes increased up to j_g= 0.12 m/s, and then decreased with increasing $j_g > 0.12$ m/s. The difference in position of the maximum bubble size might be a result of the sparger configurations, since they used an orifice gas distributor, whereas a porous sparger drilled with a central orifice diameter was used in this study.

Figure 5.13 illustrates the mean chord length, C, with respect to j_g for small orifice diameters and the porous sparger. The mean chord length was obtained by averaging the local chord lengths across the column. Equation 3.17 was used to calculate C, where the residence time and the bubble velocity were obtained from the two-point conductivity probe signals. In general, small orifice sizes, $d_o < 1$ mm, show a similar trend to the porous sparger. For $j_g < 0.06$ m/s, the mean chord length increased as the j_g increased for both the porous sparger and the orifices. For this range of j_g, the homogeneous regime was observed while carrying out these experiments, where only limited bubble coalescence takes place and the breakage of bubble did not occur greatly, or at least the rate of bubble coalescence was higher compared to the bubble breakage rate. For $j_g >$ 0.06 m/s, the bubble breakage rate appears to be higher compared to the coalescence rate; thus, the mean chord length decreased with increasing j_g. For each sparger configuration, Figure 5.13 shows that the largest chord size was obtained at about j_g = 0.05 m/s, which might relate to the $(j_g)_{trans}$; this was predicted by the Wallis plot method as its value was about j_g = 0.05 m/s. This

gives an indication of when the void fraction transition occurred for both the porous sparger and the small orifices.

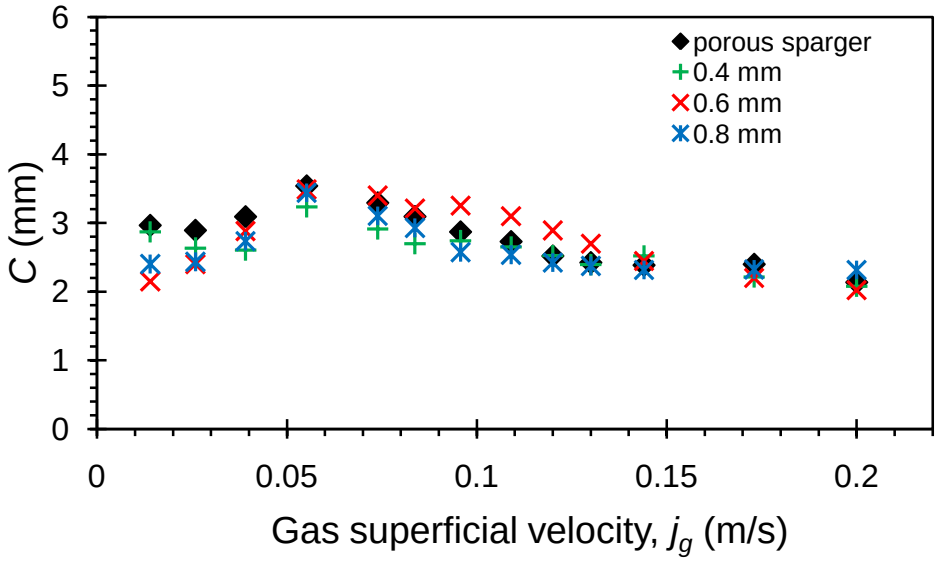


Figure 5.13 Mean chord length obtained by the conductivity probe with respect to j_g; a comparison between small orifices and a porous sparger

Figure 5.14 shows mean chord length results for the large orifice sizes, $d_o > 1$ mm, compared to the results from the porous sparger. Similar to the results for the small orifices, those for the large orifices were calculated by averaging the local chord lengths across the column; a two-point conductivity probe was also used to obtain the chord length. The effect of the large orifices on the chord length seemed to take place at low j_g as these orifices produced large bubbles (heterogeneous flow) to give $C > 4$ mm. The trend of chord length, with respect to increasing the j_g for the large orifices, seems to be different from the trend of the porous sparger for j_g >0.06 m/s. The porous sparger has a region of homogeneous flow, so an increase in C is noticed. Whereas for the heterogeneous flow region a decrease in C is observed. The bubble breakage dominates with increasing j_g, and hence the chord length decreases.

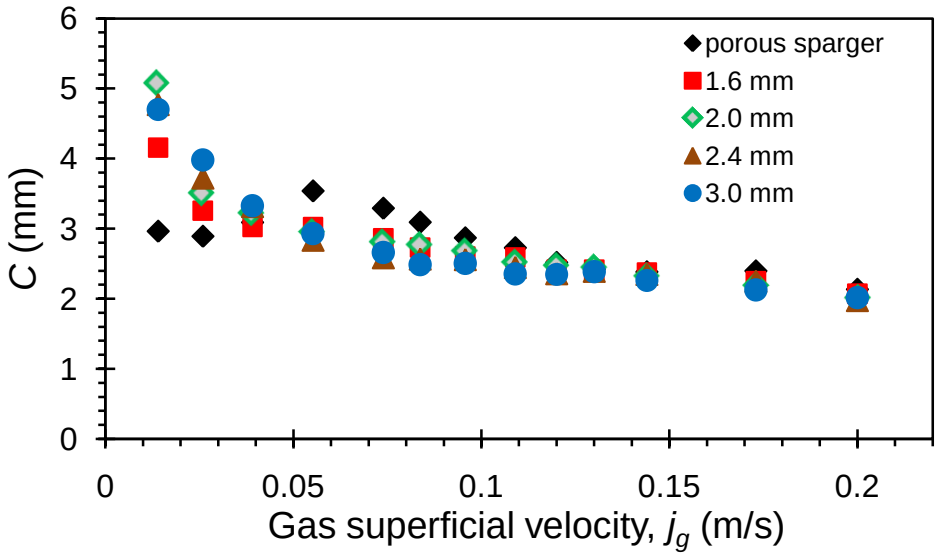


Figure 5.14 A comparison of the chord length between the porous sparger and large orifices; the results were obtained by calculating the mean of the chord length across the column at different values of j_g

5.7.2 The effect of orifices on the bubble velocity

The bubble velocity, v_g, in a liquid dispersion is one of the variables, which influences the gas phase residence time, tR, and hence the contact time for the interfacial transport. The results concerning v_g are presented and categorised as follows: (i) small orifices, $d_o < 1$ mm and (ii) large orifices, $d_o > 1$ mm. Both were compared with the results for the porous sparger.

Figure 5.15 shows values of the cross-sectionally averaged mean bubble velocity, v_g, for the two systems that were studied: the porous sparger and the small orifice, $d_o < 1$ mm. The results were obtained by averaging the local bubble velocities across the column, as these velocities were predicted by applying Equation 3.16 and by using the two-point conductivity probe to predict the bubble flying time, t_f. As can be comprehended from Figure 5.15, the small orifices give a very similar trend to the porous sparger. For $j_g < 0.04$ m/s, a reduction was noticed in the bubble velocity as the j_g increased, and beyond this point, the v_g increased as the j_g increased. The presence of large bubbles could be a reason for this, or the increase in j_g could enhance the liquid's circulation velocity and hence facilitated the bubbles rising rapidly up the column.

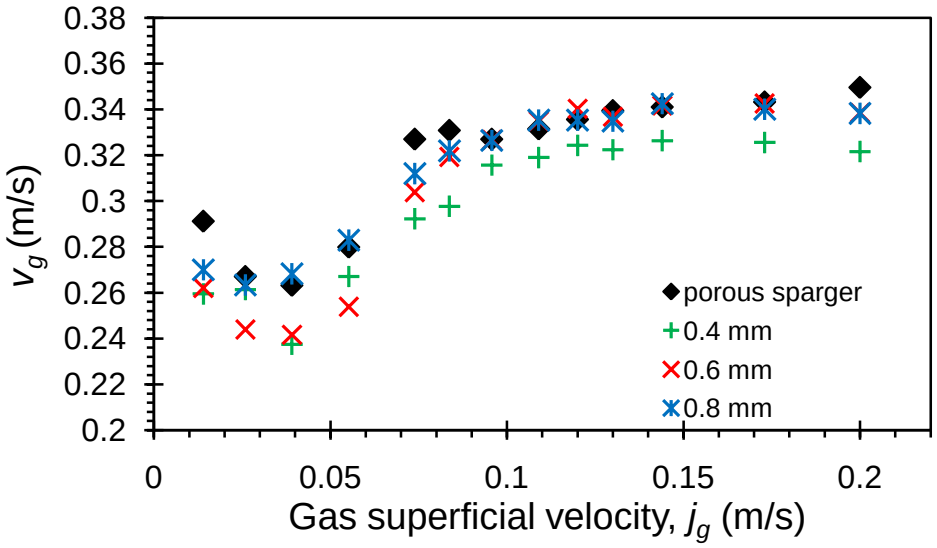


Figure 5.15 The mean bubble velocity, v_g, with respect to j_g: data for small orifices compared to data for the porous sparger as obtained using a two-point conductivity probe

A comparison of the bubble velocity is shown in Figure 5.16, where it is plotted with respect to j_g. For large orifices, $d_o \geq$ 1.6 mm; a different v_g trend to the porous sparger results has been obtained. The v_g followed a decreasing function for $j_g <$ 0.04 m/s and an increasing function for $j_g >$ 0.04 m/s. However, the range of v_g for the largest orifice size, 3 mm, was narrower, 0.322 to 0.357 m/s, compared to the porous sparger range of 0.292 to 0.350 m/s. The highest v_g value for the 3 mm orifice was 0.357 m/s at j_g= 0.014 m/s, whereas the highest v_g value for the porous sparger was 0.350 m/s at j_g= 0.200 m/s. For $j_g <$ 0.055 m/s, most of the air is likely to flow through the orifice to produce large bubbles, which rise much faster than the bubbles produced by the porous sparger as discussed in §5.2. For j_g = 0.074 m/s onwards, the flow becomes increasingly turbulent and bubble breakage rate increases for both spargers.

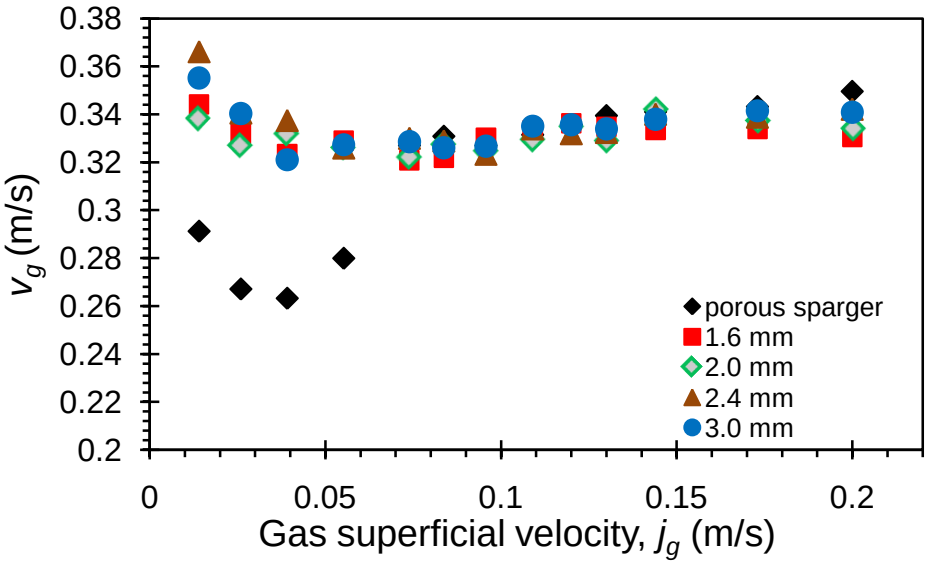


Figure 5.16 Mean bubble velocity results using large orifices with respect to j_g

5.7.3 The effect of orifices on the Sauter mean diameter

The following results for the Sauter mean diameter, d_{32}, and mean diameter, d_{43}, were obtained by the transformation model that was proposed to convert chord length to bubble size. The model was discussed in §3.4.11. Figure 5.17a and b illustrate a comparison of d_{32} for all the studied orifice sizes with those for the porous sparger. The probe's results were obtained by averaging the local d_{32} values across the column, where the local value was calculated using Equation 3.36. The small orifices with $d_o < 1$ mm, as shown in Figure 5.17a, exhibited a similar trend to the results from the porous sparger. For all the considered sparger conditions, at j_g=0.014 m/s, the average bubble size was about 4 mm. For $j_g < 0.055$ m/s, an increase was noticed in the d_{32} size for all conditions with increasing values of j_g. The increasing rate percentages were about 24, 23 and 28 % in the porous sparger, with orifices of 0.4, 0.6 and 0.8 mm respectively. On the other hand, beyond this point, d_{32} became a decreasing function as the j_g increased, with the decreasing percentages being between 50 to 60%. The large orifices, $d_o > 1$ mm, are compared to the porous sparger in Figure 5.17b. In this case, d_{32} for the large orifices decreased as j_g increased. The largest bubble size was noted, using the probe and image methods, for the sparger with a 3 mm orifice at the lowest j_g=0.014 m/s.

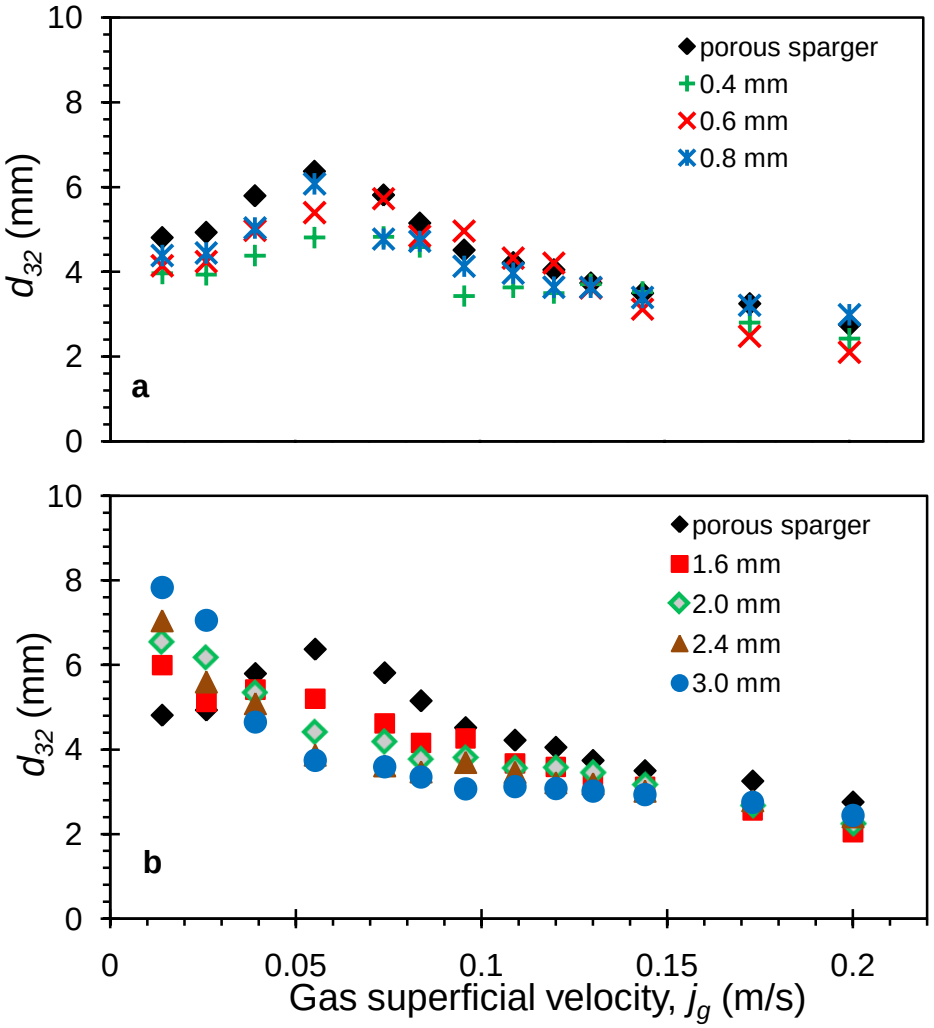


Figure 5.17 Sauter mean diameter obtained using the optimisation model with respect to j_g: the porous sparger compared to a) small orifices, d_o <1 mm and b) large orifices, d_o >1 mm.

In general, the model output confirmed the chord length results that were predicted by the two-point conductivity probe. Further confirmation was obtained for the d_o=3.0 mm orifice using image analysis of photographs at the walls. Figure 5.18 shows the d_{32} data obtained from the image analysis and the conductivity probe at the wall. The image data were calculated by counting between 250 to 300 bubbles per picture and using Equation 3.36. The results for the 3 mm orifice, which were obtained by the image method were in good agreement with those for the 3 mm orifice obtained using the probe method at the wall.

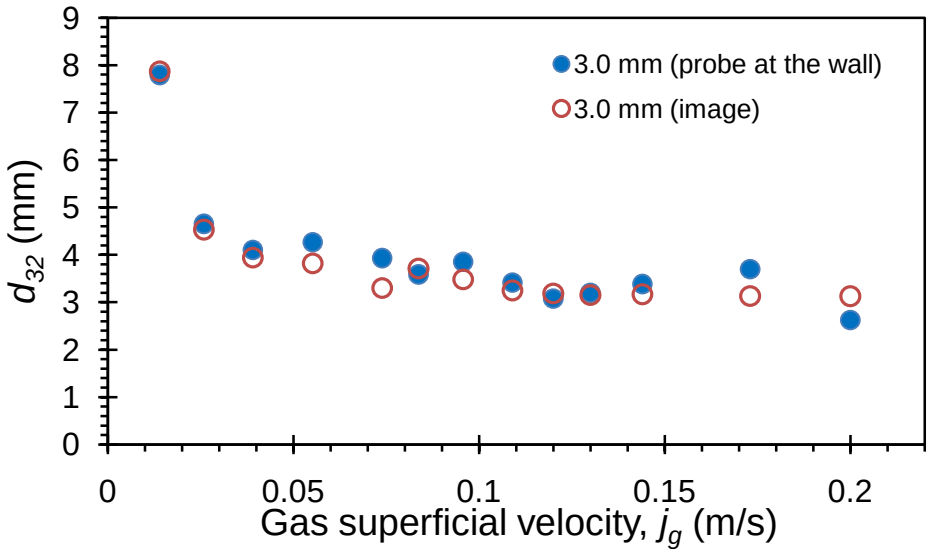


Figure 5.18 The Sauter mean diameter with respect to the gas superficial velocity for the 3.0 mm orifice: a comparison between the image method and the probe at the wall.

5.7.4 The effect of orifices on the volume average mean diameter, d_{43}

The mean diameter, d_{43}, of the considered orifices is illustrated in Figure 5.19 with respect to j_g. The data were obtained by averaging the local data across the column, where Equation 3.37 was used to calculate d_{43} for the optimised bubble size. As with the Sauter diameter results, the small orifices, as illustrated in Figure 5.19a, show that the effect of the orifices of $d_o < 1$ mm is insignificant in terms of producing relatively large bubbles. This trend is similar to that for the porous orifice as an increase was observed in d_{43} for $j_g < 0.074$ m/s, while a decreasing function was noted beyond this point. Figure 5.19b illustrates the mean diameter of the large orifices, $d_o > 1$ mm, compared to the porous sparger. An indication of the production of large bubbles from the orifices can be observed at low j_g: e.g. the average bubble size for the 3 mm orifice was about 10 mm. The decrease in d_{43} is a result of increased bubble breakage rate, as with increasing j_g, more energy is being dissipated in the flow.

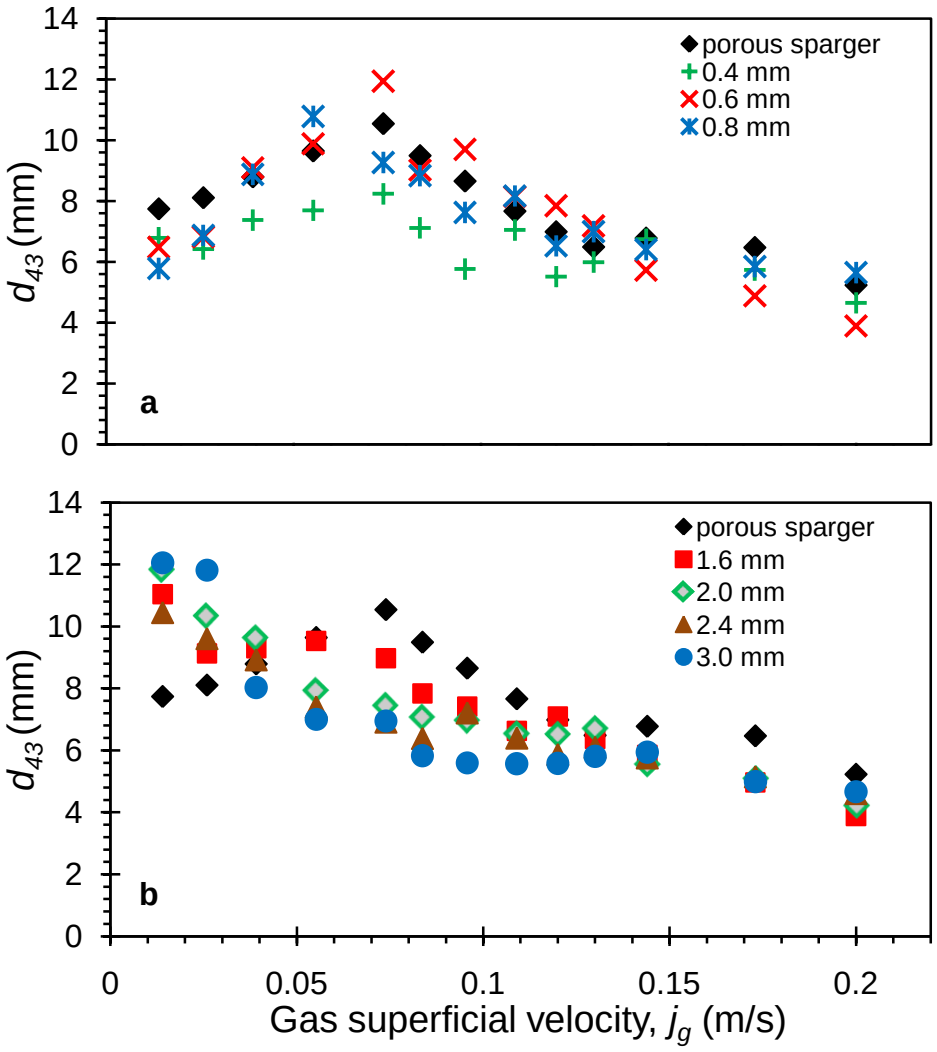


Figure 5.19 The mean diameter, d_{43} , predicted from the optimisation model with respect to j_g: the porous sparger was compared to a) small orifices, and b) large orifices.

Figure 5.20 illustrates the data of the d_{43} for image, and the conductivity probe method with respect to j_g. The trend for the result from the 3 mm orifice, which was obtained using the image method, concurred well with the 3 mm results obtained by the probe at the wall. However, the image method results gave a lower d_{43} value, because with the photographs, only the bubbles close to the wall were considered. At high j_g, large bubbles tended to rise through the centre of the column and hence it was difficult to capture the bubbles far from the wall of the column using images (see Figure 5.21 at high j_g).

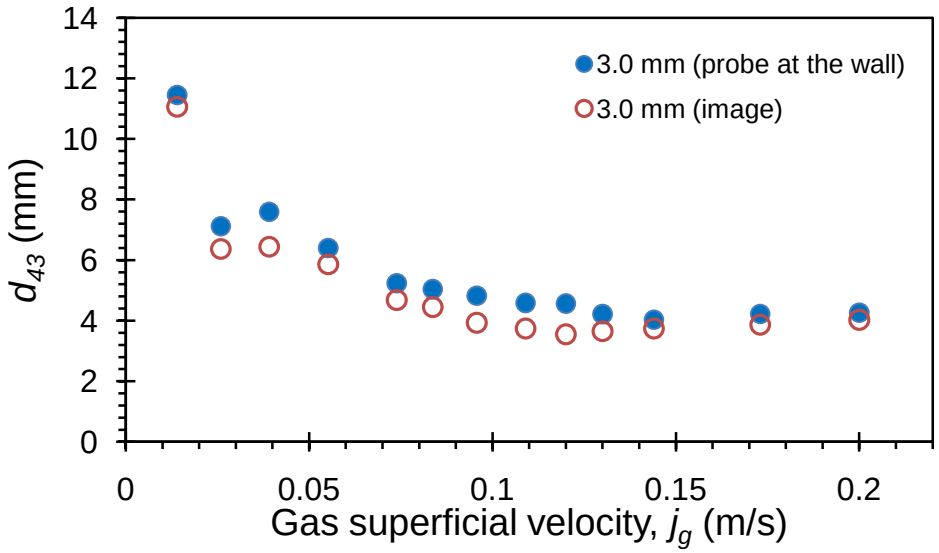
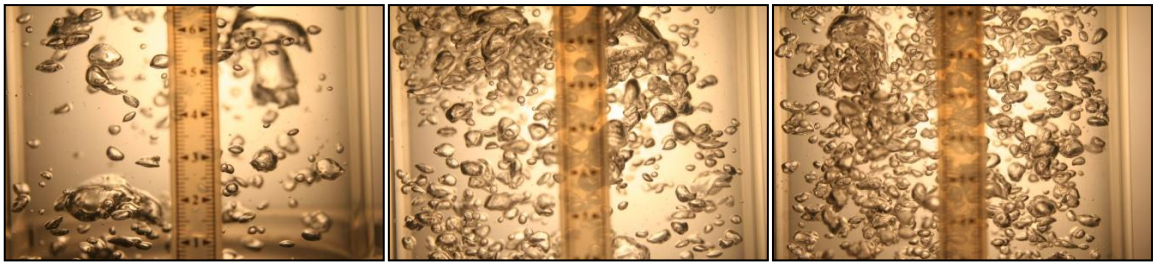


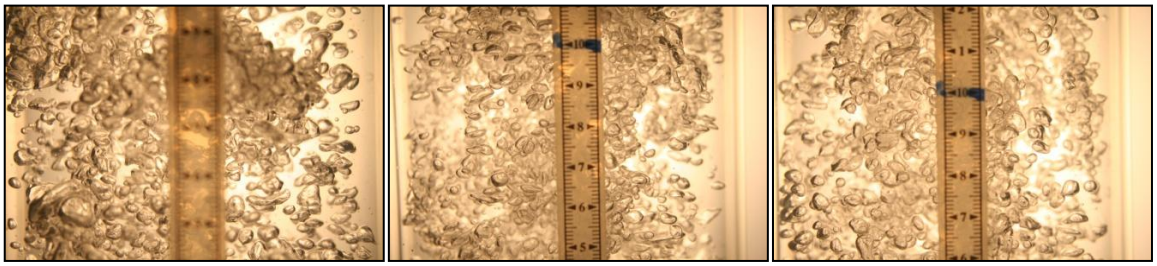
Figure 5.20 A comparison of the mean diameter, d_{43}, obtained from photographs and the conductivity probe at the wall.

Figure 5.21 shows the images that were captured from the 3 mm orifice experiments, where tap water was used as the liquid media. Despite the fact that the image technique represents only the area close to the wall of the column, the photographs confirm that, as the j_g increased, large bubbles turned into smaller ones.

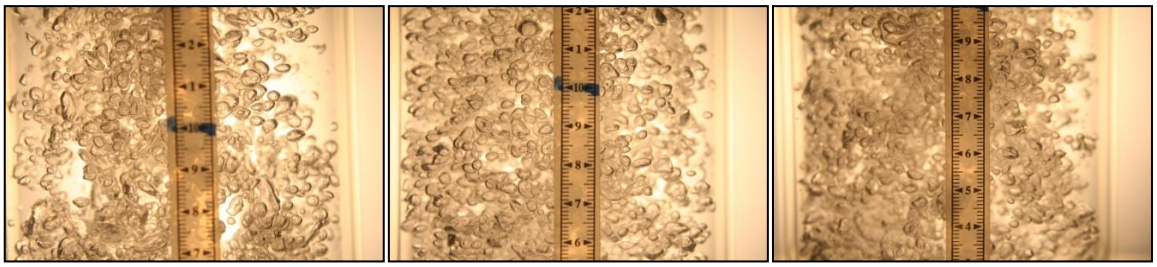
From Figure 5.3 in § 5.2, it was verified that for $d_o \geq 1.6$ mm at low air flow rates, the air was likely to flow through the orifice rather than the porous sparger and this produced large bubbles. As the air flow rate increased, an increasing fraction of the air flows through the porous sparger and then the small bubbles that were generated rose together with the large bubbles, which were produced by the orifice. This could be a reason for having a large chord length at low j_g; bubble breakage is responsible for decreasing the chord length as j_g increased. This bubble breakage is caused by the energy from the turbulent eddies as interaction occurred between bubbles. The high liquid velocity, which was caused by increasing j_g, could enhance the turbulent dispersion force and hence cause more bubble breakage.



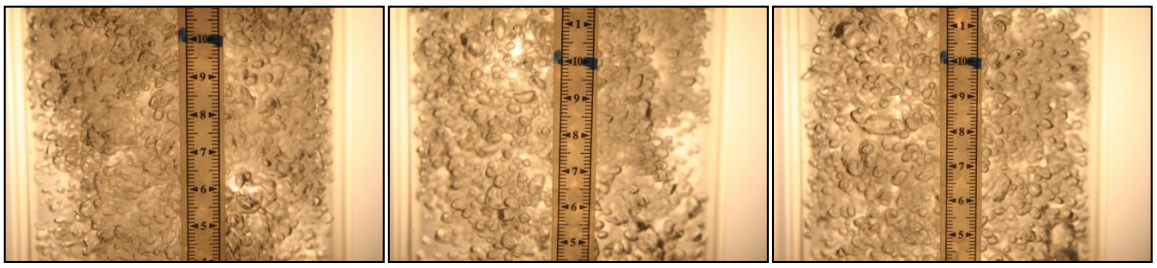
j_g=0.014 m/s j_g=0.026 m/s j_g=0.039 m/s



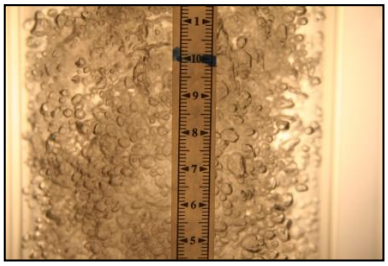
j_g=0.055 m/s j_g=0.074 m/s j_g=0.084 m/s



j_g=0.096 m/s j_g=0.109 m/s j_g=0.120 m/s



j_g=0.130 m/s j_g=0.144 m/s j_g=0.173 m/s



j_g=0.200 m/s

Figure 5.21 The bubble size as a decreasing function with respect to increasing j_g; images were taken from the 3 mm orifice experiments with tap water

5.7.5 The effect of orifices on the standard deviation

The standard deviation of the lognormal bubble size distribution was computed from the measured chord length distribution. The log mean standard deviation, σ, of bubble sizes produced by the porous sparger and the small orifices, shown in Figure 5.22, demonstrate an increased function with respect to an increase in j_g up to 0.055 m/s; thereafter σ is almost constant afterwards. These results were obtained by averaging the local σ across the column. For $j_g < 0.055$ m/s, the bubble size distributions for orifices were broader (for average log standard deviations, σ, of about 0.8 to 1.09) compared to the porous sparger bubble size distribution (σ of 0.6 to 1.06). The relatively large bubbles that were generated by the orifices are responsible for this increase in σ. For $j_g > 0.055$ m/s, both the porous sparger and the orifices gave an almost identical trend for σ. The range of σ was between 0.9 and 1.09. The presence of various leading groups of bubble sizes at high j_g would give broader distributions of the bubble size in the porous sparger and the small orifices.

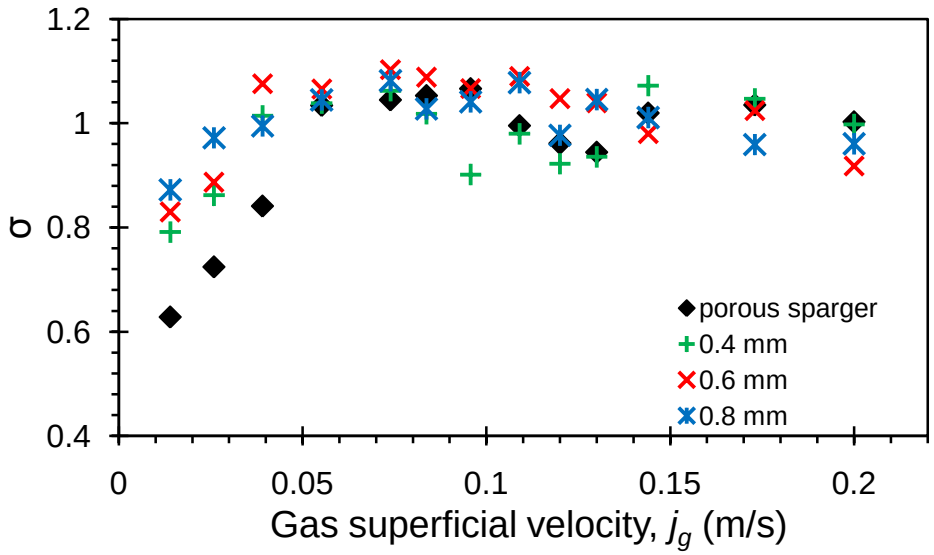


Figure 5.22 Standard deviation of the bubble size distribution for the porous sparger and the small orifices with respect to j_g

Figure 5.23 illustrates a comparison between the lognormal standard deviations of the large orifices and those of the porous sparger. The trend in the lognormal standard deviations of the large orifices at $j_g < 0.055$ m/s, seems different compared to the σ of the porous sparger. The bubble size distributions for the large

orifices were almost constant, i.e. all within heterogeneous flow, for the entire range of j_g studied. The porous sparger experiences homogeneous flow for low j_g<0.055, and then a heterogeneous regime afterwards. At this range of j_g, the bubble size distributions of the large orifices were broader (an average σ of 0.9 to 1.04). This could be due to the existence of the large bubbles. For the range beyond j_g=0.055 m/s, the trend for σ looks the same for both the porous sparger and the large orifices, because, in this range, the large bubbles could be generated by coalescence above the porous sparger and hence σ becomes broader.

The main conclusion that can be drawn from these results is that large bubbles did exist in the experiments using the large orifices for the whole range of j_g, whereas large bubbles were generated in the experiments using the porous sparger and the small orifices only beyond j_g =0.055 m/s, i.e. after flow transition had occurred.

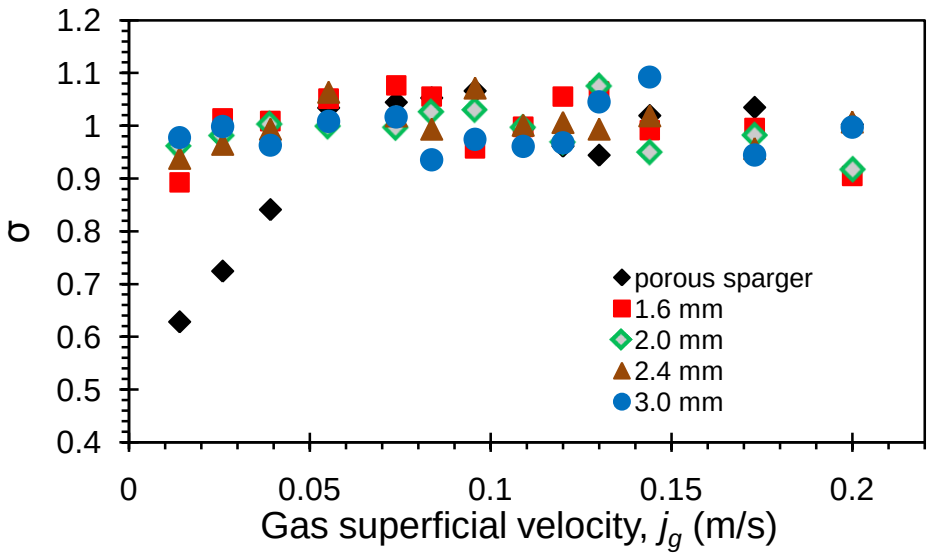


Figure 5.23 Standard deviation of the bubble size distribution were obtained using the optimisation model; a comparison the porous sparger and the large orifices.

Figure 5.24 shows the lognormal standard deviations of σ for the 3.0 mm orifice obtained from the optimisation method for the conductivity probe data at the wall compared to the image method. For $j_g < 0.11$ m/s, the 3.0 mm orifice results obtained using the image method gave a broader bubble size distribution (σ of 1.09 to 1.5). This might be because small bubbles, $d_o < 1$ mm, as well as large bubbles, were considered in the images.

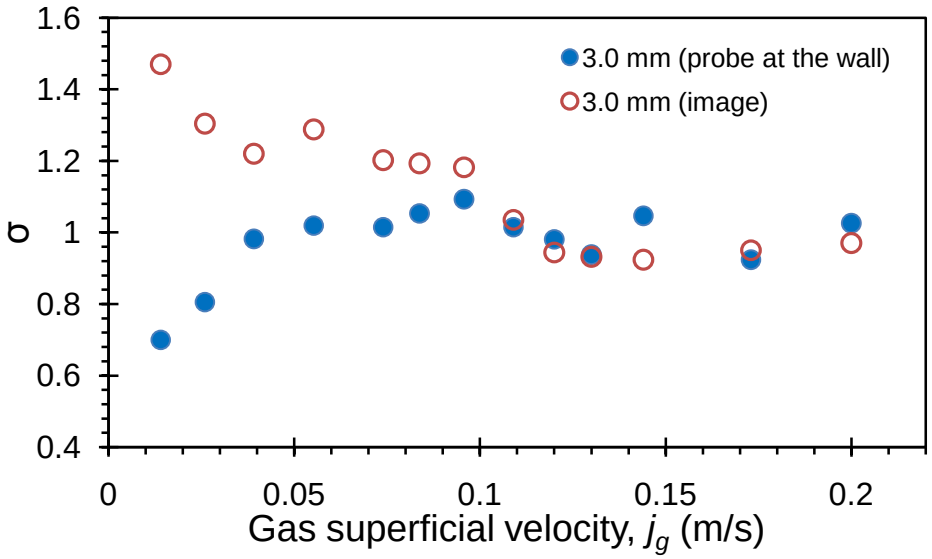


Figure 5.24 Results for the 3 mm orifice obtained from the conductivity probe method at the wall compared to the image method.

5.8 Conclusion

Equation 4.1, suggested by Hibiki and Ishii (2002), fitted quite well with the α profiles of the porous sparger, with and without orifices. At low j_g, the porous sparger without a central orifice showed an almost uniform distribution of α across the column. As j_g increased, bubbles tended to rise through the centre of the column. As a result, the local void fraction increased at the centre, α_c, and near to the wall, α_w, of the column. However, the change in the former was more obvious compared to the latter.

The orifice results presented here agree with those of Zuber and Hench (1962) as it was observed that small and uniform bubbles were generated by the porous sparger. When the porous sparger was introduced with an orifice of >1.6 mm, it generated large bubbles, which rose much faster than the smaller spherical bubbles produced by the porous sparger. These large bubbles would sweep the smaller bubbles into their wake, causing coalescence and hence forcing a transition to the heterogeneous regime. Orifice diameters of d_o > 1 mm seem to destabilise the homogeneous flow even at low j_g levels, because of the presence of large bubbles. The introduction of a stream of larger bubbles emanating from a central orifice drilled into the porous sparger has been shown to destabilise a homogeneous bubbly flow. Orifices with diameters greater than 1 mm produced

fast rising bubbles and the transition to heterogeneous flow occurred at lower mean gas void fractions than for the porous sparger with no central orifice; in some cases, the flow appeared to be heterogeneous even at very low j_g.

The results concerning mean chord lengths, d_{32} and d_{43}, show a decreasing function of the bubble size with increasing j_g; this was visually demonstrated by the images. However, the bubble size distribution offered evidence for the existence of large bubbles at high j_g in the large orifice experiments as the distributions of these orifices were broader for the whole range of j_g. As a result, it is recommended to characterise the bubble size in the column by the distribution of the bubbles rather than by calculating the mean diameter of the data or by using the visual method.

For the porous sparger and all orifices, $d_o < 1$ mm, and for $j_g < 0.05$ m/s, a reduction in the bubble velocity was observed, when increasing the j_g; beyond this point, the v_g increased as the j_g increased. This was due to the presence of large bubbles and the high liquid velocity, which could cause the bubbles to rise quickly up the column. Finally, the results using the 3 mm orifice, which were obtained using the image method concurred well with the results from the conductivity probe experiments.

CHAPTER SIX

ANNULAR GAP BUBBLE COLUMN (AGBC)

6.1 Introduction

This chapter presents the experiments conducted using an Annular Gap Bubble Column (AGBC), where the annular gap is formed between different inner tube diameters, placed concentrically in a vertical column with D_o=0.102 m. The purpose of these experiments was to study the effect of the annular gap geometry on α and on the transition from homogeneous to heterogeneous flow in air-water systems. The effects of dilute alcohol solutions on the two-phase hydrodynamics were also studied.

6.2 Experimental setup and design

The experimental setup is illustrated in Figure 6.1 and consists of a vertical column of internal diameter (i.d.) D_o = 0.102 m, made of transparent QVF® glass with a height of 2.25 m; the level of non-aerated liquid in the column was 1.00 m. Compressed air was injected through a porous plastic sparger, which covered the whole of the column base. The porous sparger had a permeability of 5.3×10^{-14} m^2, with a pore size of around 100 µm. The compressed air supply to the base of the column passed through a rotameter connected to a digital pressure gauge; a pressure correction was made to the rotameter reading, which had previously been calibrated at atmospheric pressure. Annular gap experiments were conducted using different inner tube diameters, D_i, placed inside the D_o = 0.102 m outer column. Tubes of diameters D_i= 0.025, 0.038, 0.051 and 0.070 m (o.d.) were used and are denoted by their respective diameter ratios, $\beta = D_i/D_o$ = 0.25, 0.37, 0.50 and 0.69. The inner tube height is about 2.00 m to keep the top of the tube always above the aerated level. The inner tubes were filled with water to keep them heavy and prevent floating; then they were sealed at both ends so that no gas flowed upwards within these tubes. These were supported from the top by a metallic mesh, which helped avoid any wobbling of the tubes and kept them aligned concentrically inside the column; both columns were carefully aligned to be vertical. The metallic mesh also provided an exit passage for the air

introduced at the bottom of the column. An inverted cone was attached to the bottom of the inner tube and its vertex rested at the centre of the porous sparger. Tap water was used in all cases. Prior to the start of all the experiments, the air supply was run continuously for about 30 min, to condition the water and hence obtain reproducible results as described in §4.3.1.

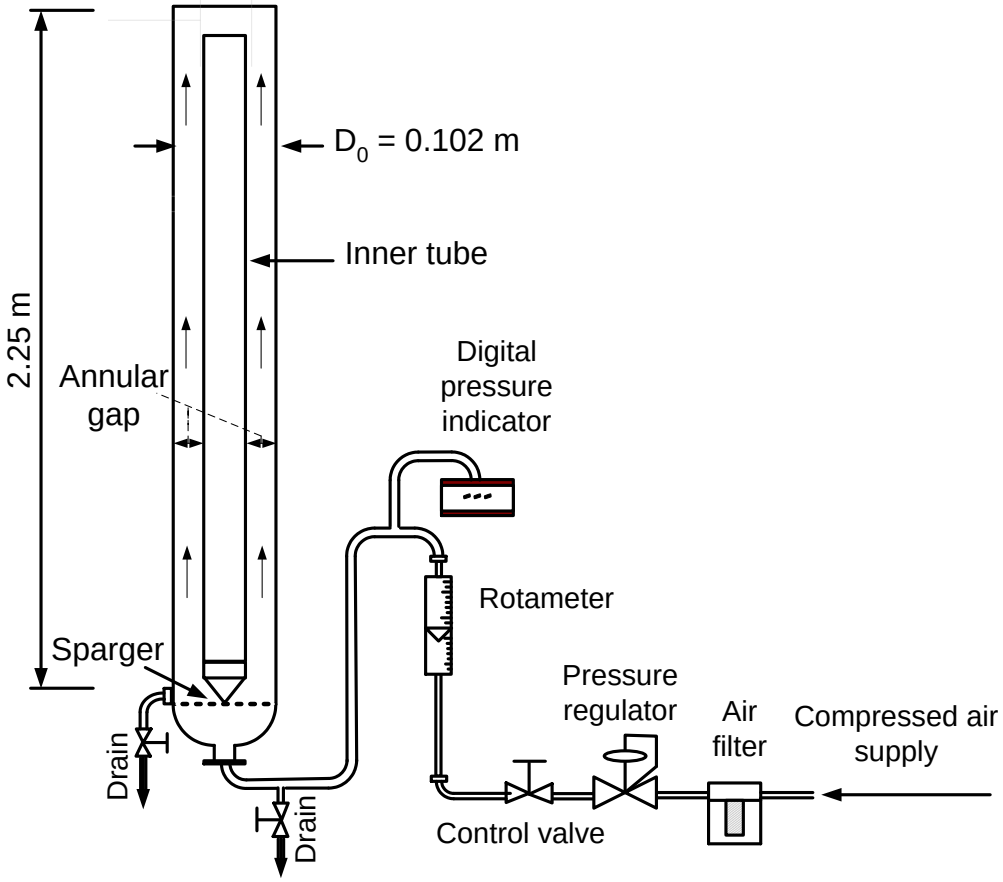


Figure 6.1 Typical annular gap setup, created by placing an inner tube with a conical bottom inside the 0.102 m column.

The drift-flux model (Equation 1.2)

$$\alpha = \frac{j_g}{C_o j_g + v_t}$$

indicates that j_g, equivalent to the gas volume flux, is the key variable in determining α as discussed in §1.3. The annular gap has a smaller cross-sectional area than the open tube, and so the gas flow rates were adjusted appropriately to cover the same range of j_g (0.014 to 0.200 m/s) as in the OTBC experiments in Chapter 4 (see Appendix C). Overall gas void fractions (volume

averages for the whole column) were obtained using the aerated level method (see §3.2). In practice, height measurements were used in place of volumes and were conveniently read from a scale on the wall of the column. Local void fractions were also measured using a two- and four-point conductivity probe, as is described in the Conductivity Technique Section (see § 3.4).

6.3 Preliminary tests

Preliminary experiments were conducted using an AGBC with β = 0.69, at different heights, bottom end shapes, tube positions and flow channels. These experiments were conducted to find out the effect on α of the inner tube geometries and positions. Table 6.1 gives an overview of the setup and output of the AGBC preliminary tests. The output column represents the geometries that were chosen for carrying out the main AGBC experiments.

Table 6.1 The setup and output of preliminary tests conducted in AGBC.

Test	Experimental setup	Experimental specifications and conditions	Output
Inner tube height above sparger	Tube height above the sparger: • 0.00 m • 0.10 m • 0.30 m	• Vertical transparent bubble column diameter, D_o =0.102 m • Inner tube diameter, D_i = 0.07 m • Plain sintered plastic sparger (without an orifice) • Tap water level =1.0 m • Prior start exp. air supply runs for 30 min. • j_g =0.014-0.200 m/s • Aerated level method was used to obtain α	An inner tube height of 0.10 m above the sparger was selected
Inner tube bottom shape	Tube end shape: • Flat • Cone • Rod		Cone shape was used for the tube bottom in AGBC experiments
Inner tube position	Tube position: • Concentric • Eccentric		Tube at a concentric position was used in AGBC experiments

6.3.1 Inner tube height

A flat bottomed tube, β = 0.69, was placed concentrically inside the bubble column (see § 6.2), as shown in Figure 6.2. The inner tube was filled with water and sealed at both ends. Table 6.1 briefly presents the main experimental conditions that were used in this set of experiments. Three inner tube heights (distance above sparger) were used: 0.00, 0.10 and 0.30 m. The purpose of

conducting the experiments was to investigate the effect of the inner tube height on the formation of bubbles from the sparger; in other words, to make sure that the inner tube had no effect on the generation of primary bubbles and did not block bubbles from being generated by the sparger.

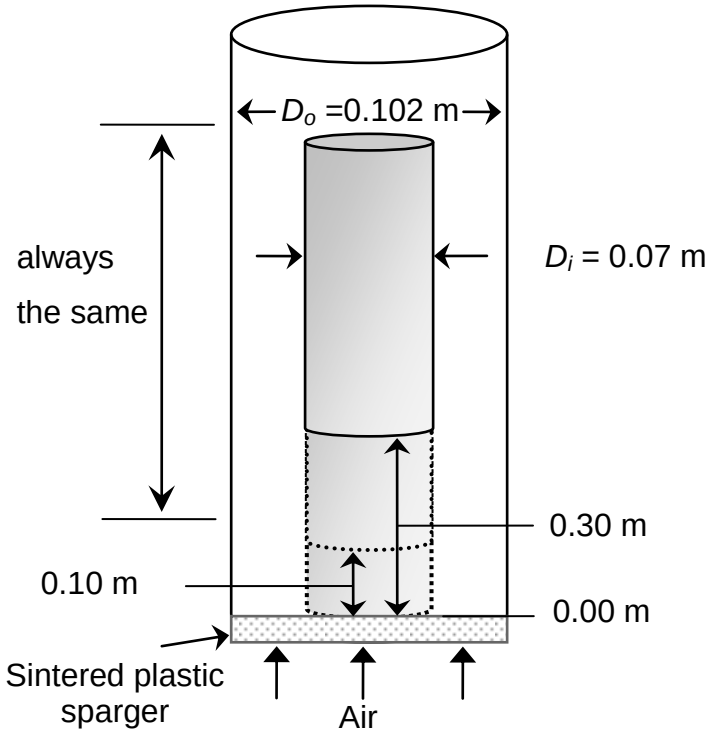


Figure 6.2 An annular 0.070 m tube at different heights inside a 0.0102 m column (not to scale).

Figure 6.3 illustrates the mean α with respect to j_g for different inner tube heights compared to the open tube data. In the open tube, as j_g increases, α also increases, except beyond the maximum void fraction point (j_g =0.12 m/s). The open tube data gave high α readings compared to AGBC data at different inner tube heights. This could be because of the presence of inner tube; this reason is discussed thoroughly in § 6.4. The inner tube height seems to affect the bubble formation at the sintered plastic sparger.

At a height of 0.0 m, the inner tube was resting directly on the sparger, and hence may have partially blocked the sparger, preventing the generation of bubbles across the full area. Therefore, bubbles may only be produced from the unblocked area of the sparger around the inner tube, giving larger primary bubbles and lower α values compared to the other tube heights. As the distance

of the inner tube above the sparger increased, α also increased. This is might be due to the region concept, discussed in § 2.2.1, which was proposed by Wilkinson *et al.* (1992) and other researchers. Millies and Mewes (1999) divided the bubble column into four regions (see §4.3.6). Initially, bubbles form at the sparger in the first region and then the primary bubbles produced by the sparger break up into small bubbles in the second region. An inner tube height of 0.10 m allows bubbles to be generated by the sparger but prevents the bubbles from breaking up. Hence, this gives low α readings compared to the 0.30 m height, which provides enough distance for the primary bubbles to break up further. For subsequent investigations, a 0.10 m inner tube height was selected to conduct experiments regarding the effect of the flat bottomed shape on α.

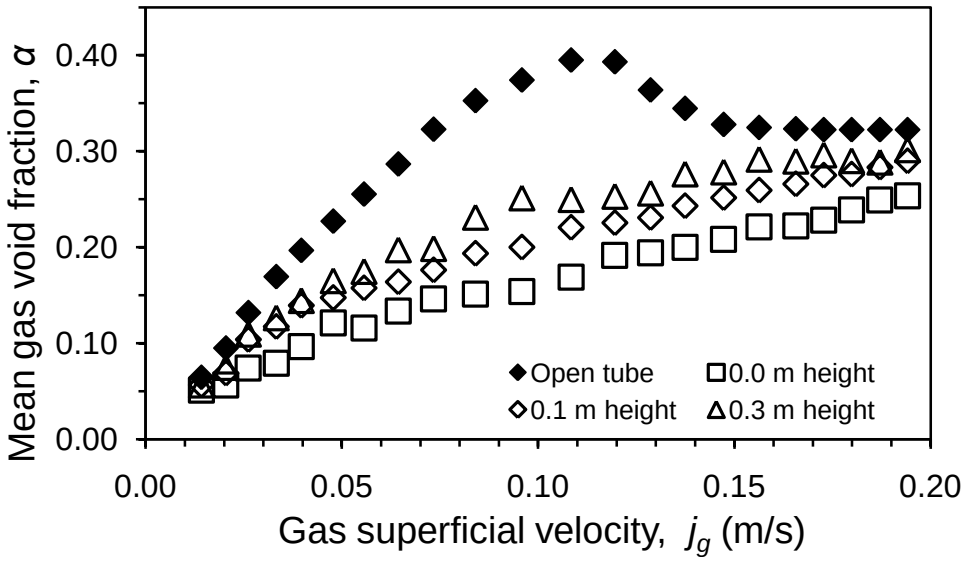


Figure 6.3 The effect of inner tube height on bubble formation from the sparger

6.3.2 Bottom end shape of the inner tube

An inner tube, D_i= 0.07 m, was filled with water, sealed at both ends, and placed concentrically inside a bubble column, D_o= 0.102 m, (see § 6.2) as shown in Figure 6.4. Three bottom shapes, rod, cone and flat (cylindrical support with the same diameter as the inner column), were considered. The tap water level was 1.0 m above the sintered plastic sparger and a j_g range of 0.014–0.2 m/s was studied. The aerated level technique was used to measure α. For more information about the experimental conditions, see Table 6.1. The inner tube was

placed inside the column resting on the sparger as illustrated in Figure 6.4; however, the inner tube used with the rod and cone shaped bottoms was elevated by 0.10 m above the sparger, as shown in Figure 6.4 a and b. The flat shaped bottom is the 0.0 m height explained in § 6.3.1.

Figure 6.5 illustrates the mean α obtained by the aerated level method with respect to j_g for various bottom end shapes and the open tube. Up to the maximum void fraction point (j_g =0.12 m/s) in the open tube data, α increases as j_g increases. The effect of the inner tube in the bubble column on α is noticeable, as it gives much lower α values compared to the open tube. As stated previously, the flat bottom end may have blocked part of the sparger, so that larger bubbles were generated in the unblocked area of the sparger; this may consequently have given lower α readings compared to the other bottom end shapes. Both rod and cone bottom end shapes were designed to avoid closing the pores of the sparger. The cone gave slightly higher α values compared to the rod shape. This could be because the rod-shaped bottom accelerates the coalescence rate by creating turbulence and resistance to upward bubble flow. The cone bottom end shape was selected to conduct subsequent AGBC experiments.

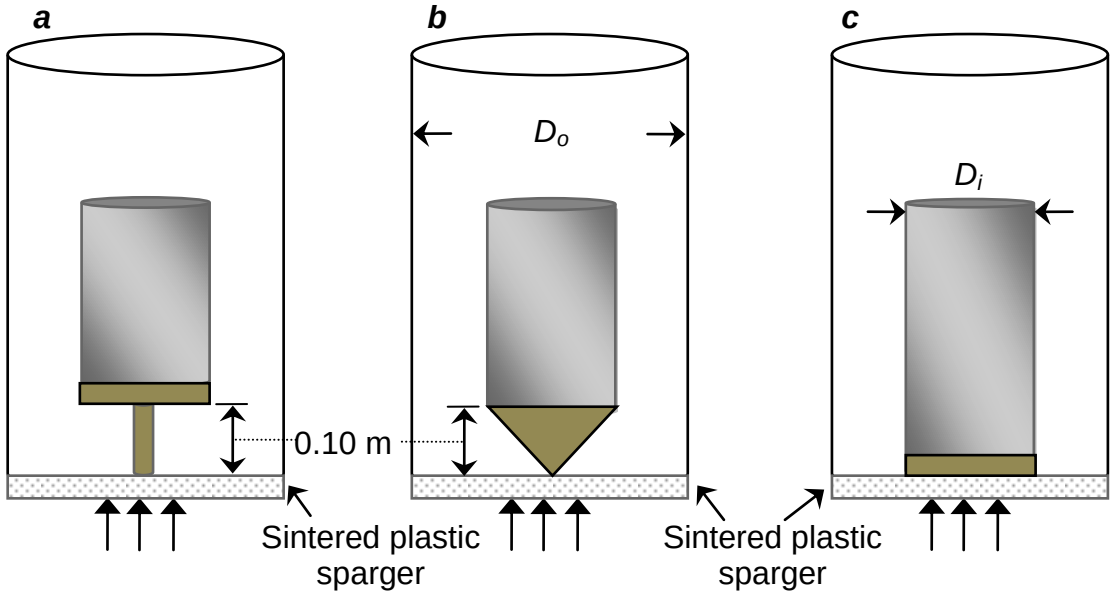


Figure 6.4 Different bottom shapes: a) rod-shaped, b) cone-shaped, c) flat (not to scale).

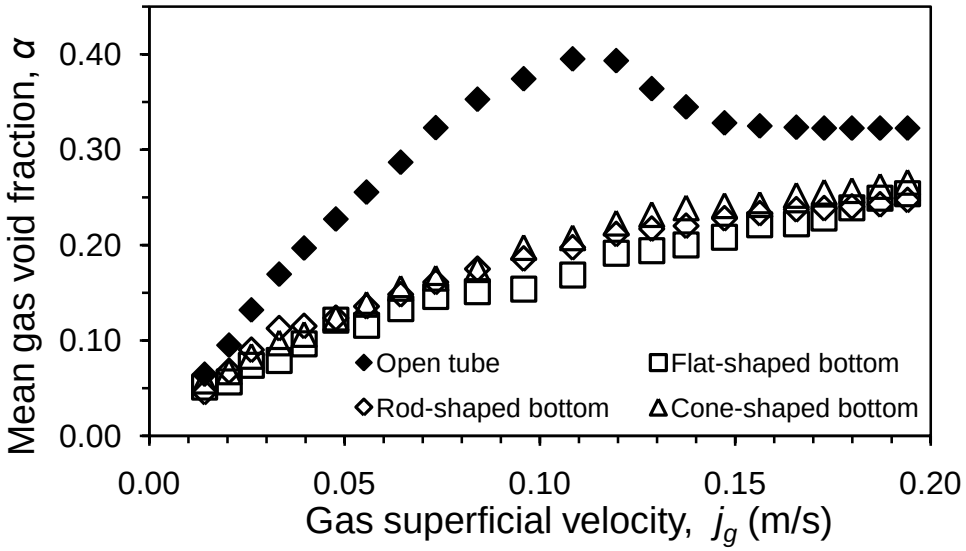


Figure 6.5 A comparison of mean α data with respect to j_g for different inner tube bottom end shapes and an open tube. The data were obtained using the aerated level technique.

6.3.3 Inner tube position

The position of the inner tube inside the column, either concentric or eccentric, was investigated. The experimental conditions are summarised in Table 6.1. The purpose of conducting the experiments was to investigate the effect of the concentricity and eccentricity of the inner tube on the measured α. Figure 6.6 schematically shows a plan view of the inner tube located inside a bubble column; the eccentric tube touches the wall of the outer column. Figure 6.7 shows the mean α with respect to j_g for an open tube, and for concentric and eccentric inner tubes. As mentioned before, an increase in j_g increases α, except beyond the maximum void fraction point (j_g =0.12 m/s) in the open tube data. The presence of the inner tube appears to generate larger bubbles and thus produces a lower α compared to the open tube data. The concentric and eccentric inner tube experiments gave almost the same α data. This result is in good agreement with the findings of Kelessidis and Dukler (1989). For a stagnant liquid phase, they concluded that the degree of eccentricity had little effect on the flow pattern transitions and the void fraction. As j_g was increased, they observed the regular occurrence of Taylor bubbles on the narrow side of the eccentric system as well. The concentric inner tube position was selected to carry out the AGBC experiments.

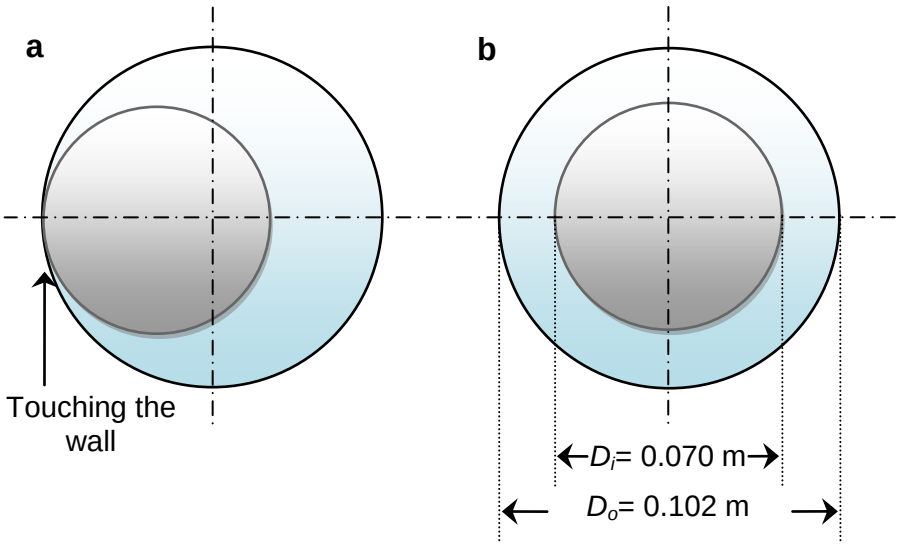


Figure 6.6 Plan view of the position of the β =0.69 inner tube in 0.102 m column: a) eccentric and b) concentric tube (not to scale).

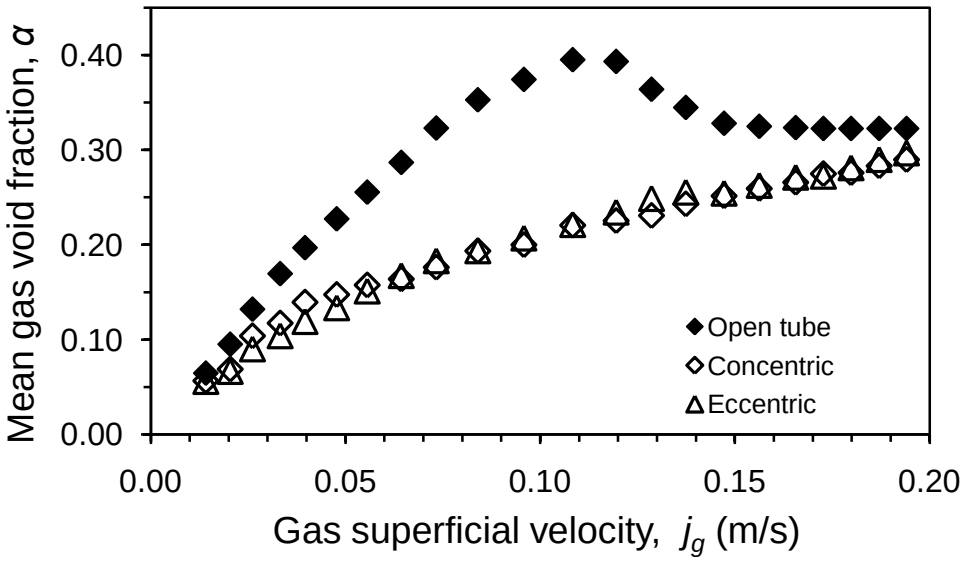


Figure 6.7 Mean α with respect to j_g, and the effect of inner tube position on α; data were obtained using the aerated level technique.

6.3.4 Conclusions from the preliminary experiments

Three inner tube distances (above the plastic sparger) were investigated. At a 0.0 m distance, part of the sparger could be blocked by the inner tube and hence a lower α was obtained. In general, the results showed that, as the inner tube distance above the sparger increased, α increased as well. The bottom end shape of the inner tube was also studied, and it was found that the cone shape gave slightly higher α compared to the rod and flat bottoms. This could be

because the shape of the cone bottom may provide less resistance to upward motion of bubbles. The results obtained from the concentric and eccentric inner tube experiments showed almost the same α data in both positions. The overall conclusion, drawn from the preliminary experiments, was to select an inner tube, with a conical bottom, at a 0.10 m distance above the sparger, and placed concentrically in the column, for use in the AGBC experiments.

6.4 Local and mean gas void fraction in AGBC

The first part of this chapter discussed preliminary experiments to investigate the basis setup of an AGBC, and decided on standardised conditions. The remainder of the chapter focuses on the effects of column diameter ratio on the local void fraction profiles, mean void fraction variations, flow transition points and bubble velocity and size measurements.

6.4.1 The local gas void fraction in an AGBC with tap water and aqueous alcohol solutions

Figure 6.8 and Figure 6.9 show the radial void fraction profiles for the four annular gap geometries that were studied in tap water and 300 ppm ethanol using the four point conductivity probe; the centreline of the annular gap at $r = (R_i + R_o)/2$ is also marked for reference. Similar trends were observed compared to the OTBC. At low gas superficial velocities, the void fraction profiles are almost flat, but grow increasingly non-uniform with increasing j_g. At higher gas superficial velocities, the profile shape becomes almost independent of j_g. Unlike the OTBC, the α profiles in the annular gap are not symmetric about the centreline; the maximum void fraction of the profile is displaced towards the inner wall. With increasing diameter ratios, $\beta = D_i/D_o = R_i/R_o$, the maximum moves closer to the inner wall of the annular gap and the maximum gas hold-up increases. By comparison, with the open tube void fraction distributions, the data shown in Figure 6.8 and Figure 6.9 suggest that there is a high void fraction and a high velocity gas stream that flows preferentially up the inner wall of the annular gap; in contrast, close to the outer wall of the annular gap, the void fraction is rather

low. However, there was no visual evidence of a strong down-flow region near the outer wall, which would have made the probe readings unreliable.

Ozar *et al.* (2008) power-law equation (Equation 3.12), as discussed in §3.4.8, characterises the void fraction profiles in AGBC in

$$\frac{\alpha}{\langle\alpha\rangle} = \frac{z+1}{z}\left(1 - \left|1 - \frac{2(r-R_i)}{R_o - R_i}\right|^z\right)$$

The effect of increasing z in Equation (3.12) is to flatten the void fraction profile. However, it remains symmetric about the centreline of the channel. Furthermore, Equation (3.12) predicts that the void fractions at the walls of the annular gap are zero. Thus, the data in Figure 6.8 and Figure 6.9 cannot be successfully correlated by an expression of the form of Equation (3.12), since they are (i) asymmetric about the centre-line and clearly the shape of the profile changes with the geometry of the annular gap, and (ii) the inner wall void fraction is non-zero and close to the maximum value in the radial profile. Ozar *et al.* (2008) considered only one gap geometry with β = 0.50, and despite their use of Equation (3.12), their profiles also show some asymmetry, with the maximum being displaced toward the inner wall, but not to the extent shown in Figure 6.8 and Figure 6.9.

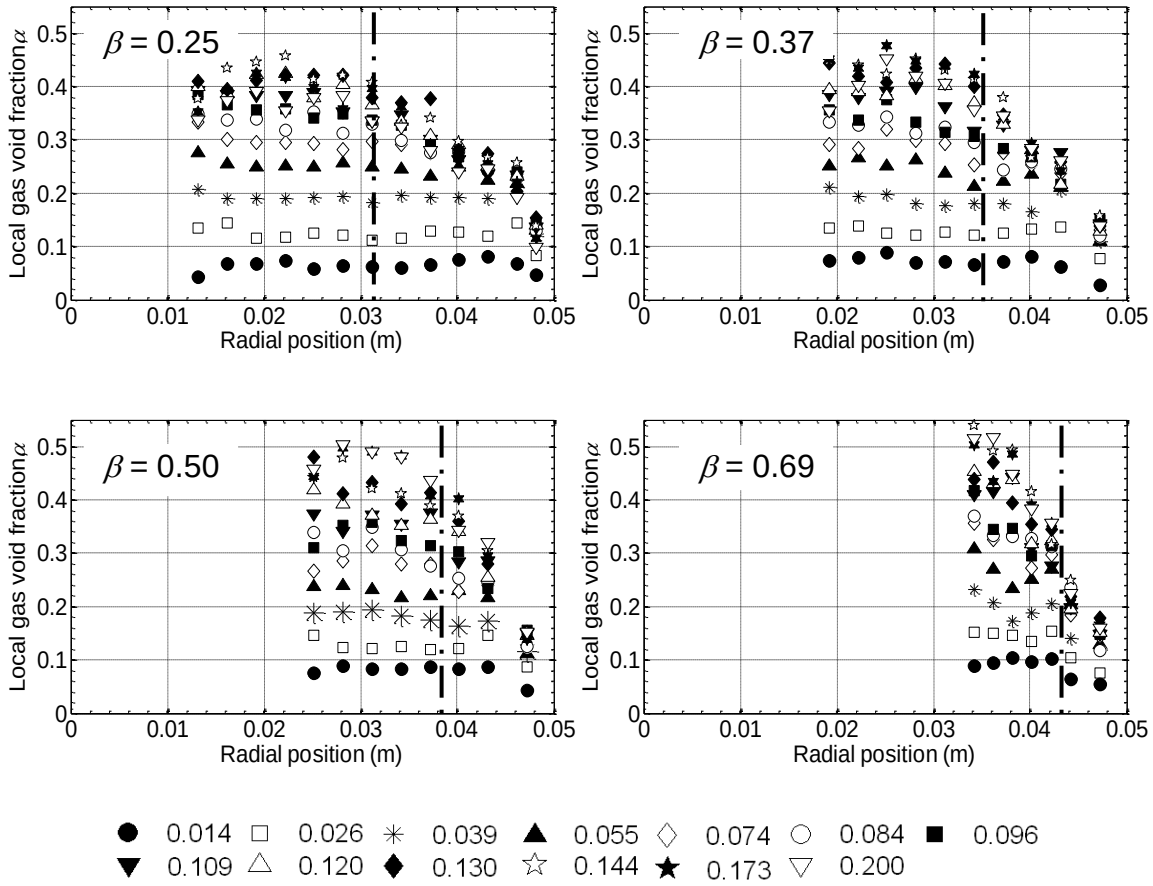


Figure 6.8 Radial profile of local gas void fraction for different geometries of the annular gap bubble column, with the porous sparger in tap water. The vertical dashed line indicates the centreline of the annulus. The legend gives the gas superficial velocity (m/s).

Gas velocity profiles are available from the conductivity probe experiments and are presented in §6.7.2, but liquid velocity profile results were not available. Hence, Equations (1.3) and (1.4)

$$C_0 = \frac{\langle \alpha (j_g + j_l) \rangle}{\langle \alpha \rangle \langle j_g + j_l \rangle}$$

and

$$v_t = \frac{\langle \alpha j_{gl} \rangle}{\langle \alpha \rangle}$$

could not be directly applied to calculate the C_0 distribution parameters for each case. Nevertheless, the results of Figure 6.8 and Figure 6.9 indicate that C_0, which is a measure of non-uniformity in the column, is likely to increase above unity, with increasing diameter ratios β. In that case, Equation (1.2) for Zuber and Findlay's (1965) drift-flux model

$$\alpha = \frac{j_g}{C_0 j_g + v_t}$$

indicates that the mean void fraction should decrease with increasing levels of β for a given gas superficial velocity. In other words, the mean gas void fraction falls when the diameter of the inner column increases, which is what has been observed experimentally in Figure 6.10.

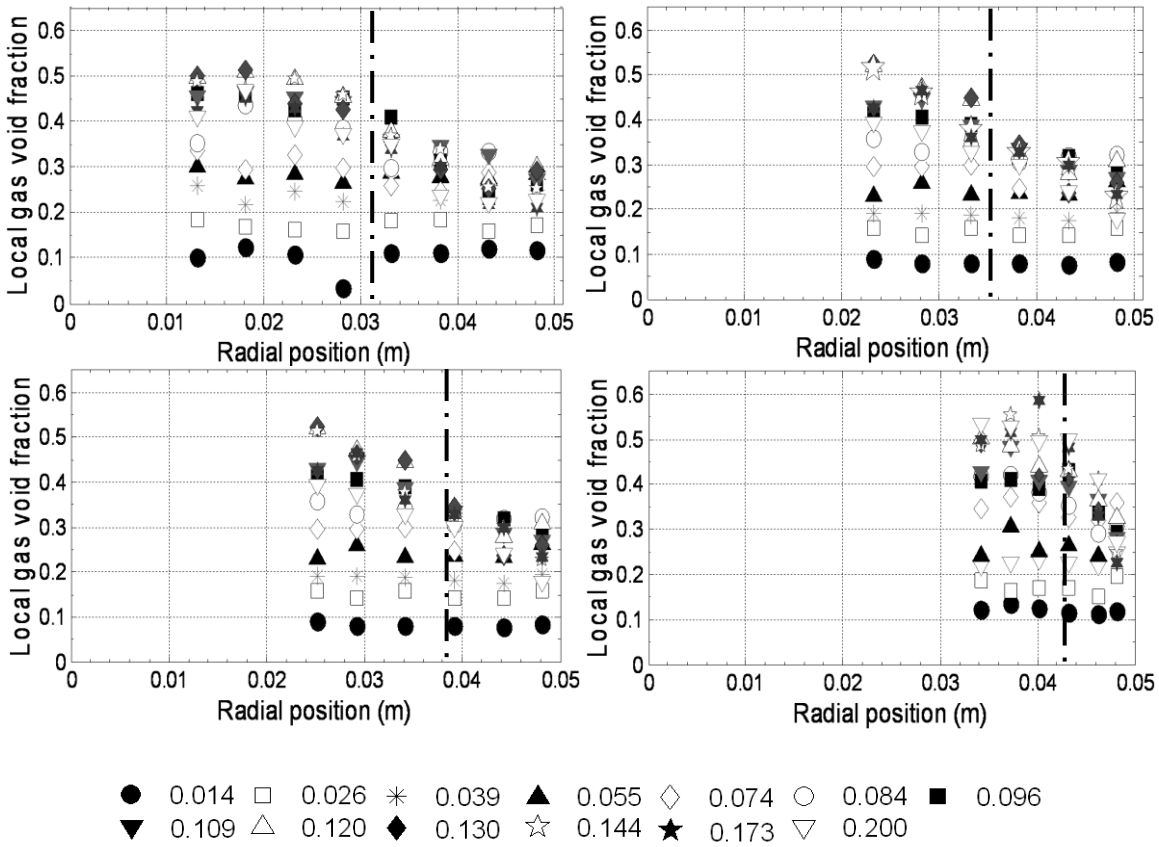


Figure 6.9 Radial profiles of local gas void fraction for different geometries of the AGBC for 300 ppm ethanol. The vertical dashed line indicates the centreline of the annulus. The legend gives the gas superficial velocity (m/s).

6.1.1 Mean gas void fraction in an AGBC with tap water

A comparison between the gas void fraction in the OTBC and in different AGBCs with tap water is illustrated in Figure 6.10. Both the aerated level (Equation 3.2) and conductivity probe methods confirm that the gas void fraction in the open tube is higher compared to α values in the annular gap. This is either because large bubbles have been generated in the annular gap, which has led to heterogeneous flow, or the radial profile of α has changed; the latter would affect the distribution parameter, C_0, in Zuber and Findlay's (1965) drift-flux model as

shown in the previous section. Figure 6.10 shows that when the inner tube size increases, then a lower mean gas void fraction results; there is a significant decrease in the mean α compared to the open tube, confirming the earlier results of Al-Oufi (2006), shown in Figure 1.2.

For an annular gap bubble column, the hydraulic mean diameter is $D_h = D_o - D_i$. Hence, for a fixed outer diameter, D_o, the hydraulic mean diameter decreases as the diameter ratio $\beta = D_i/D_o$increases. It is well known that the degree of back-mixing in a bubble column decreases with decreasing diameter (see, e.g. the recent discussion by Majumder, 2008) and this could affect both the liquid velocity and void fraction profiles, as well as the mean void fractions.

Figure 6.10 compares data obtained by measuring the changes in the aerated level from Equation (3.2) and from tip 1 of the two-point conductivity probe. The former is a volume-average over the whole column, whereas the latter is averaged across a horizontal cross-section, assuming an axisymmetric void fraction profile. As stated previously, the conductivity probes were located at a height of 0.57 m above the sparger; other heights were also studied in §4.3.6, and indicate a small reduction in the void fraction with increasing axial height in the column (due to the bubble coalescence); this is one reason for the discrepancy between the data for the two measurement methods shown in Figure 6.10. The underestimation of the α data by the conductivity method compared to the aerated level method was discussed previously in § 4.5.2.

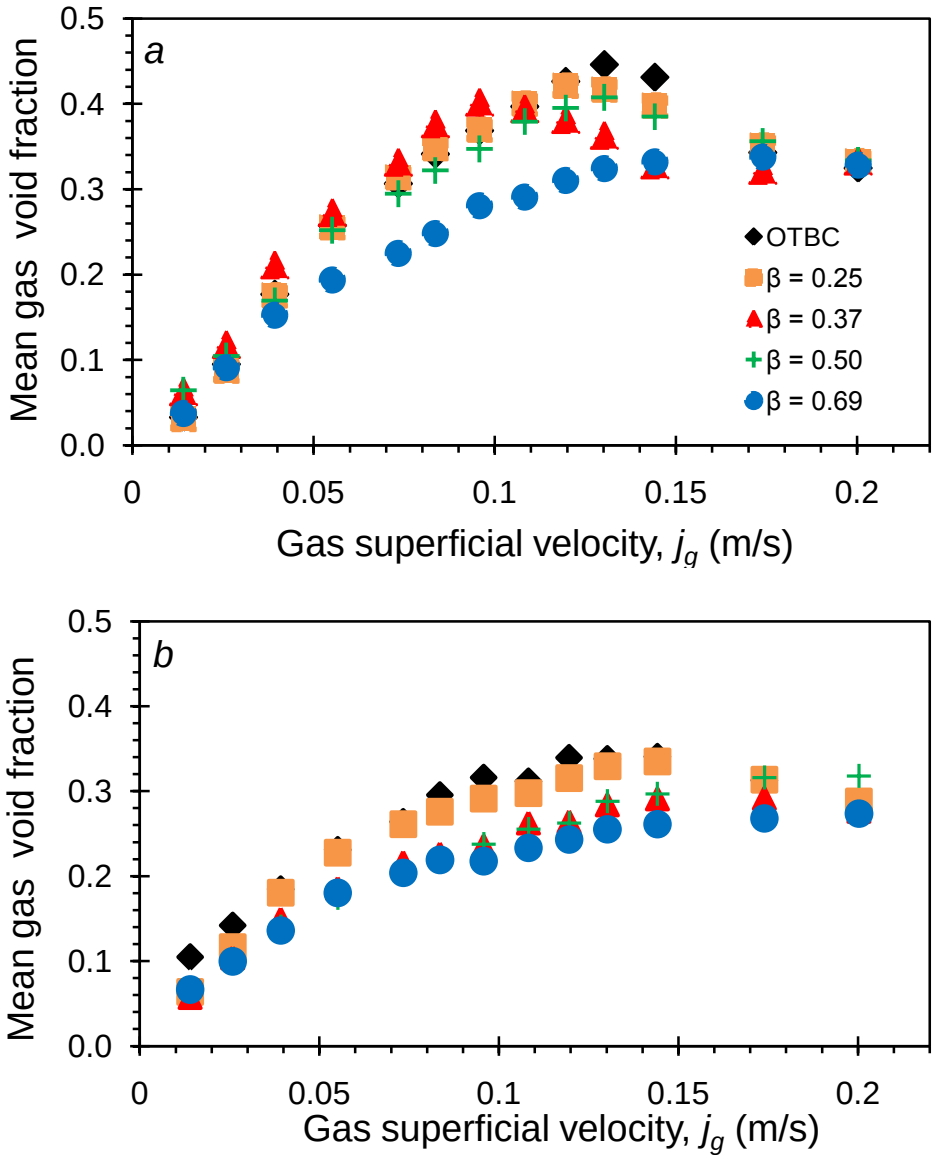


Figure 6.10 Mean gas void fraction in the AGBCs compared to the OTBC results with tap water from measurements: a) of the change of aerated height (Equation 3.1), and b) using the two-point conductivity probe.

6.4.2 Influence of alcohol on the mean gas void fraction in the AGBC

In the previous section, the mean void fractions in tap water in various geometries of AGBC decreased with increasing diameter ratio, β, for the annular gap, because of (i) the changes in the radial void fraction profile (described in §6.4.1) and (ii) an earlier transition to heterogeneous flow (discussed in the next §6.6). Figure 6.11 and Figure 6.12 show similar effects for the 300 ppm ethanol and IPA solution respectively for mean void fractions obtained using changes in the aerated level method and the conductivity probe (p1). Figure 6.11 and Figure

6.12 illustrate α variations with respect to j_g in an aqueous solution containing 300 ppm IPA and ethanol at different annular geometries. At low j_g in the homogeneous flow regime, the differences in void fraction are small, but with increasing gas superficial velocity, the mean void fractions for the larger β AGBCs fall further below the OTBC values.

The probe seems to underestimate α, which could be the result of underestimating the chord lengths (Julia *et al.*, 2005). The reasons why the probe-based method underestimates the mean void fraction are that the probe may miss down-flow bubbles, and it is also expected that very small bubbles, with diameters of less than 1–2 mm, may not impact directly on the probe. The two-point conductivity probe was used in the ethanol experiments, whereas the four-point conductivity probe was used in the IPA experiments. The difference between the two types of measurement is less than 25% for the ethanol experiments and less than 15 % for the IPA experiments, except at the very lowest gas superficial velocity, where bubble impacts are at low velocity and are infrequent.

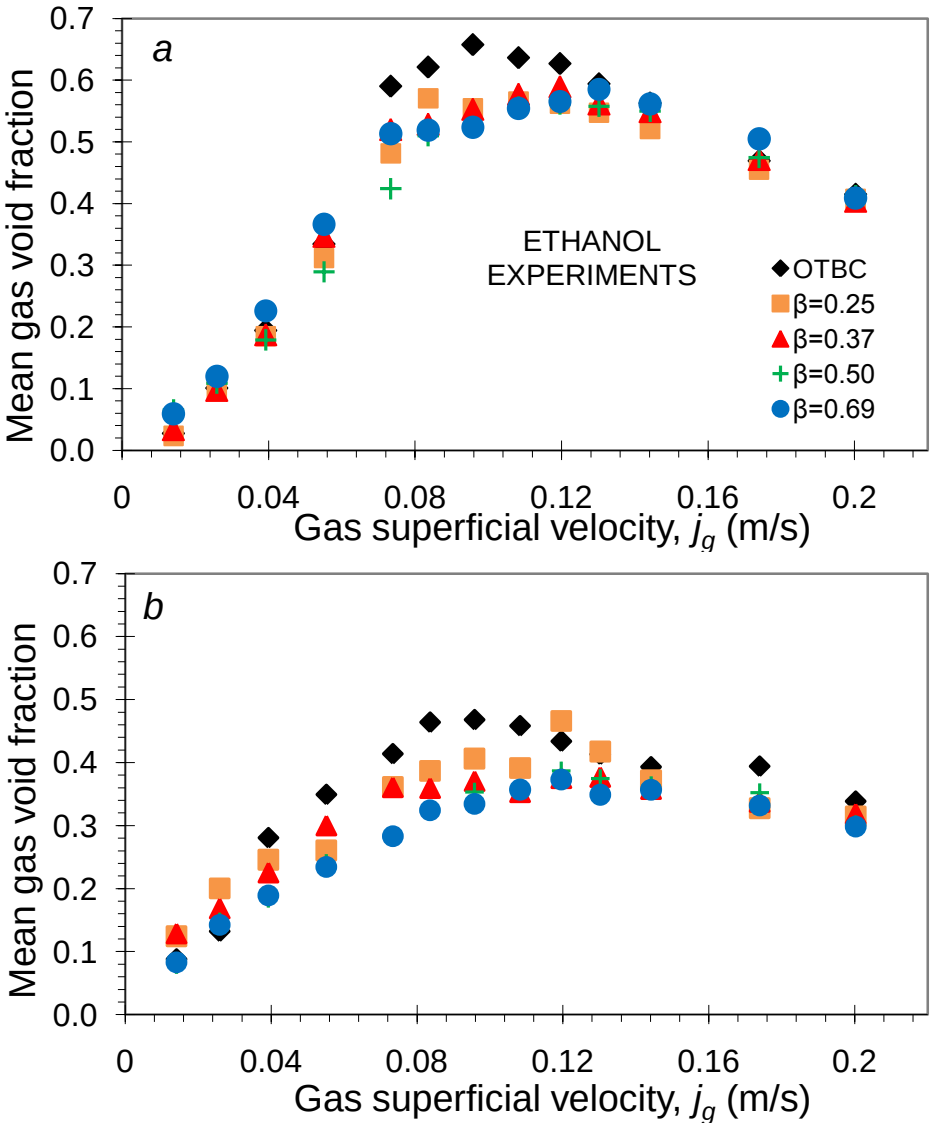


Figure 6.11 Mean gas void fraction in the AGBC compared to the OTBC for 300 ppm ethanol from measurements using a) change of aerated height (Equation 3.1), and b) two-point conductivity probe.

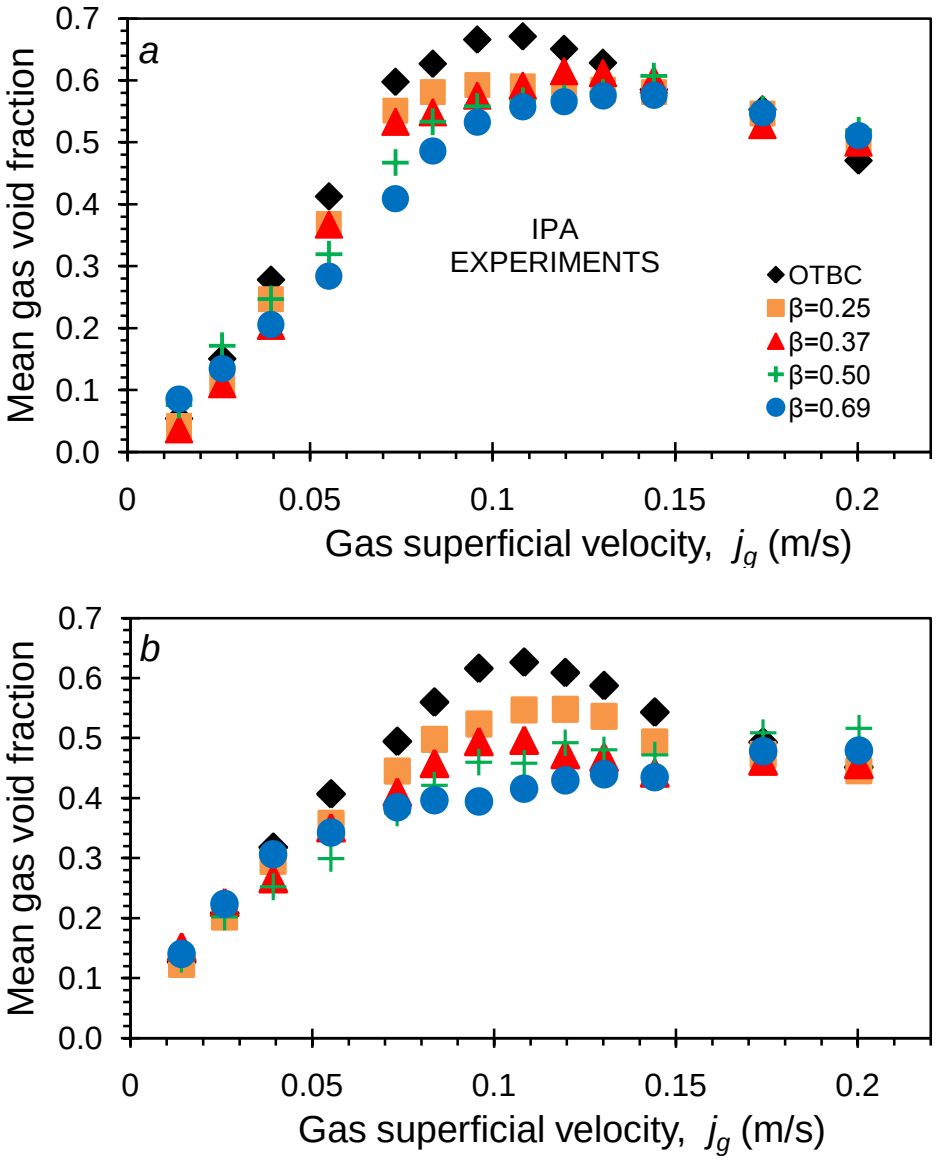


Figure 6.12 The effects of annular gap geometry on the mean gas void fraction, with a comparison to the open tube results for 300 ppm IPA from measurements using a) change of aerated height (Equation 3.1), and b) two-point conductivity probe.

6.5 The distribution parameters in the AGBC

6.5.1 The effect of annular gaps with tap water on the distribution parameter

The distribution parameter, C_o, can be obtained from Zuber and Findlay's (1965) drift-flux model (Equation 1.2)

$$\alpha = \frac{j_g}{C_0 j_g + v_t}$$

by fitting $j_g/\langle\alpha\rangle$ against j_g; the method was discussed in §5.5. Figure 6.13 illustrates the relation between C_o and the diameter ratio, β. Both C_o and v_t seem to increase as the diameter ratio, β, increases. For the open tube, β = 0, v_t was about 0.17 m/s so the bubble equivalent diameter, d_e, was between 3 and 5 mm (Clift *et al.*, 2005). Whereas for the largest diameter ratio, β =0.69, d_e was about 15 mm corresponding to v_t=0.23 m/s. The presence of large bubbles affects the distribution of void fraction in the annular gap and hence might be the reason for the transition to churn-turbulent flow.

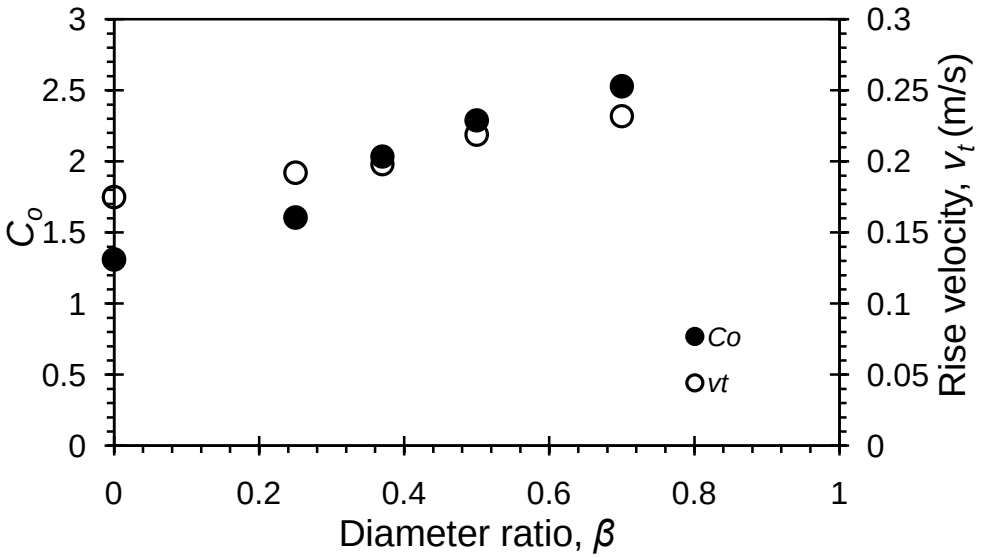


Figure 6.13 The distribution parameter and the rise velocity with respect to the gap ratio for tap water.

6.5.2 The influence of the alcohol aqueous solution on the distribution parameters in AGBC

Figure 6.14 shows the parameters C_o and v_t with respect to β for the four diameter ratios of the AGBC and the OTBC ($\beta = 0$) for 300 ppm ethanol and IPA solutions. The parameter v_t remains approximately constant, indicating that mean bubble size is not changing much with annular gap geometry. In contrast, C_o increase significantly from close to unity to about 1.8 with increasing β, which is consistent with (i) the changes shown in Figure 6.9 for the void profile profiles, and (ii) the effects of β on the mean void fraction. If v_t is interpreted as a single bubble rise velocity, then a value of 0.10 to 0.14 m/s would correspond to bubbles

of equivalent diameter of about $d_e = 1.5\,mm$ (Clift *et al.*, 2005) indicating considerably smaller sizes than would be found in tap water.

Thus the effect of changing gap geometry on the distribution parameter for the AGBCs, previously reported for tap water, has been confirmed for these alcohol solutions. However, the inference from the fitted values of v_t is that the bubble size remains small even in the annular gap geometries.

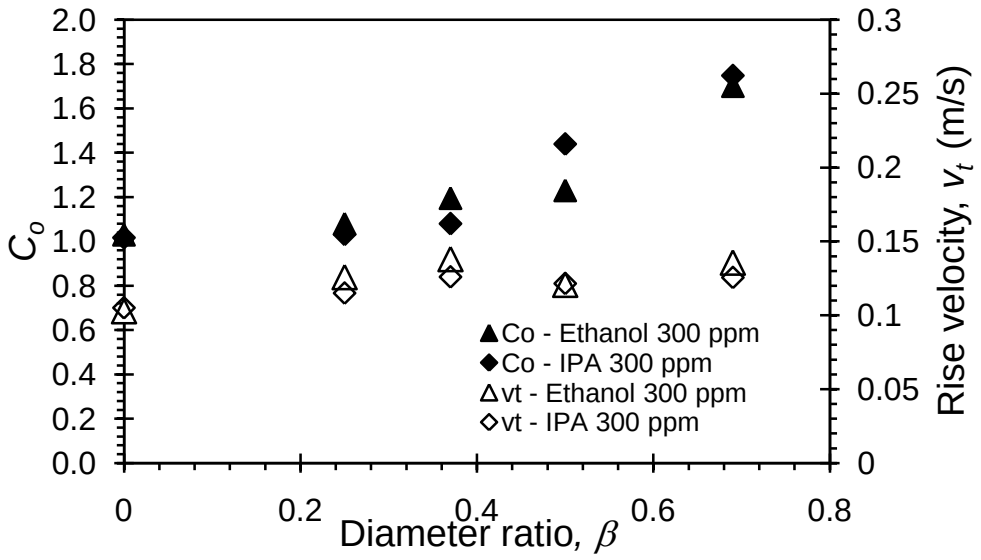


Figure 6.14 The distribution parameter and the rise velocity with respect to the AGBC diameter ratio for 300 ppm ethanol and IPA solution.

6.6 Flow regime transitions in the AGBC

The regime transition points, α_{trans} and $(j_g)_{trans}$, can be estimated from the Wallis plot (Wallis, 1969) of Figure 6.15 as discussed in §4.6, which shows the ''drift-flux'' velocity, $j_g(1-\alpha)$, and the gas void fraction, α; the smooth curve represents Richardson and Zaki's (1954) equation. For an air-water system in the homogeneous regime, n =2 (Krishna *et al.*, 2000) and the rise velocity, v_t = 0.24 m/s (Wallis, 1969). Figure 6.15 shows that Richardson and Zaki's model is valid for low gas superficial velocities in the homogeneous bubbly flow regime. The point where the data deviates from the curve is taken to indicate the regime's transition point. It is difficult to distinguish between the transition points for the open tube and the annular gap columns with β= 0.25–0.50. However, the largest inner tube (β = 0.69) clearly deviates from the Richardson and Zaki curve

mentioned earlier: α_{trans} = 0.15 and $(j_g)_{trans}$= 0.032m/s, compared with the OTBC, α_{trans} =0.26 and $(j_g)_{trans}$ = 0.048m/s. In other words, the presence of the inner tube appears to generate large bubbles, which destabilise the homogeneous flow at a lower gas superficial velocity and mean void fraction than for the OTBC.

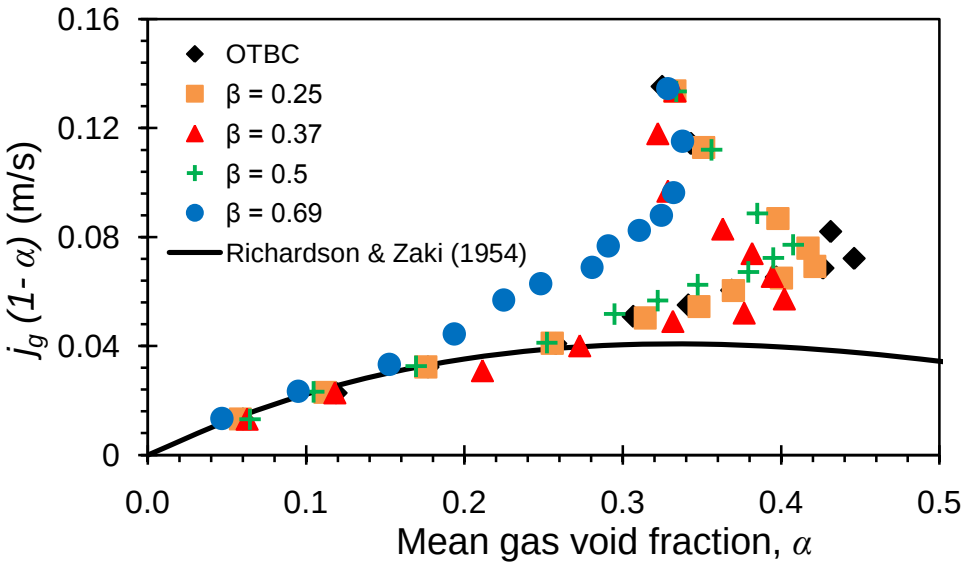


Figure 6.15 Wallis plot to determine transition parameters α_{trans} and $(j_g)_{trans}$; the mean gas void fraction data were obtained using the aerated level method.

As previously shown, Wallis plots were used to show that the transition point α_{trans} decreased slightly with increasing diameter ratio β for various AGBC geometries with tap water (see Table 6.2). A Wallis plot for the 300 ppm ethanol and IPA solutions in the OTBC and AGBCs is shown in Figure 6.16, and the transition points for different inner tube ratios are listed in Table 6.2. The effect of changing the inner tube diameter appears to be more significant with 300 ppm ethanol than for tap water, but the data do not agree so well with the Richardson and Zaki curve in Figure 6.16, and hence the values of α_{trans} are subject to some error (no single values of n and v_t for Equation 2.1 were found to be suitable). Similar analyses for 300 ppm IPA shown in Figure 6.16b are also summarised in Table 6.2, where the transition points $(j_g)_{trans}$ and α_{trans} are close to the values for ethanol. Both alcohols show the same effects as has been observed for tap water, i.e. the homogeneous flow is destabilised at a lower gas superficial velocity as the annular gap width is reduced. The presence of the alcohols extends the

homogeneous flow regime to higher j_g than for the tap water system for each diameter ratio, but the effect is not as dramatic as in the OTBC.

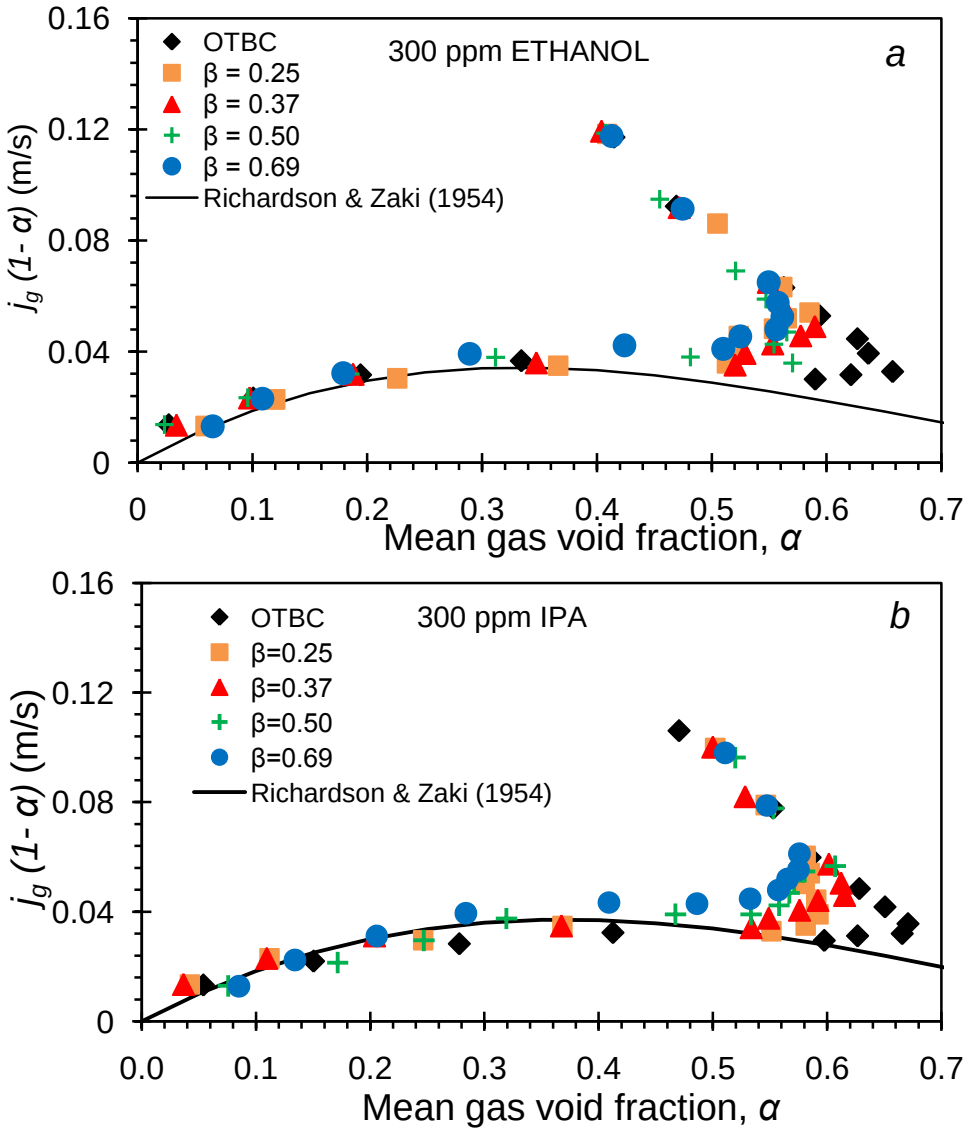


Figure 6.16 Flux model to predict the α_{trans} and $(j_g)_{trans}$ for different annular gap geometries in a) 300 ppm ethanol and b) 300 ppm IPA aqueous solution.

Figure 6.17 summarises the drift–flux velocity, $(j_g)_{trans}$, data shown in Table 6.2. The figures provides a comparison of the $(j_g)_{trans}$ between air-water and 300 ppm ethanol and IPA solutions for OTBC and an AGBC. For the air-tap water system, the transition point, $(j_g)_{trans}$, for the OTBC (at $\beta = 0$) and AGBC were 0.048 and 0.026 m/s respectively. However, the data for the OTBC in 300 ppm ethanol and IPA solutions deviate from Richardson and Zaki's curve later at $(j_g)_{trans}$= 0.060 and 0.063 m/s respectively. Similarly, AGBC (β = 0.69) data in

300 ppm ethanol and IPA solutions diverge from the curve at a later point compared to the air-water system. The results show that the addition of alcohol delays the deviation from the Richardson and Zaki curve, indicating that alcohol tends to minimise the bubble sizes by inhibiting coalescence, which then leads to stabilising the homogeneous flow.

Table 6.2 Transition point α_{trans} and $(j_g)_{trans}$ for tap water and alcohol aqueous solutions in the OTBC and AGBC

	Tap water		Ethanol 300 ppm		IPA 300 ppm	
	$(j_g)_{trans}$ (m/s)	α_{trans}	$(j_g)_{trans}$ (m/s)	α_{trans}	$(j_g)_{trans}$ (m/s)	α_{trans}
OTBC	0.048	0.26	0.060	0.58	0.063	0.60
β = 0.25	0.047	0.25	0.062	0.48	0.063	0.55
β = 0.37	0.047	0.25	0.058	0.36	0.062	0.53
β = 0.50	0.047	0.25	0.049	0.32	0.056	0.34
β = 0.69	0.026	0.15	0.030	0.18	0.034	0.20

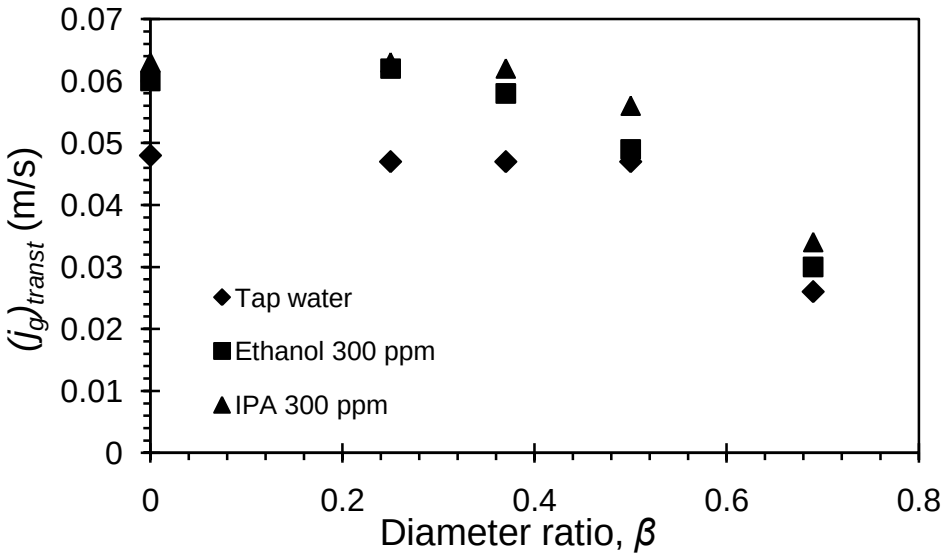


Figure 6.17 The drift-flux velocity with respect to the β ratio; influence of alcohol (300 ppm ethanol and IPA) on the stability of the homogeneous flow in OTBC and AGBC.

6.7 Measurements of bubble size and velocity

6.7.1 Mean chord length in AGBC

Figure 6.18 illustrates the mean chord length, C, of the porous sparger and various annular gaps with respect to j_g for tap water (OTBC and assorted AGBC)

and 300 ppm ethanol and IPA solution ($\beta = 0.69$). The data were obtained by averaging the local chord lengths, which were calculated using Equation 3.17

$C_i = v_{gi} tR_i$

The chord length is basically the bubble velocity, v_g, multiplied by the residence time, tR, where v_g was determined using Equation 3.16

$$v_{gi} = \frac{l_{12}}{ft_i}$$

and the residence time, tR, was obtained using the conductivity probe. For the homogeneous region, j_g < 0.055 m/s, relatively small and uniformly sized bubbles were observed while conducting the experiments for the OTBC and AGBC. At this range, coalescence could take place, bubbles were stable and the rate of breakage was insufficient to split the bubbles. These observations characterise the homogeneous regime and are the reason for the increase in the chord length in that range of j_g (see Figure 6.18). As the air flow rate increased, j_g > 0.055 m/s, progressively the flow became more churn-turbulent, and large bubbles and turbulent eddies became visible. From Figure 6.18, for j_g >0.055 m/s, the chord length is a decreasing function as j_g increased. This is because the energy input to the flow increases with increasing j_g leading to increased breakage rates. Figure 6.18 shows a reduction in C indicating smaller bubbles as the diameter ratio, β, increased. In fact, this tendency disagrees with the experimental observations since, at low j_g, more large bubbles were observed in the annular gap, β = 0.69, compared to the porous sparger experiments. This could indicate that the air-water flow is very complex, and hence it was impractical to characterise the system by looking only at the mean chord length. So, the chord length distribution is considered in the next few pages in order to make such comparisons, because it seems more realistic.

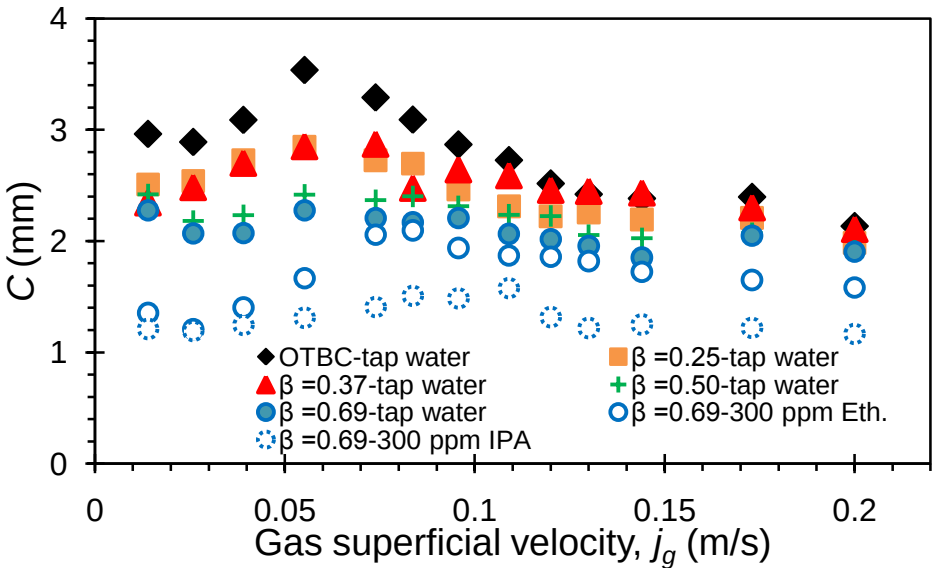


Figure 6.18 Mean chord length with respect to j_g; a comparison between assorted annular gaps and a porous sparger.

Two alcohol aqueous solutions, 300 ppm ethanol and IPA, were studied in the annular gap column, β =0.69. Figure 6.18 shows the effect on the bubble chord length of using 300 ppm of ethanol and IPA aqueous solution. In general, compared to the tap water results, the addition of alcohol seemed to decrease the bubbles' chord length over the whole range of j_g. The results were in good agreement with the observations made while the experiments were being conducted. The presence of alcohol stabilises the flow by preventing the coalescence of the bubbles. For β = 0.69, Figure 6.18 shows that the maximum chord lengths were noticed at j_g = 0.055, 0.084 and 0.109 m/s for tap water, ethanol and IPA solution respectively. This could indicate that the addition and the chain length of alcohol might stabilise the bubbles for a greater j_g range. The length of the alcohol chain also plays a role in bubble size, as the IPA aqueous solution gave smaller chord lengths compared to the ethanol aqueous solution.

6.7.2 Mean bubble velocity in AGBC

The mean bubble velocity, v_g, is presented in Figure 6.19 with respect to j_g for the assorted annular gaps and the porous sparger. The data were obtained by averaging the local bubble velocity, which was calculated using Equation 3.16,

$$v_{gi} = \frac{l_{12}}{ft_i}$$

and where the four-point conductivity probe was used to obtain the flying time, ft. In general, Figure 6.19 shows that the bubble velocity was an increasing function as j_g increased. The mean bubble velocity of the annular gap, β=0.25, seemed similar to the porous sparger. For j_g< 0.039 m/s, the bubble velocity decreased as the gas superficial velocity increased. However, beyond this point, v_g increased with an increases in j_g. The mean bubble velocity, v_g, of the annular gaps, β > 0.25, gave a similar trend as v_g was an increasing function as j_g increased. This might be the result of either the presence of large bubbles, or an increase in the liquid centreline velocity, which might cause the bubbles to hit the probe at a higher speed.

The addition of 300 ppm of ethanol and IPA to the annular gap experiments, β = 0.69, decreases v_g over the whole range of j_g compared to the tap water experiments. This was reasonable since the small bubbles in IPA rose more slowly compared to relatively large bubbles of tap water. An increase in v_g was reported with the ethanol (300 ppm) aqueous solution for the whole range of j_g. However, the IPA aqueous solution at the same concentration gave almost constant v_g.

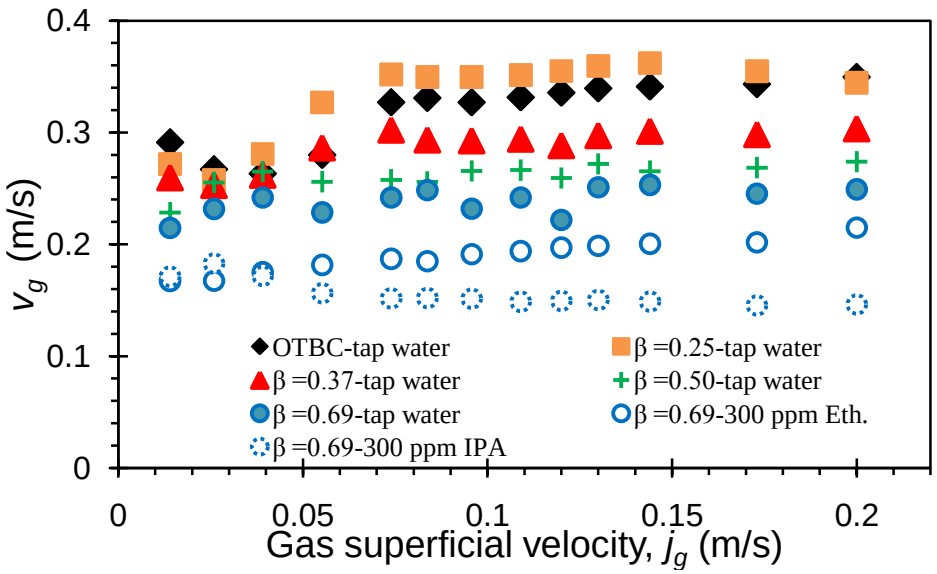


Figure 6.19 A comparison of the mean bubble velocity between different annular gap columns and a porous sparger for tap water, 300 ppm ethanol and IPA solutions.

6.7.3 Sauter mean diameter in AGBC

Figure 6.20 illustrates the Sauter mean diameter, d_{32}, for the porous sparger and annular gaps with respect to j_g. The data were obtained by averaging the local d_{32} across the column using Equation 3.36,

$$d_{32} = \frac{\sum d_e^3}{\sum d_e^2}$$

while these values were predicted using the optimisation model, which is described in §3.4.11. Figure 6.20 indicates that the optimisation model gave reasonable predictions of the bubble size since the mean bubble size showed a trend that was identical to the trend of the mean chord length. For low j_g < 0.039 m/s, the Sauter mean diameter increased with an increase in j_g. However, for j_g> 0.055 m/s, d_{32} was a reducing function as j_g increased. The coalescence and breakage rate were important factors in characterising the bubble size inside the column. For low j_g, coalescence could exist and hence the bubble size increased whereas, as j_g increased, the rate of breakage also increased. The breakage rate rises as gas velocity increases, due to an enhancement of bubble–bubble interactions. These results were in good agreement with the findings of Wongsuchoto *et al.* (2003). Bubble breakage in regions of high turbulence was most likely affected by either the turbulent velocity fluctuations or the large relative velocity gradients of the gas flow. When the maximum hydrodynamic force in the water is larger than the force of surface tension, the bubble breaks up into smaller bubbles.

The optimisation model was capable of highlighting the effect of the presence of alcohol in the annular gap column, β = 0.69. The addition of alcohol decreases the Sauter mean diameter, d_{32}, for the whole range of j_g. The addition of alcohol decreases the surface tension of the solution and suppresses coalescence, as described in §2.2.4, resulting in smaller bubbles than in tap water systems

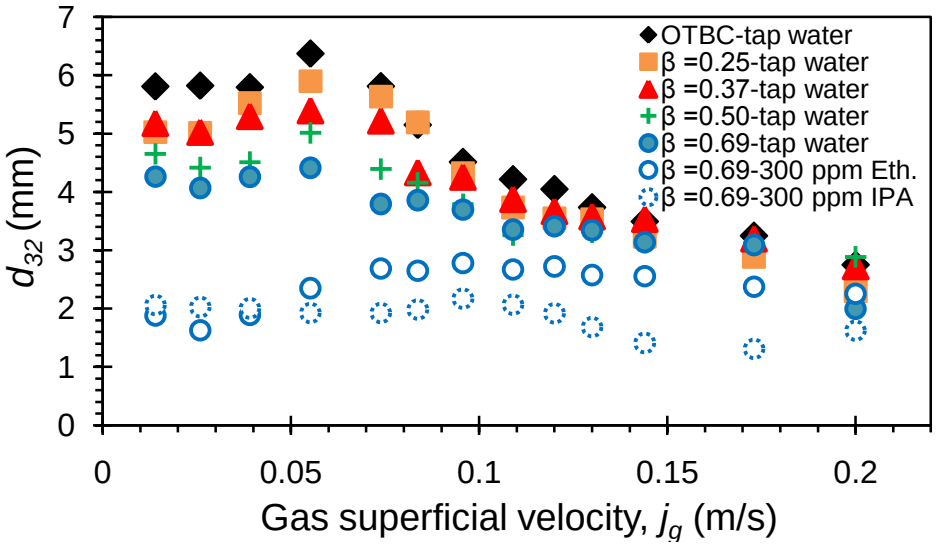


Figure 6.20 Sauter mean diameter for various annular gaps and a porous sparger.

Figure 6.21 illustrates a comparison of d_{32} for the AGBC, β=0.50, using tap water, between the image method and the conductivity probe at the wall of the column. It was noted that both methods gave almost the same results, a decrease in d_{32} with increasing j_g. However, at high j_g, the image method underestimated d_{32} compared to the conductivity probe. The bubbles close to the wall of the column were considered in both methods, and the bubbles were assumed to be evenly distributed in the annular gap around the inner tube. However, the errors may have arisen in that the four-point conductivity probe was introduced at one side of the column, while the pictures were taken from the opposite side.

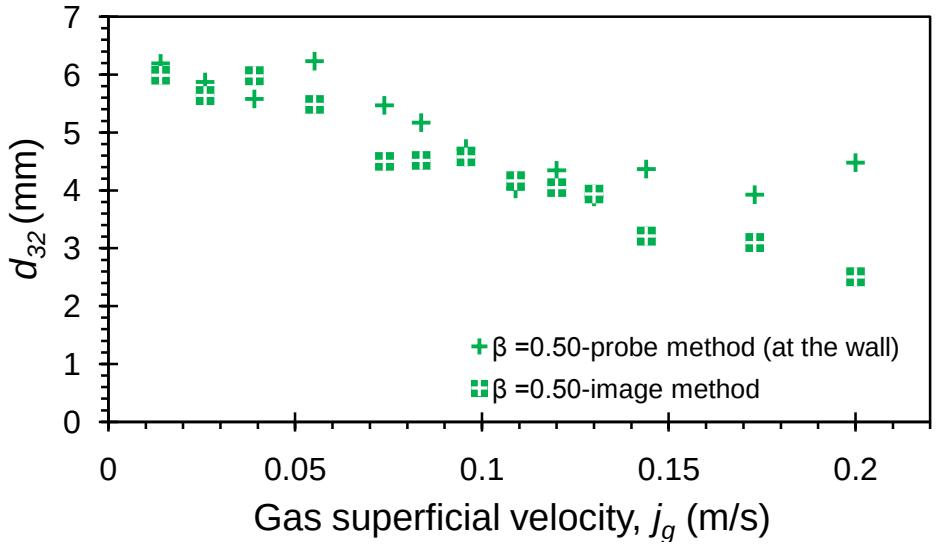


Figure 6.21 The Sauter mean diameter of β= 0.50 for tap water obtained from photographs compared to the probe method at the wall of the column.

6.7.4 Mean diameter, d_{43}, in AGBC

Figure 6.22 illustrates the mean diameters, d_{43}, of the assorted annular gaps compared to the data from the porous sparger. The data were obtained from averaging the local d_{43} across the column using Equation 3.37 and the

$$d_{43} = \frac{\sum d_e^4}{\sum d_e^3}$$

optimisation model. In general, d_{43} shows same effects as d_{32}. The AGBC results with tap water could be classified into two trends with respect to increasing j_g: i) an increasing d_{43} for j_g < 0.055 m/s, where the bubbles coalescence rate increased too, and ii) a decreasing d_{43} for j_g > 0.055 m/s as the bubbles broke up. For all annular gaps, the largest bubble sizes were obtained at j_g = 0.055 m/s where d_{43} ranged from 8 to 11 mm. The AGBC, β=0.69, with 300 ppm ethanol showed a similar trend in terms of d_{43} as for tap water. However, d_{43} increased for a broader range of j_g < 0.084 m/s and decreased for the range j_g > 0.084 m/s. The annular gap, β=0.69, with 300 ppm IPA confirmed that the mean diameter, d_{43}, was almost unaffected by increasing in j_g.

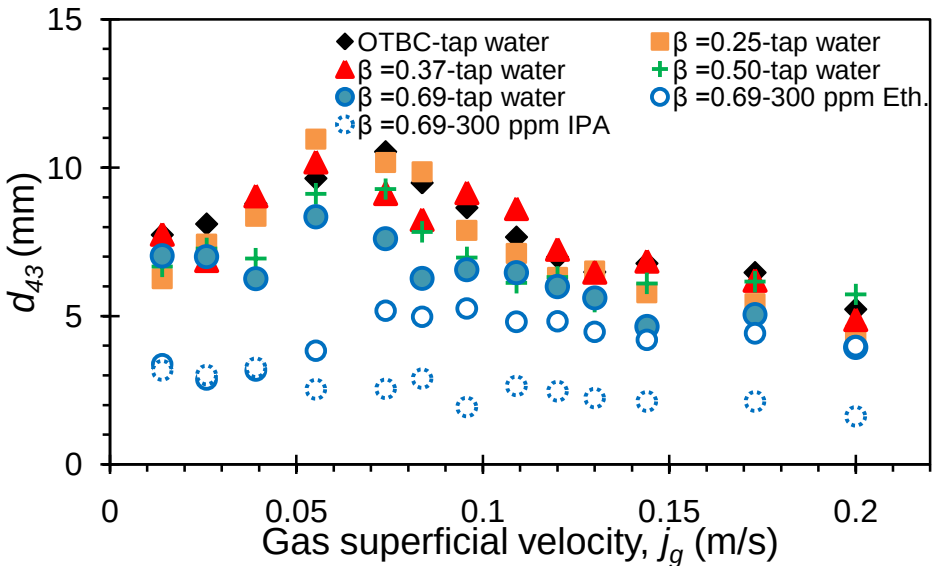


Figure 6.22 Mean diameter, d_{43}, of annular gaps with respect to j_g; legend is the same as in Figure 6.18.

Figure 6.23 shows d_{43} using the image method for the annular gap, β = 0.50, compared to the conductivity probe method at the wall of the column. The data

obtained from the probe are in good agreement with the image results. This confirms that the optimisation model provides excellent predictions of d_{43} results.

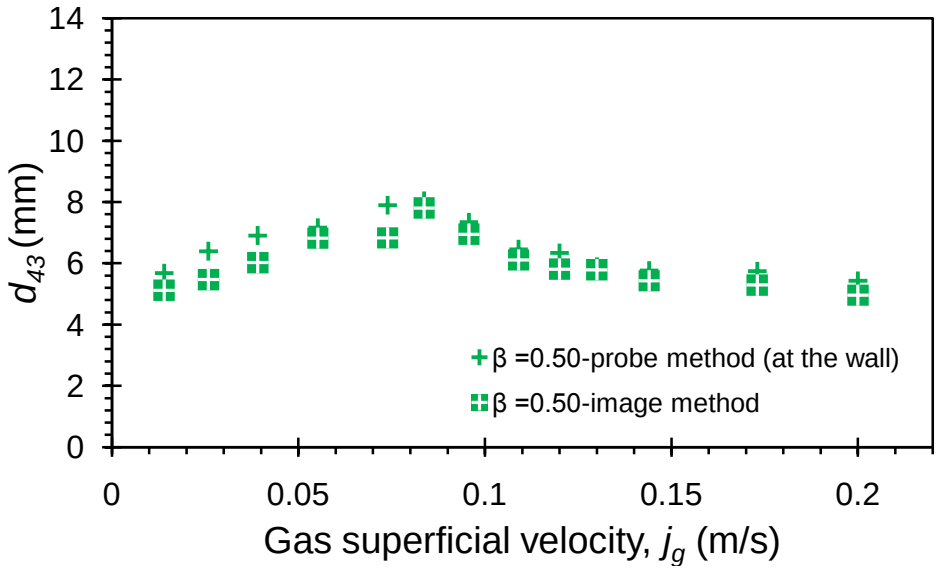


Figure 6.23 The mean diameter d_{43} of β= 0.50 in tap water for the image and the conductivity probe method.

6.7.5 Bubble size distribution in AGBC

The width of the bubble size distribution for the AGBCs and the OTBC are illustrated in Figure 6.24, which is characterised by the standard deviation, σ, of the fitted lognormal bubble size distribution. The results show that, at a low level of j_g < 0.055 m/s, the bubble size distribution for the AGBCs was broader; e.g. the lognormal standard deviations, σ, for β = 0.69 were in the range 1.02–1.12, whereas the bubble size distribution for the OTBC at the same range of j_g was narrow; the σ range was 0.63-1.05. This could indicate that, at low j_g, both large and small bubbles were present in the AGBC experiments; alternatively, large bubbles were almost imperceptible in the OTBC experiments at the same range of j_g. For j_g > 0.055 m/s in the heterogeneous flow, the AGBCs are likely to have similar bubble size distributions as found in the OTBC. This specifies the point at which the flow moved from a homogeneous to a churn-turbulent regime. The bubble size distribution in the annular gap, β = 0.69, with 300 ppm alcohol was narrower compared to tap water. This could be due to the presence of relatively

small bubbles for the whole range of j_g. Also, the IPA results gave a narrow bubble size distribution compared to the ethanol results.

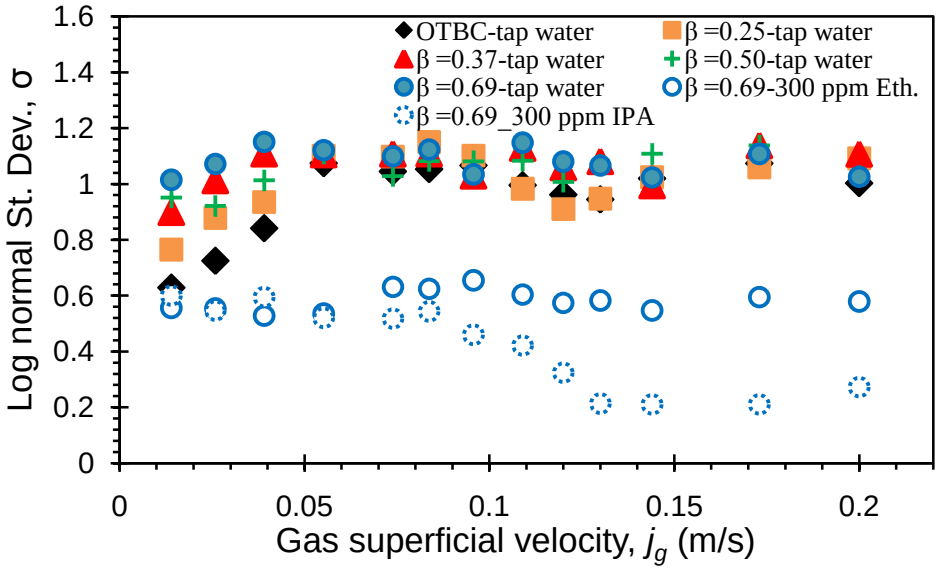


Figure 6.24 Standard deviation of the AGBC compared to the OTBC in tap water and alcohol aqueous solutions.

Figure 6.25 illustrates the lognormal standard deviation of the BSD with respect to j_g. For β = 0.50 in the tap water system, the image method data was compared to the probe results. For low j_g in the homogeneous flow, the bubbles at the wall were relatively small, and were almost all the same size. For high j_g in the heterogeneous flow, the rate of coalescence and breakage of bubbles is high, and so a combination of small and large bubbles is expected. Therefore, both image and probe methods gave broader bubble size distributions.

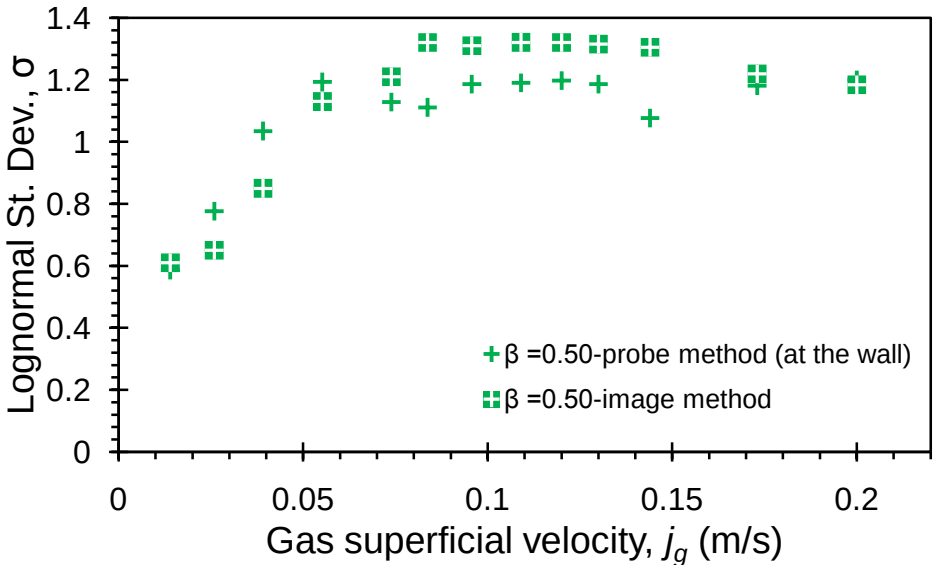


Figure 6.25 Standard deviation of the AGBC compared in tap water; a comparison between the image and probe methods.

6.8 Conclusions

For the AGBCs, the shapes of the local void fraction profiles were affected by increases in β, and the void fraction profiles became increasingly non-uniform and asymmetric. Hence, the value of C_o increased, leading to a reduction in the mean gas void fraction predicted by the drift-flux model. Thus, the combination of formation of large bubbles near the sparger, and the changing shape of the local gas void fraction profile, reduces the mean gas void fraction for a given gas superficial velocity and leads to an earlier transition to heterogeneous flow than would occur in an OTBC. Two reasons were investigated to explain the different gas void fractions between the open tube and the AGBCs: (i) large bubbles were observed in the flow, especially for a large diameter ratio, β. (ii) The local void fraction profiles changed shape with increasing j_g in the homogeneous regime, indicating that, for open tube columns, the distribution parameter, C_o, might not be constant.

It was difficult to distinguish between the transition points for OTBC and different inner tubes with and without different alcohol concentrations. However, the largest inner tube, β= 0.69, clearly deviates from the Richardson and Zaki curve

earlier when compared with the OTBC data. On the other hand, the data from the highest alcohol concentration deviate later compared with the tap water data.

The chord lengths obtained from the conductivity probe offered evidence of the bubble size decreasing as j_g increased in the heterogeneous regime. This was confirmed using the results obtained from the image method. However, the image method used for measuring bubble size distributions had some obvious limitations. At high gas void fractions only the bubbles near the column wall might be detected. Hence, the number of small bubbles might be overestimated since the liquid down flow at the column wall brings small bubbles down with it in the column.

The optimisation model used to convert chord length to bubble size produced results with good agreement, in terms of the trends of the mean chord length. The bubble sizes were reasonable compared to the image method in the annular gaps experiments with both tap water and alcohols. The presence of alcohol appears to generate small bubbles, which keep the homogeneous flow more stable at a high gas superficial velocity. The bubble size decreased and hence gas void fraction increased with an increase in the concentration and length of the carbon chain of the alcohol.

CHAPTER SEVEN

CONCLUSIONS AND RECOMMENDATIONS

7.1 Conclusions

For the purpose of measuring the value of α in an OTBC, two methods were applied, namely using (i) aerated levels and (ii) a conductivity probe. In comparison with the changing aerated level method, the values for α obtained by a two-point conductivity probe were underestimated by 25%. In the discussion of this result, it was proposed that the reason may be (i) that bubbles flowing downward were likely missing the probe needle, which was also facing down, and that (ii) the probe needle was making contact with the bubbles at an eccentric point with respect to their centre, which underestimates the bubble chord length, and as a result underestimates α. Introducing a four-point conductivity probe improved the quality of measurements, reducing the difference in measured values to 12% compared to the changing aerated level method. In all cases, the two- and four-point conductivity probes yielded promising data regarding the profiles for α within the OTBC column.

Two main effects have been considered in this study, which reduce the mean void fraction in AGBCs compared to OTBC, when operated at the same gas superficial velocity and with a porous sparger. Firstly, the introduction of a stream of larger bubbles emanating from a central orifice drilled into the porous sparger has been shown to destabilise an otherwise homogeneous bubbly flow; orifices with diameters greater than 1-2 mm produced fast rising bubbles and the transition to heterogeneous flow occurred at lower mean gas void fractions than for the porous sparer with no central orifice; in some cases the flow appeared to be heterogeneous even at very low gas superficial velocities. In the AGBC, large bubbles are observed in the flow, even at relatively low gas superficial velocities. Similar results for the effects of sparger design on the two-phase flow regime can be found in the literature; for example, in the work of Zuber and Hench (1962). Secondly, the local void fraction profiles changed shape with increasing gas superficial velocity in the homogenous regime.

Measurements of local void fractions in an OTBC showed that the profiles changed shape with increasing gas superficial velocity, particularly in the homogeneous and early transition regimes. The changing shapes of the profiles were analysed by fitting Hibiki and Ishii's (2002) radial distribution to the data, demonstrating that these effects would alter the value of distribution parameter C_o in the homogeneous regime. With the alcohol solutions, there were similar changes to the void fraction profiles and very large centre-line values could be obtained without significant bubble coalescence. Mean void fractions were up to 150% of the tap water values with low concentrations of ethanol or IPA and even the smallest addition of 8 ppm ethanol produced a noticeable effect on coalescence. IPA had a stronger effect on the two-phase hydrodynamics in the OTBC, because of its greater carbon chain length than ethanol. Transition point void fractions and gas superficial velocities were obtained, which demonstrated that the OTBC homogeneous flow regime could be significantly extended with small additions of ethanol or IPA; the transition was delayed until the void fraction exceeded $\alpha > 0.6$ in the highest alcohol concentrations.

For the AGBC, an increasing diameter ratio β (narrower annular gap) led to the local void fraction profiles becoming increasingly non-uniform and asymmetric leading to a reduction in the mean gas void fraction predicted by the drift flux model. Although existing profile models could not be satisfactorily fitted to the local void fraction data, it was evident that these shape changes would affect the distribution parameter C_o in the drift-flux model. This was confirmed by fitting values of C_o and v_t to mean void fraction results over a range of gas superficial velocities for the alcohol solutions: C_o increased with an increasing diameter ratio, reflecting the reduction in the mean gas void fraction predicted by the drift-flux model, which was consistent with the changing profile shapes. However, with the alcohol solutions there was no strong evidence of a change of bubble size with changing diameter ratio, β. The combination of large bubble formation near the sparger and changing shapes of the local gas void fraction profile, reduce the mean gas void fraction for a given gas superficial velocity, and lead to an earlier transition to heterogeneous flow than would occur in an OTBC. The presence of

surface active molecules, such as alcohols, led to transition at higher values of the void fraction, but the effect was not as strong as in the OTBC.

From the experiments on the OTBC with tap water and aqueous solutions of alcohol, two distinct trends, with respect to bubble chord length, were observed; these were dependent on the values of j_g. (i) Initially, as the values of j_g increased from a low level with homogeneous flow, mean chord length was seen to also increase. However, (ii) as j_g increased further, mean chord length values began to decrease. Therefore, bubble size represented by mean chord length was seen to reduce as j_g increased. This was confirmed by visual analysis of photographs taken of the experiment. In the AGBC, the trend of reducing chord length (i.e. bubble size) was also observed from measurements by the conductivity probe, in the heterogeneous flow regime, as j_g increased; this result was in agreement with the observations made for the OTBC, and was also confirmed by photographs taken of the experiment, and analysed, in applying the image method.

The transformation of bubble size was implemented using the forward analytical method, and an optimisation approach as a backward method. At a fixed φ, the analytical method was validated by the Monte-Carlo approach. The challenge was to consider a variable φ in the transformation method and yet the model fitted very well with the experimental results. The distribution of bubble size was calculated by a process of transforming the distribution of chord length measured in the experiment; chord length and bubble size exhibit the same trend. This transformation process was further confirmed by the image method, since the results of both, in terms of bubble size and the corresponding trends, were in good agreement. Both methods demonstrated that bubble diameter was reduced by the addition of alcohol to the water.

7.2 Recommendations and future work

The following recommendations are either a modification to the design of the column, including more additives, expanding two-phase to multiphase flow or proposing model processes. These were considered for two reasons: (i) the time constraints, and because (ii) some of the recommendations are beyond the scope of this study.

- Column design: A vertical column was considered in the current study to compare the void fraction in the OTBC with the AGBC. However, chemical processes have many examples of horizontal and inclined columns, e.g. in oil fields, for the pipes used to lift up the crude oil. Therefore, it is worth investigating the void fraction in the OTBC at various angles of inclination, and comparing it with the AGBC.
- Additive and surfactant: Air-tap water and air-aqueous solution (ethanol and IPA) were considered in the present investigation; however, it is quite important to study the influence of the addition of various organic and inorganic compounds on the void fraction and bubble size in both types of columns (OTBC and AGBC). It is recommended that the investigation is expanded to include the addition of nano-particles, and to study their effect on void fraction and bubble size.
- Fluid types: The consideration of including various liquids in the same comparison to study the effect of the density and viscosity on the transition conditions void fraction and bubble size.
- The data extracted from the four-point conductivity probe mainly considered the void fraction and axial velocity. However, the radial and azimuthal velocities could be considered to get the corresponding bubble size (Lucas and Mishra, 2005). The orientation of the bubble or the angle, θ, could be extracted from the four-point probe as it helps in understanding the behaviour of the bubbles in different regimes, and to establish, with bubble size, velocity and aspect ratio, a model of the bubbles in the homogeneous and churn-turbulent regimes.
- The model proposed by Ozar *et al.* (2008) for the profiles in AGBC was not able to characterise the profiles. These profiles are asymmetric about the

centre-line ,and the shape of the profile clearly changes with the geometry of the annular gap, while the inner wall void fraction is non-zero and close to the maximum value in the radial profile. Therefore, it is worth developing a model to describe the asymmetry of the void fraction profiles in the AGBC, which considers the non-zero void fraction at the inner wall.

- The current data gathered from the conductivity probe could be used to build a model, which simulates the flow in the OTBC and AGBC.

REFERENCES

ACUÑA, C. and FINCH, J., 2010. Tracking velocity of multiple bubbles in a swarm. *International Journal of Mineral Processing,* **94**(4), pp. 147-158.

AKITA, K. and YOSHIDA, F., 1974. Bubble Size, Interfacial Area, and Liquid-Phase Mass Transfer Coefficient in Bubble Columns. *Industrial & Engineering Chemistry Process Design and Development,* **13**(1), pp. 84-91.

ALBIJANIC, B., HAVRAN, V., PETROVIC, D., DURIC, M. and TEKIC; M., 2007. Hydrodynamics and mass transfer in a draft tube airlift reactor with dilute alcohol solutions. *AIChE J.*, **53**, pp. 2897– 2904.

AL-OUFI, F.M., 2006. *Measuring void fraction in gas-liquid flow using conductivity*, MSc Dissertation, Loughborough University.

ANASTASIOU, A., KAZAKIS, N., MOUZA, A. and PARAS, S., 2010. Effect of organic surfactant additives on gas holdup in the pseudo-homogeneous regime in bubble columns equipped with fine pore sparger. *Chemical Engineering Science,* **65**(22), pp. 5872-5880.

ANDERSON, J. and QUINN, J., 1970. Bubble columns: flow transitions in the presence of trace contaminants. *Chemical Engineering Science,* **25**(3), pp. 373-380.

ANGELI, P. and HEWITT, G., 2000. Flow structure in horizontal oil–water flow. *International Journal of Multiphase Flow,* **26**(7), pp. 1117-1140.

AZZOPARDI, B., ABDULKAREEM, L., ZHAO, D., THIELE, S., DA SILVA, M., BEYER, M. and HUNT, A., 2010. Comparison between Electrical Capacitance Tomography and Wire Mesh Sensor Output for Air/Silicone Oil Flow in a Vertical Pipe. *Industrial & Engineering Chemistry Research,* **49**(18), pp. 8805-8811.

BAO, Y., CHEN, L., GAO, Z. and CHEN, J., 2010. Local void fraction and bubble size distributions in cold-gassed and hot-sparged stirred reactors. *Chemical Engineering Science,* **65**(2), pp. 976-984.

BLANCH, H. and CLARK, D., 1996. *Biochemical engineering*; Dekker: New York.

CAETANO, E., 1984. Two-phase flow in a vertical annulus. TUFFP Report, Univ. of Tulsa, OK.

CAETANO, E., SHOHAM, O. and BRILL, P., 1992. Upward Vertical Two-Phase Flow Through an Annulus-- Part I: Single-Phase Friction Factor, Taylor Bubble Rise Velocity, and Flow Pattern Prediction. *Journal of Energy Resources Technology,* **114**(1), pp. 1-13.

CAMARASA, E., VIAL, C., PONCIN, S., WILD, G., MIDOUX, N. and BOUILLARD, J., 1999. Influence of coalescence behaviour of the liquid and of gas sparging on hydrodynamics and bubble characteristics in a bubble column. *Chemical Engineering and Processing,* **38**(4-6), pp. 329-344.

CHEN, R., REESE, J. and FAN, L., 1994. Flow structure in a three-dimensional bubble column and three-phase fluidized bed. *AICHE Journal,* **40**(7), pp. 1093-104.

CHENG, H., HILLS J. and AZZOPARDI B., 1998. A Study of the Bubble-To-Slug Transition in Vertical Gas-Liquid Flow in Columns of Different Diameter. *Int. J. Multiphase Flow,* **24**(3), pp. 431–452.

CLARK, N., and TURTON, R., 1988. Chord length distributions related to bubble size distributions in multiphase flows. *International Journal of Multiphase Flow,* **14**(4), pp. 413–424.

CLARK, N., LIU, W. and TURTON, R., 1996. Data interpretation techniques for inferring bubble size distribution from probe signals in fluidized systems. *Powder Technology,* **88**(2), pp. 179-188.

CLIFT, R., 1978. *Bubbles, drops, and particles.* New York ; London: Academic Press.

CLIFT, R., GRACE, J.R. and WEBER, M.E., 2005. *Bubbles, Drops and Particles.* Second edition. Academic Press, New York.

COLELLA, D., VINCI, D., BAGATIN, R., MASI, M. and ABU BAKR, E., 1999. A study on coalescence and breakage mechanisms in three different bubble columns. *Chemical Engineering Science* **54**(21), pp. 4767-4777.

COULSON, J., RICHARDSON, J., BACKHURST, J. and HARKER, J., 1999. *Coulson & Richardson's Chemical Engineering*, Butterworth-Heinemann, Boston MA, pp.149-195.

CUMMING, I., RIELLY, C. and MASON, A., 2002. Hydraulic Performance of an Annular Plunging Jet Factor. *Trans. I. Chem. E*., Part A **80**, pp. 543–549.

DAS, A. and DAS, P., 2010. Modelling bubbly flow and its transitions in vertical annuli using population balance technique. *The International Journal of Heat and Fluid Flow.,* **31**(1), pp. 101-114.

DAS, G., DAS, P., PUROHIT, N. and MITRA, A., 1999. Flow pattern transition during gas liquid upflow through vertical concentric annuli—part I: experimental investigations. ASME *Journal of Fluids Engineering* **121**, pp. 895–901.

DECKWER, W., 1992. *Bubble column reactors*; Wiley: New York.

DEVANATHAN, N., DUDUKOVIC, M., LAPIN, A. and LÜBBERT, A., 1995. Chaotic flow in bubble column reactors. *Chemical Engineering Science,* **50**(16), pp. 2661-2667.

DIAS, S., FRANÇA, F. and ROSA, E., 2000. Statistical method to calculate local interfacial variables in two-phase bubbly flows using intrusive crossing probes. *International Journal of Multiphase Flow,* **26**(11), pp. 1797-1830.

DRAHOŠ, J., ZAHRADNÍK, J., PUNČOCHÁŘ, M., FIALOVÁ, M. and BRADKA, F., 1991. Effect of operating conditions on the characteristics of pressure fluctuations in a bubble column. *Chemical Engineering and Processing: Process Intensification,* **29**(2), pp. 107-115.

GAUDIN, A., 1957. *Flotation*. Second edition. McGraw-Hill Book Co.: New York.

HAMAD, F., IMBERTON, F. and BRUUN, H., 1997. An Optical Probe for Measurements in Liquid-Liquid Two-phase Flow. *Meas. Sci. Technol.,* **8**, pp. 1122-1132.

HANSELMANN, W. and WINDHAB, E., 1999. Flow characteristics and modelling of foam generation in a continuous rotor/stator mixer. *Journal of Food Engineering*, **38**, pp. 393–405.

HARMATHY, T., 1960. Velocity of large drops and bubbles in media of infinite or restricted extent. *AICHE Journal,* **6**(2), pp. 281-288.

HASAN, A. and KABIR, C., 1988. A study of multiphase flow behaviour in vertical oil wells. *SPE Prod. Eng.,* **3**(a), pp. 263-272.

HASAN, A. and KABIR, C., 1988. Predicting multiphase flow behaviour in a deviated well. *SPE Prod. Eng.,* **3**(b), pp. 474-482.

HASAN, A. and KABIR, C., 1992. 2-phase flow in vertical and inclined annuli. *International Journal of Multiphase Flow,* **18**(2), pp. 279-293.

HASAN, A., KABIR, C. and RAHMAN, R., 1988. Predicting the liquid gradient in a pumping-well annulus. *SPE Prod. Eng.* **3**, pp. 113-120; Trans. AIME 285.

HERRINGE, R. and DAVIS, M., 1976. Structural development of gas-liquid mixture flows. *Journal of Fluid Mechanics,* **73**, pp. 97-123.

HIBIKI, T. and ISHII, M., 2002. Distribution parameter and drift velocity of drift-flux model in bubbly flow. *International Journal of Heat and Mass Transfer,* **45**(4), pp. 707-721.

HILLS, J. and DARTON, R., 1976. Rising velocity of a large bubble in a bubble swarm. *Transactions of the Institution of Chemical Engineers,* **54**(4), pp. 258-264.

HONG, M., CARTELLIER, A. and HOPFINGER, E., 2004. Characterization of phase detection optical probes for the measurement of the dispersed phase parameters in sprays. *International Journal of Multiphase Flow,* **30**(6), pp. 615-648.

HU, B., PANAGIOTA, A., OMAR M., CHRISTOPHER, L. and GEOFFREY, H., 2006. Evaluation of drop size distribution from chord length measurements. *AIChE Journal* **52**(3), pp. 931-939.

HUGHMARK, G., 1967. Holdup and Mass Transfer in Bubble Columns. *Industrial & Engineering Chemistry Process Design and Development,* **6**(2), pp. 218-220.

INGRAM, C., 2006; *The drinking Water book: how to eliminate harmful toxins from your water*, 2nd ed.; Celestial Arts: Berkeley, CA.

ISHII, M., 1975. *Thermo-fluid dynamic theory of two-phase flow*. Paris: Eyrolles.

JAMIALAHMADI, M. and MÜULLER-STEINHAGEN, H., 1992. Effect of alcohol, organic acid and potassium chloride concentration on bubble size, bubble rise velocity and gas hold- up in bubble columns. *The Chemical Engineering Journal and The Biochemical Engineering Journal,* **50**(1), pp. 47-56.

JAMIALAHMADI, M. and MÜULLER-STEINHAGEN, H., 1993. Effect of Superficial Gas Velocity on Bubble Size, Terminal Bubble Rise Velocity and Gas Hold-up in Bubble Columns. *Developments in Chemical Engineering and Mineral Processing,* **1**(1), pp. 16-31.

JAMIALAHMADI, M., BRANCH, C. and MÜLLER-STEINHAGEN, H., 1994. Terminal bubble rise velocity in liquids. *CHEMICAL ENGINEERING RESEARCH & DESIGN,* **72**, pp. 119-122.

JAMIALAHMADI, M., MULLER-STEINHAGEN, H., SARRAFI, A. and SMITH, J., 2000. Studies of Gas Holdup in Bubble Column Reactors. *Chemical Engineering and Technology,* **23**(10), pp. 919-921.

JONES, O. and DELHAYE, J., 1976. Transient and statistical measurement techniques for two-phase flows: A critical review. *International Journal of Multiphase Flow,* **3**(2), pp. 89-116.

JULIA, J., HARTEVELD, W., MUDDE, R. and VAN DEN AKKER, H., 2005. On the accuracy of the void fraction measurements using optical probes in bubbly flows. *Review of Scientific Instruments,* **76**(3), pp. 035103-035103-13.

JUNKER, B., 2006. Measurement of bubble and pellet size distributions: past and current image analysis technology. *Bioprocess and Biosystems Engineering,* **29**(3), pp. 185-206.

KANTARCIA, N., BORAKB, F. and ULGENA, K., 2005. Bubble Column Reactors. *Process Biochem.*, ***40***, pp. 2263-2283.

KASTANEK, F., ZAHRADNIK, J., KRATOCHVIL, J. and CERMAK, J., 1993. *Chemical reactors for gas-liquid systems.* New York ; London: Ellis Horwood.

KAZAKIS, N., MOUZA, A. and PARAS, S., 2008. Experimental study of bubble formation at metal porous spargers: Effect of liquid properties and sparger characteristics on the initial bubble size distribution. *Chemical Engineering Journal,* **137**(2), pp. 265-281.

KAZAKIS, N., PAPADOPOULOS, I. and MOUZA, A., 2007. Bubble columns with fine pore sparger operating in the pseudo-homogeneous regime: Gas hold up prediction and a criterion for the transition to the heterogeneous regime. *Chemical Engineering Science,* **62**(12), pp. 3092-3103.

KELESSIDIS, V. and DUKLER, A., 1989. Modelling flow pattern transitions for upward gas-liquid flow in vertical concentric and eccentric annuli. *International Journal of Multiphase Flow,* **15**(2), pp. 173-191.

KELKAR, B., GODBOLE, S., HONATH, M., SHAH, Y., CARR, N. and DECKWER, W., 1983. Effect of addition of alcohols on gas holdup and backmixing in bubble columns. *AICHE Journal,* **29**(3), pp. 361-369.

KRISHNA, R., 2000. Scale-up strategy for a commercial scale bubble column slurry reactor for Fischer-Tropsch synthesis. *Oil and Gas Science and Technology,* **55**(4), pp. 359-393.

KRISHNA, R., DREHER, A. and URSEANU, M., 2000. Influence of alcohol addition on gas hold-up in bubble columns: Development of a scale up model. *International Communications in Heat and Mass Transfer,* **27**(4), pp. 465-472.

KRISHNA, R., URSEANU, M. and DREHER, A., 2000. Gas hold-up in bubble columns: influence of alcohol addition versus operation at elevated pressures. *Chemical Engineering and Processing,* **39**(4), pp. 371-378.

KULKARNI, A. and JOSHI, J., 2005. Bubble Formation and Bubble Rise Velocity in Gas-Liquid Systems: A Review. *Industrial & Engineering Chemistry Research,* **44**(16), pp. 5873-5931.

LAGE, P. and ESPÓSITO, R., 1999. Experimental determination of bubble size distributions in bubble columns: prediction of mean bubble diameter and gas hold up. *Powder Technology,* **101**(2), pp. 142-150.

LEE, S., SORIA, A. and LASA, H., 1990. Evolution of Bubble Length Distributions in Three-Phase Fluidized Beds. *AIChE J.,* **36**, pp. 1763–1767.

LIU, W. and CLARK, N., 1995. Relationships between distributions of chord lengths and distributions of bubble sizes including their statistical parameters. *International Journal of Multiphase Flow,* **21**(6), pp. 1073-1089

LUCAS, D. KREPPER, E. and PRASSER, H., 2005a. Development of co-current air–water flow in a vertical pipe, *International Journal of Multiphase Flow*, **31**, pp. 1304–1328

LUCAS, G. and MISHRA, R., 2005. Measurement of bubble velocity components in a swirling gas-liquid pipe flow using a local four-sensor conductance probe. *Measurement Science & Technology,* **16**(3), pp. 749-758.

LUCAS, G., MISHRA, R. and PANAYOTOPOULOS, N., 2004. Power law approximations to gas volume fraction and velocity profiles in low void fraction vertical gas–liquid flows. *Flow Measurement and Instrumentation,* **15**(5-6), pp. 271-283.

LUO, X., ZHANG, J., TSUCHIYA, K. and FAN, L., 1997. On the rise velocity of bubbles in liquid-solid suspensions at elevated pressure and temperature. *Chemical Engineering Science,* **52**(21), pp. 3693-3699.

LUTHER, S., RENSEN, J. and GUET, S., 2004. Bubble aspect ratio and velocity measurement using a four-point fiber-optical probe. *Experiments in Fluids,* **36**(2), pp. 326-333.

MAJUMDER, A., 2008. Analysis of dispersion coefficient of bubble motion and velocity charactersisation factor in downflow and upflow bubble column reactor. *Chem. Eng. Sci.*, **63**, pp. 3160–3170.

MARQUARDT, D., 1963. An algorithm for least squares estimation of nonlinear parameters, *SIAM J. Appl. Math.* **11** (2), pp. 431–441.

MARUYAMA, T., YOSHIDA, S. and MIZUSHINA, T., 1981. Flow transition in a bubble column. *Journal of Chemical Engineering of Japan,* **14**(5), pp. 352-357.

MENDELSON, H., 1967. The prediction of bubble terminal velocities from wave theory. *AICHE Journal,* **13**(2), pp. 250-253.

MERCHUK, J., CONTRERAS, A., GARCÍA, F. and MOLINA, E., 1998. Studies of mixing in a concentric tube airlift bioreactor with different spargers. *Chemical Engineering Science,* **53**(4), pp. 709-719.

MILLIES, M. and MEWES, D., 1999. Interfacial area density in bubbly flow. *Chemical Engineering and Processing,* **38**(4-6), pp. 307-319.

MISHRA, R., LUCAS, G. and KIECKHOEFER, H., 2002. A model for obtaining the velocity vectors of spherical droplets in multiphase flows from measurements using an orthogonal four-sensor probe. *Measurement science & technology.,* **13**, pp. 1488-1498.

MIYAHARA, T. and NAGATANI, N., 2009. Influence of alcohol addition on liquid-phase volumetric mass transfer coefficient in an external-loop airlift reactor with a Porous Plate. *Journal of chemical engineering of Japan,* **42**, pp. 713-719.

MIYAHARA, T. and TANAKA A., 1997. Size of bubbles generated from porous plates. *Journal of Chemical Engineering of Japan*, **30**, pp. 353-355.

MIYAHARA, T., HAMAGUCHI, M., SUKEDA, Y. and TAKAHASHL, T., 1986. Size of bubbles and liquid circulation in a bubble column with a draught tube and sieve plate. *The Canadian Journal of Chemical Engineering,* **64**(5), pp. 718-725.

MOLERUS, O., 1993. *Principles of flow in disperse systems.* London: Chapman & Hall.

NAHRA, H. and KAMOTANI, Y., 2003. Prediction of bubble diameter at detachment from a wall orifice in liquid cross-flow under reduced and normal gravity conditions. *Chemical Engineering Science,* **58**(1), pp. 55-69.

OHKI, Y. and INOUE, H., 1970. Longitudinal mixing of the liquid phase in bubble columns. *Chemical Engineering Science,* **25**(1), pp. 1-16.

ONG, B., GUPTA, P., YOUSSEF, A., AL-DAHHAN, M. and DUDUKOVICÌ, M., 2009. Computed Tomographic Investigation of the Influence of Gas Sparger Design on Gas Holdup Distribution in a Bubble Column. *Industrial & Engineering Chemistry Research,* **48**(1), pp. 58-68.

OZAR, B., JEONG, J., DIXIT, A., JULIA, J., HIBIKI, T. and ISHII M., 2008. Flow Structure of Gas–Liquid Two-Phase Flow in an Annulus. *Chem. Eng. Sci.* **63**, pp. 3998–4011.

PANAGIOTOPOULOS, N., 2009. PhD Thesis, *Measurement of the Local Properties of Multiphase Flows*, Huddersfield University, UK.

PRESS, W., TEUKOLSKY, S., VETTERLING, W. and FLANNERY, B., 1992. *Numerical Recipes in Fortran*, 2nd edn. Cambridge University Press, Cambridge.

PRINCE, M. and BLANCH, H., 1999. Bubble coalescence and break-up in air-sparged bubble columns, *AICHE J.*, **36**, pp. 1485-1499.

RAKOCZY, R. and MASIUK, S., 2009. Experimental study of bubble size distribution in a liquid column exposed to a rotating magnetic field. *Chemical Engineering and Processing: Process Intensification,* **48**(7), pp. 1229-1240.

RICHARDSON, J. and ZAKI, W., 1954. Sedimentation and fluidisation., *Transactions of the Institute of Chemical Engineering* **32**, pp. 35–53.

RUZICKA, M., DRAHOS, J., FIALOVÁ, M. and THOMAS, N., 2001. Effect of bubble column dimensions on flow regime transition. *Chemical Engineering Science,* **56**(22), pp. 6117-6124.

RUZICKA, M., ZAHRADNÍK, J., DRAHOS, J. and THOMAS, N., 2001. Homogeneous–heterogeneous regime transition in bubble columns. *Chemical Engineering Science,* **56**(15), pp. 4609-4626.

SADA, E.; KUMAZAWA, H. and LEE, C., 1986. Influences of Suspended Fine Particles on Gas Holdup and Mass Transfer Characteristics in a Slurry Bubble Column. *AIChE J.*, **32**, pp. 853-856.

SADATOMI, M., SATO, Y. and SARUWATARI, S., 1982. Two-phase flow in vertical noncircular channels. *International Journal of Multiphase Flow,* **8**(6), pp. 641-655.

SARRAFI, A., JAMIALAHMADI, M., MULLER-STEINHAGEN, H. and SMITH, J., 1999. Gas holdup in homogeneous and heterogeneous gas-liquid bubble column reactors. *Canadian Journal of Chemical Engineering,* **77**(1), pp. 11-21.

SCHUGERL, K., LUCKE, J. and OELS, U., 1977. Bubble Column Bioreactors. *Adv. Biochem. Eng.* **7**, pp. 1–84.

SCOTT, D.W., 1979. On optimal and data-based histograms. *Biometrika,* **66**(3), pp. 605-610.

SERIZAWA, A., KATAOKA, I. and MICHIYOSHI, I., 1975. Turbulence structure of air-water bubbly flow—I. measuring techniques. *International Journal of Multiphase Flow,* **2**(3), pp. 221-233.

SERIZAWA, A., KATAOKA, I. and MICHIYOSHI, I., 1975. Turbulence structure of air-water bubbly flow—II. local properties. *International Journal of Multiphase Flow,* **2**(3), pp. 235-246.

SHAH, Y., KELKAR, B., GODBOLE, S. and DECKWER, W., (1982). Design parameters estimations for bubble column reactors. *AIChE Journal*, **28**(3), pp. 353-379.

SHAIKH, A. and AL-DAHHAN, M., 2007. A Review on Flow Regime Transition in Bubble Columns. *International Journal of Chemical Reactor Engineering,* Vol. **5**: R1

SHAMLOU, P., POLLARD, D., ISON, A. and LILLY, M., 1994. Gas holdup and liquid circulation rate in concentric-tube airlift bioreactors. *Chemical Engineering Science,* **49**(3), pp. 303-312.

SHEN, G., and FINCH, J., 1997. Bubble swarm velocity in a column: a two-dimensional approach. *Chemical Engineering Science,* **52**(19), pp. 3287-3293.

SHNIP, A., KOLHATKAR, R., SWAMY, D. and JOSHI, J., 1992. Criteria for the transition from the homogeneous to the heterogeneous regime in two-dimensional bubble column reactors. *International Journal of Multiphase Flow,* **18**(5), pp. 705-726.

SHOLLENBERGER, K., GEORGE, D., and TORCZYNSLCI, J., 2000. Effect of Sparger Geometry on Gas-Volume-Fraction in Bubble-Column Flows Measured by Gamma Densitometry Tomography (GDT). *AIChE 2000 Annual Meeting*, Los Angeles, CA, US.

SIJACKI, I., COLOVIC, R., PETROVIC, D. TEKIC, D. and DURIC, M., 2010. Diluted alcohol solutions in bubble columns and draft tube airlift reactors with a single orifice sparger: experiments and simple correlations. *Journal of Chemical Technology and Biotechnology.,* **85**(1), pp. 39-49.

STEINEMANN, J. and BUCHHOLZ, R., 1984. Application of an Electrical Conductivity Microprobe for the Characterization of bubble behavior in gas-liquid bubble flow. *Particle & Particle Systems Characterization,* **1**(1-4), pp. 102-107.

SUN, X., KURAN, S. and ISHII, M., 2004. Cap bubbly-to-slug flow regime transition in a vertical annulus. *Experiments in Fluids,* **37**(3), pp. 458.

TEYSSEDOU, A., TAPUCU, A. and LORTIE, M., 1988. Impedance probe to measure local void fraction profiles. *Review of Scientific Instruments,* **59**(4), pp. 631-638.

THORAT, B., SHEVADE, A., BHILEGAONKAR, K., AGLAWE, R., PARASU VEERA, U., THAKRE, S., PANDIT, A., SAWANT, S. and JOSHI, J., 1998. Effect of Sparger Design and Height to Diameter Ratio on Fractional Gas Hold-up in Bubble Columns. *Chemical Engineering Research and Design,* **76**(7), pp. 823-834.

TINGE, J. and DRINKENBURG, A., 1986. The influence of slight departures from vertical alignment on liquid dispersion and gas hold-up in a bubble column. *Chemical Engineering Science,* **41**(1), pp. 165-169.

TSE, K., MARTIN, T., MCFARLANE, C. and NIENOW, A., 2003. Small bubble formation via a coalescence dependent break-up mechanism. *Chemical Engineering Science,* **58**(2), pp. 275-286.

TSUCHIYA, K. and NAKANISHI, O., 1992. Gas holdup behavior in a tall bubble column with perforated plate distributors. *Chemical Engineering Science,* **47**(13-14), pp. 3347-3354.

TURTON, R. and CLARK, N., 1989. Interpreting probe signals from fluidized beds. *Powder Technology,* **59**(2), pp. 117-123.

UEYAMA, K. and MIYAUCHI, T., 1979. Properties of recirculating turbulent two phase flow in gas bubble columns. *AICHE Journal,* **25**(2), pp. 258-266.

UEYAMA, K., TSURU, T. and FURUSAKI, S., 1989. Flow transition in a bubble column. *International Chemical Engineering,* **29**(3), pp. 523-529.

URSEANU, M., 2000. *Scaling up bubble column reactors*, PhD Thesis, University of Amsterdam, Netherlands.

VAN BATEN, J. and KRISHNA, R., 2001. Eulerian simulations for determination of the axial dispersion of liquid and gas phases in bubble columns operating in the churn-turbulent regime. *Chemical Engineering Science,* **56**(2), pp. 503-512.

VAN DER WELLE, R., 1985. Void fraction, bubble velocity and bubble size in two-phase flow. *International Journal of Multiphase Flow,* **11**(3), pp. 317-345.

VARMA, R. and AL-DAHHAN, M., 2007. Effect of sparger design on hydrodynamics of a gas recirculation anaerobic bioreactor. *Biotechnology and bioengineering,* **98**(6), pp. 1146-1160.

VAZQUEZ, G., ALVAREZ, E. and NAVAZA, J., 1995. Surface Tension of Alcohol Water + Water from 20 to 50 degreesC. *Journal of Chemical & Engineering Data,* **40**(3), pp. 611-614.

VIJAYAN, M., SCHLABERG, H. and WANG, M., 2007. Effects of sparger geometry on the mechanism of flow pattern transition in a bubble column. *Chemical Engineering Journal,* **130**(2-3), pp. 171-178.

WALLIS, G., 1969. *One-dimensional two-phase flow*. New York: McGraw-Hill.

WALLIS, G., 1974. The terminal speed of single drops or bubbles in an infinite medium. *International Journal of Multiphase Flow*, **1**(4), pp.491-511.

WANG, H., and DONG, F., 2009. A method for bubble volume calculating in vertical two-phase flow. *Journal of Physics: Conference Series,* **147**, pp. 012018.

WELLEK, R., ARAWAL, A. and SKELLAND, A., 1966. Shapes of liquid drops moving in liquid media. *A.I.Ch.E. Journal,* **12**, pp. 854–862.

WERTHER, J., 1974a. Bubbles in gas fluidized beds—Part I. *Trans. Inst. Chem. Engrs* **52** (1974), pp. 149–159.

WERTHER, J., 1974b. Bubbles in gas fluidized beds—Part II. *Trans. Inst. Chem. Engrs* **52** (1974), pp. 160–169.

WHALLEY, P., 1996. *Two-phase flow and heat transfer.* Oxford: Oxford University Press.

WILKINSON, P., 1991. *Physical aspects and scale-up of high pressure bubble columns*, PhD Thesis, University of Groningen, Netherlands.

WILKINSON, P., SPEK, A. and VAN DIERENDONCK, L., 1992. Design parameters estimation for scale-up of high-pressure bubble-columns. *AICHE Journal,* **38**(4), pp. 544-554.

WONGSUCHOTO, P., CHARINPANITKUL, T. and PAVASANT, P., 2003. Bubble size distribution and gas–liquid mass transfer in airlift contactors, *Chem. Eng. J.* **92**, pp. 81–90.

WU, Q., WELTER, K., MCCREARY, D. and REYES, J., 2001. Theoretical studies on the design criteria of double-sensor probe for the measurement of bubble velocity. *Flow Measurement and Instrumentation,* **12**(1), pp. 43-51.

YAMASHITA, F., 1985. Effect of liquid depth, column inclination and baffle plates on gas holdup in bubble-columns. *Journal of Chemical Engineering of Japan,* **18**(4), pp. 349-353.

YAMASHITA, F., 1995. Effect of Foam Layer on Gas Holdup in a Bubble Column. *Journal of Chemical Engineering of Japan*, **28**(6), pp. 837-940.

YAMASHITA, F., 1998. Effect of clear liquid height and gas inlet height on gas holdup in a bubble column. *Journal of Chemical Engineering of Japan,* **31**(2), pp. 285-288.

YANG, G., DU, B. and FAN, L., 2007. Bubble formation and dynamics in gas–liquid–solid fluidization—A review. *Chemical Engineering Science,* **62**(1-2), pp. 2-27.

ZAHRADNÍK, J., FIALOVÁ, M., RUZICKA, M., DRAHOS, J., KASTÁNEK, F. and THOMAS, N., 1997. Duality of the gas-liquid flow regimes in bubble column reactors. *Chemical Engineering Science,* **52**(21-22), pp. 3811-3826.

ZAHRADNIK, J., KUNCOVA, M. and FIALOVA M., 1999 .The effect of surface active additives on bubble coalescence and gas holdup in viscous aerated batches. *Chem. Eng. Sci.,* **54**, 2401-2408.

ZHAO, D., GUO, L., LIN, C. and ZHANG, X., 2005. An experimental study on local interfacial area concentration using a double-sensor probe. *International Journal of Heat and Mass Transfer,* **48**(10), pp. 1926-1935.

ZHAO, X, LUCAS, G., and PRADHAN, S., 2009. Signal Processing method in using four-sensor probe for measuring the velocity vector of air-liquid two phase flow. *Journal of the Japanese Society of Experimental Mechanics (JSEM)*, **9**, pp. 19-24.

ZUBER, H. and HENCH, J., 1962. *Steady State and Transient Void Fractions of Bubbling Systems and Their Operating Limits.* 62GL100. General Electric Company.

ZUBER, N. and FINDLAY, J. , 1965. Average volumetric concentration in two-phase flow system. *J. Heat Transf.*, **87**, pp. 453-468.

APPENDICES

APPENDIX A

IMAGE ANALYSIS CODES

The following MATLAB codes were used in the image analysis method described in § 3.3. This method was implemented in this study to obtain bubble sizes for the air-water system. The main outputs from these MATLAB codes were the long and short axes, and the orientation angle. It should be acknowledged that some of these codes were taken from the work of others, and were amended to help extract the desired information in order to achieve the aim of the study.

The steps can be expressed as follows:

1. Loading: the image file should be the first mfile to be run; this offers an optional choice for selecting the image that needs to be analysed.
2. Calibrating pixels: to mm with the help of the scale on the picture and is carried out to improve the quality of the picture by using contrast, brightness etc, as well as to magnify the field of view.
3. Selecting six points on the surface edges of bubbles.
4. Fitting an ellipse.
5. Obtaining the long, a, and short, b, axes and the orientation angle, θ.

Five MATLAB codes should be in the same directory as the image that needs to be analysed

1. Load _image

```
warning off all      % to stop warnings about images being too big to
display
close all            % close existing figures

fname=uigetfile('*.*','Select input file');  % read image data file
[X, map] = imread(fname);

scrsz = get(0,'ScreenSize');
f = figure('Visible','on','Name','Bubble Size Measurement', ...
           'Position',[1 1 scrsz(3)-100 scrsz(4)-100]);
himage=imshow(X);
hold on
```

```
zoom(1);
n=0;  % no of bubbles measured; reset for each new image loaded
button = questdlg('Calibrate image using reference line?','Image
Calibration');
if button=='Yes'
    calibrate
end
```

2. Calibrate

```
    msgbox('Use the mouse to select a line of known length,', ...
           'Image Calibration','help','modal')

    h=imline(gca,[]);                    % use mouse to define reference
line for calibraion
    api=iptgetapi(h);
    pos=api.getPosition();              % get position of the centre of the
image
    x1=pos(1,1);
    y1=pos(1,2);
    x2=pos(2,1);
    y2=pos(2,2);
    Lmm=inputdlg('Enter the line length in mm','Image Calibration');
    pix=sqrt((x2-x1)^2+(y2-y1)^2);
    L=cell2mat(Lmm);
    L=str2num(L);
    CF=pix/L;
    measure;
```

3. Measure

```
button = questdlg({'Start measuring bubble sizes?', ...
                   'Use left mouse button to select sets of 6 points',...
                   'Any other button will finish measurement'},'Measure
                   sizes');

if strcmp(button,'No')
    return
end

button=1;
while button == 1
    clear x;
    clear y;
    for j=1:6 % collect sets of 6 points
        [x(j),y(j),button] = ginput(1)
        if button ~= 1
            return
        end
    end
    n=n+1;
    [Xc(n),Yc(n),A(n),B(n),Phi(n),P]=ellipsefit(x,y);
    hold on
    ellipse(A(n),B(n),Phi(n),Xc(n),Yc(n));
    A(n)=A(n)/CF;
    B(n)=B(n)/CF;
    Xc(n)=Xc(n)/CF;
    Yc(n)=Yc(n)/CF;
End
```

4. Ellipse

```
function h=ellipse(ra,rb,ang,x0,y0,C,Nb)
% Ellipse adds ellipses to the current plot
%
% ELLIPSE(ra,rb,ang,x0,y0) adds an ellipse with semimajor axis of ra,
% a semimajor axis of radius rb, a semimajor axis of ang, centered at
% the point x0,y0.
%
% The length of ra, rb, and ang should be the same.
% If ra is a vector of length L and x0,y0 scalars, L ellipses
% are added at point x0,y0.
% If ra is a scalar and x0,y0 vectors of length M, M ellipse are with the
same
% radii are added at the points x0,y0.
% If ra, x0, y0 are vectors of the same length L=M, M ellipses are added.
% If ra is a vector of length L and x0, y0 are  vectors of length
% M~=L, L*M ellipses are added, at each point x0,y0, L ellipses of radius
ra.
%
% ELLIPSE(ra,rb,ang,x0,y0,C)
% adds ellipses of color C. C may be a string ('r','b',...) or the RGB
value.
% If no color is specified, it makes automatic use of the colors
specified by
% the axes ColorOrder property. For several circles C may be a vector.
%
% ELLIPSE(ra,rb,ang,x0,y0,C,Nb), Nb specifies the number of points
% used to draw the ellipse. The default value is 300. Nb may be used
% for each ellipse individually.
%
% h=ELLIPSE(...) returns the handles to the ellipses.
%
% as a sample of how ellipse works, the following produces a red ellipse
% tipped up at a 45 deg axis from the x axis
% ellipse(1,2,pi/8,1,1,'r')
%
% note that if ra=rb, ELLIPSE plots a circle
%

% written by D.G. Long, Brigham Young University, based on the
% CIRCLES.m original
% written by Peter Blattner, Institute of Microtechnology, University of
% Neuchatel, Switzerland, blattner@imt.unine.ch


% Check the number of input arguments

if nargin<1,
  ra=[];
end;
if nargin<2,
  rb=[];
end;
if nargin<3,
  ang=[];
end;

%if nargin==1,
```

```
%  error('Not enough arguments');
%end;

if nargin<5,
  x0=[];
  y0=[];
end;

if nargin<6,
  C=[];
end

if nargin<7,
  Nb=[];
end

% set up the default values

if isempty(ra),ra=1;end;
if isempty(rb),rb=1;end;
if isempty(ang),ang=0;end;
if isempty(x0),x0=0;end;
if isempty(y0),y0=0;end;
if isempty(Nb),Nb=300;end;
if isempty(C),C=get(gca,'colororder');end;

% work on the variable sizes

x0=x0(:);
y0=y0(:);
ra=ra(:);
rb=rb(:);
ang=ang(:);
Nb=Nb(:);

if isstr(C),C=C(:);end;

if length(ra)~=length(rb),
  error('length(ra)~=length(rb)');
end;
if length(x0)~=length(y0),
  error('length(x0)~=length(y0)');
end;

% how many inscribed elllipses are plotted

if length(ra)~=length(x0)
  maxk=length(ra)*length(x0);
else
  maxk=length(ra);
end;

% drawing loop

for k=1:maxk

  if length(x0)==1
```

```
    xpos=x0;
    ypos=y0;
    radm=ra(k);
    radn=rb(k);
    if length(ang)==1
      an=ang;
    else
      an=ang(k);
    end;
  elseif length(ra)==1
    xpos=x0(k);
    ypos=y0(k);
    radm=ra;
    radn=rb;
    an=ang;
  elseif length(x0)==length(ra)
    xpos=x0(k);
    ypos=y0(k);
    radm=ra(k);
    radn=rb(k);
    an=ang(k)
  else
    rada=ra(fix((k-1)/size(x0,1))+1);
    radb=rb(fix((k-1)/size(x0,1))+1);
    an=ang(fix((k-1)/size(x0,1))+1);
    xpos=x0(rem(k-1,size(x0,1))+1);
    ypos=y0(rem(k-1,size(y0,1))+1);
  end;

  co=cos(an);
  si=sin(an);
  the=linspace(0,2*pi,Nb(rem(k-1,size(Nb,1))+1,:)+1);
%  x=radm*cos(the)*co-si*radn*sin(the)+xpos;
%  y=radm*cos(the)*si+co*radn*sin(the)+ypos;
  h(k)=line(radm*cos(the)*co-
si*radn*sin(the)+xpos,radm*cos(the)*si+co*radn*sin(the)+ypos);
  set(h(k),'color',C(rem(k-1,size(C,1))+1,:),'linewidth',2);

end;
```

5. *Ellipsefit*

```
function [varargout]=ellipsefit(x,y)
%ELLIPSEFIT Stable Direct Least Squares Ellipse Fit to Data.
% [Xc,Yc,A,B,Phi,P]=ELLIPSEFIT(X,Y) finds the least squares ellipse that
% best fits the data in X and Y. X and Y must have at least 5 data
points.
% Xc and Yc are the x- and y-axis center of the ellipse respectively.
% A and B are the major and minor axis of the ellipse respectively.
% Phi is the radian angle of the major axis with respect to the x-axis.
% P is a vector containing the general conic parameters of the ellipse.
% The conic representation of the ellipse is given by:
%
% P(1)*x^2 + P(2)*x*y + P(3)*y^2 + P(4)*x + P(5)*y + P(6) = 0
%
% S=ELLIPSEFIT(X,Y) returns the output data in a structure with field
names
% equal to the variable names given above, e.g., S.Xc, S.Yc, S.A, S.B,
% S.Phi and S.P
%
```

```
% Reference: R. Halif and J. Flusser, "Numerically Stable Direct Least
% Squares FItting of Ellipses," Department of Software Engineering,
Charles
% University, Czech Republic, 2000.

% Conversion from conic to conventional ellipse equation inspired by
% fit_ellipse.m on MATLAB Central

% D.C. Hanselman, University of Maine, Orono, ME 04469
% Mastering MATLAB 7
% 2005-02-28
% Rotation angle fixed 2005-08-09

%--------------------------------------------------------------------------
--
x=x(:); % convert data to column vectors
y=y(:);
if numel(x)~=numel(y) || numel(x)<5
   error('X and Y Must be the Same Length and Contain at Least 5
Values.')
end

D1=[x.*x x.*y y.*y]; % quadratic terms
D2=[x y ones(size(x))]; % linear terms
S1=D1'*D1;
S2=D1'*D2;

[Q2,R2]=qr(D2,0);
if condest(R2)>1.0e10
   warning('ellipsefit',...
      'Data is Poorly Conditioned and May Not Represent an Ellipse.')
end
T=-R2\(R2'\S2'); % -inv(S3) * S2'

M=S1+S2*T;
CinvM=[M(3,:)/2; -M(2,:); M(1,:)/2];
[V,na]=eig(CinvM);
c=4*V(1,:).*V(3,:) - V(2,:).^2;
A1=V(:,c>0);
P=[A1; T*A1];

% correct signs if needed
P=sign(P(1))*P;

Phi=atan(P(2)/(P(3)-P(1)))/2;
c=cos(Phi);
s=sin(Phi);

% rotate the ellipse parallel to x-axis
Pr=zeros(6,1);
Pr(1)=P(1)*c*c - P(2)*c*s + P(3)*s*s;
Pr(2)=2*(P(1)-P(3))*c*s + (c^2-s^2)*P(2);
Pr(3)=P(1)*s*s + P(2)*s*c + P(3)*c*c;
Pr(4)=P(4)*c - P(5)*s;
Pr(5)=P(4)*s + P(5)*c;
Pr(6)=P(6);

% extract other data
```

```
XcYc=[c s;-s c]*[-Pr(4)/(2*Pr(1));-Pr(5)/(2*Pr(3))];
Xc=XcYc(1);
Yc=XcYc(2);
F=-Pr(6) + Pr(4)^2/(4*Pr(1)) + Pr(5)^2/(4*Pr(3));
AB=sqrt(F./Pr(1:2:3));
A=AB(1);
B=AB(2);
Phi=-Phi;
if A<B % x-axis not major axis, so rotate it pi/2
   Phi=Phi-sign(Phi)*pi/2;
   A=AB(2);
   B=AB(1);
end
S.Xc=Xc;
S.Yc=Yc;
S.A=A;
S.B=B;
S.Phi=Phi;
S.P=P;
if nargout==1
   varargout{1}=S;
else
   outcell=struct2cell(S);
   varargout=outcell(1:nargout);
end
```

APPENDIX B

LABVIEW BLOCK DIAGRAM AND INTERFACE

National Instruments' LabVIEW software was used for data acquisition, and to monitor and record the bubble signals. The bubbles were detected by the two- or the four-point conductivity probe. The probe was connected to a conductivity meter, which was designed in the workshop of the Chemical Engineering Department at Loughborough University. Figure B.1 shows the circuit of the four-point probe; the input voltage coming from the conductivity box was about 10 V and current through a 510kΩ resistor was applied to each needle of the four-point probe. The conductivity meter was connected to a data acquisition device, DAQ USB6210 (see Figure B.2), which converted the analogue voltage into a digital signal. The output signals were recorded digitally using LabVIEW software. Figure B.3 presents the block diagram, which was built to record the electrode signal as a text file for further analysis. Figure B.4 shows a screenshot of the LabVIEW interface chart. The chart represents the voltage with respect to the time.

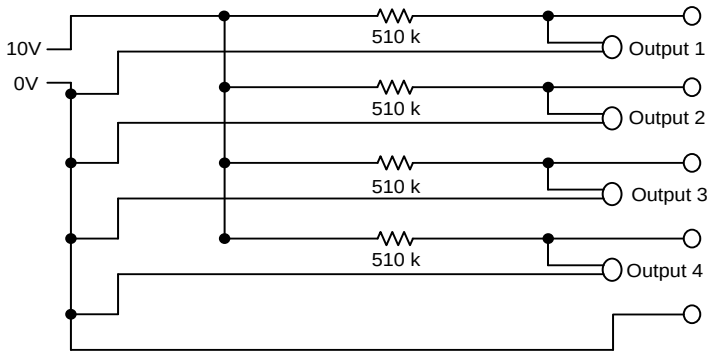


Figure B.1 A diagram of the electrical circuit for the four-point probe.



Figure B.2 Data acquisition device (DAQ USB6210) used in the study.

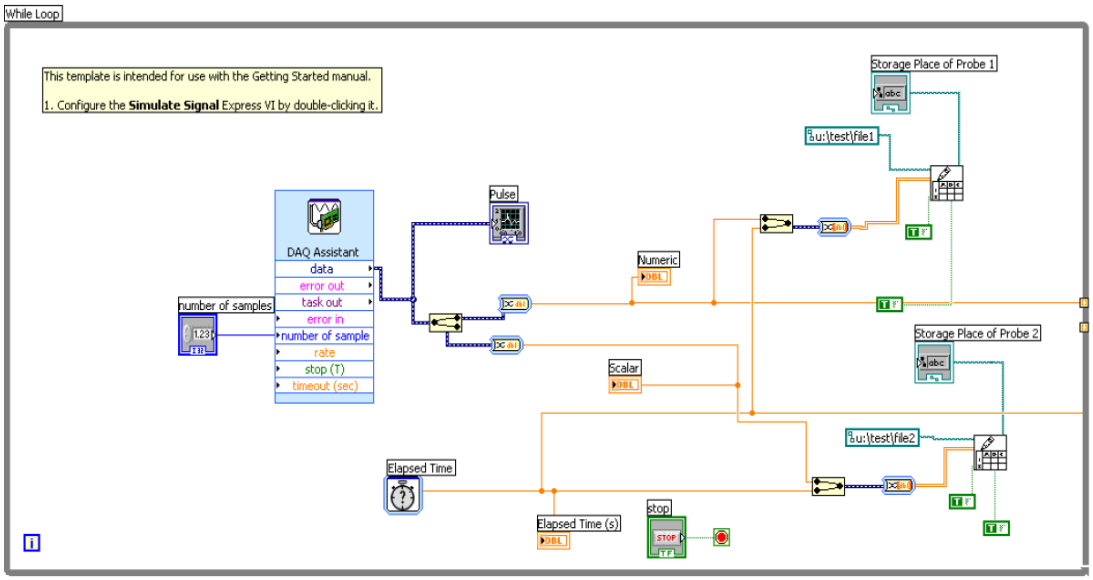


Figure B.3 A screenshot of a LabVIEW block diagram used in the study.

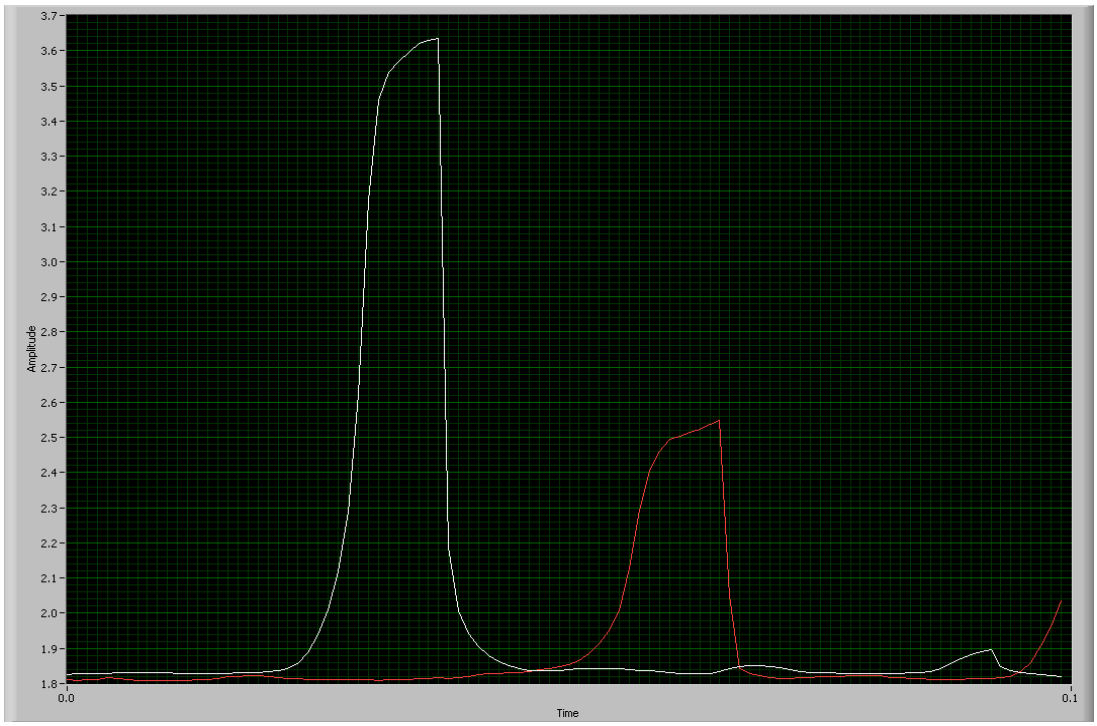


Figure B.4 LabVIEWinterface chart to monitor the bubble signal; a single bubble hitting the two-point probe.

APPENDIX C

SAMPLE CALCULATION

C.1 Void fraction and gas superficial velocity in an open tube and annular gap column

In this section, sample calculations of the variables (e.g. α and A of the open and annular gap column) are presented. The calculation used for correcting the rotameter reading is also demonstrated, and the main parts of the rotameter and its air flow rate chart are presented. Table C.1 shows a sample of an Excel sheet that was used to calculate α in the open column at certain air flow rates; the values of the parameters are used to demonstrate the sample calculations.

Table C.1 A sample of the Excel sheet to calculate the *α* in the open column at an air flow rate of q_m 25 l/min

q_m	H	h	P_r	Q_f		A	j_g	α
l/min	cm	cm	mbar	l/min	m^3/s	m^2	m/s	
25	100	147.7	1036	35.67	5.95E-04	8.11E-03	7.33E-02	0.323

C.1.1 Calculating the void fraction

The void fraction can be calculated easily by knowing the aerated level, h, and the level of the stagnant water, H:

$$\alpha = \frac{h - H}{h} \qquad C.1$$

α = 0.323

C.1.2 Correcting the rotameter reading

For the range of gas flow rates studied here, the rotameter reading is affected by (i) the pressure drop across the sparger, and (ii) the hydrostatic head of liquid in the bubble column. The rotameter reading was corrected using the following equation:

$$Q_f = q_m \sqrt{\frac{1+p}{p_{atm}}} \qquad C.2$$

From Table C.1, the rotameter reading, q_m is 25 l/min, the digital pressure reading, p is 1.036 bar and atmospheric pressure, p_{atm} is 1 bar. Therefore, the corrected air flow rate, Q_f is 35.67 l/min.

The rotameter used in the present study, a Platon (A10), was manufactured by Roxspur Measurement & Control Ltd. The main parts and the air flow chart provided are presented in Figure C.1.

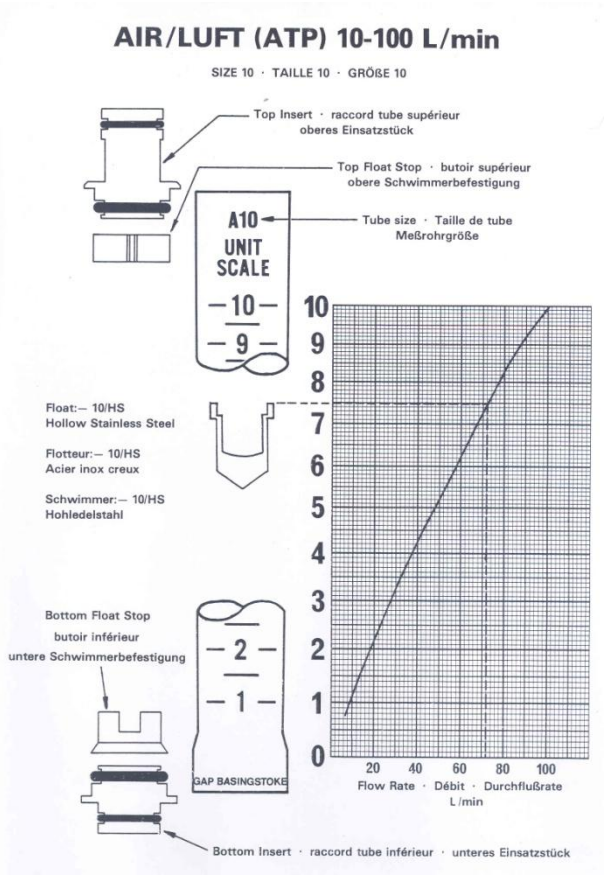


Figure C.1 The main parts of the rotameter and the corresponding air flow rate chart.

C.1.3 Superficial velocity, j_g calculation

The gas superficial velocity, j_g, is given by:

$$j_g = \frac{Q_f}{A} \qquad C.3$$

From Table C.1, the air flow rate, Q_f should be converted as follows:

Q_f= 35.67 = 35.67/(1000x60) m^3/s = 5.95 x 10^{-4} m^3/s

The open column internal diameter (i.d.) D is 0.1016 m and from the area equation:

$$A = \frac{\pi}{4} D^2 \qquad C.4$$

the area of the open column, A is 8.11 x 10^{-3} m^2. So, the gas superficial velocity is: j_g=0.0733 m/s.

C.1.4 Annular area and required air flow rate

For a logical comparison, the main issue was to operate the annular gap column at the same j_g as the open column. So, the calculations below were followed to calculate the required rotameter air flow rate:

The inner tube's outside diameter, (o.d.) D_E is 0.0601 m (see Figure C.2). Therefore, the inner tube's area, A_E is 2.84 x 10^{-3} m^2 and the area of the annular gap is given by:

$$A_a = A - A_E \qquad C.5$$

So A_a=5.27 x 10^{-3} m^2 and the required annular Q_f at the same j_g as in the open column is given by:

$$Q_f(annular) = j_g A_a \qquad C.6$$

Therefore, the air flow rate for the annular gap,$Q_f(annular)$ is 3.863 x 10^{-4} m^3/s.

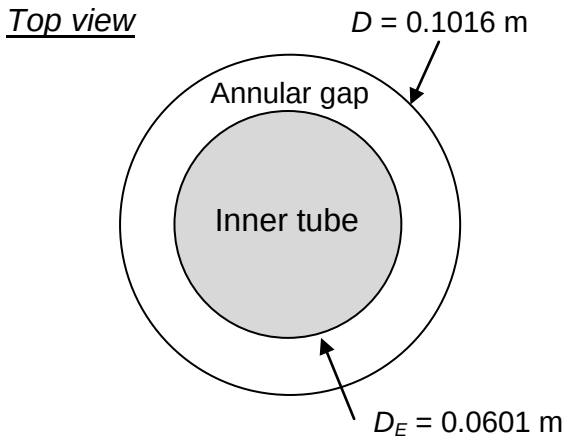


Figure C.2 Top view of the annular gap column.

C.2 Permeability of the porous sparger and air flow through an orifice

C.2.1 Permeability of the porous sparger

The permeability of the gas sparger gives an indication of the bubble size and the homogeneity of the flow. In the orifice experiments, it was crucial to calculate the amount of air flowing through the orifice and the porous sparger as a function of j_g. This section provides the calculation that was used to find the permeability of the porous sparger and the fraction of the air flow through the orifice to the sparger. Table C.2 presents the values of the variables that were used in this calculation.

Table C.2 The values of the variables that were used in the permeability calculation.

Q_s	A_s	p_b	p_a	μ_g	L	K	Δp
m^3/s	m^2	N/m^2	N/m^2	N-s/m^2	m	m^2	N/m^2
1.15E-	8.11E-	980	1.98E+04	1.73E-05	4.00E-03	5.212E-14	1.88E+04

To calculate the permeability, k (m^2), of the sparger, Darcy's law was used:

$$Q_s = \frac{-kA_s}{\mu_g}\frac{\Delta p}{L} \qquad C.7$$

where Q_s is the air flow rate through the sparger (m^3/s), A_s is the area of the sparger (m^2), μ_g is the viscosity of gas (N s/m^2), L is the thickness of the sparger (m) and Δp is the pressure difference (N/m^2), given by:

$$\Delta p = (p_b - p_a) \qquad C.8$$

where p_b is the static head pressure (N/m^2) and p_a is the pressure below the sparger (N/m^2).

The static head pressure, p_b , can be expressed as follows:

$$p_b = \rho_l g h(1-\alpha) \qquad C.9$$

where ρ_l = density of water (kg/m^3), g = acceleration gravity (m/s^2), h = the height of aerated water (m) and α = gas void fraction.

For ρ_l=1000 kg/m^3, g=9.81 m/s^2, h =106.9 cm and α =0.065.

Therefore p_b is 980 N/m^2 and the pressure below the sparger, p_a, is given by:

$$p_a = P * 100 \qquad C.10$$

where P is the digital gauge pressure reading for P = 198 mbar; thus p_a is 1.98E+04 N/m^2. By substituting in Equation C.8, the values of Δp can be obtained. Figure C.3 shows the pressure difference with respect to the range of the studied; the slope is the Δp (1.88 N/m^2).

By substituting the value of variables using Darcy's law (Equation C.7), the permeability, k, is equal to 5.212 x 10^{-14} m^2.

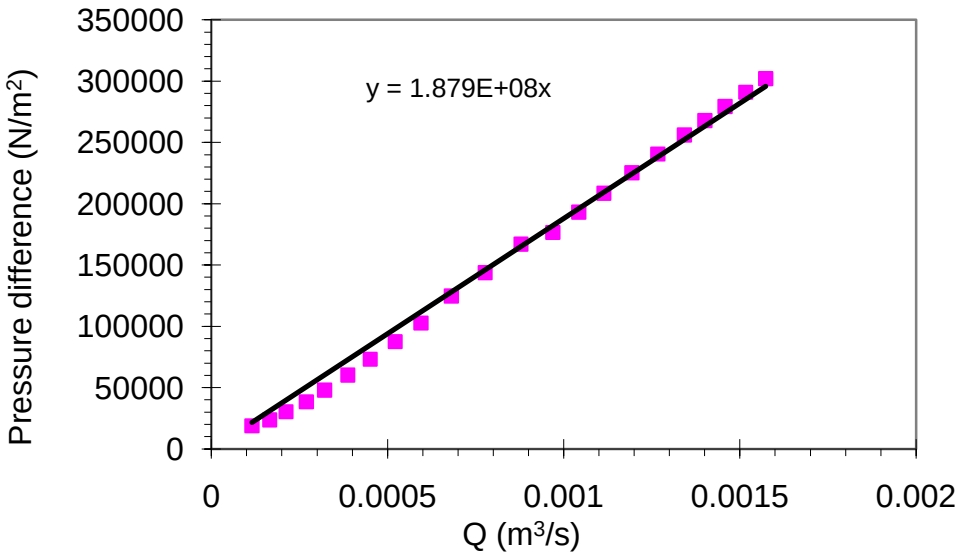


Figure C.3 The pressure difference around the sparger with respect to the range of air flow rates.

C.2.2 Orifice air flow rate

The air flow rate through an orifice, Q_o (m^3/s), is given by:

$$Q_o = C_d A_o \sqrt{2\frac{\Delta p}{\rho_g}} \qquad C.11$$

where C_d is the discharge coefficient, A_o is the orifice area (m^2), ρ_g is the air density (kg/m^3) and Δp is the pressure difference, as shown in Equation C.8.

The total gas flow rate is the sum of the flow rates for the porous sparger and the orifice:

$$Q_{tot} = Q_s + Q_o \qquad C.12$$

and, by rearranging Equation (C.7), (C.11) and (C.12):

$$Q_{tot} = Q_s + C_d A_o \sqrt{2\frac{Q_s \mu_g}{A_s k \rho_g}} \qquad C.13$$

Figure C. presents the fractions of the air flow through the sparger and the pressure difference with respect to the total air flow rate for a 1.6 mm orifice diameter drilled into the porous sparger.

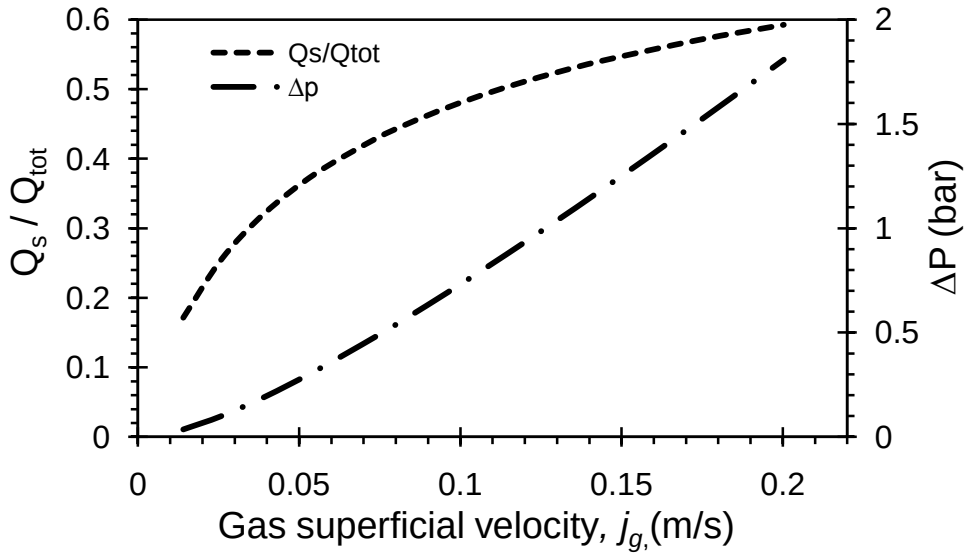


Figure C.4 The fractions of the air flow rate and the pressure drop for the sparger with a 1.6 mm orifice.

APPENDIX D

SIGNAL PROCESSING DEVELOPMENT

D.1 Threshold and number of standard deviations, σ.

This section discusses the signal processing development in order to choose the most appropriate value of the signal's standard deviation, σ, to set the threshold above the baseline. The value of σ should be a positive number: either an integer or a rational. This is an important factor in the signal treatment process, as low values of σ would pick up the noises in the baseline and count them as bubbles. In contrast, high values would fail to pick up the weak signals of the small bubbles. Four integer numbers were considered for σ, i.e. 1, 2, 3, 4; their signals were tested by looking closely at the signal time history. Figure D.1 shows the base of the signals obtained by the conductivity probe (p1) for different σ values. The threshold of σ=1 above the baseline seems to be set very low and hence picks up noise: for instance, the pointed cases. At σ = 2, the threshold shifts up a little to avoid the noise in the signals. At σ = 3 and 4, the threshold level is set high and there is an increased chance that weak bubble signals will be missed; hence, the void fraction could be underestimated compared to the aerated level method.

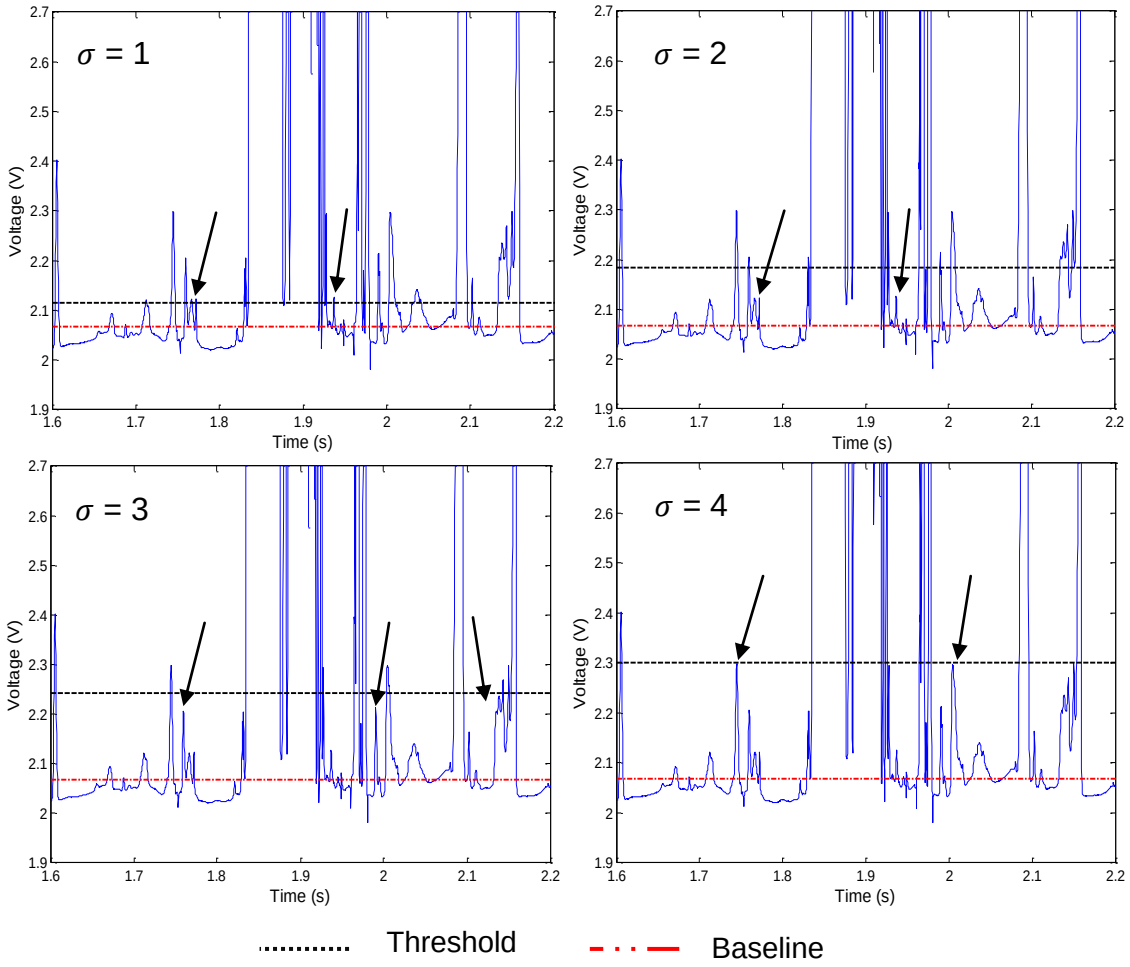


Figure D.1 Threshold set above the baseline at different standard deviation values.

D.2 Investigation in the bubble matching criteria

For all the criteria, the mean chord length results show almost similar trends, but with different chord length ranges. The results for each criterion were tested to emphasise the main issues that lead to the results being accepted or rejected. The ranking method, shown in Table D.1, was based on the fit of the predicted chord size, $P_c fitted$, which was obtained from the optimisation scheme for the measured chord size, P_c, of the probe. For instance, for criterion (1) in Table D.1, where V_{min} = 0.05 to V_{max} = 0.5 m/s and $Mode\ 0$, the range of velocity rise covers bubble diameters between 0.5 to more than 40 mm (Clift *et al.*, 2005). From the literature, e.g. Jamialahmadi *et al.* (1994) reported that the gas velocity was expected to increase as the j_g increases. However, Figure D.2*b* shows the mean gas velocity,V_g, decreases with respect to increases in j_g. This leads to bad predictions regarding the local d_{32} and d_{43} (see Figure D.2*i* and *j*). Thus, the criterion has only one * as it predicts the chord length (*C*).

In general, $Mode\ 1$ gives better results compared to $Mode\ 0$ except for the range of rises in velocity, 0.1 to 0.9 m/s. Criterion No. (*2*) in Table D.1has the same range of velocity rise as criterion No. (*1*) but using $Mode\ 1$ gives almost the expected shape for the gas velocity profile, as shown in Figure D.3*h*. The velocity range for the rising bubbles seems insufficient to include cases of large bubbles rising more than 0.5 m/s. This effect can be noted in the local d_{32} and d_{43} (see Figure D.3*i* and *j*) as some of the $P_c fitted$ failed to predict the P_c and hence hit values close to zero.

Those criteria that gave good results in terms of the local and mean of the variables, and where no sign of fault was noticed in the optimisation scheme were placed in the highest ranks. From Table D.1, criteria nos. (*3, 4, 6* and *10*) gained the highest rankings while criterion no. (*10*), V_{min} = 0.1 to V_{max} = 0.8 m/s and $Mode 1$ seems a reasonable choice, since it covers the whole range of the expected bubble sizes. Figure D.10*b* verifies that V_g is far from the boundary of the investigated range and criteria nos. (*3*) and (*4*) include small bubbles ($<$ 1 mm), which cannot in fact be determined by the probe. Criterion No. (*6*) includes bubble sizes beyond those that were expected.

Table D.1 Ranking of the criteria used to investigate the bubble matching conditions according to quality of fit.

Rise velocity range (m/s)	*Criteria*	*Mode*	*C*	V_g	d_{32}	d_{43}	d_{gm}	*StdDev*	*Total*
0.05 – 0.5	1	0	*					*	**
	2	1	*	*				*	***
0.05 – 0.8	3	0	*	*	*	*	*	*	******
	4	1	*	*	*	*	*	*	******
0.05 – 0.9	5	0	*					*	**
	6	1	*	*	*	*	*	*	******
0.1 – 0.5	7	0	*					*	**
	8	1	*	*				*	***
0.1 – 0.8	9	0	*					*	**
	10	1	*	*	*	*	*	*	******
0.1 – 0.9	11	0	*	*	*		*	*	*****
	12	1	*					*	**

* The criterion offers a good fit and predicts a reasonable value.

The figures for each criterion are presented in the following pages and illustrate the local and mean values of the variables below: chord length, gas velocity, Sauter, mean, geometric diameters and log standard deviation.

1. V_{min} = 0.05 to V_{max} = 0.5 m/s and Mode = 0 (find all matching bubbles).

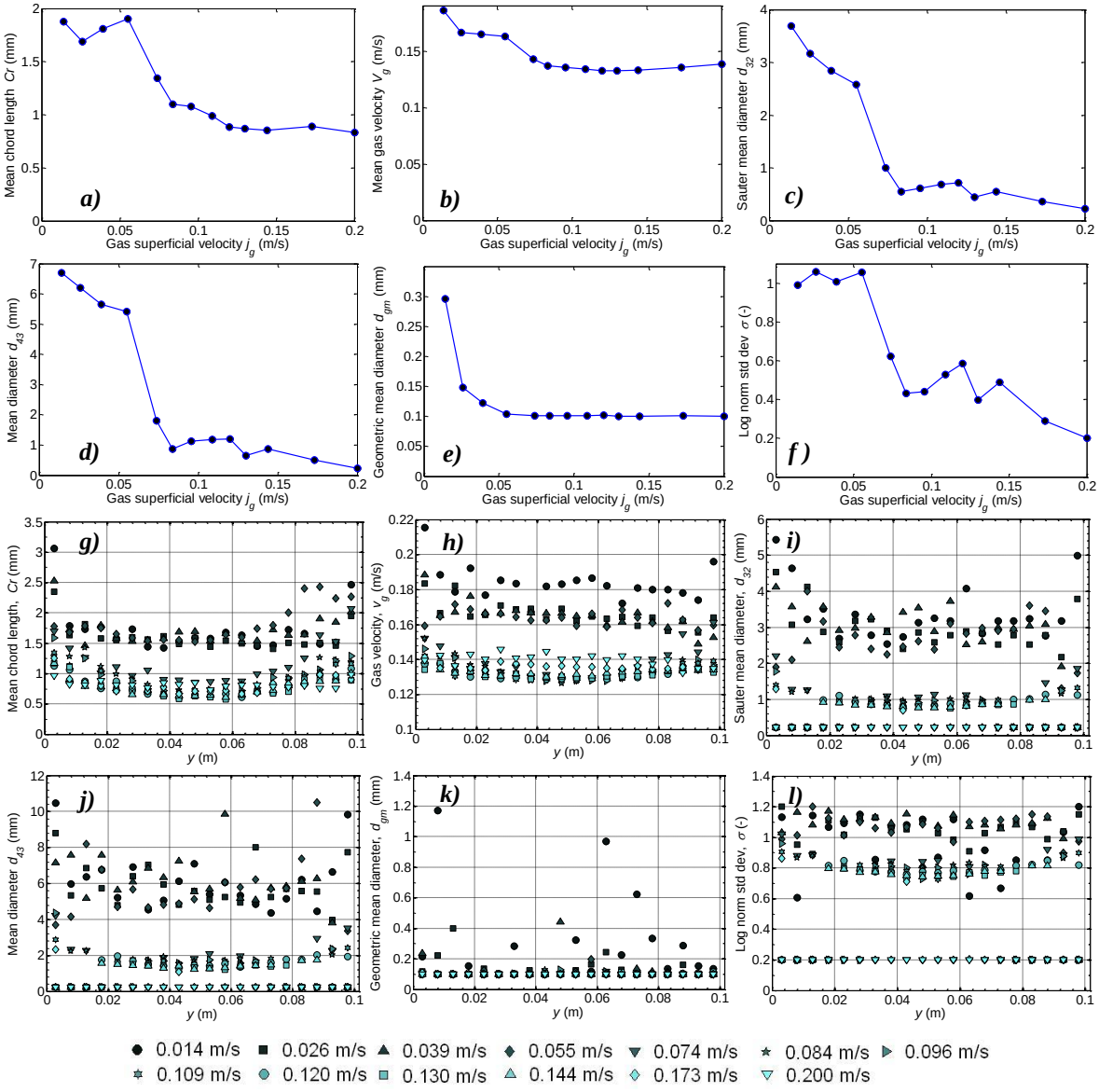


Figure D.2 Bubble transformation analysis output: the bubble rise velocity range is 0.05 to 0.5 m/s (FIND ALL MATCHING BUBBLES MODE).

2. V_{min} = 0.05 to V_{max} = 0.5 m/s and Mode = 1 (accept the 1st matching bubble).

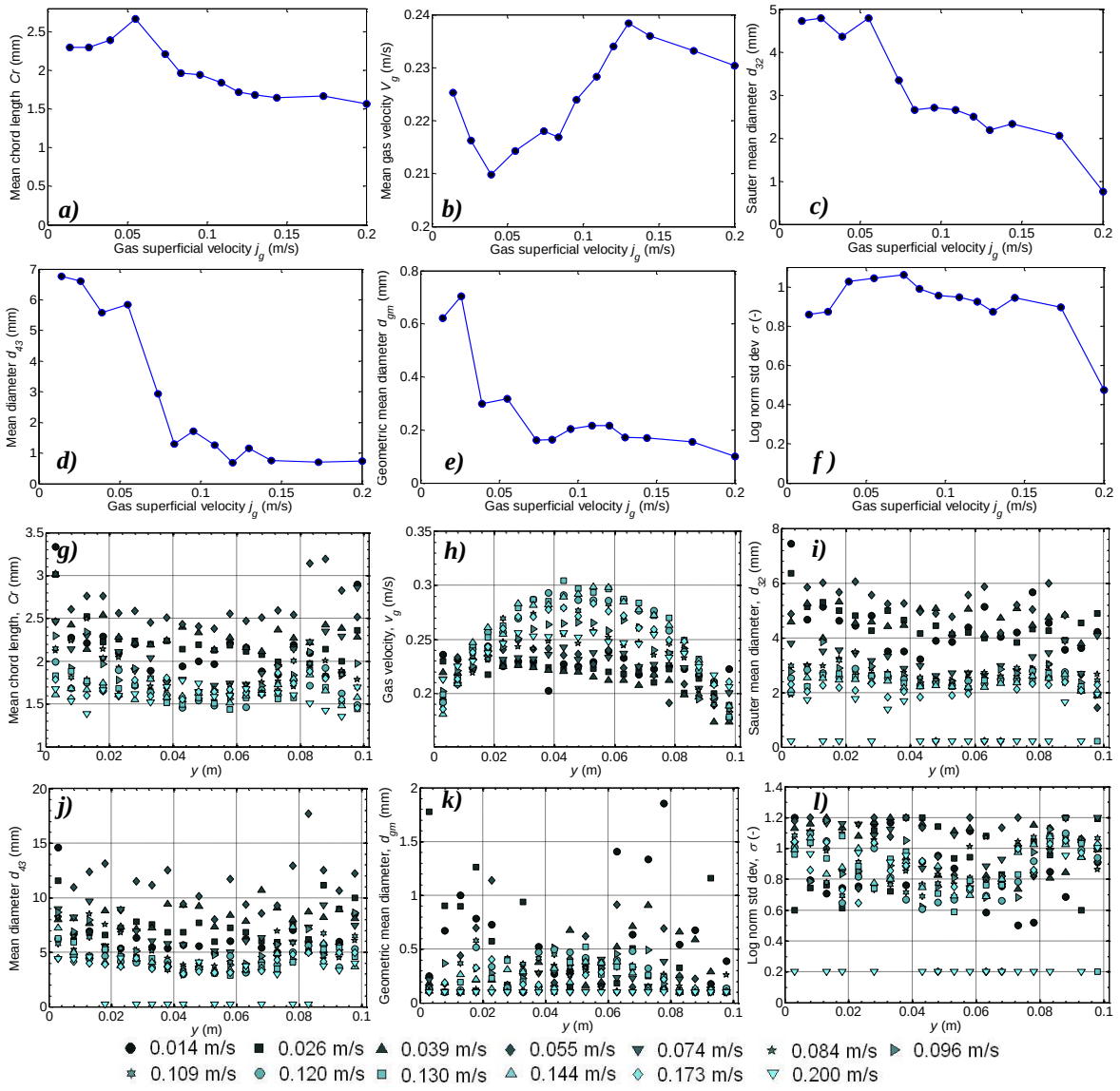


Figure D.3 Bubble transformation analysis output: the bubble rise velocity range is <u>0.05 to 0.5 m/s (ACCEPT THE FIRST MATCHING BUBBLE MODE).</u>

3. V_{min} = 0.05 to V_{max} = 0.8 m/s and Mode = 0 (find all matching bubbles).

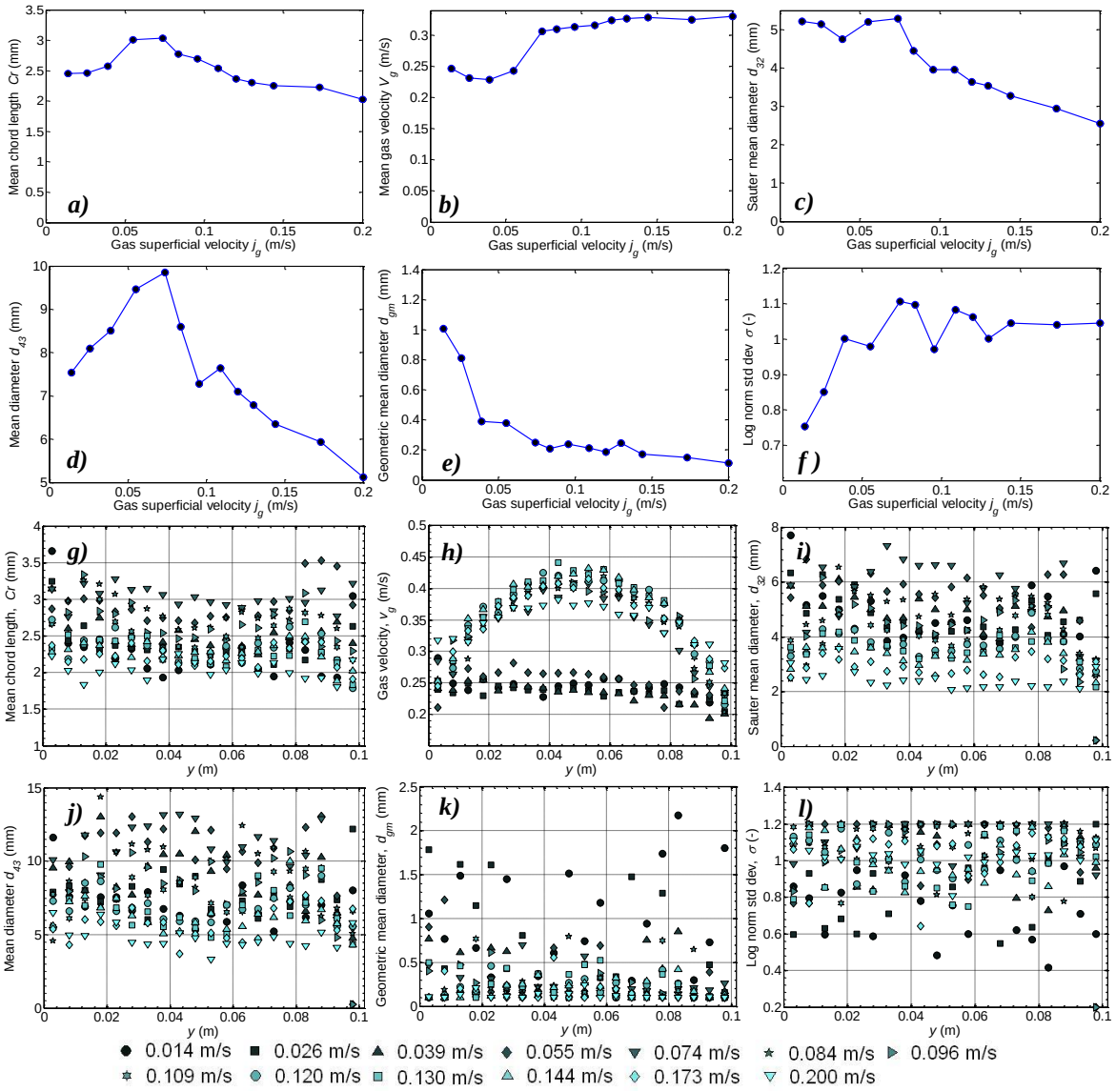


Figure D.4 Bubble transformation analysis output: the bubble rise velocity range is 0.05 to 0.8 m/s (FIND ALL MATCHING BUBBLES MODE).

4. V_{min} = 0.05 to V_{max} = 0.8 m/s and Mode = 1 (accept the 1st matching bubble).

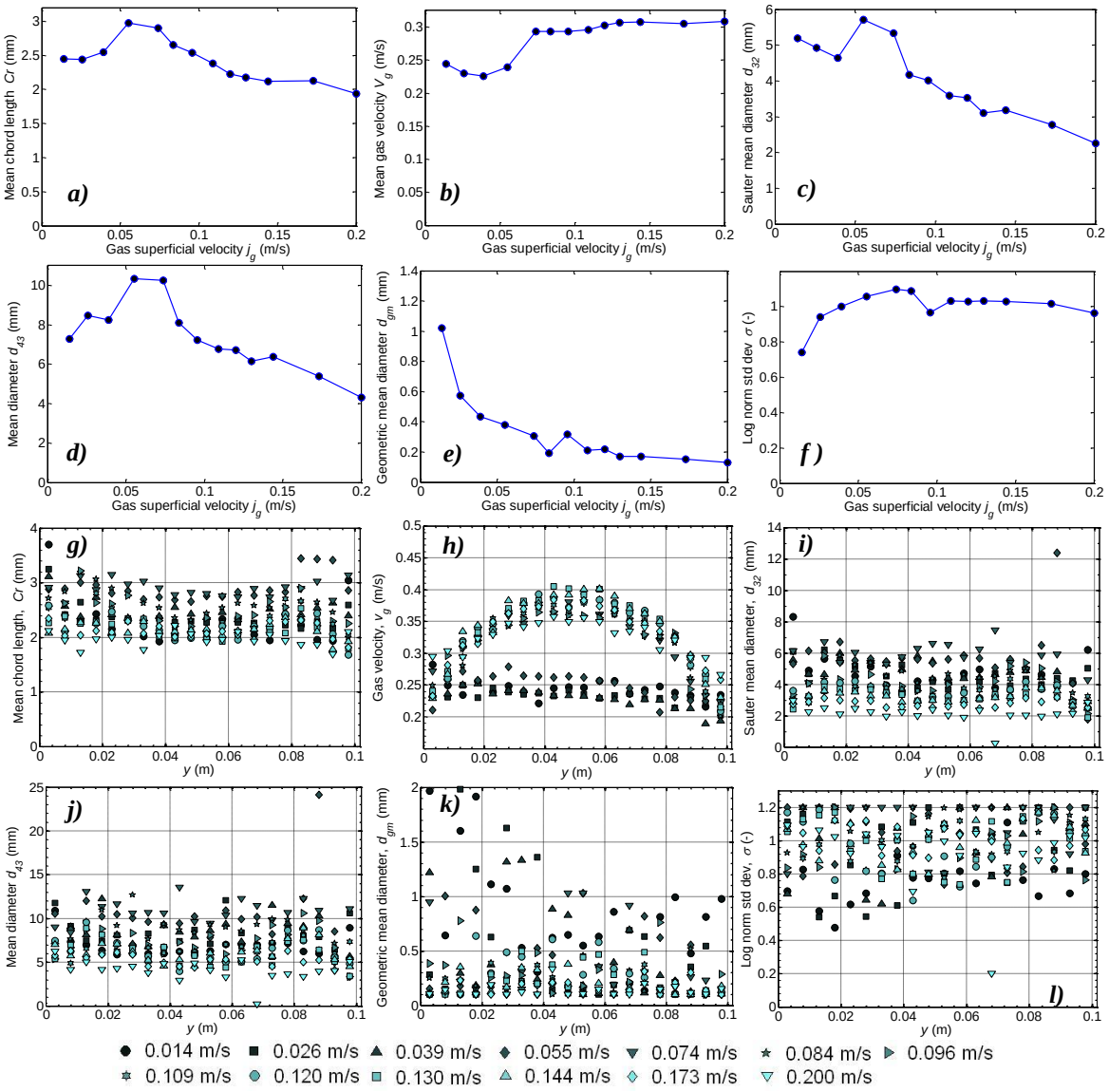


Figure D.5 Bubble transformation analysis output: the bubble rise velocity range is 0.05 to 0.8 m/s (ACCEPT THE FIRST MATCHING BUBBLE MODE).

5. V_{min} = 0.05 to V_{max} = 0.9 m/s and Mode = 0 (find all matching bubbles).

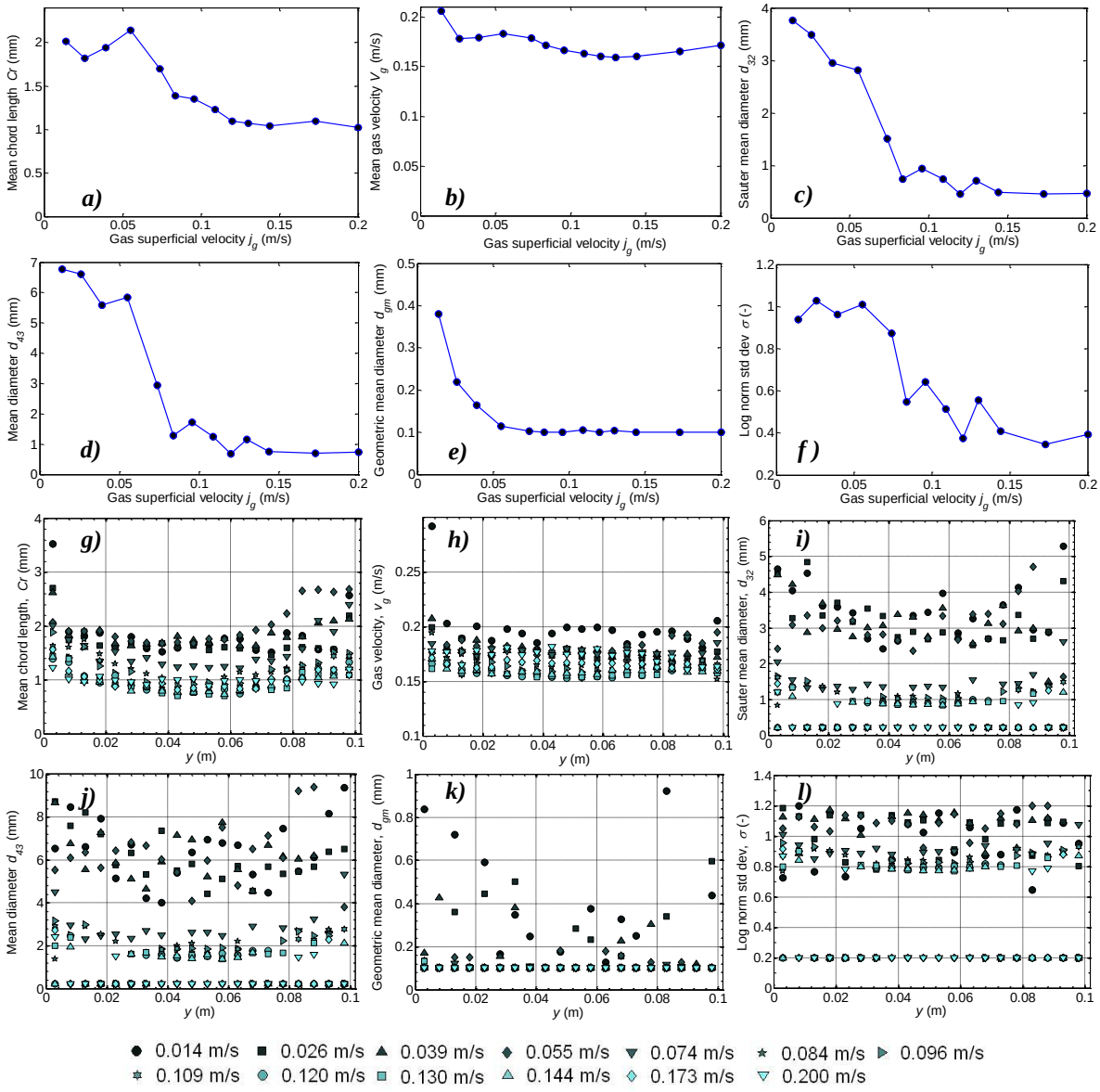


Figure D.6 Bubble transformation analysis output: the bubble rise velocity range is 0.05 to 0.9 m/s (FIND ALL MATCHING BUBBLES MODE).

6. V_{min} = 0.05 to V_{max} = 0.9 m/s and Mode = 1 (accept the 1st matching bubble).

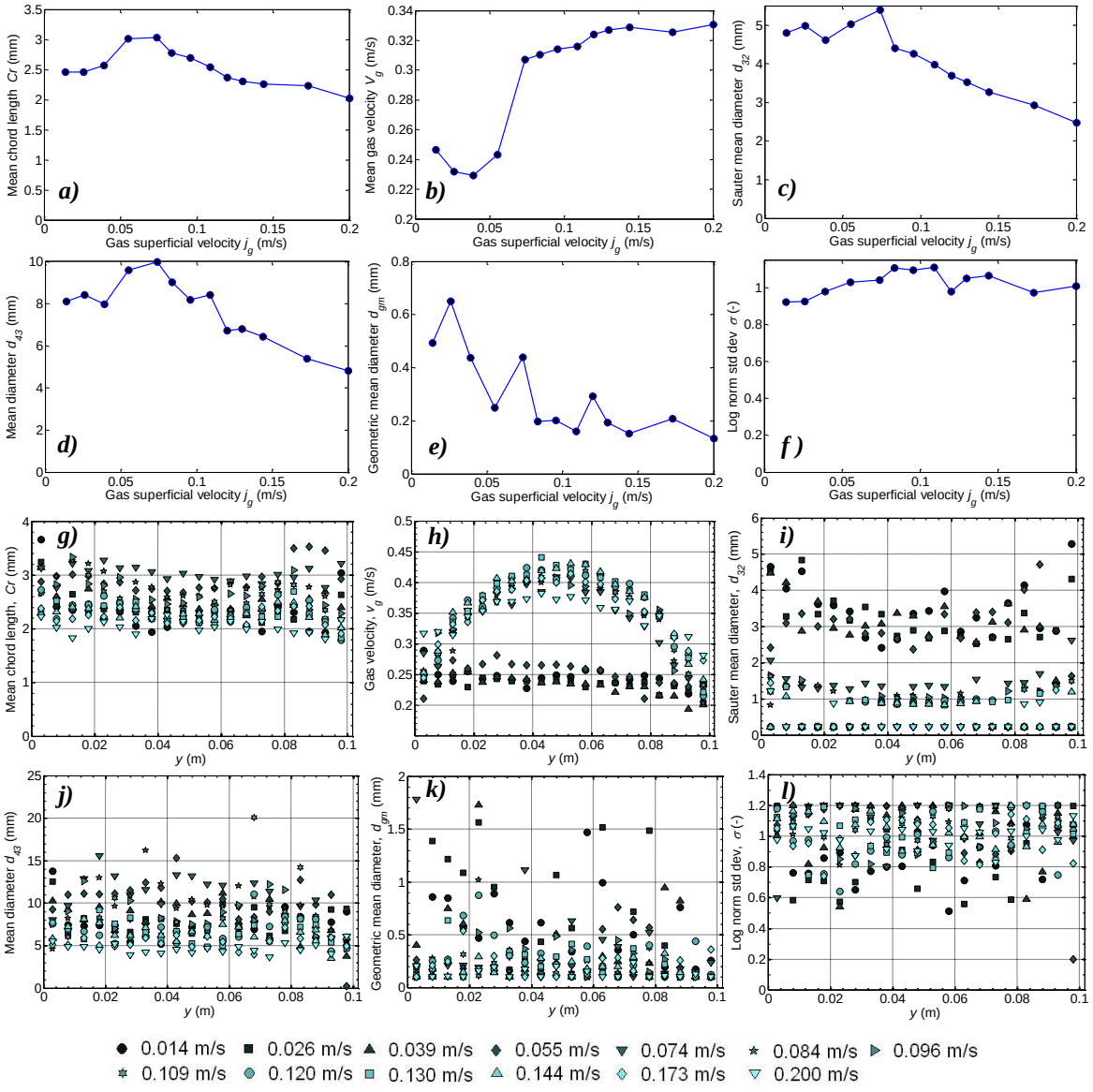


Figure D.7 Bubble transformation analysis output: the bubble rise velocity range is <u>0.05 to 0.9 m/s (ACCEPT THE FIRST MATCHING BUBBLE MODE).</u>

7. V_{min} = 0.1 to V_{max} = 0.5 m/s and Mode = 0 (find all matching bubbles).

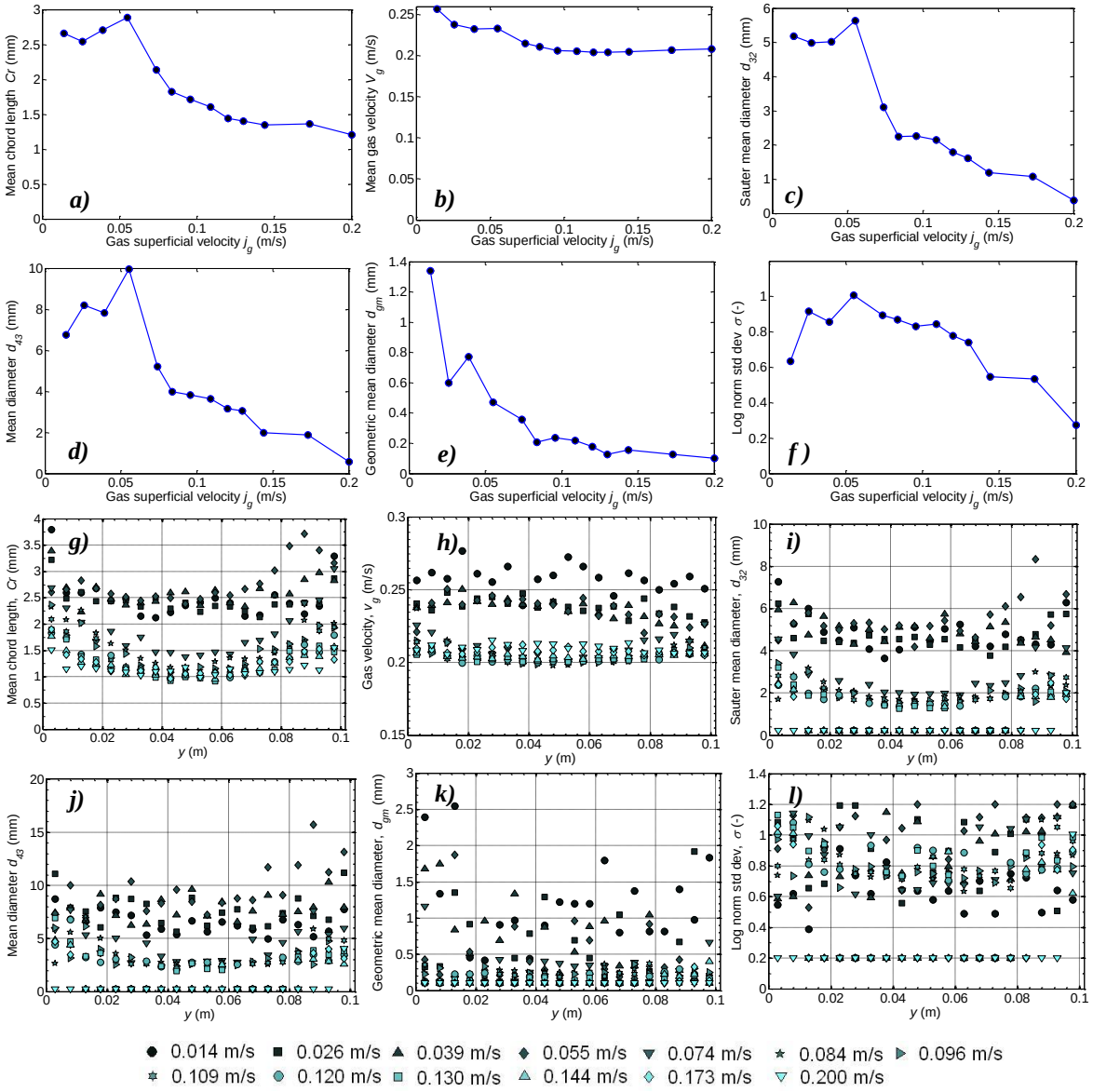


Figure D.8 Bubble transformation analysis output: the bubble rise velocity range is <u>0.1 to 0.5 m/s (FIND ALL MATCHING BUBBLES MODE).</u>

8. ***V_{min} = 0.1 to V_{max} = 0.5 m/s and Mode = 1 (accept the 1st matching bubble).***

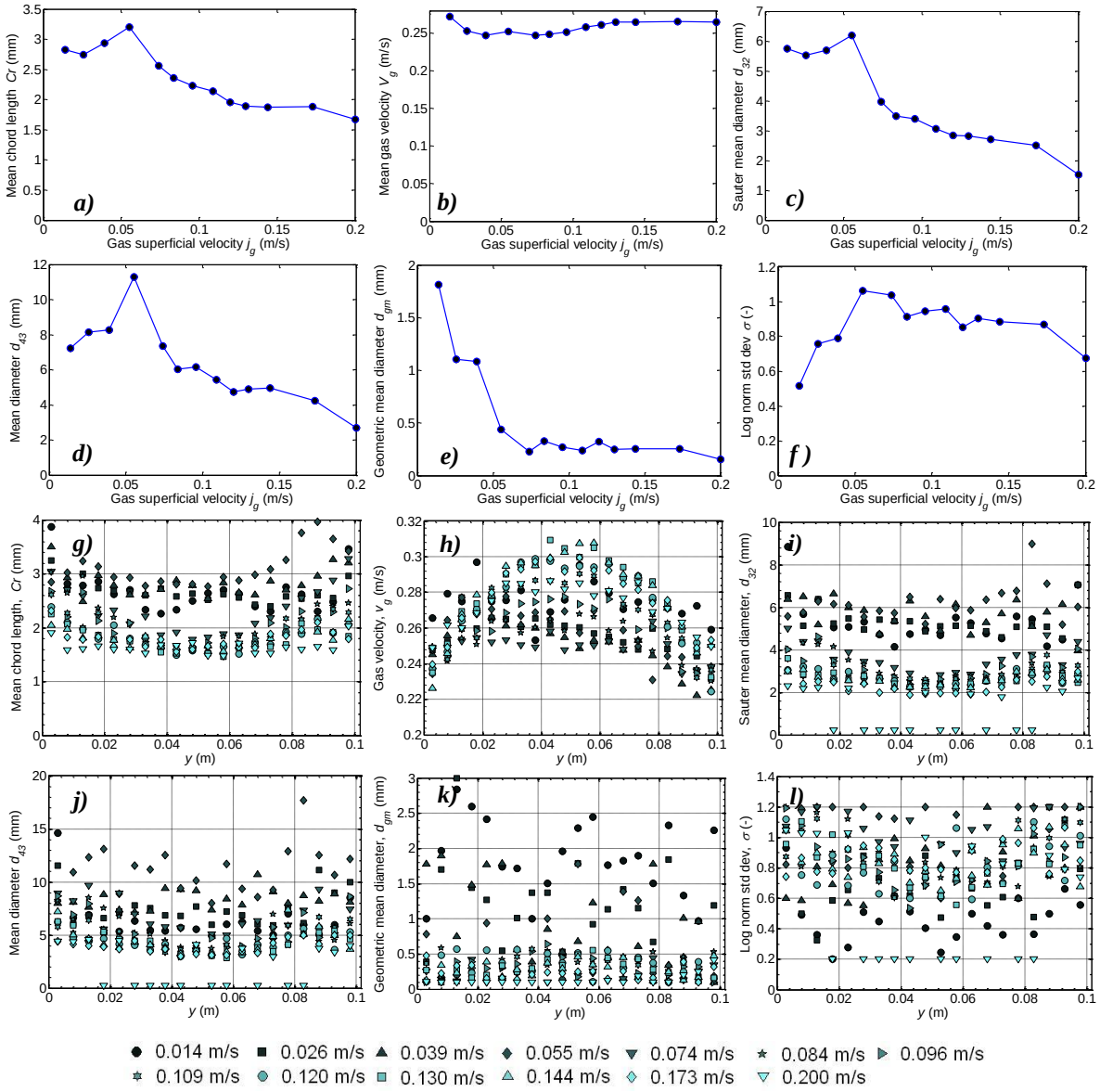


Figure D.9 Bubble transformation analysis output: the bubble rise velocity range is <u>0.1 to 0.5 m/s (ACCEPT THE FIRST MATCHING BUBBLE MODE).</u>

9. V_{min} = 0.1 to V_{max} = 0.8 m/s and Mode = 0 (find all matching bubbles).

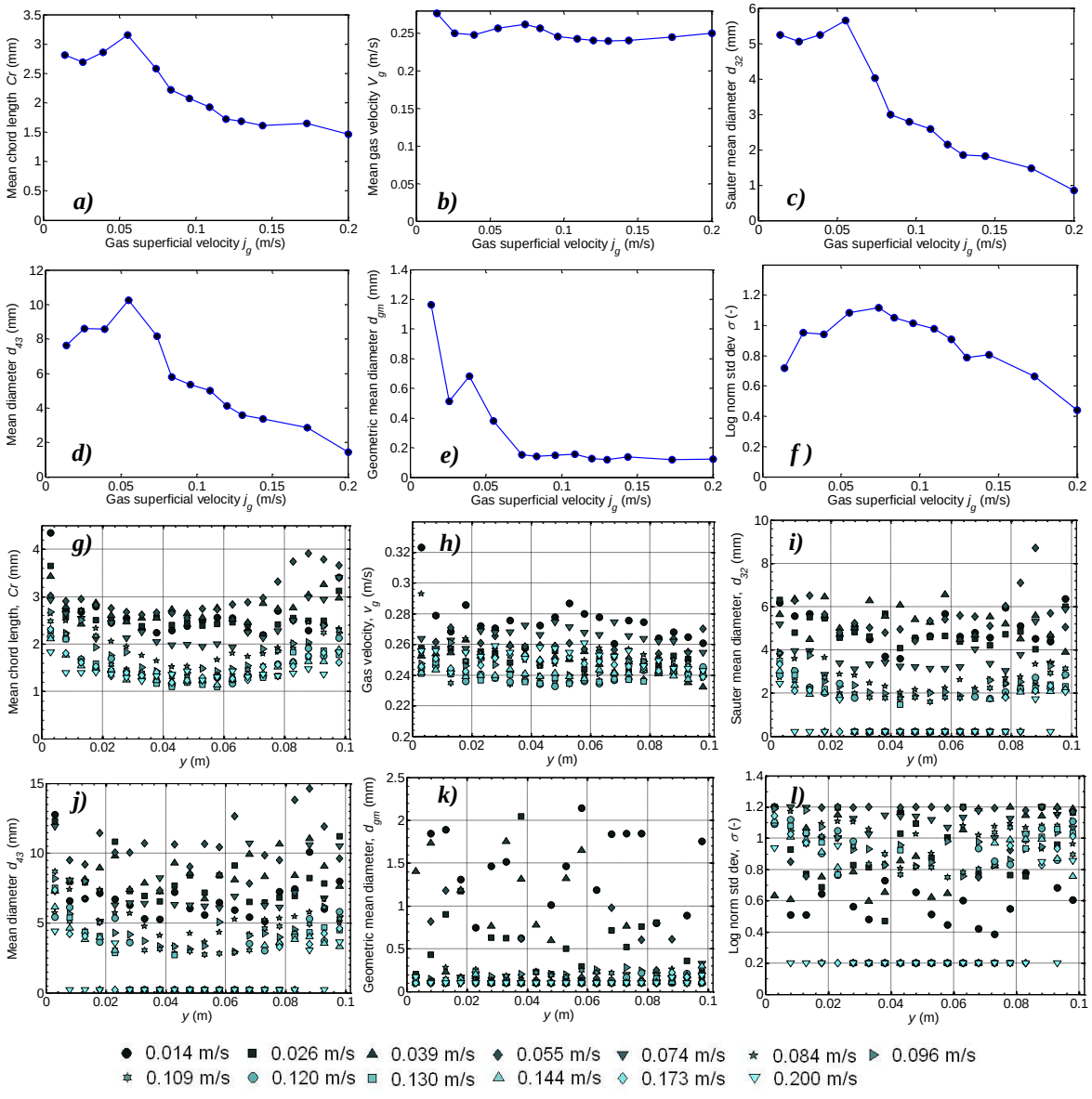


Figure D.10 Bubble transformation analysis output: the bubble rise velocity range is <u>0.1 to 0.8 m/s (FIND ALL MATCHING BUBBLES MODE).</u>

10. V_{min} = 0.1 to V_{max} = 0.8 m/s and Mode = 1 (accept the 1st matching bubble).

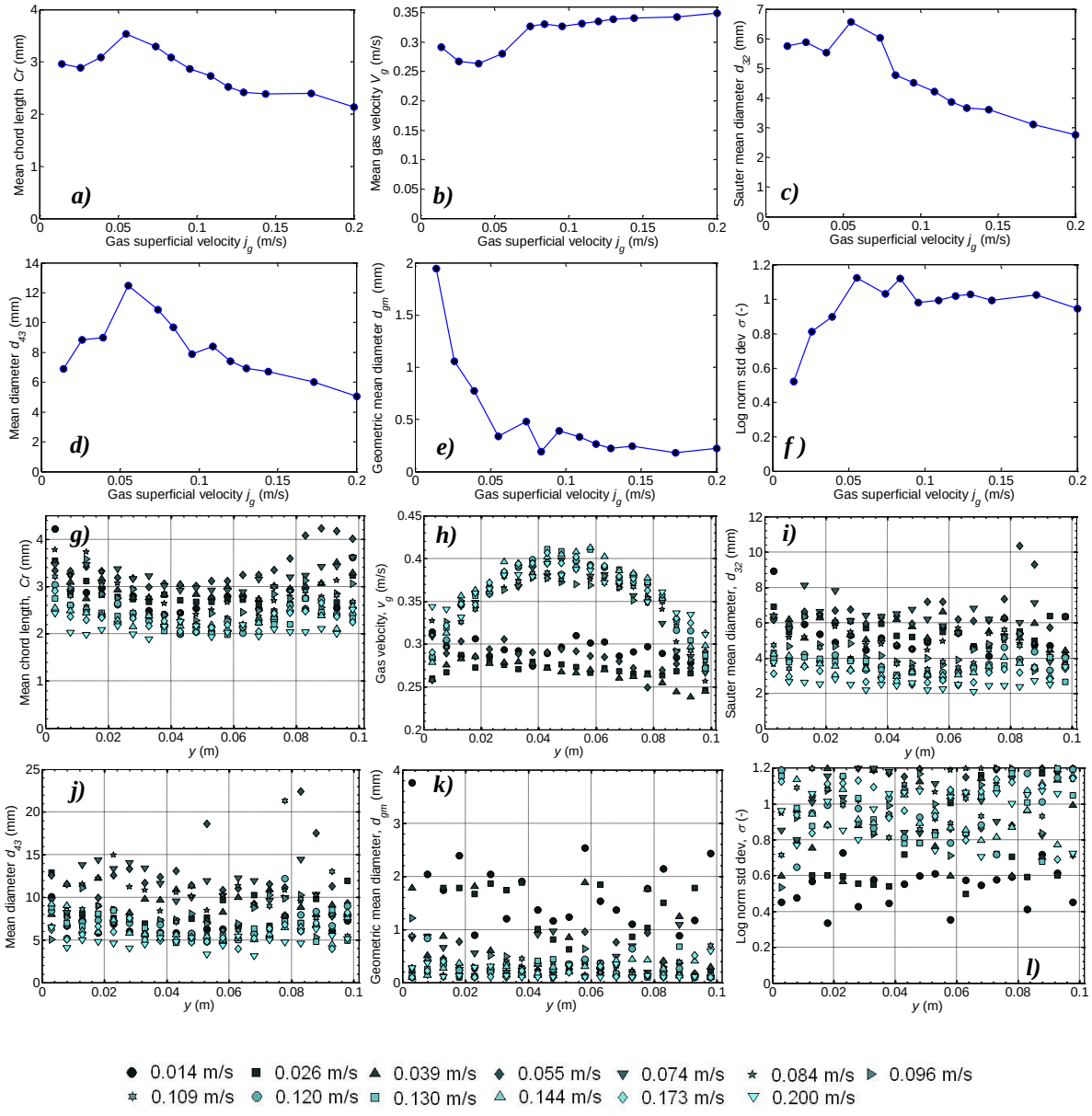


Figure D.11 Bubble transformation analysis output: the bubble rise velocity range is <u>0.1 to 0.8 m/s (ACCEPT THE FIRST MATCHING BUBBLE MODE).</u>

11. V_{min} = 0.1 to V_{max} = 0.9 m/s and Mode = 0 (find all matching bubbles).

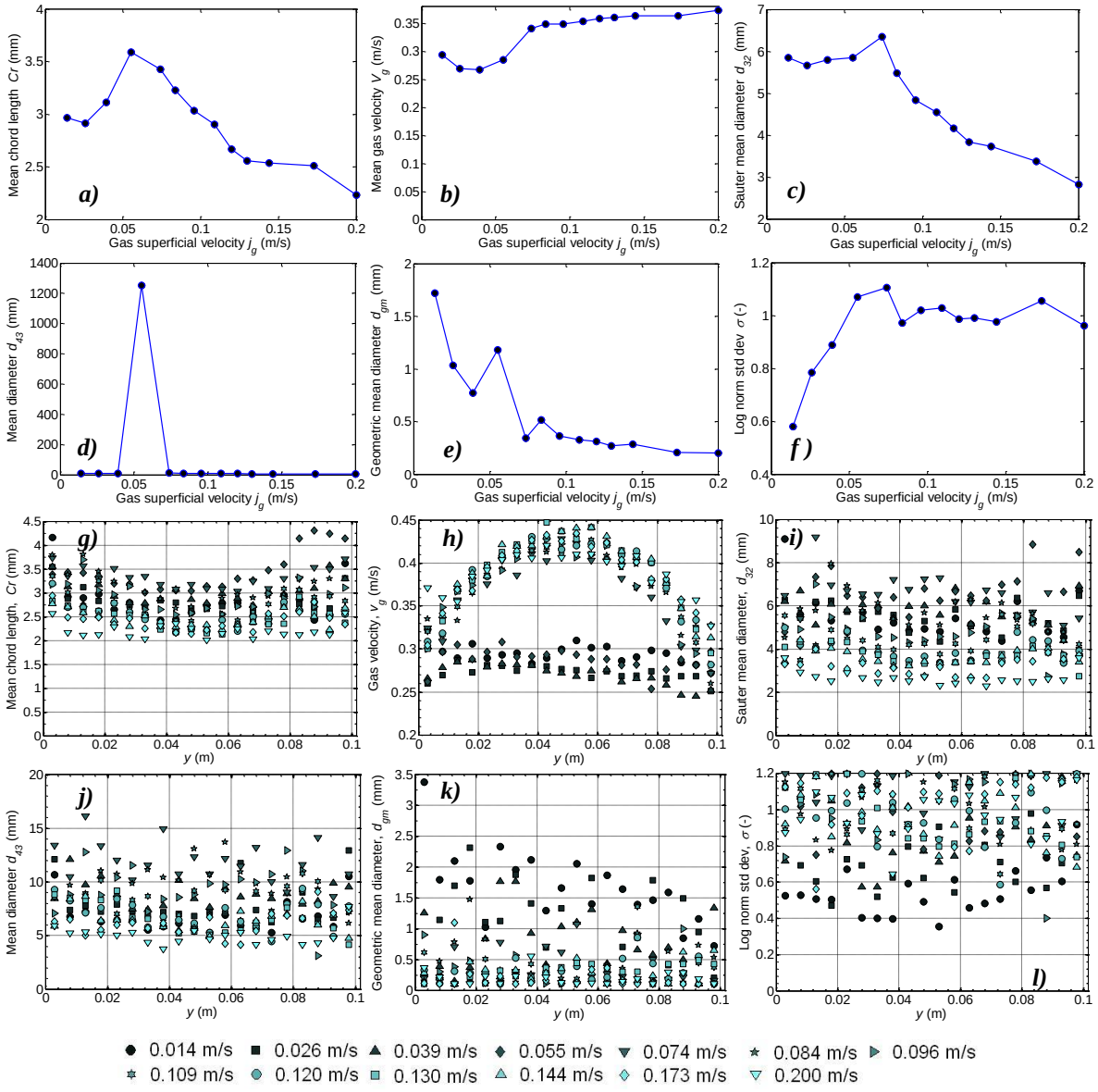


Figure D.12 Bubble transformation analysis output: the bubble rise velocity range is <u>0.1 to 0.9 m/s (FIND ALL MATCHING BUBBLES MODE).</u>

12. V_{min} = 0.1 to V_{max} = 0.9 m/s and Mode = 1 (accept the 1st matching bubble).

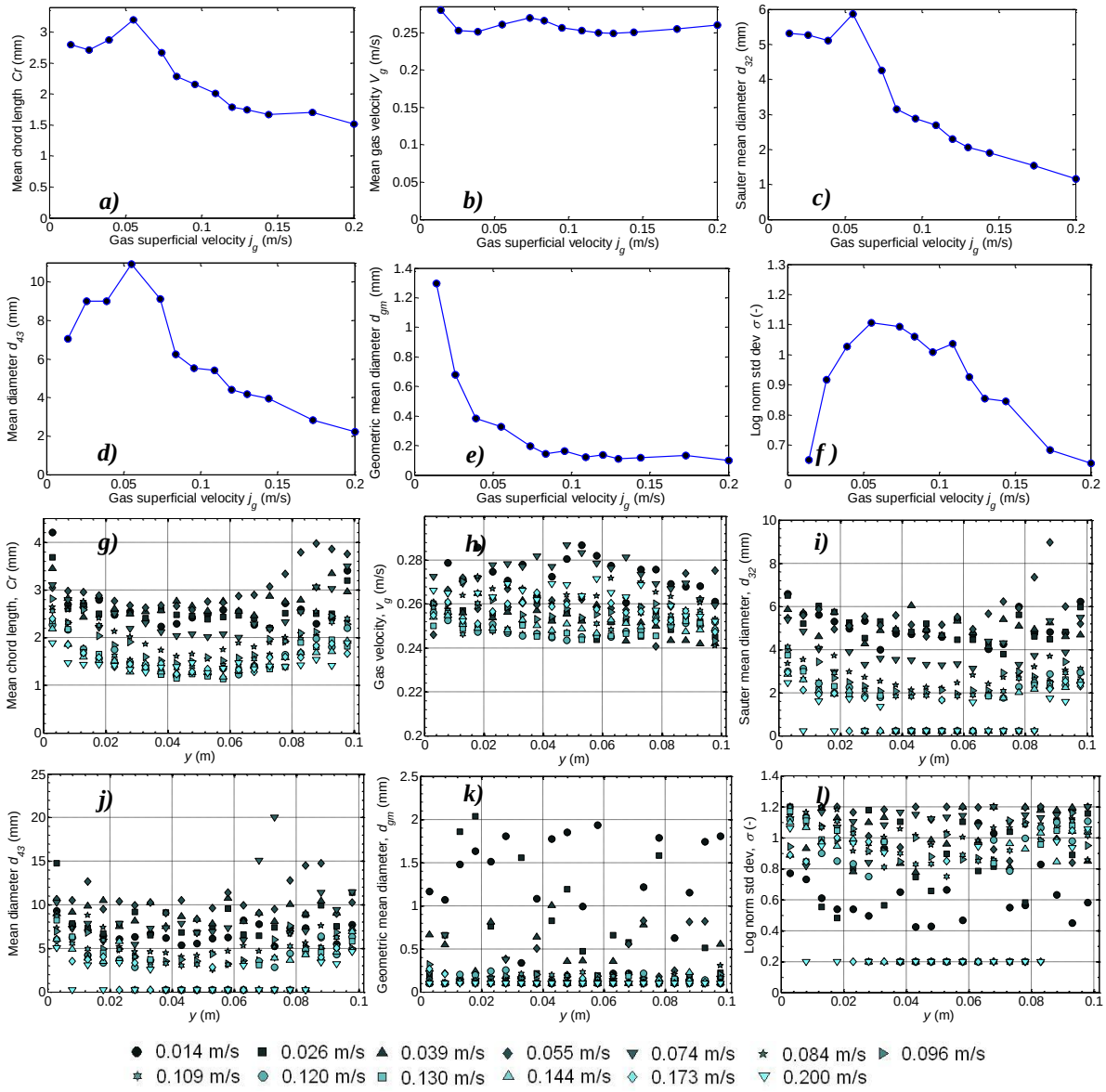


Figure D.13 Bubble transformation analysis output: the bubble rise velocity range is <u>0.1 to 0.9 m/s (ACCEPT THE FIRST MATCHING BUBBLE MODE).</u>

LIST OF PUBLICATIONS

JOURNAL PAPERS

AL-OUFI, F.M., RIELLY, C.D. and CUMMING, I.W., An experimental study of gas void fraction in dilute alcohol solutions in annular gap bubble columns using a four-point conductivity probe, Chemical Engineering Science (accepted for publication).

Fahd M. Al-Oufi, Iain W. Cumming and Chris D. Rielly, 2010, Destabilisation of Homogeneous Bubbly Flow in an Annular Gap Bubble Column , Canadian Journal of Chemical Engineering, 88, 482-490.

ORAL PRESENTATION

AL-OUFI, F.M., RIELLY, C.D. and CUMMING, I.W., An experimental study of gas void fraction in dilute alcohol solutions in annular gap bubble columns using a four-point conductivity probe, GLS 10 conference, June 2011, Braga, Portugal (accepted for oral presentation).

AL-OUFI, F.M., CUMMING, I.W. and RIELLY, C.D., 2009. Destabilisation of a homogeneous bubbly flow in an annular gap bubble column IN: Chemical Engineering. 8th World Congress of Chemical Engineering- GLS 09, Montreal, Canada, 23rd – 27th August.

AL-OUFI, F.M., CUMMING, I.W. and RIELLY, C.D., 2009. Experimental study on bubbly flow transition in vertical annular gap bubble column. IN: Chemical Engineering. The Saudi International Conference, University of Surrey, United Kingdom, 5th-6th June.

AL-OUFI, F.M., RIELLY, C.D. and CUMMING, I.W., 2007. Experimental study of void fraction behaviour in vertical bubbly gas-liquid flow using conductivity and measurements. Proceedings of the Saudi Innovation Conference, Newcastle-upon-Tyne, United Kingdom, 11th- 12th May, pp. 178-186.

Canadian Journal of Chemical Engineering, 88, 482-490, 2010

Destabilization of homogeneous bubbly flow in an annular gap bubble column

Fahd M Al-Oufi, Iain W Cumming, Chris D Rielly1

Department of Chemical Engineering, Loughborough University,

Loughborough, Leics, LE11 3TU, UK

ABSTRACT

Experimental results are presented to show that there are very significant differences in the mean gas void fractions measured in an open tube and a annular gap bubble column, when operated at the same gas superficial velocity, using a porous sparger. The mean gas void fraction decreases with increasing ratio of the inner to outer diameter of the annular gap column and the transition to heterogeneous flow occurs at lower gas superficial velocities and lower void fractions. Two reasons are proposed and validated by experimental investigations: (1) the presence of the inner tube causes large bubbles to form near the sparger, which destabilize the homogeneous bubbly flow and reduce the mean void fraction; this was confirmed by deliberately injecting large bubbles into a homogeneous dispersion of smaller bubbles and (2) the shape of the void fraction profiles changes with gap geometry and this affects the distribution parameter in the drift flux model.

Keywords

void fraction profiles, heterogeneous flow, flow transition, two-point conductivity probe

1 *Corresponding author email: C.D.Rielly@lboro.ac.uk, Tel:+44 (0) 1509 222504, Fax: +44 (0) 1509 223923*

Chemical Engineering Science (accepted for publication)

An experimental study of gas void fraction in dilute alcohol solutions in annular gap bubble columns using a four-point conductivity probe

Fahd M. Al-Oufi, Prof. Chris D. Rielly[*] and Dr. Iain W. Cumming

Department of Chemical Engineering, Loughborough

University, Loughborough, LE11 3TU, UK.

ABSTRACT

The influence of alcohol concentration on the gas void fraction in open tube and annular gap bubble columns has been investigated using a vertical column with an internal diameter of 0.102 m, containing a range of concentric inner tubes which formed an annular gap; the inner tubes had diameter ratios from 0.25 - 0.69. Gas (air) superficial velocities in the range 0.014-0.200 m/s were investigated. Tap water and aqueous solutions of ethanol and isopropanol, with concentrations in the range 8 - 300 ppm by mass, were used as the working liquids. Radial profiles of the local void fraction were obtained using a four-point conductivity probe and were cross-sectionally averaged to give mean values that were within 12% of the volume-averaged gas void fractions obtained from changes in aerated level. The presence of alcohol inhibited the coalescence between the bubbles and consequently increased the mean gas void fraction at a given gas superficial velocity in both the open tube and the annular gap bubble columns. This effect also extended the range of homogeneous bubbly flow and delayed the transition to heterogeneous flow. Moreover, isopropanol results gave slightly higher mean void fractions compared to those for ethanol at the same mass fraction, due to their increased carbon chain length. It was shown that the void fraction profiles in the annular gap bubble column were far from uniform, leading to lower mean void fractions than were obtained in an open tube for the same gas superficial velocity and liquid composition.

Keywords: *flow transition, homogeneous flow, void fraction profile, conductivity probe, coalescence inhibition*

Corresponding author email: C.D.Rielly@lboro.ac.uk, Tel:+44 (0) 1509 222504, Fax: +44 (0) 1509 223923